UNIVERSITY OF CALIFORNIA, SAN DIEGO

Quantitative Near-field Microscopy of Heterogeneous and Correlated Electron Oxides

A dissertation submitted in partial satisfaction of the requirements for the degree of
Doctor of Philosophy

in

Physics

by

Alexander Swinton McLeod

Committee in charge:

Professor Dimitri N. Basov, Chair
Professor Yeshaiahu Fainman
Professor Andrew Kummel
Professor Brian Maple
Professor Congjun Wu

2017

The Dissertation of Alexander Swinton McLeod is approved, and it is acceptable in quality and form for publication on microfilm and electronically:

_____

_____

_____

_____

_____

Chair

University of California, San Diego

2017

DEDICATION

To my beloved parents, who have made me the scientist I am today.

EPIGRAPH

"*To see a World in a Grain of Sand,*

And a Heaven in a Wild Flower,

Hold Infinity in the palm of your hand,

And Eternity in an hour."

William Blake

"...can the human soul be glimpsed through a microscope? Maybe, but you'd definitely need one of those very good ones with two eyepieces."

Woody Allen

TABLE OF CONTENTS

TABLE OF FIGURES

ACKNOWLEDGEMENTS

I would like to acknowledge Professor Dimitri N. Basov for his support as the chair of my committee. Through all the countless investigations and revisions that culminated with the published works included herein, his wisdom and attentiveness have been irreplaceable. Had he not first chanced hiring an inexperienced young theorist, I surely would never have made it so far.

I would also like to acknowledge the collaborators with whom it has been my distinct pleasure to co-author the works of this dissertation. In particular, G. Dominguez, Z. Gainsforth, M. D. Goldflam, and E. van Heumen are consummate scientists without whom many of my achievements would have proved impossible. Their tireless enthusiasm and collaborative spirits have embodied the joy of scientific pursuit; their knowledgeable contributions to my thesis work are inestimable. The laboratories of M. Thiemens, R. Kostecki, and I. K. Schuller also warrant my sincere thanks for their patient and productive collaboration. It has also been my joy to mentor and work with P. Kelly, whose good-natured intellect was at least as helpful to me as the professional guidance I could offer. The enthusiasm and charisma of G. Andreev, who provided mentorship in the first formative years of my PhD, has left a lasting and positive impact on my capabilities and outlook as a experimental physicist. For that he deserves my sincere thanks. Lastly, my close friends and familiy deserve acknowledgement for the patience and support they provided me all throughout my thesis work.

Chapter 2, in full, is a reprint of the material as it appears in the following published article: A. S. McLeod, P. Kelly, M. D. Goldflam, Z. Gainsforth, A. J. Westphal, G. Dominguez, M. H. Thiemens, M. M. Fogler, D. N. Basov. Model for quantitative tip-enhanced spectroscopy and the extraction of nanoscale-resolved optical constants. *Phys. Rev. B.* 90, 085136 (2014). The dissertation/thesis author was the co-primary investigator and author of this material.

Chapter 3, in full, is a reprint of the material as it appears in the following published article: A. S. McLeod, I. T. Lucas, J. S. Syzdek, D. S. Middlemiss, C. P. Grey, D. N. Basov, R. Kostecki. IR Near-Field Spectroscopy and Imaging of Single Li_xFePO_4 Microcrystals. *Nano Lett.*

15, 1 (2015). The dissertation/thesis author was the co-primary investigator and author of this material.

Chapter 4, in full, is a reprint of the material as it appears in the following published article: A. S. McLeod, G. Dominguez, Z. Gainsforth, P. Kelly, H. A. Bechtel, F. Keilmann, A. Wesphal, M. Thiemens, D. N. Basov. Nanoscale infrared spectroscopy as a non-destructive probe of extraterrestrial samples. *Nat. Commun.* 5, 5445 (2014). The dissertation/thesis author was the co-primary investigator and author of this material.

Chapter 5 comprises a discussion of hardware development undertaken in close collaboration with M. D. Goldflam and D. N. Basov.

Chapter 6, in full, is a reprint of the material as it appears in the following published article: A. S. McLeod, E. van Heumen, J. G. Ramirez, S. Wang, T. Saerbeck, S. Guenon, M. D. Goldflam, L. Anderegg, P. Kelly, A. Mueller, M. K. Liu, I. K. Schuller, D. N. Basov. Nanotextured phase coexistence in the correlated insulator V_2O_3. *Nat. Phys.* DOI: 10.1038/NPHYS3882. The dissertation/thesis author was the co-primary investigator and author of this material.

VITA

a. Professional Preparation.

University of California	Berkeley	Physics & Astrophysics	B.A.	2010
University of California	San Diego	Physics	M.Sc.	2013
University of California	San Diego	Physics	Ph.D.	2017

b. Appointments.

2010	U.S. Naval Nuclear Propulsion Program
2010 – 2011	Research Associate, Molecular Foundry, Lawrence Berkeley National Laboratory, Berkeley, CA
2011 – 2015	PhD student in Physics, Department of Physics, University of California San Diego, San Diego, CA
2015 – 2016	Candidate for the PhD in Physics, Department of Physics, University of California San Diego, San Diego, CA

c. Awards:

2012 – 2015	U.S. Department of Energy Office of Science Graduate Fellowship
2014	Microscopy and Microanalysis Presidential Scholars Award
2011	UC San Diego Dept. of Physics Graduate Excellence Award

d. Selected Publications

A. S. McLeod, E. van Heumen, J. G. Ramirez, S. Wang, T. Saerbeck, S. Guenon, M. Goldflam, L. Anderegg, P. Kelly, A. Mueller, M. K. Liu, Ivan K. Schuller & D. N. Basov. "*Nanotextured phase coexistence in the correlated insulator V_2O_3*". Nature Physics. DOI: 10.1038/NPHYS3882

Gerardo Dominguez, A.S. McLeod, Zack Gainsforth, P. Kelly, Hans A. Bechtel, Fritz Keilmann, Andrew Westphal, Mark Thiemens & D.N. Basov "*Nanoscale infrared spectroscopy as a non-destructive probe of extraterrestrial samples*" Nature Communications 5:5445 | DOI: 10.1038/ncomms6445 |(2014).

A. S. McLeod, P. Kelly, M. D. Goldflam, Z. Gainsforth, A. J. Westphal, G. Dominguez, Mark. H. Thiemens, Michael M. Fogler, and D. N. Basov *"Model for quantitative tip-enhanced spectroscopy and the extraction of nanoscale-resolved optical constants." Phys. Rev. B* **90**, 085136 (2014).

A. S. McLeod, G. Dominguez, Z. Gainsforth, A. J. Westphal, F. Keilmann, D. N. Basov, and M. Thiemens. *"NanoFTIR for the Analysis of Planetary Materials"*, in: 44th Lunar and Planetary Sciences Conference (2013)

A. S. McLeod, I. T. Lucas, J. S. Syzdek, D. S. Middlemiss, C. P. Grey, D. N. Basov, and R. Kostecki *"IR Near-Field Spectroscopy and Imaging of Single Li_xFePO_4 Microcrystals."* Nano Letters 15(1), 1-7 (2015)

F. Keilmann, R. Hillenbrand, and A. S. McLeod *"Nano-FTIR – The Chemical Nanoscope."* Imaging & Microscopy (2013)

S. Dai, Z. Fei, Q. Ma, A. S. Rodin, M. Wagner, A. S. McLeod, M. K. Liu, W. Gannett, W. Regan, K. Watanabe, T. Taniguchi, M. Thiemens, G. Dominguez, A. H. Castro Neto, A. Zettl, F. Keilmann, P. Jarillo-Herrero, M. M. Fogler, D.N.Basov "*Tunable Phonon Polaritons in Atomically Thin van der Waals Crystals of Boron Nitride*" Science 343, 1125 (2014)

G. X. Ni, L. Wang, M. D. Goldflam, M. Wagner, Z. Fei, A. S. McLeod, M. K. Liu, F. Keilmann, B. Ozyilmaz, A. H. Castro Neto, J. Hone, M. Fogler, D. Basov. "*Ultrafast optical switching of plasmon polaritons in high-mobility graphene*" Nature Photonics 10, 244 (2016).

Martin Wagner, Zhe Fei, Alexander S. McLeod, Aleksandr S. Rodin, Wenzhong Bao, Eric G. Iwinski, Zeng Zhao, Michael Goldflam, Mengkun Liu, Gerardo Dominguez, Mark Thiemens, Michael M. Fogler, Antonio H. Castro Neto, Chun Ning Lau, Sergiu Amarie,

Fritz Keilmann, and D. N. Basov "*Ultrafast and Nanoscale Plasmonic Phenomena in Exfoliated Graphene Revealed by Infrared Pump–Probe Nanoscopy*" Nanoletters 14, 894 (2014).

Z. Fei, A. S. Rodin, G. O. Andreev, W. Bao, A. S. McLeod, Z. Zhao, M. Thiemens, G. Dominguez, M. M. Fogler, A. H. Castro Neto, C. N. Lau, F. Keilmann & D. N. Basov, *"Gate-tuning of graphene plasmons revealed by infrared nano-imaging"* Nature 487 82 (2012).

e. Graduate advisor: Dimitri N. Basov, University of California San Diego

f. Undergraduate advisees: Loic Anderegg, Priscilla Kelly, Rubin Iraheta

ABSTRACT OF THE DISSERTATION

Quantitative Near-Field Microscopy of Heterogeneous and Correlated Electron Oxides

by

Alexander Swinton McLeod

Doctor of Philosophy in Physics

University of California, San Diego, 2017

Professor Dimitri N. Basov, Chair

Scanning near-field optical microscopy (SNOM) is a novel scanning probe microscopy technique capable of circumventing the conventional diffraction limit of light, affording unparalleled optical resolution (down to 10 nanometers) even for radiation in the infrared and terahertz energy regimes, with light wavelengths exceeding 10 micrometers. However, although this technique has been developed and employed for more than a decade to a qualitatively impressive effect, researchers have lacked a practically quantitative grasp of its capabilities, and its application scope has so far remained restricted by implementations limited to ambient atmospheric conditions. The two-fold objective of this dissertation work has been to address both these shortcomings. The first half of the dissertation presents a realistic, semi-analytic, and benchmarked theoretical description of probe-sample near-field interactions that form the basis of

SNOM. Owing its name to the efficient nano-focusing of light at a sharp metallic apex, the "lightning rod model" of probe-sample near-field interactions is mathematically developed from a flexible and realistic scattering formalism. Powerful and practical applications are demonstrated through the accurate prediction of spectroscopic near-field optical contrasts, as well as the "inversion" of these spectroscopic contrasts into a quantitative description of material optical properties. Thus enabled, this thesis work proceeds to present quantitative applications of infrared near-field spectroscopy to investigate nano-resolved chemical compositions in a diverse host of samples, including technologically relevant lithium ion battery materials, astrophysical planetary materials, and invaluable returned extraterrestrial samples. The second half of the dissertation presents the design, construction, and demonstration of a sophisticated low-temperature scanning near-field infrared microscope. This instrument operates in an ultra-high vacuum environment suitable for the investigation of nano-scale physics in correlated electron oxides at cryogenic temperatures, thus vastly expanding the scope of applications for infrared SNOM. Performance of the microscope is demonstrated through quantitative exploration of the canonical insulator-metal transition occuring in the correlated electron insulator V_2O_3. The methodology established for this investigation provides a model for ongoing and future nano-optical studies of phase transitions and phase coexistence in correlated electron oxides.

CHAPTER 1: Introduction to scanning near-field optical microscopy (SNOM)

1.1 Introduction

In life, it is often claimed *a man's reach should extend beyond his grasp*. A fine and worthwhile adage for the everyday, this mantra pertains no less to the spheres of scientific endeavour. And yet, the *scientific method* calls us always, in the end, to test our predictions (however creative or ingenious) against objective reality. By implication then, scientific pursuit demands another standard that rises beyond our cherished maxim: Steadily, unwaveringly, we scientists strive to meet and match our *grasp* with the far-flung reaches of our scientific imagination. There are natural divisions to this labor. But the builders, developers, and tinkerers of experimental science in this way quietly stand out as the unsung heroes- those whose technical achievements slowly and often inconspicuously bring the scientist's *grasp* at last into contact with his *reach*. Pursuing and attaining these cherished moments of contact is perhaps nowhere more thrilling than in the field of microscopy, where biological cells, chemical molecules, atomic vibrations, and electronic fluctuations are the actors in a complex and beautiful drama. The role of a microscope is to cast light on this stage, at all angles and in all settings, allowing the biologist, the chemist, and the physicists make contact with structures and events that all too naturally play out at microscopic (sizes $\sim 10^{-6}$ meters) and even nanoscopic (10^{-9} meters) scales.

This chapter of the thesis serves by way of introduction to highlight the rapidly advancing position of near-field microscopy, a sub-diffractional microscopy technique, in the context super-resolution microscopies. The unique ability of scanning near-field optical microscopy (SNOM) to probe subtle optical properties of materials and physical systems within precise nanometer volumes has inspired its application to select problems of chemical analysis and condensed matter physics research presented within this thesis work.

1.2 1 Introduction

Conventional microscopy relies upon the far-field stimulation and detection of electromagnetic fields from samples that can be as small as micrometers in size. The resolving power of far-field microscopy however is subject to the *diffraction limit*, expressed quantitatively through the Raleigh criterion: $d \approx 6.1\,\lambda/NA$ - two objects can be resolved at wavelength λ with a numerical aperture of *NA* by *at best* a distance d.

The first documented suggestion of an imaging technique capable of subverting the diffraction limit was proposed by E. H. Synge in 1928, in a letter to Albert Einstein [9]. Synge envisioned bringing a nano-scale aperture, punctured through a highly reflective film, to just above the surface of a semi-transparent sample illuminated by focused light from below. According to Synge, the light transmitted to the far-field above the film could then be attributable *only* to the sub-diffraction sample region at the aperture spot on account of local *near-field coupling*.

Einstein reportedly remained skeptical, unconvinced of the potential throughput of the underlying near-field coupling. In response, Synge proposed the use of a sharply tapered aperture, capable in theory of more efficient near-field coupling to nano-resolved sample regions. Indeed, he even envisioned the rapid raster-scanning of a sample with this technique using high-precision piezo-electric crystal translators, an essential element of today's scanning probe microscopes. Though neglected for decades after its inception, Synge's original idea has recently become an exciting reality. Modern near-field microscopes are variously configured, but the two most common configurations - aperture-based and apertureless (scattering) - are depicted in Fig. 1.1. Somewhat unlike Synge's original conception, the scattering configuration confers notable advantages by way of of improved resolution, throughput [3], and a more straightforward theoretical understanding of the operational mechanism [1].

1.3 2 Essential theory of near-field interactions in SNOM

Scattering-mode SNOM (or sSNOM, abbreviated elsewhere in the thesis to simply SNOM or to ApperturelessNSOM / ANSOM) may be simply understood and theoretically modeled by considering the mutual electromagnetic polarization of a pointed metal probe under the influence of 1) incident laser light at frequency ω, 2) the local dielectric properties of the sample characterized by optical constant ϵ_s, and 3) the polarizability of the tapered metallic probe tip with radius of curvature a and optical constant ϵ_t. During measurement, these elements participate in a mutual near-field interaction, resulting in back-scattered light ("signal") sensitive to the nano-scale environment of the probe. This self-consistent near-field interaction is depicted schematically in Fig. 1.1, indicating how it can be leveraged in an experimental context to glean nano-scale information about the optical permittivity of heterogeneous and nano-structured samples.

The most basic understanding of this interaction models the probe as uniformly polarizable sphere with polarizability $\alpha_0 = 4\pi a^3 \frac{\epsilon_t - 1}{\epsilon_t + 2}$. When illuminated by an incident electric field $\vec{\mathbf{E}}$, the dipole moment induced in the probe is given approximately by:

$$\begin{aligned} \vec{\mathbf{p}} &= \alpha_0(\vec{\mathbf{E}} + \mathbf{G}_{dp}\vec{\mathbf{p}}) \\ \therefore \quad \vec{\mathbf{p}} &\approx \frac{\alpha_0 \vec{\mathbf{E}}}{1 - \alpha_0 \mathbf{G}_{dp\,zz}} \\ \mathbf{G}_{dp\,zz} &= r_p(\omega)/4\pi(a+z)^3 \end{aligned} \tag{1}$$

Here $\mathbf{G}_{dp}$ is the Green's dyadic function for a radiating dipole over a surface in the quasi-static approximation. The Fresnel coefficient for p-polarized radiation $r_p(\omega)$ characterizes the local influence of the sample through $r_p(\omega) \approx \frac{\epsilon_s - 1}{\epsilon_s + 1}$. Since the intensity of back-scattered radiation from the probe is proportional to its induced dipole moment, Eq. 1 provides a theory for the material contrast observed in sSNOM through dependence on the local value of $\epsilon_s(\omega)$. This

theory can be understood as a mutual interaction of the probe tip with its “mirror image" dipole, as depicted in Fig. 1.2a. Several more realistic variants of this near-field theory have been proposed and are finding promising application in the quantitative description of nano-scale dielectric properties through comparison with experimental sSNOM imaging and spectroscopy measurements. One such variation treats explicitly the sensitivity of sSNOM to sub-surface material properties and multiple reflection effects in multilayered media (depicted schematically in Fig. 1.2b) [1]. This formulation provides a starting point for describing light momentum-dependent near-field interactions between an illuminated probe tip and surface modes such as surface phonon- and plasmon-polaritons. The present thesis work detailed in Chapter 2 was undertaken to provide a fully quantitative description of these phenomena without resort to undue theoretical simplifications. Consequently, as so was uncovered, a great deal more can be gleaned from the measurables of near-field experiments than simple models of the near-field interaction might lead one to expect.

1.4 Detection of minute probe-scattered signals in SNOM

Fig. 1.3 details the conceptual configuration of an SNOM microscope and the optical components that are employed for effective *interferometric* detection of minute radiation signals back-scattered from the near-field probe. One of several sources of coherent radiation (typically laser sources as shown, especially for SNOM in the infrared frequency range) illuminates an optical beam-splitter, which divides the radiation into two arms (paths) of, effectively, a *Michelson interferometer*. The first arm simply employs reflection from a flat mirror, radiation from which serves as a “reference” field in an interferometric detection scheme. This radiation partially reflects from the beam splitter towards a photodetector.

Meanwhile, in the second interferometer arm, radiation is carefully focused to the apex of the near-field probe, which is typically a sharp metal-coated tip adjoined to a cantilever, and mounted as the probe of an atomic force microscope (AFM). The role of the AFM is to

controllably raster-scan the sample below the sharp near-field probe, while carefully maintaining precise contact between the tip and the sample surface. This is typically accomplished by operating the AFM and the probe in a “non-contact” mode, where the cantilever is oscillated at its natural frequency (many tens or hundreds of kHz) at an amplitude of 10s of nanometers above the sample. By way of the distance dependent probe-sample near-field interaction, this “dithering” in turn modulates all back-scattered radiation associated with the near-field interaction at higher harmonics of the dither frequency, which serves as a “carrier frequency” for probe-scattered radiation.

When using a monochromatic radiation source, SNOM images of the sample’s near-field response can be registered by the following method. The probe-scattered radiation, upon reaching the photodetector, *interferes* with the far more intense reference field, yielding a total detected intensity signal. The dithered near-field scattering of interest is in this way multiplicatively enhanced in magnitude by the reference field, and further can be isolated from radiation background (often two or three orders of mangnitude larger in amplitude) by means of lock-in amplification of the detected intensity at harmonics of the dither frequency. This step is called “demodulation” of the signal. In the so-called pseudo-heterodyne detection scheme[14], the reference arm is further phase-modulated, which cleverly allows a segregation of amplitude and phase signals associated with the near-field interaction (Fig. 1.4), on the basis of which images of both can be resolved across the sample surface with nano-scale resolution limited only by sharpness of the near-field probe.

Alternatively, when using a broadband radiation source (often a pulsed laser, such as that exmplified in Fig. 1.4, boxed red), demodulated detector intensity can be registered as a function of overall displacement of the interferometer reference arm mirror, yielding a so-called “interferogram” whose Fourier transform with respect to the mirror displacement resolves the near-field response of the sample spectrally, according to the frequency of light. With infrared laser illumination, this method dubbed nano-scale Fourier transform infrared (or nano-FTIR)

spectroscopy.[15] Especially when used in tandem, the imaging and spectroscopic capabilities of a SNOM enable impressive characterizations of nano-structured samples. Both modalities are used throughout the present thesis work.

1.5 Example applications: Nanoscale mapping and spectroscopy of mobile carriers

The sensitivity of near-field microscopy to local material properties has been demonstrated in measurements of nano-structured semiconductor devices, fabricated with regions of varying carrier concentration [6]. Image scans of a multiple transistor device acquired with sSNOM at infrared (IR) and terahertz (THz) frequencies are shown in Fig. 1.5. Illumination of the probe tip was provided with lasers tuned to the desired frequencies, providing a means to *near-field spectroscopy* at the nano-scale.

At IR frequencies, pronounced near-field contrast is evident only between materials of differing lattice composition. In the second panel of Fig. 1.5, high signal (red) is attained only over $NiSi$ contacts at the top of the device, and is characteristic of a nearby phonon resonance relative to the ambient Si (blue). In contast, THz frequencies enable the direct probing of mobile carriers (electrons and holes) through the probe tip's local excitation and response to plasma oscillations. Near-field contrast is correlated with proximity to the local on-resonance plasma frequency $\omega_p \propto \sqrt{n}$, providing a nano-resolved mapping of relative carrier concentration at locations throughout the device. The theoretical calculations shown in Fig. 1.6 enable a qualitative description of these relative carrier concentrations by correlating the Drude response at a given carrier density with the expected near-field signal through the formalism discussed in Sec. 1.2. The origin of contrast at THz rather than at IR frequencies in the Si portions of the semiconductor device becomes evident.

1.6 Example applications: Spatial mapping of collective electromagnetic surface modes - *polaritons*

Extensions of the theoretical formalism presented in Sec. 1.2 have been used to describe the radiation field at the apex of an illuminated near-field probe as a superposition of plane waves. Because of the intense field localization (the “lightning rod effect"), these plane waves are characterized by extremely high momentum in the direction tangent to the sample surface. These high-momentum fields can be used both to excite and detect novel surface modes in materials which could not otherwise be coupled into far-field radiation due to conservation of momentum.

Recent experiments demonstrate this novel application. Fig. 1.7a displays a real-space sSNOM measurement of surface phonon-polariton wave-patterns on the surface of a SiC crystal. These were produced by the scattering of illuminating IR laser light into these high-momentum modes via polarization of $\sim 10\mu m$ gold nanodisks fabricated on the surface of the crystal.[7] The induced local dipolar fields of these nanodisks are shown simulated in the lower left panel of Fig. 7a.

The agreement between theoretically computed surface phonon amplitude and phase patterns with the measured near-field scans is remarkable, exhibiting the possibility of directly measuring the dispersion of such surface modes using near-field spectroscopy. By tuning the frequency of the illumination laser, wave-patterns of the sort shown can be acquired in entire frequency bands to construct the functional dependence $\lambda(\omega)$, providing a direct *dispersion map* of novel high-momentum surface modes. As a proof of concept, the observed wavelength in the provided images can be compared with the theoretical dispersion of SiC surface optical phonons displayed in Fig. 1.7b.

1.7 Example applications: Nano-plasmonic imaging

The superb nano-scale resolution of near-field imaging has proven a useful tool for mapping the field distributions around nano-plasmonic antenna structures, designed and

fabricated as the building-blocks of tomorrow's nano-plasmonic devices. These structures were envisioned as nano-scale counterparts to classical antenna circuits, but designed for length scales consistent with surface-plasmon resonances in the noble metals (such as Au and Ag). Characterization of their *in situ* properties has previously relied on far-field measurements of mesoscopic ensembles, but near-field microscopy is capable of directly addressing the electromagnetic modes of individual nano-structures.

Fig. 1.8 displays the simulated and measured field distributions of an IR-resonant gold nano-plasmonic dipole antenna fabricated on a transparent substrate, illuminated from below and measured with a "passive" (nominally non-perturbative) crystalline silicon near-field probe.[11] The demonstrated agreement between theory and experiment demonstrates that these antennae perform as-designed, with a tunable impedance loading controlled by opening or closing the antenna feedgap. This experiment confirms the simultaneous sensitivity of sSNOM to nano-scale field *intensity and phase*.

1.8 Example applications: Graphene plasmonics

The possibility to both excite and detect high-momentum surface modes using near-field finds ideal application in the study of novel 2-dimensional conducting materials such as *graphene*, a single atomic layer carbon allotrope exfoliated or grown on a substrate. A recent notable experiment has utilized *near-field spectroscopy* to detect the excitation of *Dirac plasmons* in single-layer graphene on an SiO_2 substrate.[5] The Dirac plasmon is so-named as a collective charge oscillation of quasiparticles subject to Dirac-Hamiltonian-like dynamics at the Fermi level in graphene, and is theorized to exhibit low-loss propogation, a promising feature for future plasmonics applications.

By exciting single-layer graphene at different frequencies in the vicinity of SiO_2 surface phonon resonance at $\omega \approx 1125 cm^{-1}$ with illumination from a bank of tunable quantum cascade lasers, a reference-normalized near-field spectrum was acquired in a nano-scale region at the

interface of graphene, SiO_2, and the Si substrate. The resulting spectrum (Fig. 1.9c) displays a remarkable enhancement of the SiO_2 surface phonon, resulting from the hybridization of the SiO_2 phonon with the Dirac plasmon.

As suggested previously in Sec. 4, near-field microscopy is capable not only of exciting and detecting high-momentum surface modes, but also directly imaging their real-space patterns. Real-space images of Dirac plasmons confined to a nano-cone of single layer graphene on SiO_2 substrate are displayed in Fig. 1.9b, exhibiting standing wave patterns in both amplitude and phase. To confirm the authenticity of the plasmon oscillation, theoretical calculations were performed to model the wave-pattern induced by localized tip excitation at each position in the scan. These theoretical predictions exhibit remarkable agreement with the measured wavelength of the graphene plasmon in these patterns. As of this writing, this work is part of an ongoing effort to map spectroscopically and in real-space the dispersion and propagation of plasmons in graphene.

1.9 Example applications: Tip-enhanced Raman spectroscopy

One of the newest near-field spectroscopy techniques developed in recent years draws inspiration from the phenomenon of *surface-enhanced Raman scattering*, whereby the inelastic scattering of light by molecules and other chemical structures is enhanced by many orders of magnitude due to the high-intensity electromagnetic “hot spots" of a nearby rough, metallic surface. The Raman scattering “fingerprint" serves as a unique spectroscopic identifier for many substances, and techniques for the enhancement of inelastic scattering has made this phenomenon a practical and powerful technique for chemical identification.

In analogy, a *tip-enhanced* form of Raman scattering and spectroscopy (TERS) with nano-scale resolution is made possible through the local focusing of high-intensity electromagnetic fields at the apex of a laser-illuminated metallic probe tip, as in sSNOM. Recent experiments have utilized special surface-plasmon resonant probe tips with high intensity optical

illumination to boost Raman signal for the rapid spectroscopic chemical identification of sample surfaces.

One such experiment has claimed to resolve the spectroscopic fingerprint of individual nucleotides along a chain of RNA with nano-scale resolution.[2] Spectra collected at the positions given in Fig. 1.10a are shown in Fig. 1.10b, in which the Raman fingerprint of the cytosine nucleotide can be discerned in the signal. By pushing the resolution limits of this technique, one might envision direct sequencing of nucleic acids with metallic probe tips through TERS detection and identification.

The ongoing design of plasmon-resonant probe tips has improved the Raman signal levels attainable with TERS by orders of magnitude. This effort focuses on improving the resonance matching condition for a probe illuminated at a particular Raman excitation frequency - as from a $\lambda = 523\,nm$ green diode laser for example. Recent experiments with resonant coaxial aperture probes have demonstrated the possibility of *hyperspectral imaging*, whereby usable millisecond-exposure Raman spectra are acquired at each pixel of a conventional AFM/near-field scan.[13] This technique was demonstrated for the detection of carbon nanotubes by spatially resolving the strength and frequency shift of the D and G vibrational bands (characteristic of carbon allotropes), as displayed in figure 8c, ideally providing a local probe of carbon lattice structure with nano-scale precision.

1.10 Conclusion: A technique for diverse applications in nano-science

Near-field microscopy has emerged as an experimental technique at the forefront of sub-diffraction (often called “super-resolution”) imaging and spectroscopic methods. Though predicated on a nearly century-old experimental concept, recent applications such as surface mode spectroscopy and tip-enhanced Raman continue to re-invigorate and extend this microscopy technique, pushing the boundaries of nano-scale detection. The examples presented

in this survey demonstrate the continued utility and necessity of sub-diffraction techniques for the nano-scale study of plasmonic nano-structures, novel materials such as graphene, and even biological systems, promising an unbounded future for applications and extensions near-field microscopy. Basic technical aspects of SNOM implementation and application not otherwise presented here may find ample presentation in the excellent thesis work of N. Ocelic,[16] one of the early pioneers of quantitative SNOM measurements. The present thesis work builds upon such various and inspiring efforts at the levels of 1) theory, 2) applications, and 3) instrumentation, thus extending near-field microscopy to the spatio-spectral study of chemical composition in heterogeneous and correlated electron oxides.

1.11 Figures

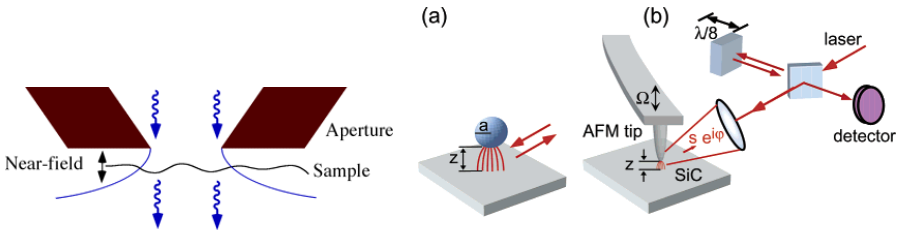

(a) Aperture-based detection [10]

(b) Apertureless (scattering) detection [12]

Figure 1.1: Synge's original proposal was based on illumination and/or collection via a nano-aperture in pointed metallic probe.

(Left) In spite of limited throughput, this configuration is commonly implemented using metal-coated fiber probes. (Right) The apertureless (scattering) configuration improves throughput via the polarization of an elongated antenna-like probe tip. This concept is presented in (a) the abstract and (b) an experimental implementation.

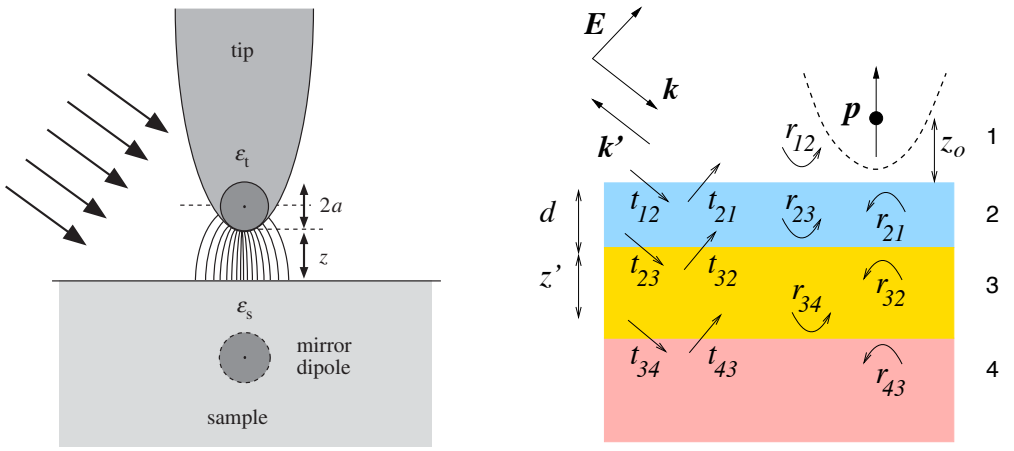

(a) Image dipole model of the tip-sample near-field interaction

(b) Multilayer reflection formalism

Figure 1.2: Basic theoretical description of the probe-sample near-field interaction in SNOM.

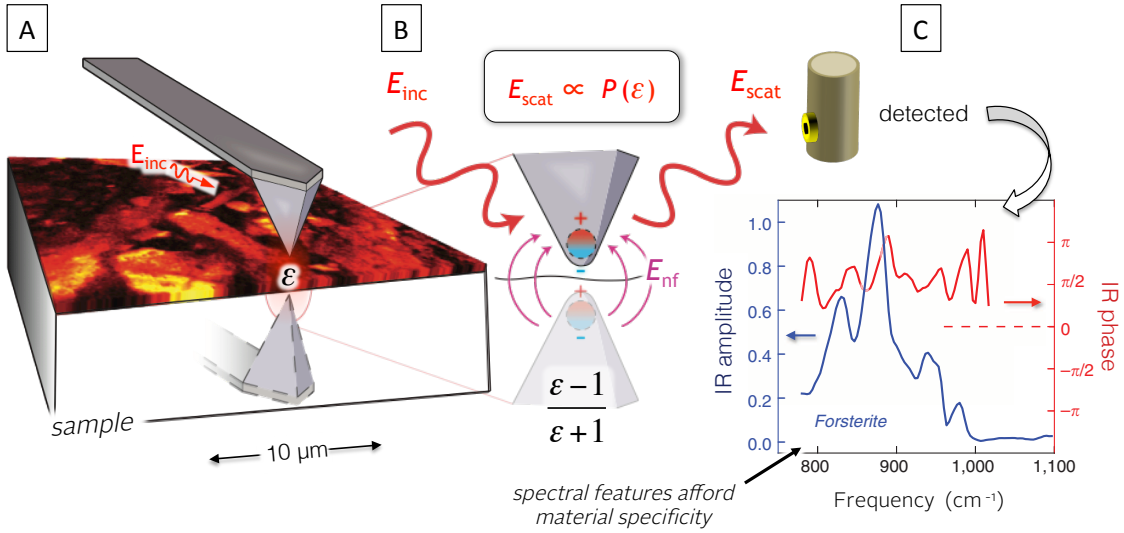

Figure 1.3: Schematic depiction of the probe-sample near-field interaction relevant to s-SNOM.

(A) The probe tip interacts with a thin surface volume characterized by permittivity ε, which may dependent strongly on the optical frequency on incident light. (B) The incident electromagnetic field E_{inc} induces a strong dipole moment in the tip, which interacts with an induced mirror dipole in the sample. The strength of the mirror dipole is determined by the local permittivity (expression given above). Resulting near-field interactions E_{nf} affect the tip polarization p_z in a way that depends sensitively on ε, locally modulating the amplitude and phase of the tip-scattered field E_{scat}. (C) E_{scat} detected in the far-field affords sub-diffractional sensitivy to the sample permittivity. Shown are amplitude and phase of the optical frequency-dependent scattered signal, revealing spectral features that afford material specificity on the nanometer-scale.

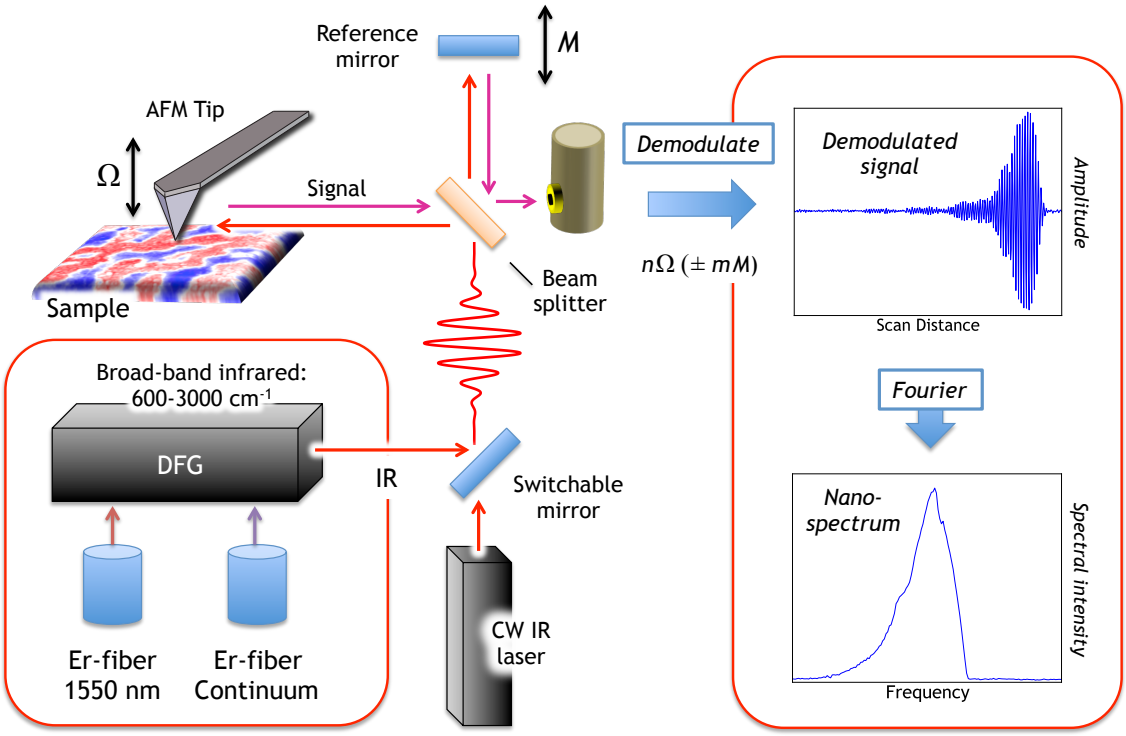

Figure 1.4: Experimental configuration of an infrared scanning near-field optical microscope (SNOM).

An infrared SNOM can perform both broad-band spectroscopy and single-frequency imaging. These modalities are enabled by, respectively, (bottom left) a broad-band infrared source, such as a lamp or difference-frequency generation source (pictured) based on ultrafast fiber lasers, and a continuous wave (CW) laser, with the option to switch between these sources. A beam-splitter divides incident light between illumination of a near-field probe (AFM tip) and a flat reference mirror. (middle) At the detector element, interference between back-scattered light collected from the near-field probe and "reference light" enables interferometric detection of minute near-field signals. *Viz.*, when the probe and reference mirror are dithered at frequencies Ω and *M*, respectively, detected intensity demodulated at harmonic frequencies $n\Omega(\pm mM)$ is guaranteed proportional to the desired field E_{nf}. With a broadband source, sweeping the reference mirror position (undithered, *M=0*) allows collecting an interferogram (top left) whose Fourier transform reveals the spectroscopic near-field response.

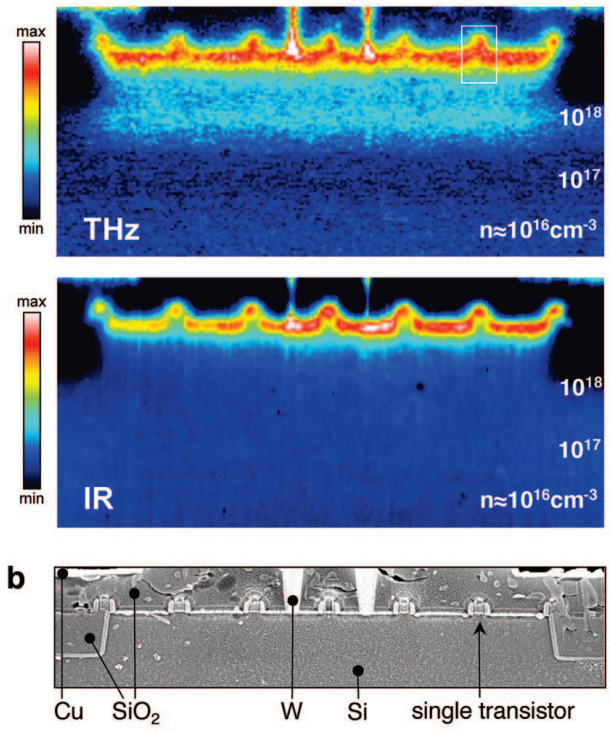

Figure 1.5: High-resolution sSNOM images acquired for a sliced semiconductor device several microns in size.

Contrast between regions of differing carrier concentration is improved at THz frequencies. An SEM image of the device topography is shown in the bottom panel.[6]

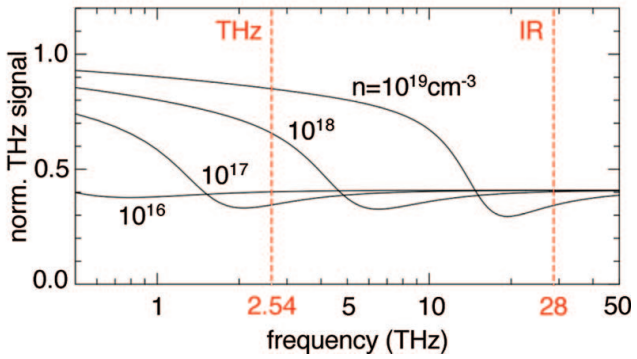

Figure 1.6: Drude theory for the response of free carriers in a metal predicts high near-field contrast at frequencies $\omega \sim \omega_p$, the local free carrier plasma frequency.[6]

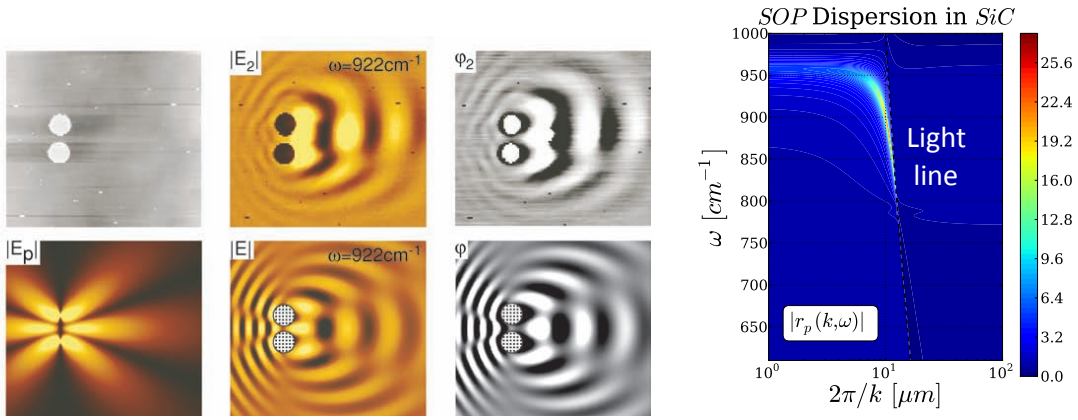

Figure 1.7: Real-space near-field measurements and theoretical predictions of surface phonon-polaritons.

(Left 6 panels) Measured and simulated surface phonon wave-patterns. AFM topography of $\sim 10\mu m$ diameter gold nanodisks on the SiC surface is shown in the upper left panel. At $\omega = 922cm^{-1}$ the patterns exhibit $\lambda \approx 20\mu m$, in agreement with the predicted surface phonon-polariton dispersion of SiC. [7] **(Right panel)** Theoretical dispersion of polaritons at the SiC-air interface. Characteristic momenta $k > \omega/c$ outside the light-line make these modes challenging to excite or detect using far-field techniques.

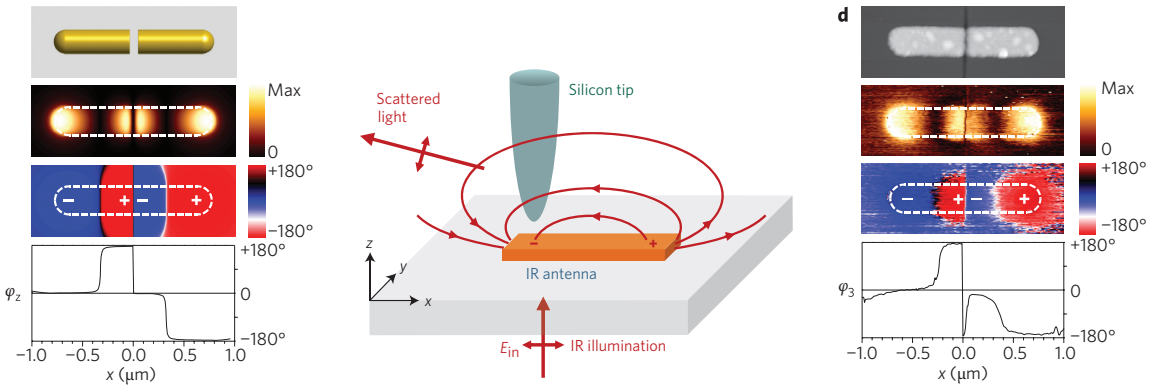

Figure 1.8: Local mapping of the field distributions of nano-plasmonic antenna structures.

(a) Simulated field distribution of a nano-dipole antenna[11] (b) Experimental configuration[11] (c) Field distribution measured with sSNOM[11]

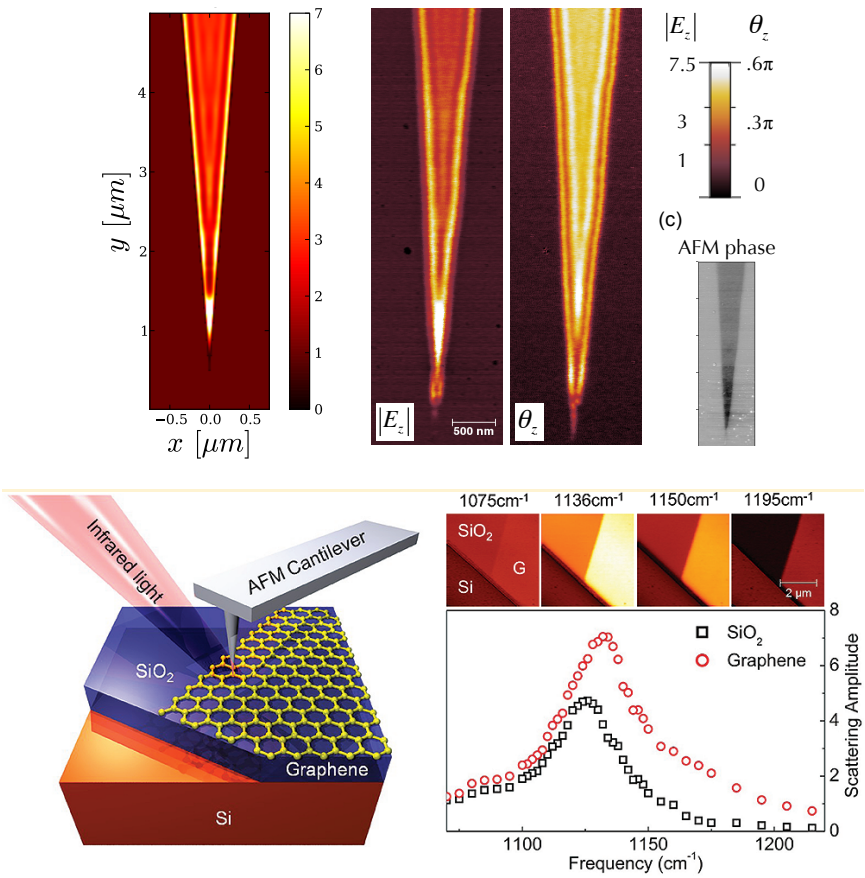

Figure 1.9: Near-field excitation and measurement of *Dirac plasmons* in exfoliated single-layer graphene.

(Top panels) Simulated (left) and measured (right) plasmons proagating on a graphene nano-cone, both excited and detected using a sharp near-field probe tip. **(Bottom panels)** *Spectroscopic evidence:* Characteristic enhancement and blue-shift of the SiO_2 surface phonon due to hybridization with a graphene Dirac plasmon.[5]

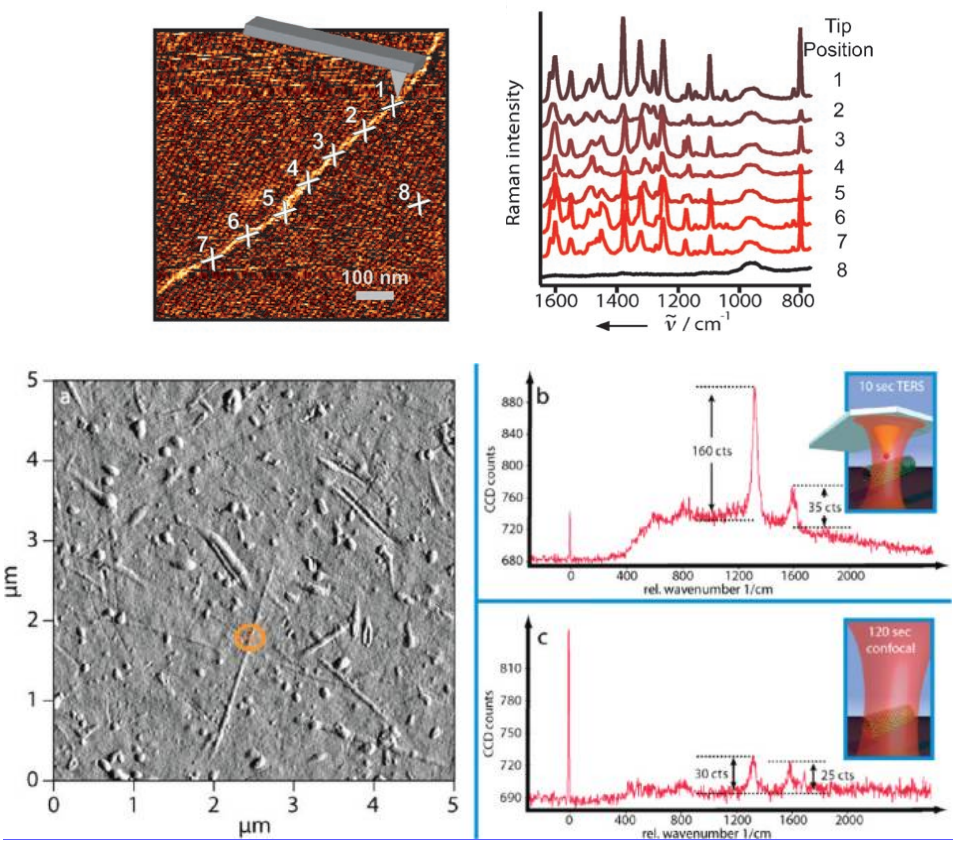

Figure 1.10: Successful demonstrations of TERS, demonstrating the potential for spectroscopic chemical identification with nano-scale resolution.

(Top Left) AFM topography of RNA on mica substrate[2] (Top Right) Individual TERS spectra from nano-resolved positions. (Bottom Panels) TERS of individual carbon nanotubes, displaying an increase of orders of magnitude in sensitivity over conventional Raman microscopy[13]

1.12 References

1. Javier Aizpurua, Thomas Taubner, F. Javier García de Abajo, Markus Brehm, and Rainer Hillenbrand. Substrate-enhanced infrared near-fieldspectroscopy. *Opt. Express*, 16(3):1529–1545, Feb 2008.

2. Elena Bailo and Volker Deckert. Tip-Enhanced Raman Spectroscopy of Single RNA Strands: Towards a Novel Direct-Sequencing Method. *Angewandte Chemie International Edition*, 9999(9999):NA+, 2008.

3. M. Brehm, A. Schliesser, F. Cajko, I. Tsukerman, and F. Keilmann. Antenna-mediated back-scattering efficiency in infrared near-field microscopy. *Opt. Express*, 16(15):11203–11215, Jul 2008.

4. Dana Cialla, Tanja Deckert-Gaudig, Christian Budich, Michael Laue, Robert Möller, Dieter Naumann, Volker Deckert, and Jürgen Popp. Raman to the limit: tip-enhanced raman spectroscopic investigations of a single tobacco mosaic virus. *Journal of Raman Spectroscopy*, 40(3):240–243, 2009.

5. Zhe Fei, Gregory O. Andreev, Wenzhong Bao, Lingfeng M. Zhang, Alexander S. McLeod, Chen Wang, Margaret K. Stewart, Zeng Zhao, Gerardo Dominguez, Mark Thiemens, Michael M. Fogler, Michael J. Tauber, Antonio H. Castro-Neto, Chun Ning Lau, Fritz Keilmann, and Dimitri N. Basov. Infrared nanoscopy of dirac plasmons at the graphene-sio_2 interface. *Nano Letters*, 11(11):4701–4705, 2011.

6. A J Huber, F Keilmann, J Wittborn, J Aizpurua, and R Hillenbrand. Terahertz near-field nanoscopy of mobile carriers in single semiconductor nanodevices. *Nano Letters*, 8(11):3766–70, 2008.

7. A. J. Huber, N. Ocelic, and R. Hillenbrand. Local excitation and interference of surface phonon polaritons studied by near-field infrared microscopy. *Journal of Microscopy*, 229(3):389–395, 2008.

8. Fritz Keilmann and Rainer Hillebrand. Near-field microscopy by elastic light scattering from a tip. *Philosophical Transactions of the Royal Society of London. Series A: Mathematical, Physical and Engineering Sciences*, 362(1817):787–805, 2004.

9. L. Novotny. *Chapter 5: The history of near-field optics*, volume 50 of *Progress in Optics*, pages 137–184. Elsevier, 2007.

10. L. Novotny and S.J. Stranick. Near-field optical microscopy and spectroscopy with pointed probes. *Annu Rev Phys Chem*, 57, 2006.

11. M. Schnell, A. Garcia Etxarri, A. J. Huber, K. Crozier, J. Aizpurua, and R. Hillenbrand. Controlling the near-field oscillations of loaded plasmonic nanoantennas. *Nature Photonics*, 3(5):287–291, May 2009.

12. T. Taubner, F. Keilmann, and R. Hillenbrand. Nanomechanical resonance tuning and phase effects in optical near-field interaction. *Nano Letters*, 4(9):1669–1672, 2004.

13. Alexander Weber-Bargioni, Adam Schwartzberg, Matteo Cornaglia, Ariel Ismach, Jeffrey J. Urban, Yuanjie Pang, Reuven Gordon, Jeffrey Bokor, Miquel B Salmeron, D Frank Ogletree, Paul Ashby, Stefano Cabrini, and P James Schuck. Hyperspectral

nanoscale imaging on dielectric substrates with coaxial optical antenna scan probes. *Nano Lett*, 2011.

14. Ocelic, N.; Huber, A.; & Hillenbrand, R. Pseudoheterodyne detection for background-free near-field spectroscopy. Applied Physics Letters 89, 101124 (2006)

15. Huth, F.; Govyadinov, A.; Amarie, S.; Nuansing, W.; Keilmann, F.; & Hillenbrand, R. Nano-FTIR Absorption Spectroscopy of Molecular Fingerprints at 20 nm Spatial Resolution. Nano Lett. 2012, 12, 3973–3978

16. Ocelic, N. (2007). Quantitative Near-field Phonon-polariton Spectroscopy. PhD Thesis, Technische Universität, München.

CHAPTER 2: The Quantitative Description of Optical Contrasts in Scattering-Type Near-Field Optical Microscopy and Spectroscopy

2.1 Abstract

Near-field infrared spectroscopy by elastic scattering of light from a probe tip resolves optical contrasts in materials at dramatically sub-wavelength scales across a broad energy range, with the demonstrated capacity for chemical identification at the nanoscale. However, current models of probe-sample near-field interactions still cannot provide a sufficiently quantitative interpretation of measured near-field contrasts, especially in the case of materials supporting strong surface phonons. We present a model of near-field spectroscopy derived from basic principles and verified by finite-element simulations, demonstrating superb predictive agreement both with tunable quantum cascade laser near-field spectroscopy of SiO_2 thin films and with newly presented nanoscale Fourier transform infrared (nanoFTIR) spectroscopy of crystalline SiC. We discuss the role of probe geometry, field retardation, and surface mode dispersion in shaping the measured near-field response. This treatment enables a route to quantitatively determine nano-resolved optical constants, as we demonstrate by inverting newly presented nanoFTIR spectra of an SiO_2 thin film into the frequency dependent dielectric function of its mid-infrared optical phonon. Our formalism further enables tip-enhanced spectroscopy as a potent diagnostic tool for quantitative nano-scale spectroscopy.

2.1 Introduction

Since Synge's 1928 letter to Einstein proposing a bold method for optical imaging beyond the diffraction limit [1], sub-wavelength optical characterization techniques have remained subjects of intensive interest and fierce debate owing to their transformative potential. Among such techniques, apertureless near-field scanning optical microscopy (ANSOM)[2, 3] has shattered the diffraction limit, achieving optical resolutions better than $\lambda/1000$ at infrared and THz frequencies [4, 5, 6].

Recent coupling of ANSOM to a broadband coherent infrared light source and asymmetric Michelson interferometer has enabled Fourier transform infrared spectroscopy at the nanometer length scales (nanoFTIR)[7, 8, 9], in switchable combination with single-frequency imaging by the pseudo-heterodyne (PSHet) detection scheme [10, 11]. These novel interferometric techniques detect both amplitude and phase[12, 13, 14] of the probe-scattered "near-field signal", which encodes nano-scale near-field optical contrasts from the sample and transmits them to the far-field. While applications to nanoscale chemical sensing at vibrational "fingerprint" energies are obvious [15, 9, 16], the utility of this instrument for fundamental nano-scale studies of correlated electron systems are equally compelling [17, 18, 19, 20, 21, 22, 23, 24].

ANSOM employs a conductive or dielectric AFM probe as both an intense near-field source and scatterer of light into the far-field. The mechanism of optical contrast has long been understood intuitively via the simple point dipole model [25, 26], in which radiation scattered from a small polarizable sphere of radius a illuminated by an incident field E_{inc} is modulated through electrostatic interaction with a material surface located a distance d away in the z-direction:

$$\alpha_{\text{eff}} \equiv P_z \,/\, E_{\text{inc}} = \frac{\alpha}{1 - \alpha\beta/\left(16\pi(a+d)^3\right)}$$
$$\text{with} \quad \alpha \equiv 4\pi a^3 \quad \text{and} \quad \beta \equiv \frac{\epsilon - 1}{\epsilon + 1}. \qquad (1)$$

Here α denotes the “bare" polarizability of the sphere producing a vertical dipole moment P_z, and β denotes the quasi-static limit of the Fresnel coefficient $r_p(q,\omega)$. A function of both frequency ω and in-plane momentum q, the Fresnel coefficient describes the relative magnitude and phase of p-polarized light reflected from the surface of material with frequency-dependent dielectric function $\epsilon(\omega)$.

While important theoretical advances have brought near-field spectroscopy beyond qualitative descriptions [27, 28, 29, 30, 31, 32], available models describing the probe-sample near-field interaction remain beset by critical limitations:

1. Many general formulations, although formally exact, prove cumbersome to implement for practical calculation beyond reduction to the simple point dipole model [33, 34]. Field retardation and antenna effects of the probe are explored formally, but not quantitatively.
2. Although the near-field interaction may be described as an exact scattering problem, many solution methods rely on perturbation expansions in powers of the sample response factor β or r_p. [9, 35, 32, 34] One can show that such series are divergent beyond modest values of r_p (the “strong coupling" regime), leaving this method inapplicable for the analysis of crystalline solids and strongly resonant plasmonic systems. [31]
3. A number of tunable geometric parameters with *ad hoc* or empirical values are introduced to quantitatively fit measured data. These include fractional weights of relevant probe surface charge,[30, 31] effective probe size and geometry,[29, 28, 30] the bare tip polarizability, etc. [20] The multitude of *ad hoc* tunable parameters provides an unreliable recipe for predictive modeling or quantitative interpretation of data.

To address these extant shortcomings, the aim of the present work is threefold. We first present a new model of probe-sample near-field interaction, the *lightning rod model*, whose

generality allows exploring the influence of both probe geometry and electrodynamic effects, while remaining formally exact in both theory and implementation. Mathematical reduction of this formalism back to the point dipole model will make clear that unnecessary *ad hoc* assumptions underpin prevailing models [30, 31], and that geometric and electrodynamic considerations must ultimately play a role in their vindication.

Second, we demonstrate this model's capability to predict spectroscopic near-field contrast in the case of layered structures, which exhibit a strongly momentum-dependent optical response, as well as strongly resonant systems, through comparison with near-field spectra measured on thin films of silicon dioxide (SiO_2) and bulk silicon carbide (SiC). Our measurement apparatus is a novel infrared near-field microscope equipped for both PSHet imaging and broadband nanoFTIR spectroscopy, described in Appendix A.

Finally, we present a method to *invert* the *lightning rod model* to extract a material's complex dielectric function with nanoscale resolution, which we demonstrate explicitly for an SiO_2 thin film sample. This procedure, combined with the unifying formalism of the *lightning rod model*, provides a powerful diagnostic tool for quantitatively studying the nano-resolved optical properties of molecular systems, phase-separated materials, and confined nanostructures using ANSOM.[17]

2.2 The Lightning Rod Model

Our model describes the near-field interaction between an ANSOM probe and a sample surface through a general formalism that is in principle exact, without appealing to empirical or *ad hoc* parameters. The chief observable of ANSOM is the radiation field of a polarized probe placed in proximity to a sample (experimental details described in Appendix A). Since the field originates from reorganization of charges developing on the probe surface in response to an incident illumination field, together with the near-field of the proximate sample, we begin by forming an expression for this instantaneous charge distribution.

Constraining our attention to nearly axisymmetric probe geometries, the charge distribution is succinctly expressed through a linear charge density $\lambda_Q(z) \equiv dQ/dz(z)$, Q denoting charge and z the probe's axial coordinate. In the quasi-static approximation, the field E_{rad} re-radiated or back-scattered from the probe is proportional to its induced dipole moment

$$P_z = \int dz\, z\, \lambda_Q(z). \tag{2}$$

Appendix E presents how the radiated field is obtained from $\lambda_Q(z)$ when electrodynamic phenomena are of fundamental importance, *i.e.* when the size of the scatterer is comparable to the light wavelength. This relationship highlights the central role of the induced charge distribution in determining the measured observables of near-field spectroscopy.

$\lambda_Q(z)$ can be written as the sum of charges induced by the incident field and those differential contributions $d\lambda_{Q\,\mathrm{nf}}(z)$ induced by reflection of probe-generated near-fields off the proximate sample:

$$\lambda_Q(z) = E_{\mathrm{inc}}\, \Lambda_0(z) + \int d\lambda_{Q\,\mathrm{nf}}(z). \tag{3}$$

Here $\Lambda_0(z)$ denotes the induced charge per unit field resulting from incident illumination. Its functional form depends on the nature of the incident field and the probe geometry, but its contribution to $\lambda_Q(z)$ scales with the magnitude of the incident field E_{inc}. The induced charge elements $d\lambda_{Q\,\mathrm{nf}}(z)$ take the form:

$$\begin{aligned} d\lambda_{Q\,\mathrm{nf}}(z) = dQ \iint_0^\infty & dq\, dq'\, \mathcal{G}(q)\, \Gamma_{dQ\to s}(q) \\ & \times R(q,q')\, \Gamma_{s\to t}(q')\, \Lambda(q',z). \end{aligned} \tag{4}$$

Here q and q' denote in-sample-plane momenta for Fourier components of the near-field reflected by the sample in response to the polarized probe. Provided a planar sample geometry, this parameterization offers a sparse basis in which to efficiently solve the problem, in contrast with real-space treatments (*e.g.* the finite element method). Eq. (4) can be understood through the

physical mechanism shown schematically in Fig. 2.1b and described as follows in terms of field emission from the probe and sample reflection.

Charge elements $dQ = dz' \lambda_Q(z')$ on the probe form rings with radii $\mathcal{R}_{z'}$ along its surface. Considered in the angular spectrum decomposition (Appendix B), each ring emits a distribution of axisymmetric p-polarized evanescent fields whose Fourier components are weighted by $\mathcal{G}(q) = q\, J_0(q\mathcal{R}_{z'})$. Hereafter $J_i(\ldots)$ denotes a Bessel function of the first kind at order i, with cylindrical coordinates ρ and z. These emitted fields (so-called evanescent Bessel beams) reach the sample surface a distance d below the tip apex ($z = 0$) via propagator $\Gamma_{dQ\to s}(q) = e^{-q(z'+d)}$ and in the empty tip-sample gap $-d < z < 0$ take the divergence-free form (per unit charge):

$$\vec{E}_q(\vec{r}) = \mathcal{G}(q)\,(J_0(q\rho)\,\hat{z} + J_1(q\rho)\,\hat{\rho})\; e^{q(z-z')}. \tag{5}$$

In general, the sample may subsequently scatter evanescent fields with momentum q into distinct Fourier components q' as described through a differential sample response function $R(q, q')$. For samples with continuous in-plane translational symmetry (*e.g.* flat surfaces, layered structures) this response function reduces to the Fresnel reflection coefficient for p-polarized light,

$$R(q, q') = r_p(q)\,\delta(q - q'), \tag{6}$$

written here as a function of the in-plane momentum q of incident light, with $\delta(\ldots)$ denoting the Dirac delta distribution. These scattered fields extend from the sample surface via propagator $\Gamma_{s\to t}(q') = e^{-q'd}$ and re-polarize the probe, inducing a linear charge density (per unit field) described by a *probe response function* $\Lambda(q', z)$. This formalism accommodates the non-trivial influence of realistic tip geometries on the functional form of illumination- and sample-induced charge distributions $\Lambda_0(z)$ and $\Lambda(q', z)$. The omission of a term $e^{-q'z}$ in $\Gamma_{s\to t}(q')$ requires that the definition of $\Lambda(q', z)$ account implicitly for the decay of sample-reflected excitation fields along the probe's length.

Induced charge densities can be pre-computed for an axisymmetric probe of arbitrary geometry using a simple boundary element method (Appendices C and D). Fig. 2.1c displays

$\Lambda(q,z)$ for several values of q, computed for the case of a hyperboloidal (conical with rounded tip) probe geometry with tip curvature radius a. As shown in Fig. 2.1c, the density of charge dramatically accumulating at the probe apex - the celebrated *lightning rod effect* - increases roughly as $1/q$. This results from the requisite screening of evanescent fields by induced charges distributing a distance $\delta z = 1/q$ along the probe surface. The momentum-dependent *lightning rod effect* is critically absent from models of the probe-sample near-field interaction lacking a faithful geometric description.

Confining our attention to planar sample geometries, Eqs. (3), (4), and (6) together describe a self-consistent quasi-one-dimensional scattering process:

$$\lambda_Q(z) = E_{\mathrm{inc}}\,\Lambda_0(z) - \int_0^\infty dq\,\widetilde{\lambda}_Q(q)\cdot q\,e^{-2qd}\,r_p(q)\,\Lambda(q,z) \tag{7}$$

with

$$\widetilde{\lambda}_Q(q) \equiv \int_0^L dz'\lambda_Q(z')\cdot e^{-qz'}\,J_0(q\,\mathcal{R}_{z'}). \tag{8}$$

The integral transform in Eq. (8), whose action on a function henceforth we indicate by a tilde, denotes summation of near-fields emitted from charges along the entire length of the probe, $0 < z < L$. A similar integral transformation $z \to s$ applied to $\lambda(z)$ and $\Lambda(q,z)$ in Eq. (7) yields an integral equation in $\widetilde{\lambda}(s)$:

$$\widetilde{\lambda}_Q(s) = E_{\mathrm{inc}}\,\widetilde{\Lambda}_0(s) - \int_0^\infty dq\,\widetilde{\lambda}_Q(q)\cdot q\,e^{-2qd}\,r_p(q)\,\widetilde{\Lambda}(q,s). \tag{9}$$

This resembles the Lippman-Schwinger equation of scattering theory [36], wherein $\widetilde{\Lambda}_0(s)$ and $\widetilde{\Lambda}(q,s)$ here play the role of in- and out-going “scattering states". The axisymmetric approximation, preserving most fundamental aspects of the system geometry, affords tractability in this scattering formalism. Furthermore, computations presented in this work leverage the concise momentum-space (q and s) description conferred by Eq. (9).

Provided knowledge of the probe response functions $\Lambda_0(z)$ and $\Lambda(q', z)$ (to wit, their integral transforms $\widetilde{\Lambda}_0(s)$ and $\widetilde{\Lambda}(q, s)$), Eq. (9) is soluble by traditional methods[37] after discretizing q to a set of Gauss-Legendre nodes $\{q_i\}$. We found evaluation at $N_q \approx 200$ such nodes sufficient for numerical accuracy to within 1%. Only a finite range of momenta $0 \leq q \leq q_{\max}$ need be considered in practice, since $\widetilde{\Lambda}_0(s)$ and $\widetilde{\Lambda}(q, s)$ drop precipitously in magnitude above a cutoff momentum $s \sim 1/a$, with a the smallest length scale relevant to the probe geometry, in this case the radius of curvature at the probe apex, $a \approx 30$ nm for many commercial probe tips. This reflects the inability of strongly confined fields (*e.g.* $q \sim \mathrm{nm}^{-1}$) to efficiently polarize the probe.

The momentum-space solution to Eq. (9) is then

$$\vec{\lambda}_Q = \frac{\vec{\Lambda}_0}{\mathbf{I} - \mathbf{\Lambda G}} E_{\mathrm{inc}}, \tag{10}$$

where the denominator is taken in the sense of matrix inversion, vectors imply functional evaluation at momenta $\{q_i\}$, $\mathbf{I}$ is the identity operator, and other matrices are defined as

$$\mathbf{\Lambda}_{ij} \equiv \widetilde{\Lambda}(q_j, s_i) \quad \text{and} \quad \mathbf{G}_{ij} \equiv -q_i \, e^{-2q_i d} \, r_p(q_i) \, \delta q_i \, \delta_{ij}. \tag{11}$$

Here δq_i is the measure of q_i and δ_{ij} denotes the Kronecker delta function. Defining similarly a vector of charge distribution functions $\left[\vec{\Lambda}(z)\right]_i \equiv \Lambda(q_i, z)$, the total induced charge is provided through Eq. (7) as:

$$\lambda_Q(z) \,/\, E_{\mathrm{inc}} = \Lambda_0(z) + \vec{\Lambda}(z) \cdot \mathbf{G} \, \frac{\vec{\Lambda}_0}{\mathbf{I} - \mathbf{\Lambda G}} \tag{12}$$

This expression casts Eq. (10) into the real-space representation necessary for computing the probe's total radiated field, contributions to which result from a functional relation $\vec{e}_{\mathrm{rad}} \equiv E_{\mathrm{rad}}\left[\vec{\Lambda}\right]$ derived in Appendix E. Finally, this implies

$$E_{\mathrm{rad}} \,/\, E_{\mathrm{inc}} = e_{\mathrm{rad},\,0} + \vec{e}_{\mathrm{rad}} \cdot \mathbf{G} \, \frac{\vec{\Lambda}_0}{\mathbf{I} - \mathbf{\Lambda G}}. \tag{13}$$

Note that dependence on both the tip-sample distance d and the local optical properties of the sample enter these expressions through $\mathbf{G}$, whereas geometric properties of the probe enter separately through $\mathbf{\Lambda}$. When applied to a realistic probe geometry, these expressions constitute the *lightning rod model* of probe-sample interaction, so named for its quantitative description of the strong electric fields localized by an elongated geometry to a pointed apex. The product of $\mathbf{\Lambda}$ and $\mathbf{G}$ signifies that strong near-fields from the probe multiplicatively enhance optical interactions with the sample surface. Expanding the Eq. (13) inverse matrix as a geometric series reveals an infinite sequence of probe polarization and sample reflection events, equivalent to the perturbation expansions presented elsewhere [9, 35, 32, 34].

Eq. (13) can also recover the point dipole model (Eq. (1)). After simplifying the probe geometry to a metallic sphere of radius a and assuming that all center-evaluated ($z = a$) fields polarize like the homogeneous incident field E_{inc}, we have:

$$\Lambda(q, z) = 3/2\,(z - a)\,e^{-qa}, \tag{14}$$

$$\widetilde{\Lambda}(q, s) = -a^3\,s\,e^{-(s+q)a}, \tag{15}$$

$$\text{and} \quad p_z(q) = \int_0^{2a} dz\,z\,\Lambda(q, z) = a^3\,e^{-qa}. \tag{16}$$

$\widetilde{\Lambda}(q, s)$ is obtained from semicircular $\mathcal{R}_z$ in Eq. (8), and exhibits a characteristic maximum followed by a sharp decay in magnitude near $s \sim a^{-1}$. In this case, Eq. (9) yields $\widetilde{\lambda}_Q(s)$ in closed form owing to the separability of $\widetilde{\Lambda}(q, s)$:

$$\widetilde{\lambda}_Q(s) = \frac{-a^3\,s\,e^{-sa}}{1 - a^3 \int_0^\infty dq\,q^2\,e^{-2q(d+a)}\,r_p(q)}\,E_{\text{inc}}. \tag{17}$$

The sphere's polarization is obtained through Eqs. (7) and (2) as

$$\alpha_{\text{eff}} \equiv P_z / E_{\text{inc}} = \frac{a^3}{1 - a^3 \int_0^\infty dq\,q^2\,e^{-2q(d+a)}\,r_p(q)}. \tag{18}$$

If the sample material is weakly dispersive for $q \gg \omega/c$, $r_p(q) \approx \beta$ and Eq. (1) is recovered.

Such simplifications are instructive, but this work makes full implementation of Eq. (13) without recourse to approximation, thus revealing aspects of the probe-sample near-field interaction unresolved by the point dipole model. While perturbative expansions and the point-dipole model may be attractive for their relative simplicity, they are certainly not expected to be accurate. In particular, for large β, nothing short of the full numerical solution to Eq. (11) is acceptable for predicting experimental observables with quantitative reliability. Our procedure for doing so is detailed in the following sections.

The near-field experiments presented in this work utilize lock-in detection of the probe's back-scattered field at harmonics n of the probe tapping frequency Ω to suppress noise and unwanted background. Simulating this technique, the probe's back-scattered field E_{rad} (Eq. (13)) is connected to experimentally observed amplitude S_n and phase ϕ_n signals through a sine transform under sinusoidally varying tip-sample distance d:

$$s_n(\omega) = \mathcal{I}(\omega) \int_{-\pi/\Omega}^{\pi/\Omega} dt \, \sin(n\Omega t) \, E_{\mathrm{rad}}\big(d, r_p(q,\omega)\big) \quad \text{with} \quad d = A\left(1 + \sin(\Omega t)\right), \tag{19}$$

$$S_n(\omega) \equiv |s_n(\omega)|, \quad \text{and} \quad \phi_n \equiv \arg\{s_n(\omega)\}. \tag{20}$$

Here Ω and A are the tapping frequency and amplitude of the near-field probe, respectively, and $\mathcal{I}(\omega)$ denotes the frequency-dependent instrumental response of the collection optics, interferometer and detector used for the measurement. This factor can be removed by normalizing experimental $s_n(\omega)$ to "reference" near-field signal values, as collected from a uniformly reflective sample material such as gold or undoped silicon. This normalization process is further discussed in Sec. IV.

A prediction of near-field contrast using the *lightning rod model* therefore requires calculation of Eq. (13) at several values of d; in practice we find 20 such values sufficient, with evaluation of Eq. (13) for each requiring several milliseconds on a single 2.7 GHz processor.

Cumulatively, the calculation remains both realistic and fast, more so than previously reported semi-analytic solutions for realistic probe geometries.[38, 39] For example, typical calculations of a demodulated and normalized near-field spectrum across 100 distinct frequencies require less than 10 seconds of computation time.

We conclude this formal introduction with a conceptual clarification. Although the geometry and material composition of the near-field probe implicitly determine its response function $\Lambda(q, z)$, the formalism embodied by Eq. (13) is general and outwardly irrespective of specific properties of the probe. Also, while plasmonic enhancement may be encompassed in $\Lambda(q, z)$, it is *not* a prerequisite for effective near-field enhancement at the probe apex. Near-field enhancement is attainable through a combination of three distinct mechanisms:[40]

1. the *lightning rod effect* proper, due to accumulation of charge at geometric singularities, an essentially electrostatic effect,
2. *plasmonic enhancement*, due to the correlated motion of surface charges near the plasma frequency of metals,
3. and *antenna resonances*, in which the size of an optical antenna correlates with the incident wavelength in a resonant fashion, a purely electrodynamic effect.

The quasi-static boundary element utilized in this work (Appendix C) reproduces the first of these mechanisms by way of $\Lambda(q, z)$, whereas its electrodynamic counterpart (Appendix D) reproduces all three. Although plasmonic enhancements are scarcely attainable in metallic probes at infrared frequencies, Secs. III and IV establish the important influence of both the *lightning rod effect* and antenna resonances in near-field spectroscopy.

2.3 The Quasi-static case

We now apply Eq. (13) to realistic probe geometries in the quasi-static limit to investigate whether the quasi-static approximation is appropriate for quantitative prediction of near-field contrasts. By reducing the physical system to electrostatics, this approximation is strictly justified

only in treating light-matter interactions at length scales much smaller than the wavelength of light, whereas a typical near-field probe consists of an AFM tip tens of microns in height (Fig. 2.1a), comparable to typical wavelengths encountered in infrared near-field spectroscopy. Consequently, for the assumptions of a quasi-static probe-sample interaction to remain valid, the emergent behavior of a realistic near-field probe must be shown nearly equivalent to those of a deeply sub-wavelength one.

To test this assumption, we consider the near-field interaction between a metallic ellipsoidal probe oriented vertically over a planar sample of 300 nm of thermal silicon dioxide (SiO_2) on silicon substrate. This sample system and model probe geometry were considered in a previous work [38], demonstrating the capacity of near-field spectroscopy to resolve the $\omega \approx 1130$ cm^{-1} surface optical phonon of thermal oxide films as thin as 2 nm. We extend the theoretical study presented therein to investigate the influence of the probe length L on the amplitude of experimentally measurable back-scattered near-field signal $S_3(\omega)$ (normalized to silicon) predicted by the *lightning rod model*. The outcome is presented in Fig. 2.2.

The probe tapping amplitude is 80 nm in these simulated experiments, and the radius of curvature a at the probe apex (equal to the inverse surface concavity) is held constant at 30 nm, typical of experiments with commercially available near-field probes. The minimum probe-sample distance is taken as $d = 0$ nm throughout (*viz.* physical contact, consistent with the established description of tapping mode AFM). We describe the thin-film optical response with a momentum-dependent Fresnel coefficient [41] (further discussed in Sec. V) using optical constants of thermal oxide taken from literature[42].

The probe response function $\Lambda(q, z)$ is computed in the quasi-static approximation once for each probe geometry according to a simple boundary element method. Mathematical details are provided in Appendix C. Whereas in this work we present calculations only for ideally conducting metallic probes, Appendix C presents also the general formulation suitable for application to dielectric probes. Consequently, the case of a dielectric probe presents no formal

difficulty for the model presented here. However, previously reported models present a suitably simpler description of the “weak coupling regime" in which externally excited near-fields may be mapped non-perturbatively [43, 44, 13]. We identify this as the regime in which a perturbation expansion of Eq. (13) is found to converge, and several terms therein might be summed for a sufficient estimate of near-field scattering.

As shown in Fig. 2.2, the most dramatic feature of our quasi-static calculations is the strong variation in normalized scattering amplitude with increasing probe length at the probe-sample polariton resonance. The implication is worrisome: there is no clear rational choice for “effective probe length" when computing the strength of probe-sample near-field interaction in the quasi-static approximation. With a free-space wavelength of light $\lambda \sim 10\ \mu$m, although the largest credibly quasi-static probe length $L \sim \lambda/10$ (or $L \sim 20a$) provides reasonable qualitative agreement with data acquired by nanoFTIR under identical experimental conditions (Fig. 2.7), quantitative agreement is clearly only attainable *a posteriori*, for example by fitting to agreeable values of L. Furthermore, the extreme dependence on probe geometry exhibited here discredits the utility of quantitative “fits" to experimental data. The ill-posed description of near-field coupling afforded by this quasi-static treatment lacks clear predictive power. We are therefore compelled towards a consistent electrodynamic treatment, which as we will show provides an unambiguous description of near-field interactions with wavelength-scale probes – a case applicable to the vast majority of near-field experiments at infrared and THz frequencies.

2.4 The electrodynamic case: near-field probe as antenna

Near-field microscopy is occasionally described as an antenna-based technique, in which the antenna-like near-field probe efficiently converts incident light into strongly confined fields at the probe-sample feed-gap[45, 46, 47, 17]. The antenna’s scattering cross section is consequently modulated through strong interactions with the sample surface to provide the nano-resolved optical contrasts of ANSOM [48, 4]. At a formal level, these considerations leave the

mathematical form of the *lightning rod model* unaltered; nevertheless, the probe response function $\Lambda(q, z)$ must encapsulate the probe's role as an antenna, particularly in the probe's response $\Lambda_0(z)$ to illumination fields.

As for any antenna, due to retardation and radiative effects, the field scattered by a near-field probe is manifestly dependent on both its size relative to the free space light wavelength as well as its geometric profile relative to the incident light polarization. Such electrodynamic effects have been demonstrated experimentally [49, 47]. To characterize how these length scales influence the observables of near-field spectroscopy, the full electrodynamic responses of two probe geometries were computed numerically as a function of their overall length L relative to the free-space wavelength of incident light.

A *fully retarded* boundary element method taking account of field retardation and radiative forcing (mathematical details provided in Appendix D) was used to calculate charge distributions $\Lambda_0(z)$ induced on metallic ellipsoidal and hyperboloidal probe geometries by incident 10 μm wavelength light ($\omega = 1000$ cm$_{-1}$). We consider here the hyperboloidal geometry to faithfully reflect the cone-like structure of conventional near-field probes which exhibit a taper angle $\theta \approx 20°$ relative to their axis in our experiments. A similar hyperboloid probe geometry was applied previously by Behr and Raschke to explore plasmonic field enhancements [39]. However, their fully analytic treatment necessitates a semi-infinite probe geometry treated in the quasi-static approximation, requiring an unconventional field normalization method to obtain finite values for the probe response. Their formalism also left back-scattering from the ANSOM probe unexplored. For our examination, we explore the explicit electrodynamics of probes with lengths between $L = 60$ nm (rendering a sphere in the ellipsoidal case) and 30 μm, with the apex curvature radius held constant at $a = 30$ nm.

The axisymmetry favored by the *lightning rod model* was maintained throughout these calculations by approximating plane wave illumination by an inwards-propagating cylindrical field bearing a local phase velocity angled towards the tip apex at 60$_{\circ}$ from the probe axis (see

Appendix D). Validity of this axisymmetric approximation was confirmed through comparison of resultant surface charge density profiles with those predicted by full finite-element simulations (*Comsol Multiphysics*), consisting of a realistic metallic probe geometry ($\theta = 20°$ and $L = 19\ \mu$m) including AFM cantilever, subject to plane-wave illumination. Differences in charge density were found to be negligible within microns of the tip apex, suggesting the robustness of key near-field parameters to fine details of the extended probe geometry. Fig. 2.3a displays finite-element predictions for the magnitude of the probe's scattered field $\vec{E}_{sca}$ illustrating the characteristically standing wave-like pattern of charge density along the probe's conical surface, a consequence of field retardation.

The resultant field enhancement at the probe apex in the absence of a sample calculated by our fully retarded boundary element method is shown in Fig. 2.3b (lower panel) in comparison with the quasi-static case, demonstrating several key phenomena: First, quasi-static probe geometries exhibit field enhancements that increase monotonically with the geometric "sharpness" L/a due to the electrostatic lightning rod effect, originating the divergent quasi-static near-field contrast displayed in Fig. 2.2. Second, at lengths $L = m\,\lambda/2$ for odd integers $m \geq 1$, the electrodynamic ellipsoidal probe exhibits resonant enhancement, whereas minima are observed for m even. These features signify antenna modes with antisymmetric and symmetric surface charge densities [50], respectively, such as those experimentally characterized among similarly elongated near-field probe geometries [47]. Due to the axially polarized incident field, Resonant enhancement modes of the hyperboloidal probe are less pronounced and more complicated in character; we discuss them here in no further detail. Finally, it is clear that quasi-static predictions depart from their electrodynamic counterparts near a probe length $L \sim \lambda/10$, precisely where quasi-static approximations might be expected to falter lacking the antenna enhancement mechanism. Field retardation halts subsequent increases in enhancement from the quasi-static lightning rod effect, conferring a practical limit to realistically attainable near-field enhancements outside the plasmonic regime.

Similarly, the onset of antenna modes is expected to modulate the intensity of frequency-dependent back-scattered radiation from wavelength-scale near-field probes, opening the possibility to optimally enhance absolute near-field signals through application-driven design of novel probe geometries. However, the need for a broadband and normalizable probe response is equally crucial for spectroscopy applications [51]. A typical infrared near-field spectroscopy experiment involves normalizing acquired signals to a reference material that exhibits a nominally flat optical response (*e.g.* gold or undoped silicon) in order to remove the influence of instrumental sensitivities[20, 38, 9], including the probe's frequency-dependent antenna response. Normalizability of this response is typically assumed, but we predict here for the first time the breakdown of this assumption in the vicinity of strong antenna resonances.

Fig. 2.3b (upper panel) displays the result of fully electrodynamic *lightning rod model* predictions for the near-field signal $S_{3\,\mathrm{SO}}$ obtained at the peak probe-sample resonance frequency ($\omega \approx 1130$ cm$_{-1}$) induced by the strong SiO_2 surface optical phonon, normalized to the signal from silicon. Whereas an *increase* in *absolute* back-scattered signal is expected near the onset of a (radiative) antenna mode, this evidently accompanies a remarkable *decrease* in *relative* material contrast. The effect results from strong cross-talk between the implicit probe response coincident with that of a resonant sample.

The explanation becomes clear when considering that an antenna's resonance can be strongly detuned by its dielectric environment.[52, 53] The point dipole model (Eq. (1)) admits interpretation as a dipole interacting with its mirror image projected from the sample surface. Extending this interpretation to an antenna, the electrodynamic system consists then not of a single antenna, but of a coupled antenna-mirror pair, and it is well established that coupling an antenna with an exact mirror copy induces a resonance red-shift[54, 55]. Whereas the mirror coupling scales with the inverse dimer gap size in the case of physical antenna pairs, this coupling scales with r_p in our case, and could be appropriately considered a case of *dielectric loading*.[44, 52]

Consequently, an $\mathrm{SiO_2}$ film is expected to detune antenna resonances more strongly at ω_{SO} than a Si substrate, rendering their respective probe back-scattering signals potentially incomparable even when collected at the same frequency, since there is no clear way to normalize out the effect. Stated another way, interaction with a resonant sample can not only *enhance* the strength of a probe's antenna mode, it can *modify* the antenna behavior outright, driving the probe towards a regime of destructive radiative interference. Normalized S_3 signals calculated for the electrodynamic ellipsoid (Fig. 2.3a, solid blue line) therefore resemble a quotient of two resonance functions, oscillatory but shifted versus the light frequency relative to one another. For this extreme case, we might conclude that fluctuations observed in the frequency-dependent near-field signal radiated from the probe could associate more with variable dielectric loading of the antenna response than with genuine near-field contrast.

Antenna detuning is considerably moderated in the case of the hyperboloidal probe, whose normalized near-field response at frequencies $\lambda < L$ exhibits much weaker dependence on the probe length (or, complementarily, on probing frequency). The normalization procedure therefore appears sufficient for systematic removal of the probe sensitivity at the 20% level in the absence of strong antenna resonances. Furthermore, given the clear asymptotic character of near-field contrast for the broadband hyperboloidal probe, it would appear acceptable to quantitatively model normalized near-field signals from such a probe geometry using electrodynamic charge distributions $\Lambda(q, z)$ computed only for a *single* characteristic frequency. In the case of weak antenna resonances, this renders implementation of the *fully retarded lightning rod model* no more complex than the quasi-static version. Therefore, all following calculations presented in this work are electrodynamic and calculated in this fashion unless otherwise indicated.

Nevertheless, this examination tells a cautionary tale concerning the use of strongly resonant probes[47] for quantitative near-field spectroscopy, wherein convolution of the probe's antenna response may not be easily removed. However, the resonant enhancement of back-

scattered fields by $L \sim \lambda/2$ probes can provide a fortunate trade-off, with encouraging applications to resonantly enhanced THz near-field imaging experiments.

2.5 5 Momentum-dependent light-matter coupling

To test the *lightning rod model* description of systems exhibiting explicit momentum-dependent light-matter coupling, we consider a thin film of phonon-resonant SiO_2 on silicon substrate. The film thickness t introduces a characteristic length scale to the sample geometry, associated with a characteristic crossover momentum $q \sim t^{-1}$. Incident evanescent fields exceeding this momentum are reflected much as though bulk SiO_2 were present, whereas lower momentum fields can penetrate the film and reflect from the substrate [38]. With the *lightning rod model* we consider this momentum dependence exactly and directly compare its predictions to near-field spectroscopy measurements performed using the experimental apparatus described in Appendix A.

Mid-infrared near-field images of SiO_2 thin films of varying thickness were acquired with a tunable QCL at a probe tapping amplitude of 50 nm, taking signal from the underlying silicon substrate for normalization (Fig. 2.4a). These data were first presented in an earlier work[38]. Controlled film thicknesses were produced through selective etching (*NT-MDT Co.*) and confirmed by AFM height measurements acquired simultaneously with the collection of near-field images. Spectroscopy was obtained from area-averaged near-field contrast levels.

Momentum-dependent Fresnel reflection coefficients were used to describe these systems[41] and provided to the *lightning rod model* in order to predict spectroscopic near-field contrast:

$$\begin{aligned} r_p(q,\omega) &= \frac{\rho_1 + \rho_2\, e^{2ik_{z,1}\,t}}{1 + \rho_1\rho_2\, e^{2ik_{z,1}\,t}} \\ \text{with} \quad \rho_i &\equiv \frac{\epsilon_i\, k_{z,i-1} - \epsilon_{i-1}\, k_{z,i}}{\epsilon_i\, k_{z,i-1} + \epsilon_{i-1}\, k_{z,i}}, \\ \text{and} \quad k_{z,i} &\equiv \sqrt{\epsilon_i\,(\omega/c)^2 - q^2}. \end{aligned} \tag{21}$$

Here numeric subscripts $0, 1, 2$ correspond with air, SiO_2, and silicon, respectively, ϵ_i denotes the complex frequency-dependent dielectric function of the relevant material (ellipsometric optical constants for thermal oxide taken from literature [42]), and t denotes the oxide film thickness.

Lightning rod model predictions are presented in Fig. 2.4b for comparison with measured data. Agreement is superior to that of the simple dipole model and at least as good as earlier quasi-static predictions with an ad-hoc probe geometry [38]. In contrast to the prediction of a blue-shifting phonon resonance with decreasing film thickness (originating entirely in the Fresnel formula Eq. 21), experimental data indicate a slight red-shift among ultra-thin films. This discrepancy should not be counted against our model: although identical optical constants were employed for predictions at all film thicknesses, a growing body of experimental and *ab initio* evidence suggests legitimate phonon confinement effects can modify the intrinsic optical properties of nanostructured samples[56]. Clear discernment of these effects by near-field spectroscopy opens the possibility for quantitatively evaluating the optical properties of nanostructures that exhibit and utilize *bona fide* three-dimensional confinement[57].

A clear physical description of the depth sensitivity exhibited in Fig. 2.4 proves just as valuable as quantitative agreement. The onset of a dramatic decrease in near-field signal at the phonon resonance near $t \sim a$ can be understood on the basis of the momentum decomposition of electric fields emitted by the near-field probe. A straightforward analysis building on Eq. (12) reveals the following decomposition for probe-generated electric fields by their momenta in the plane of the sample (the basis given by Eq. (5)):

$$\delta E(q_i) \,/\, E_{\mathrm{inc}} = \left[\mathbf{\Gamma}_{t\to s}\, \mathbf{\Lambda G}\, \frac{\vec{\Lambda}_0}{\mathbf{I} - \mathbf{\Lambda G}} \right]_i \delta q \tag{22}$$

with

$$\left[\mathbf{\Gamma}_{t\to s}\right]_{ij} \equiv e^{-q_i d}\, \delta_{ij},$$

where d is the tip-sample distance and $\delta E(q)/\delta q$ is understood in the sense of a distribution function.

Fig. 2.5b displays $\delta E(q)$ calculated on resonance with the SiO_2 phonon in comparison with the example dispersion of a 100 nm SiO_2 film on silicon shown in Fig. 2.5a. The surface optical phonon is evident at ω_{SO}, characteristically centered in the *Restrahlen* band between the transverse optical (ω_{TO}) and longitudinal optical (ω_{LO}) phonon frequencies. Given that our SiO_2 forms an amorphous layer, indication of these phonon frequencies is approximate. Nanoscale thickness introduces considerable momentum dependence in the regime relevant to probe-sample near-field interactions ($q \sim a^{-1}$), effecting a strong phonon response only for momenta $q > t^{-1}$ as mentioned earlier. The spectroscopic character of the probe-sample near-field response can therefore be inferred from the momentum-space integral of $\delta E(q) \times r_p(q, \omega)$. Note however the explicit r_p- and d-dependence of $\delta E(q)$ by way of $\mathbf{G}$ in Eq. (22) amounts to a near-field response strongly super-linear in the sample's intrinsic surface response.

2.6 6 The strongly resonant limit: silicon carbide

We can critically evaluate the generality of the *lightning rod model* formalism through comparison with measurements of crystalline SiC, a strongly resonant material in the mid-infrared owing to an exceedingly strong surface optical phonon at $\omega \approx 950\,\mathrm{cm}_{-1}$. Here we find the limit at which contingent assumptions for alternative near-field models [26, 9, 35, 32, 34] are expected to break down, since resonant materials can interact non-perturbatively along the entire length of the near-field probe. This breakdown signals the importance of both probe geometry and field retardation effects. Lacking these considerations, previous models have dramatically overestimated the near-field contrast generated by SiC [58, 17], leaving the estimation of optical properties through quantitative analysis of near-field observables quite ambiguous.

Fig. 2.6 displays quantitative agreement between newly presented nanoFTIR spectroscopy of a 6H SiC crystal and *lightning rod model* predictions. Asymmetry in the observed

phonon-induced probe-sample resonance spectrum mimics that of the underlying surface response function $\beta(\omega)$. To ensure unambiguous comparison between experiment and theory, uniaxial optical constants of our crystal were directly determined by in-house infrared ellipsometry and were found consistent with literature data for similar crystals [59]. A 100 nm gold film was deposited onto the crystal surface to provide a normalization material for nanoFTIR measurements, which were conducted at 60 nm tapping amplitude across the SiC-gold interface. The right inset of Fig. 2.6a displays strong interfacial contrast in near-field amplitude measured across the interface by pseudoheterodyne (PSHet) imaging [11] with a CO_2 laser tuned to 890 cm $^{-1}$, with nanoFTIR acquisition positions indicated. As confirmed by nanoFTIR, near-field resonance with the SiC surface optical phonon produces a stronger signal than gold across a considerable energy range, 800-940 cm^{-1}. Such strong near-field resonances enable potential technological applications for guiding and switching of confined infrared light within nanostructured polar crystals, as suggested in related work [60].

Predicted spectra presented in Fig. 2.6b reveal that explicit consideration of field retardation effects according to the findings of Sec. IV (spectra labeled *Ret.*) significantly improves quantitative agreement with experimental spectra in contrast to the quasi-static prediction (labeled *QS*), which drastically overestimates the near-field contrast of SiC up to a factor of 20 over gold. The *QS* curve additionally reflects an excessive red-shift of the probe-sample resonance peak on account of the overly predominant low-momentum phonon excitations permitted in the quasi-static approximation; these reside at lower energy due to the typical positive group velocity of surface phonon polaritons. We furthermore explored the influence of particular probe geometries on the predicted near-field spectrum by employing charge distributions $\Lambda(q, z)$ calculated for both the ideal hyperboloidal probe geometry as well as for the actual profile of an used probe tip, obtained from an SEM micrograph (displayed as the blue curve in Fig. 2.1a). The Fig. 2.6b comparison of SiC spectra predicted with these geometries reveals that only essential features of the probe geometry, such as the overall conical shape and

taper angle ($\theta \approx 20°$) shared by both, are relevant for predicting near-field contrasts at the 10% level of accuracy. Further quantitative refinements to near-field spectroscopy will therefore benefit from the standardization of reproducible probe geometries[61].

2.7 7 Nano-resolved extraction of optical constants

Systematic improvements in the light sources and detection methods available for near-field spectroscopy now enable sufficiently high signal-to-noise levels and fast acquisition times for routine, reproducible measurements [7, 8]. Fig. 2.7 displays newly presented nanoFTIR measurements acquired on a 300 nm SiO_2 film with silicon used for normalization, displaying both the amplitude S and phase ϕ of the probe's back-scattered radiation demodulated at the 2nd and 3rd harmonics of the probe frequency, collected at 60 nm tapping amplitude. Such broadband data are ideally eligible for the quantitative extraction of SiO_2 optical constants in the vicinity of the transverse optical phonon ($\omega_{TO} \approx 1075$ cm$_{-1}$).

Using the *lightning rod model*, a method requiring minimal computational effort was developed to solve the inverse problem of near-field spectroscopy, proceeding as follows: The connection between optical properties of a sample material (*e.g.* the complex dielectric function, $\epsilon = \epsilon_1 + i\epsilon_2$) and near-field observables (*e.g.* S and ϕ, or equivalently the real and imaginary parts of the complex back-scattered signal $s = s_1 + is_2$ at a given harmonic $n \geq 2$) is described by a smooth map $\mathrm{NF} : \mathbb{C} \to \mathbb{C}$, with $\mathbb{C}$ the set of complex numbers. A "trajectory" $s(\omega)$ through the space of observable near-field signals therefore corresponds to a trajectory $\epsilon(\omega)$ through the space of possible optical constants. The uniqueness of this correspondence was confirmed for bulk and layered sample geometries by computing $s = \mathrm{NF}(\epsilon)$ across the parameter range of interest for real materials ($\epsilon_2 > 0$) and ensuring local invertibility of the map, conditional on the determinant of the Jacobian matrix of NF:

$$|J(\epsilon_1, \epsilon_2)| > 0 \quad \text{with} \quad J(\epsilon_1, \epsilon_2) = \frac{\partial(s_1, s_2)}{\partial(\epsilon_1, \epsilon_2)}. \tag{23}$$

Because parameters internal to the operation of NF are frequently variable (*e.g.* sample thickness, tip radius of the probe, tapping amplitude), instead of establishing the inverse map NF^{-1} as a “look-up table" by brute computation, we instead introduce a method for nucleated growth of the trajectory $\epsilon(\omega)$ which optimizes consistency with the forward mapping $s = \mathrm{NF}(\epsilon)$ beginning at some initial frequency ω_0. We re-imagine the problem as a particle navigating ϵ-space under the influence of external forces penalizing displacements δs from measured signal values $s(\omega)$. The trajectory $\epsilon(\omega)$ for such a particle solves, for example, the equation of motion for a damped harmonic oscillator equilibrating to $s = \mathrm{NF}(\epsilon)$:

$$\frac{d^2}{d\omega^2}\delta s + 2\zeta\,\Omega\,\frac{d}{d\omega}\delta s + \Omega^2\,\delta s = 0 \tag{24}$$

with

$$\delta s(\omega) \equiv s(\omega) - \mathrm{NF}\big(\epsilon(\omega)\big).$$

Here ζ denotes a damping constant tuned to induce critical damping (ζ=1), and Ω is a force constant ensuring decay to equilibrium over an interval $\delta\omega = 2\pi/\Omega$ comparable to the frequency resolution of measurement. This equation of motion enables adiabatic tracking of experimentally observed signal values while both penalizing deviations δs and dissipating their energy. Eq. (24) may alternatively be parametrized by an auxiliary independent variable x for which $\omega(x)$ increments only when $|\delta s(\omega)| < \delta s_{\mathrm{thresh}}$, a threshold value ensuring system equilibration arbitrarily close to the measured signal value at each ω. This also ensures solutions to Eq. (24) are relatively insensitive to the “guessed" initial condition $\epsilon(\omega_0)$, amounting to a robust relaxation method.

Our inversion of measured $s(\omega)$ consists of numerically solving Eq. (24) for ϵ by finite difference techniques [62]. This requires at least five evaluations of NF per ω- or x-step in order to estimate local first and second derivatives of NF with respect to real and imaginary parts of ϵ. Although consequently the procedure is more computationally costly than forward evaluation by

the *lightning rod model*, it is at least as efficient in principle as global nonlinear least-squares methods (*e.g.* Levenberg-Marquardt [63]) and often considerably faster, furthermore requiring no *a priori* knowledge for the form of the fitting function. This is considerably advantageous in cases where spectra are not available in a sufficiently wide frequency range to permit well-determined fitting to $\epsilon(\omega)$ by Kramers-Kronig-consistent oscillators[64].

We applied our inversion technique to the spectroscopic data displayed in Fig. 2.7 by parametrizing NF with the reflection coefficient of an “unknown" 300 nm layer (film thickness determined by AFM) on silicon substrate. For mapping the film’s optical constants $\epsilon_{\mathrm{film}}(\omega) = \epsilon_1(\omega) + i\,\epsilon_2(\omega)$ to a measurable, normalized near-field spectrum $s_n(\omega)$, the form for NF used here is that given by the *lightning rod model*, namely:

$$\mathrm{NF}\big(\epsilon_1(\omega), \epsilon_2(\omega)\big) = s_n^{\mathrm{film}}(\omega)/s_n^{\mathrm{Si}} \tag{25}$$

with

$$s_n^{\mathrm{film}}(\omega) = \int_{-\pi/\Omega}^{\pi/\Omega} dt\, \sin(n\Omega t)\, E_{\mathrm{rad}}^{\mathrm{film}}(d,\omega), \tag{26}$$

and

$$E_{\mathrm{rad}}^{\mathrm{film}}(d,\omega) = \vec{e}_{\mathrm{rad}} \cdot \mathbf{G}_{\mathrm{film}}(d,\omega)\, \frac{\vec{\Lambda}_0}{\mathbf{I} - \mathbf{\Lambda}\mathbf{G}_{\mathrm{film}}(d,\omega)}, \tag{27}$$

and $d = A\,(1 + \sin(\Omega t))$. Describing the near-field response of the film, $\mathbf{G}_{\mathrm{film}}(d,\omega)$ is given by Eq. (11) in terms of the film reflection coefficient $r_p^{\mathrm{film}}(q,\omega)$, which is in turn a function of $\epsilon_{\mathrm{film}}(\omega)$ via Eq. (21). The silicon normalization signal s_n^{Si} is computed analogously, but using the reflection coefficient for a bulk surface with frequency-independent dielectric constant $\epsilon_{\mathrm{Si}} \approx 11.7$. All other parameters are defined as detailed in Sec. II.

In Fig. 2.8 we present the favorable comparison of our extracted $\epsilon_{\mathrm{film}}(\omega)$ with typical literature optical constants for three thermal oxide films measured by conventional infrared ellipsometry[42]. Fig. 2.8a makes clear the typical variation in optical constants expected among

oxide films grown even under nominally fixed conditions. Furthermore, our extraction technique produced virtually identical output when conducted on both 2nd and 3rd harmonic near-field spectra ($s_2(\omega)$ and $s_3(\omega)$), attesting to the internal consistency of the *lightning rod model*.

Although near-field inversion has been very recently demonstrated on measurements of prepared polymers, the existing technique relies on a polynomial expansion in β strictly limited to weakly resonant samples, *vis.* the perturbative limit of Eq. (13), and employs a model with tunable *ad hoc* parameters [30, 32]. Our procedure removes both shortcomings. These advantages make Eq. (24) a suitable technique for the unconditional on-line analysis of near-field spectroscopy data in a diagnostic setting. Combining for the first time the powerful nanoFTIR instrumentation with a quantitative inversion methodology unlimited by sample characteristics, this procedure makes possible potent new applications of nano-spectroscopy to the quantitative optical study of phase-separated materials[17, 18] and nano-engineered devices[21, 22], as well for the nano-resolved chemical identification of structures in biological or surface science applications[7, 9, 32, 16].

2.8 Conclusions and Outlook

The *lightning rod model* provides a general quantitative formalism for predicting and interpreting the experimental observables of near-field spectroscopy. Simplified descriptions of the probe-sample near-field interaction such as the point dipole model can be obtained as special cases resulting from convenient though unnecessary physical assumptions. In particular, the choice of effective probe length L[30, 32] was shown to be *ad hoc* in the quasi-static approximation, and consequently susceptible to dubious *a posteriori* fitting to experimental data.

We find a fully electrodynamic treatment renders the effective length construct unnecessary, since field retardation effects modify the distribution of probe charge interacting with the sample. While this provides a resolution to problems of convergence inherent to the quasi-static treatment, sample-induced dielectric loading of strong antenna resonances (*e.g.* for the long ellipsoidal probe) was found to deceivingly modulate relative material contrasts predicted in the

vicinity of sample resonances, such as the surface optical phonon of SiO_2, an important caveat and consideration for the rational design of optimized spectroscopic probes [47]. Nevertheless, fine details of the probe geometry for realistic conical probe geometries are predicted to impact observable near-field material contrasts at or below a 10% level of variation.

Using the *fully retarded lightning rod model* with a realistic probe geometry, we obtain quantitatively predictive agreement compared both with tunable QCL near-field spectroscopy of SiO_2 films with varying thickness and with newly presented nanoFTIR spectroscopy measurements of the strongly resonant polar material SiC. This exhibits our model's proper momentum-space description of the probe-sample optical interaction, as well as its suitability for the truly quantitative description of strongly resonant near-field interactions, in contrast with the capabilities or implementations of the alternative models heretofore demonstrated.[58, 34, 35]

Finally, we present a deterministic method to *invert* the *lightning rod model* without recourse to *ad hoc* parameters or over-simplifications. This rather general technique flexibly solves the inverse problem of near-field spectroscopy at a computational cost significantly lower than exhaustive lookup-tables or oscillator fitting methods, offering exciting opportunities for the on-line interpretation of nano-resolved near-field spectra acquired in a diagnostic setting. We envision the inverse *lightning rod model* employed quantitatively for deeply sub-wavelength optical studies of naturally or artificially heterogeneous and phase-separated materials, promising further novel applications to systems like energy storage nanostructures,[65] transition metal oxide heterostructures,[66] and single- or multi-layered graphene plasmonic devices [20, 21].

There remain outstanding challenges for the present model, including its extension to cases where deviations from axisymmetry are crucial, as for *s*-polarization of incident light, or for probe geometries with strong rotational asymmetry. We envision an expansion of our boundary element methods and of the lightning rod model into basis components with differing rotational "quantum numbers"[67] to capture the features of irrotational geometries in a computationally inexpensive fashion. Furthermore, the explicit application of our model to dielectric probes,

particularly in the plasmonic regime, is an undertaking of great potential interest for which the extension of our electrodynamic boundary element (Appendix D) to materials of non-negligible skin depth might play a crucial role. However, even at its present stage the quantitative scattering formalism presented here also lays a solid foundation for the rational analysis and optimization of tip-enhanced optical phenomena in an ever-growing number of exciting experimental applications, including single-molecule Raman spectroscopy[15, 68] and other novel partnerings of optics with scanning tunneling microscopy.[69, 70]

2.9 Acknowledgments

This work was supported through NASA grants NNX08AI15G and NNX11AF24G. Alexander S. McLeod acknowledges support from a U. S. Department of Energy Office of Science Graduate Fellowship.

This chapter, in full, is a reprint of the material as it appears in the following published article: A. S. McLeod, P. Kelly, M. D. Goldflam, Z. Gainsforth, A. J. Westphal, G. Dominguez, M. H. Thiemens, M. M. Fogler, D. N. Basov. Model for quantitative tip-enhanced spectroscopy and the extraction of nanoscale-resolved optical constants. *Phys. Rev. B.* 90, 085136 (2014). The dissertation/thesis author was the co-primary investigator and author of this material.

2.10 Figures

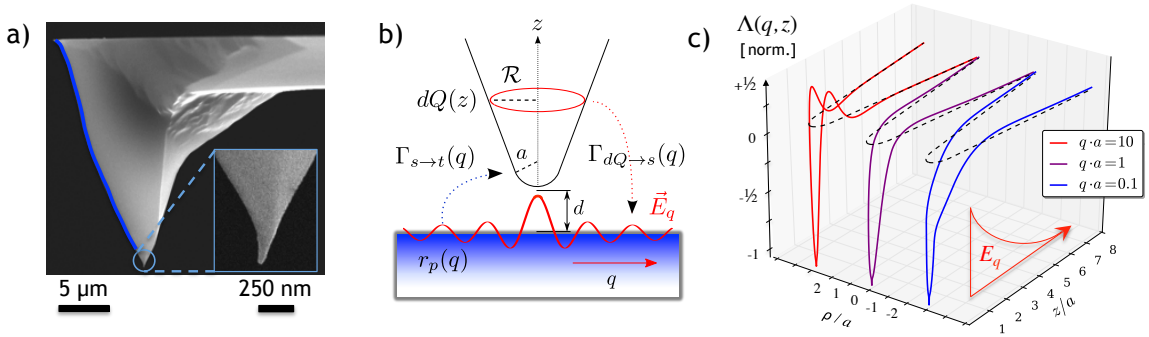

Figure 2.1: Scattering formulation of probe-sample interaction in near-field optical microscopy.

a) Scanning electron micrograph of a typical commercial near-field probe exhibiting a conical geometric profile and characteristic length scales (probe length and tip radius) separated by nearly three orders of magnitude. The surface profile (blue) is considered in Sec. VI. **b)** Schematic description of the probe-sample near-field interaction, involving emission of cylindrical evanescent fields from charge elements in the probe and their reflection by the sample. **c)** Probe response function $\Lambda(q,z)$ (defined in the main text) computed by the boundary element method (Appendix C) for evanescent fields $\vec{E}_q$ of increasing momenta q. Dashed curves indicate the geometric profile of the probe, and surface charge distribution profiles are normalized by their minimum values for viewing purposes.

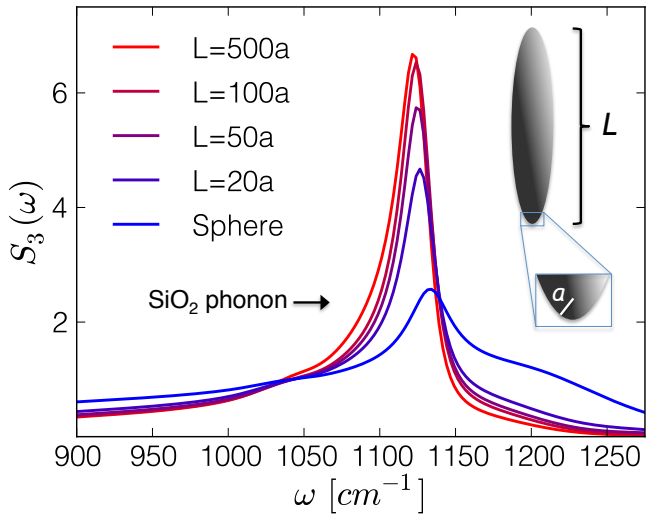

Figure 2.2: Spectral near-field contrast between the 1130 cm_{-1} surface phonon polariton of SiO_2 and silicon (providing normalization) as predicted by the *lightning rod model* for an ellipsoidal probe in the quasi-static approximation.

Contrast increases monotonically beyond experimentally observed levels as the probe length is increased.

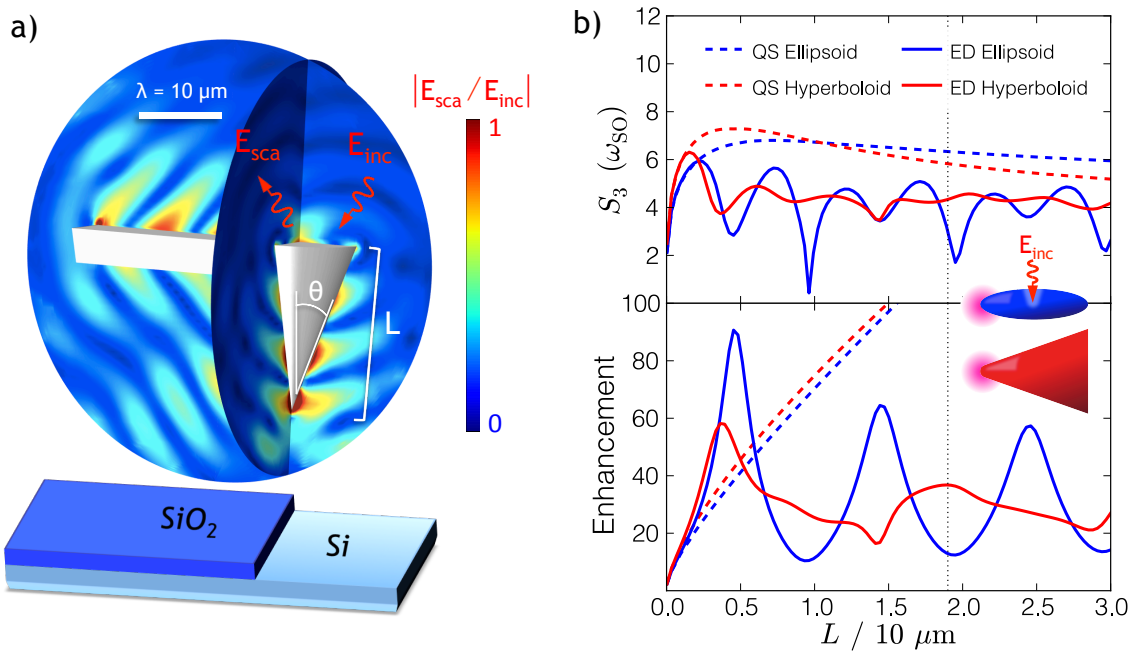

Figure 2.3: Comparison of quasi-static and electrodynamic responses of the near-field probe.

a) Scattered field of a realistic near-field probe geometry under plane wave illumination (incident along the viewing angle) as computed by the finite-element method. Oscillatory fields near the tip apex are associated with standing wave-like surface charge densities resulting from field retardation. **b) Lower panel:** Field enhancement at the tip apex computed quasi-statically (QS) and electrodynamically (ED) for two probe geometries of varying size illuminated perpendicular to their principle axes. **Upper panel:** Near-field S_3 contrast between SiO_2 at the surface optical phonon resonance (ω_{SO}) and silicon simulated by the *fully retarded lightning rod model*. The vertical dashed line indicates the length of a typical near-field probe, $L \approx 19\,\mu$m.

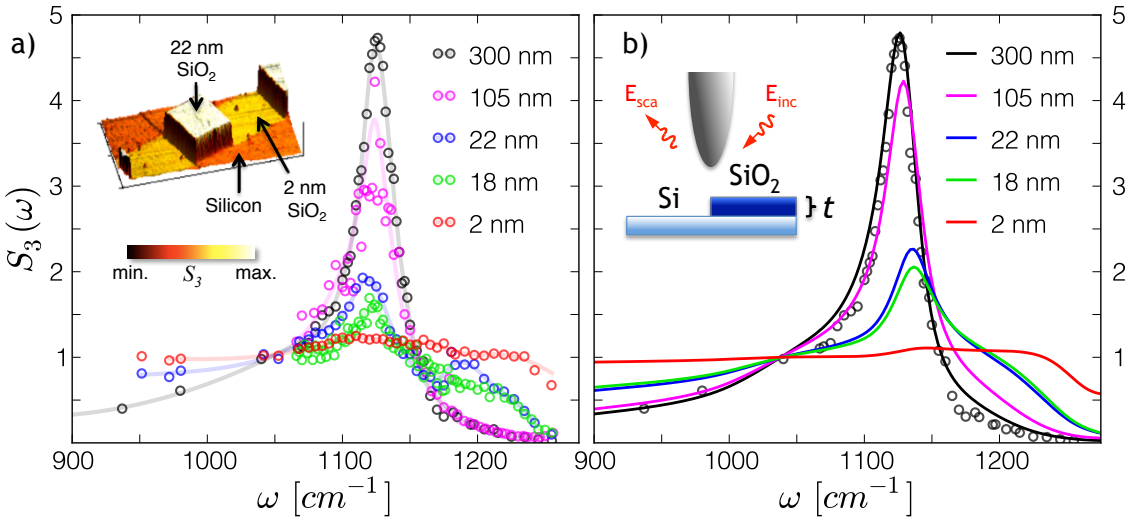

Figure 2.4: A comparison of the measured and predicted evolution of the spectroscopic near-field response from thin film oxides.

a) Near-field response of SiO_2 thin films etched to varying thicknesses on a silicon substrate measured by tunable QCL spectroscopy and normalized to silicon[38] (see text). The faint curves are provided as guides to the eye. **Inset:** Sample near-field signal S_3 at $\omega = 1130$ cm$_{-1}$ overlaid on simultaneously acquired AFM topography. **b)** Near-field S_3 spectra predicted by the *lightning rod model* using optical constants from literature [42]. Data points from the 300 nm film are superimposed for point of comparison. Our model captures the key features of the data; we infer that discrepancies with ultra-thin film data result from substantial variations in optical properties.

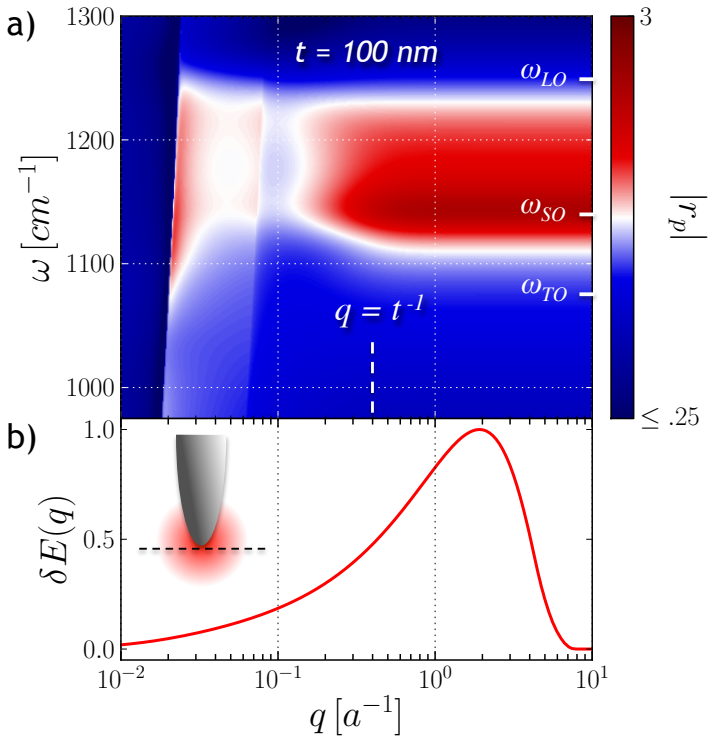

Figure 2.5: Momentum-dependent dispersion in the Fresnel reflection coefficient.

a) Example of strong surface optical phonon dispersion for a 100 nm thick SiO_2 film on silicon computed by the Fresnel reflection coefficient $r_p(q,\omega)$ (Eq. (21)). **b)** The momentum-dependent distribution of electric fields at the sample surface (dashed line) calculated by the *lightning rod model* at the tip-sample phonon resonance for a conical tip in full contact.

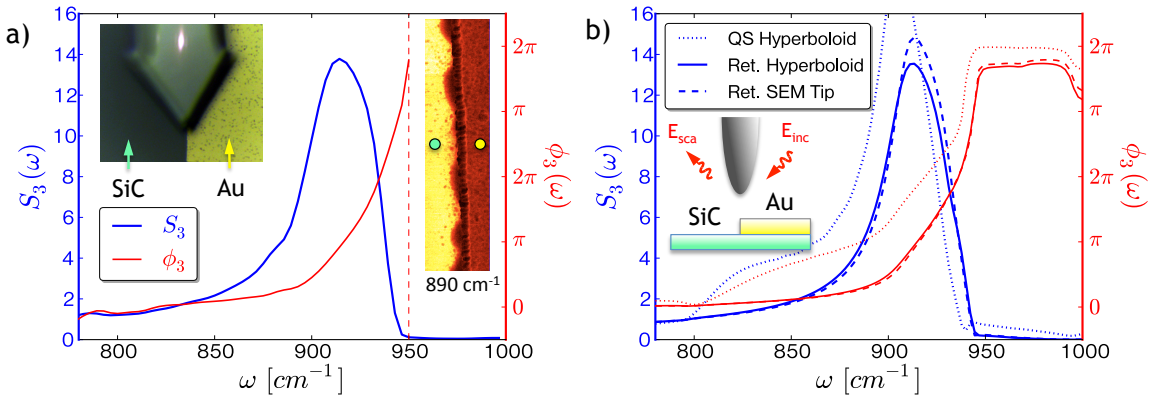

Figure 2.6: Spectroscopic near-field response in the limit of strongly resonant probe-sample interactions.

a) Amplitude S_3 and phase ϕ_3 of the back-scattered near-field signal from a 6H SiC crystal, measured in the vicinity of the surface optical phonon and referenced to a surface-deposited gold film, as obtained in a single acquisition by nanoFTIR. **Left inset:** Visible light image (width 60 μm) above the near-field probe at the SiC/gold interface. **Right inset:** PSHet near-field S_3 image (width 1 μm) of the interface with sample and reference nanoFTIR locations indicated. **b)** Lightning rod model predictions for near-field signal from SiC using optical constants measured by in-house ellipsometry. While insensitive to details of probe geometry (see text), fully retarded (*Ret.*) calculations provide superior agreement to the experimental spectra than the quasi-static (*QS*) approximation.

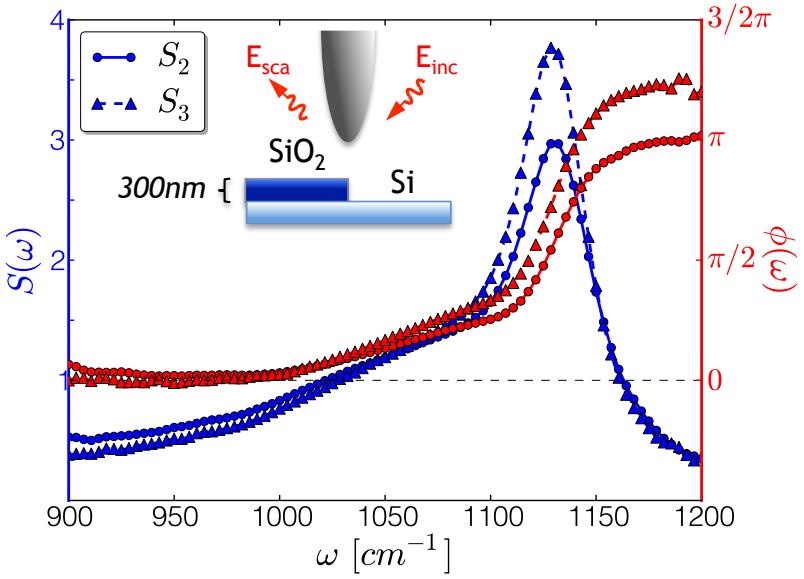

Figure 2.7: Spectroscopic near-field response of an oxide film suitable for “inversion”.

Amplitude S and phase ϕ of the back-scattered near-field signal from a 300 nm SiO_2 film, measured in the vicinity of the surface optical phonon and referenced to the silicon substrate, as obtained in a single acquisition by nanoFTIR.

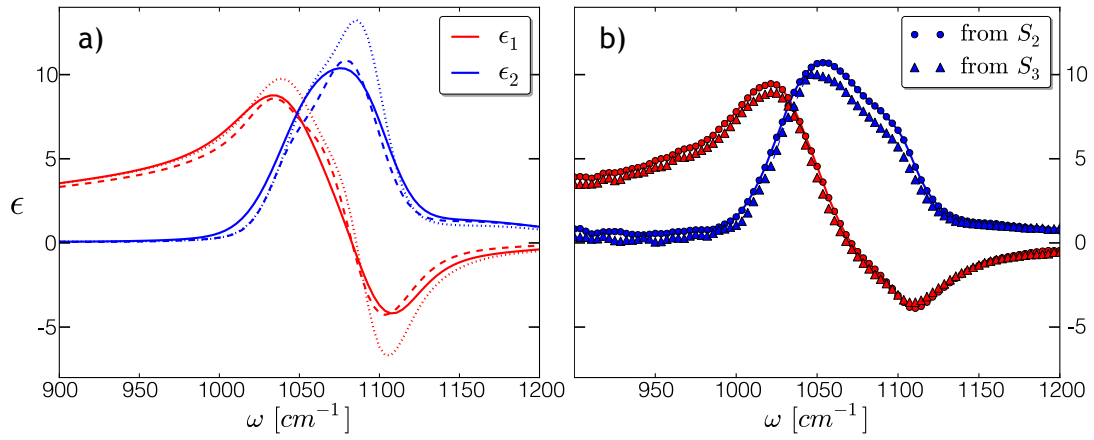

Figure 2.8: Inversion of the spectroscopic near-field response to extract material optical constants.

a) Typical variation in optical constants among thermal oxide thin films taken from literature ellipsometry. Pairs of red and blue curves with identical line style are associated with distinct thin film samples.[42] **b)** Optical constants of a 300 nm SiO_2 film extracted from near-field spectra $S_2(\omega)$ and $S_3(\omega)$ following the method of Eq. (24).

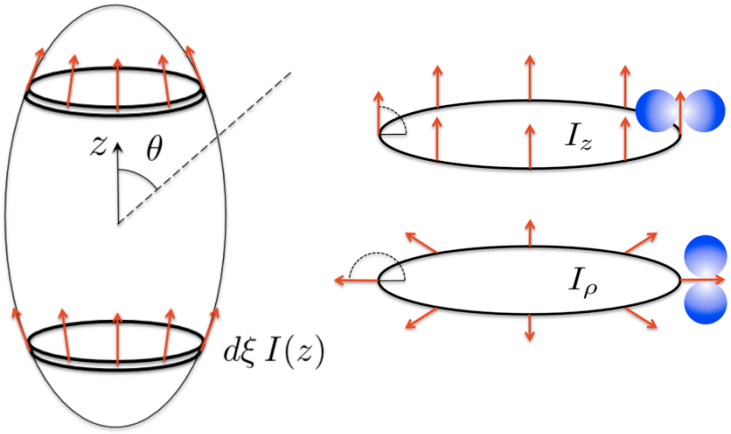

Figure 2.9: Conceptual decomposition of the radiation from an axisymmetric conductor.

(Left) The field radiated from an axisymmetric body to an observation point at inclination angle θ is constructed from the contributions of currents (shown in red) through infinitesimal surface annuli. **(Right)** The two independent polarizations composing any annular axisymmetric current distribution, with associated angular radiation profiles (Eq. E1) shown schematically in blue.

2.11 Appendix A Experimental methods

In the following sections, we apply the *lightning rod model* in comparison with near-field spectra measured for SiO_2 thin films and SiC, acquired with the following experimental apparatus. Infrared nano-imaging and nano-spectroscopy measurements were performed with a NeaSNOM scanning near-field optical microscope (*Neaspec GmBH*) by scanning a platinum silicide AFM probe (PtSi-NCH, *NanoAndMore USA*; cantilever resonance frequency 300 kHz, nominal radius of curvature 20-30 nanometers) in tapping mode over the sample while illuminating with a focused infrared laser beam, resulting in back-scattered radiation modulated at the probe tapping frequency Ω and harmonics thereof. In our pseudo-heterodyne detection setup, this back-scattered radiation interferes at a mercury-cadmium-telluride detector (*Kolmar Technologies Inc.*) with a reference beam whose phase is continuously modulated by reflection from a mirror piezoelectrically oscillated at a frequency $\delta\Omega$ (≈ 300 Hz). Demodulation of the detector signal at frequency side-bands $n\Omega \pm m\,\delta\Omega$ for integral m supplies the background-free amplitude S_n and phase ϕ_n of the infrared signal at harmonics n of the probe's tapping frequency.[4, 10, 11]

The super-linear dependence of near-field interactions versus the tip-sample separation distance implies that, in the case of harmonic tapping motion, signal harmonics at $n \geq 2$ are directly attributable to near-field polarization of the tip[48]. Contrasts in near-field signal intensity and phase at these harmonics therefore correspond to variations in local optical properties of the sample[26]. Tunable fixed-frequency CW quantum cascade lasers (QCLs, *Daylight Solutions Inc.*) and a tunable CO_2 laser (*Access Laser Co.*) were used for imaging and spectroscopy of SiO_2 films and SiC, respectively.

NanoFTIR spectroscopy[7][8] was enabled by illumination from a broadband mid-infrared laser producing tunable radiance across the frequency range 700-2400 cm_{-1}. This coherent mid-infrared illumination is generated through the nonlinear difference-frequency combination of beams from two near-infrared erbium-doped fiber lasers – one at 5400 cm_{-1} and the other a tunable supercontinuum near-infrared laser (*TOPTICA Photonics Inc.*) – resulting in 100 fs

pulses at a repetition rate of 40 MHz. An asymmetric Michelson interferometer with 1.5 millimeter travel range translating mirror enables collection of demodulated near-field amplitude $S_n(\omega)$ and phase $\phi_n(\omega)$ spectra with 3 cm$_{-1}$ resolution.

2.12 Appendix B Resolution of the field from a charged ring into evanescent waves

The xy-plane Fourier decomposition of the Coulomb field of a point charge Q located at the origin is well known[71]:

$$\vec{E}(\vec{r}) = -\frac{Q}{2\pi}\iint_{-\infty}^{\infty} dk_x\, dk_y\, \left(i\frac{k_x\hat{x}+k_y\hat{y}}{q}+\hat{z}\right)$$

$$\times e^{i(k_x x+k_y y)+qz}$$

$$= -Q\int_0^{\infty} dq\, q\, \left(J_0(q\rho)\hat{z}+J_1(q\rho)\hat{\rho}\right) e^{qz} \qquad (28)$$

for $z<0$ and with $q \equiv \sqrt{k_x^2+k_y^2}$. This decomposition can be applied similarly to a ring of charge with radius $\mathcal{R}$, centered in a plane through the origin with z-axis normal:

$$\vec{E}_{\mathcal{R}}(\vec{r}) = \frac{Q}{4\pi^2}\int_0^{2\pi} d\phi' \int_0^{\infty} dq \int_0^{2\pi} d\phi\, \vec{\mathcal{E}}_{\mathcal{R}}(q,\vec{r},\phi')$$

$$\vec{\mathcal{E}}_{\mathcal{R}} \equiv -\left(\hat{z}+i\frac{k_x\hat{x}+k_y\hat{y}}{q}\right) e^{iq\left(\rho\cos\phi-\mathcal{R}\cos(\phi-\phi')\right)+qz}.$$

Here ϕ' is an angular integration variable about the circumference of the ring. We obtain

$$\vec{E}_{\mathcal{R}}(\vec{r}) = -Q\int_0^{\infty} dq\, q\, J_0(q\mathcal{R})\left(J_0(q\rho)\hat{z}+J_1(q\rho)\hat{\rho}\right) e^{qz}. \qquad (29)$$

The total field is thus a sum of axisymmetric p-polarized evanescent waves weighted by the geometry-induced prefactor $q\,J_0(q\mathcal{R})$. Eq. (B2) constitutes the central result of this section.

2.13 Appendix C Quasi-static boundary element method for an axisymmetric dielectric and conductor

A tractable electrostatic boundary element method applicable to systems of homogeneous dielectrics can be developed as follows [67]. Gauss's law constrains the density of bound charge ρ_b at the boundaries between dielectric media as:

$$\nabla \cdot \vec{E} = \nabla \cdot \frac{\vec{D}}{\epsilon} = 4\pi\rho_b$$
$$\therefore \quad 4\pi\rho_b = \delta_S \left(\frac{1}{\epsilon_2} - \frac{1}{\epsilon_1} \right) \hat{n}_{12} \cdot \vec{D} \tag{30}$$

Eq. C1 follows in the case that free charge is absent at dielectric boundaries such that $\nabla \cdot \vec{D} = 0$, and δ_S is a surface Dirac delta function associated with the boundary between media of dielectric constant ϵ_1 and ϵ_2, with $\hat{n}_{12}$ the unit vector perpendicular to this boundary oriented from medium 1 to medium 2. Continuity of the surface normal displacement field across the dielectric interface permits its evaluation at positions $\vec{r}$ along the boundary as a limit taken infinitesimally inside medium 2:

$$\hat{n}_{12} \cdot \vec{D}\,(\vec{r}) = \epsilon_2 \lim_{t \to 0^+} -\hat{n}_{12} \cdot \nabla V\,(\vec{r} + t\,\hat{n}_{12})\,. \tag{31}$$

The scalar potential $V(\vec{r})$ finds contributions from both incident (external) fields $\vec{E}_{\text{inc}}$, originating as from distant free charges, as well as from bound charges at the dielectric boundary. Taking the bound charge ρ_b as the product of a surface density σ_Q (distinguished from electrical conductivity σ) with the surface Dirac delta function, the latter contribution comprises a surface integral on the boundary S:

$$V_b(\vec{r}) = \int_S dS' \, \frac{\sigma_Q(\vec{r}\prime)}{|\vec{r} - \vec{r}\prime|} \tag{32}$$

Evaluating the discontinuous surface normal electric field $-\hat{n}_{12} \cdot \nabla V_b$ from this contribution involves:

$$\lim_{t\to 0+} -\hat{n}_{12}\cdot\nabla\left(1/\left|\vec{r}+t\,\hat{n}_{12}-\vec{r}\prime\right|\right) = 2\pi\delta(\vec{r}-\vec{r}\prime) - F(\vec{r},\vec{r}\prime)$$
$$\text{with}\quad F(\vec{r},\vec{r}\prime) \equiv -\frac{\hat{n}_{12}\cdot(\vec{r}-\vec{r}\prime)}{\left|\vec{r}-\vec{r}\prime\right|^3}. \tag{33}$$

Gauss's law (Eq. C1) therefore yields an integral equation in the surface bound charge density $\sigma_Q(\vec{r})$:

$$4\pi\frac{\epsilon_1\epsilon_2}{\epsilon_1-\epsilon_2}\sigma_Q(\vec{r}) = \epsilon_2\Bigg[\hat{n}_{12}\cdot\vec{E}_{\text{inc}}(\vec{r}) + 2\pi\sigma_Q(\vec{r}) - \int_S dS'\,F(\vec{r},\vec{r}\prime)\,\sigma_Q(\vec{r}\prime)\Bigg], \tag{34}$$

which upon consolidation yields:

$$2\pi\frac{\epsilon_1+\epsilon_2}{\epsilon_1-\epsilon_2}\sigma_Q(\vec{r}) = \hat{n}_{12}\cdot\vec{E}_{\text{inc}} - \int_S dS'\,F(\vec{r},\vec{r}\prime)\,\sigma_Q(\vec{r}\prime). \tag{35}$$

Without loss of generality, this equation can be utilized to pre-compute the quasi-electrostatic response of an axisymmetric body of dielectric constant ϵ_2 to incident fields, taking $\epsilon_1 = 1$ as air, parametrizing the integral kernel F by axial and surface radial coordinates z and $\mathcal{R}_z$, respectively, and expressing $\hat{n}_{12}$ through axial derivatives of the latter.

However, to unambiguously present our method of solution to equations like Eq. C6 and to promote its application for the description of metallic near-field probes, we confine our attention specifically to the ideally conducting limit, wherein ϵ_2 is divergent. For Eq. C1 to hold with finite normal displacement in Eq. C2 therefore requires a vanishing normal gradient of the total potential V just inside the probe surface. Lacking free or bound charges within its volume, the probe interior and surface therefore reside at constant total potential, signifying zero internal field and perfect screening by the surface:

$$V_{\text{inc}}(\vec{r}) + V_b(\vec{r}) = V_0 \quad \text{on } S. \tag{36}$$

This criterion follows equivalently from Eq. (C6) in the limit $\epsilon_2 \gg \epsilon_1$ through reverse application of Eq. (C4).

The incident potential of an axisymmetric evanescent field is given in cylindrical coordinates ρ, ϕ, and z by $V_{\mathrm{inc}}(\vec{r}) = J_0(q\rho)/q\, e^{-qz}$. The potential V_b is generated by the surface charge density $\sigma_Q(\vec{r})$, which may be divided into a continuum of rings, each with charge $dQ = \lambda_Q(z)\, dz$ and radius $\mathcal{R}_z$:

$$\begin{aligned} V_b(\vec{r}) &= \int_S dS' \, \frac{\sigma_Q(\vec{r}\prime)}{|\vec{r}\prime - \vec{r}|} \\ &= \int_0^\infty dz' \, \Phi(\vec{r}, z') \, \lambda_Q(z') \end{aligned} \tag{37}$$

with

$$\begin{aligned} \Phi &\equiv \int_0^{2\pi} \frac{d\phi'}{2\pi} \frac{1}{\sqrt{(z'-z)^2 + \rho^2 + \mathcal{R}_{z'}^2 - 2\rho\mathcal{R}_{z'}\cos\phi'}} \\ &= \frac{2K\left(-\frac{4\rho\mathcal{R}_{z'}}{(\rho-\mathcal{R}_{z'})^2+(z-z')^2}\right)}{\pi\sqrt{(\rho-\mathcal{R}_{z'})^2+(z-z')^2}}. \end{aligned} \tag{38}$$

Here Φ constitutes the Coulomb kernel for a ring of charge, and $K(\ldots)$ denotes the elliptic integral of the first kind. Evaluating V_{obj} at the boundary of the object ($\rho = \mathcal{R}_z$) and discretizing z in Eqs. (C7) and (C8) as by Gauss-Legendre quadrature, we obtain the linear system

$$\begin{aligned} \mathbf{M}\,\vec{\lambda}_Q &= V_0 - \vec{V}_{\mathrm{inc}} \\ \text{with} \quad \mathbf{M}_{ij} &\equiv \Phi(z_i, z_j)\, \delta z_j. \end{aligned} \tag{39}$$

Vectors denote evaluation at positions $\{z_i, \mathcal{R}(z_i)\}$. The condition of overall charge neutrality fixes the value of V_0:

$$\begin{aligned} \sum_i \vec{\lambda}_Q \, \delta z_i = 0 &= \sum_i \delta z_i \, \mathbf{M}^{-1} \left(V_0 - \vec{V}_{\mathrm{inc}}\right) \\ \therefore \quad V_0 &= \frac{\sum_i \delta z_i \left[\mathbf{M}^{-1}\, \vec{V}_{\mathrm{inc}}\right]_i}{\sum_i \delta z_i \left[\mathbf{M}^{-1}\, \vec{I}\right]_i}. \end{aligned} \tag{40}$$

Here $\vec{I}$ denotes a vector with all entries unity. While Eq. (C10) would appear to be directly solvable, such Fredholm integral equations of the first kind are notoriously ill-conditioned. Consequently, we adopt regularization methods [72][73] to invert the integral operator (matrix) $\mathbf{M}$,

yielding smooth functions $\lambda(z)$ in accord with standard quasi-static solutions for well-studied geometries like the conducting sphere and ellipsoid. (It is worth noting that, since Eq. (C6) presents a well-conditioned Fredholm integral equation of the second kind, no such regularization of the solution is required in the case of a dielectric solid.) Once the inverse operator $\mathbf{M}^{-1}$ has been computed for a given geometry, calculation of $\lambda(z)$ for arbitrary $V_{\mathrm{inc}}(\vec{r})$ is fast and trivial.

For an axisymmetric system, Eqs. (C10) and (C11) together with this solution method are sufficient to calculate the linear charge density induced on a conducting body due to an incident quasi-static field, and constitute the central result of this section. In practice, the converged calculation of $\mathbf{M}^{-1}$ for a particular axisymmetric geometry takes no longer than a few tens of seconds on a single 2.7 GHz processor. Calculation of $\lambda(z)$ for a range of q values sufficient for converged *lightning rod model* calculations requires only several seconds using the same processor. In this work, the incident potential appropriately used for V_{inc} at $q = 0$ corresponds with a homogeneous axially polarized field, $V_{\mathrm{inc}}(\vec{r}) = E_{\mathrm{inc}}\, z$. Thereby $\lambda(z)$ computed for $q = 0$ and $q \neq 0$ across discretized momenta q_i are taken as an adequately-sampled representation for $\Lambda_0(z)$ and $\Lambda(q, z)$, respectively.

2.14 Appendix D Electrodynamic boundary element method for an axisymmetric conductor

As in the quasi-static case, the charge distribution induced on a nearly perfectly conducting object by an incident electrodynamic field oscillating at frequency ω resides exclusively at the object's surface. To compute this distribution, we begin with detailed force balance at the boundary S along directions tangential to the surface. Assuming axisymmetry, we need only consider without loss of generality the surface tangential directions $\hat{\xi}$ orthogonal to $\hat{\phi}$ that possess positive $\hat{z}$-component:

$$\hat{\xi} \cdot \left(\vec{E}_{\text{inc}} + \vec{E}_{obj} \right) = \vec{0} \quad \text{on} \quad S. \tag{41}$$

Since $\vec{E} = -\nabla V + i\omega \vec{A}$ for scalar and vector potentials V and $\vec{A}$, we have

$$\begin{aligned} E_{inc\,\xi}(\vec{r}) &= \int_S \left(\partial_\xi \, dV_{obj}(\vec{r}) - i\omega \, \hat{\xi} \cdot d\vec{A}_{obj}(\vec{r}) \right) \quad \text{on} \quad S \\ &= \int_0^L dz' \Big[\partial_\xi \Phi(z, z') \, \lambda_Q(z') \\ &\quad - i\omega \, \mathcal{A}_\xi(z, z') \, I(z') \Big], \end{aligned} \tag{42}$$

where we have parametrized points on S by the object's axial coordinate $0 < z < L$; meanwhile $\lambda_Q(z) \equiv dQ/dz$ denotes the linear charge density and $I(z)$ denotes the total current passing along the object surface through a $\hat{z}$-normal plane at z. Φ and $\mathcal{A}_\xi$ denote integration kernels for the scalar and vector potentials, respectively.

The continuity equation for charge implies $\partial_z I(z) = i\omega \, \lambda_Q(z)$, and since current is forbidden to flow from the hypothetically isolated object, integration by parts yields:

$$\begin{aligned} E_{inc\,\xi}(z) = \int_0^L dz' \lambda_Q(z') \Big[&\partial_\xi \Phi(z, z') \\ &- \omega^2 \int_0^{z'} d\mathfrak{z}' \, \mathcal{A}_\xi(z, \mathfrak{z}') \Big] \end{aligned} \tag{43}$$

In terms of the azimuthal angle ϕ and surface radial coordinate at z denoted $\mathcal{R}_z$, the scalar potential kernel is given by

$$\Phi(z,z') = \int_0^{2\pi} \frac{d\phi'}{2\pi} \frac{e^{i\omega/c\,\Delta(z,z',\phi)}}{\Delta(z,z',\phi)}$$
$$\text{with} \quad \Delta \equiv \sqrt{(z-z')^2 + \mathcal{R}_z^2 + \mathcal{R}_{z'}^2 - 2\,\mathcal{R}_z \mathcal{R}_{z'} \cos\phi}, \tag{44}$$

which may be computed straightforwardly for a given object geometry by adaptive quadrature. The exponential phase ensures the integrand is evaluated at retarded time. The vector potential kernel may be established from

$$\vec{A}(\vec{r}) = \frac{1}{c^2} \int dS' \frac{\vec{K}(\vec{r}\,')}{|\vec{r} - \vec{r}\,'|}\, e^{i\omega/c\,|\vec{r}-\vec{r}\,'|} \tag{45}$$

and

$$\mathcal{A}_\xi(z,z') \equiv \hat{\xi}_z \cdot \frac{d\vec{A}}{dz'}(z),$$

with $\vec{K}(z) \equiv I(z)/2\pi\mathcal{R}_z\,\hat{\xi}$ denoting the local surface current. Noting that $dS' = 2\pi\mathcal{R}'_z\sqrt{1+\partial_{z'}\mathcal{R}'_z}\,dz'$ and that the direction of $\hat{\xi}$ is manifestly z- and ϕ-dependent (expressed here as $\hat{\xi}_{z\phi}$), we obtain

$$\frac{dA_\xi}{dz'}(z) = \sqrt{1+\partial_{z'}\mathcal{R}'_z}\,\frac{I(z')}{c^2} \int_0^{2\pi} \frac{d\phi'}{2\pi} \frac{\hat{\xi}_{z\phi} \cdot \hat{\xi}_{z'\phi'}}{|\vec{r} - \vec{r'}|}\, e^{i\,\cdots},$$

with the exponential factor unchanged. The ϕ-dependence of A_ξ is rendered moot on account of axisymmetry, and so is suppressed.

Finally, since the surface tangential unit vector at height z and azimuthal angle ϕ is expressed in terms of the radial coordinate $\mathcal{R}_z$ and the radial unit vector $\hat{\rho}_\phi$ as

$$\hat{\xi}_{z\phi} = \frac{\partial_z \mathcal{R}_z\,\hat{\rho}_\phi + \hat{z}}{\sqrt{1+\partial_z\mathcal{R}_z^2}}, \quad \text{with} \quad \hat{\rho}_\phi \cdot \hat{\rho}_{\phi'} = \cos(\phi - \phi'),$$

we obtain the vector potential kernel as:

$$\mathcal{A}_\xi(z,z') = \frac{1}{c^2}\left[\int_0^{2\pi}\frac{d\phi'}{2\pi}\frac{e^{i\omega/c\,\Delta(z,z',\phi')}}{\Delta(z,z',\phi')} + \partial_z\mathcal{R}_z\,\partial_{z'}\mathcal{R}_{z'}\int_0^{2\pi}\frac{d\phi'}{2\pi}\frac{e^{i\omega/c\,\Delta(z,z',\phi')}}{\Delta(z,z',\phi')}\cos\phi'\right] \times \frac{1}{\sqrt{1+\partial_z\mathcal{R}_z^2}}.$$

Here Δ is defined as in Eq. (D4), and note that the first term within brackets in fact equates with the scalar potential kernel. Only the second term must be computed anew, and similarly by adaptive quadrature.

We now define a convenient quasi-potential function for the incident field:

$$V_{\rm inc}(z) \equiv -\int dz\sqrt{1+\partial_z\mathcal{R}_z^2}\;\hat{\xi}_z\cdot\vec{E}_{\rm inc}(z) = -\int dz\;\left(\partial_z\mathcal{R}_z\,E_{inc\,\rho} + E_{inc\,z}\right).$$

Proceeding with Eq. (D3), we relabel $z \to \mathfrak{z}$ before applying the operation $\int_0^{\xi_z} d\xi = \int_0^z d\mathfrak{z}\sqrt{1+\partial_{\mathfrak{z}}\mathcal{R}_{\mathfrak{z}}^2}$ to both sides, resulting in:

$$\int_0^L dz'\lambda_Q(z')\left[\Phi(z,z') - \frac{\omega^2}{c^2}\int_0^z d\mathfrak{z}\int_0^{z'} d\mathfrak{z}'\;\bar{\mathcal{A}}_\xi(\mathfrak{z},\mathfrak{z}')\right] = V_0 - V_{\rm inc}(z).$$

Here we have applied Eq. (D7) and taken V_0 as a constant of integration. Furthermore we have defined a new vector potential kernel $\bar{\mathcal{A}}_\xi(z,z') \equiv \sqrt{1+\partial_z\mathcal{R}_z^2}\,\mathcal{A}_\xi(z,z')$, which is now symmetric in its two arguments. Note that the first term in brackets in Eq. (D8) accounts for the retarded Coulomb force among surface charges, whereas the second term describes radiative forces with strength of order $\mathcal{O}^2(L/\lambda)$ produced by conduction currents, where λ the free-space wavelength of light.

As in Appendix C, discretizing z results in a linear system

$$\left[\mathbf{\Phi} - \frac{\omega^2}{c^2}\overline{\mathbf{W}}^T\bar{\mathcal{A}}\,\overline{\mathbf{W}}\right]\mathbf{W}\vec{\lambda}_Q = V_0 - \vec{V}_{\rm inc}, \tag{46}$$

where $\mathbf{\Phi}_{ij} \equiv \Phi(z_i, z_j)$, $\mathbf{W} \equiv \mathrm{diag}\{\delta z_i\}$, $\bar{A}_{ij} \equiv \bar{A}_\xi(z_i, z_j)$, $\overline{\mathbf{W}}_{ij} \equiv \delta z_i\, \theta(j-i)$, and $\theta(\ldots)$ denotes the Heaviside unit step function. The superscript T denotes matrix transpose. Vectors again denote evaluation at axial and radial coordinates $\{z_i, \mathcal{R}(z_i)\}$ along the object surface. Self-consistency requires a value of V_0 ensuring charge neutrality. Taking $\mathbf{M}$ to be the full integral operator preceding $\vec{\lambda}_Q$ in the linear system above, V_0 is again given by Eq. (C11), and $\vec{\lambda}_Q$ is obtained via inversion of $\mathbf{M}$. Note that the particular selections of lower integration bounds on V_{inc} in Eq. (D7) and $\bar{A}$ in Eq. (D8) are naturally rendered arbitrary when this condition is satisfied. As in the quasi-static case, once $\mathbf{M}^{-1}$ has been computed for a given geometry (less than one minute of computation on a 2.7 GHz processor), the calculation of $\lambda_Q(z)$ for arbitrary $\vec{E}_{\mathrm{inc}}(\vec{r})$ is both fast and trivial (several milliseconds). To emulate plane wave illumination from an inclination angle θ with respect to the z-axis, in this work we substitute the axisymmetric analog

$$\vec{E}_{\mathrm{inc}}(\vec{r}) = \left(J_0(q\rho)\,\hat{z} + i\frac{\sqrt{k^2-q^2}}{q} J_1(q\rho)\,\hat{\rho} \right) \times e^{-i\sqrt{k^2-q^2}z} \tag{47}$$

with

$$q \equiv k\,\sin\theta \quad \text{and} \quad k \equiv \omega/c.$$

This field profile equates with a rotational sum of θ-directed plane waves inbound from all azimuthal angles ϕ.

For an axisymmetric system, Eqs. (D4), (D6), and (D9) are sufficient to calculate the linear charge density induced on a conducting body due to an incident electrodynamic field, and constitute the central result of this section. In practice, the converged electrodynamic calculation of $\mathbf{M}^{-1}$ for a particular axisymmetric geometry takes only twice as long as for the quasi-static case.

2.15 Appendix E Radiation from an axisymmetric conductor

The far-field radiation profile from an arbitrary current distribution can be obtained by integrating the far-field contribution $\overleftrightarrow{G}_{\mathrm{FF}}$ to the Green's dyadic function $\overleftrightarrow{G}$ [74] from infinitesimal current elements at positions $\vec{r}\,\prime$, here for demonstration considered oriented along the $\hat{z}$-direction, as

$$d\vec{E}_{\mathrm{rad}}(\vec{r}) = \frac{i\omega}{4\pi}\vec{G}_{\mathrm{FF},z}(\vec{r},\vec{r}\,\prime)\, j_z(\vec{r}\,\prime)\, dV' \tag{48}$$

with

$$\vec{G}_{\mathrm{FF},z}(\vec{r},\vec{r}\,\prime) \equiv -\frac{1}{c^2}\,\frac{e^{i\omega/c\,|\vec{r}-\vec{r}\,\prime|}}{|\vec{r}-\vec{r}\,\prime|}\,\sin\theta\,\hat{\theta},$$

exhibiting the familiar field profile of a radiating dipole. Here θ denotes the inclination angle of the observation point $\vec{r}$ from the z-axis in a spherical coordinate system.

The dimension of a nearly perfect conductor is by definition much greater than the magnetic skin depth of the constituent material. Consequently, volume integration reduces to an integral over surface current contributions $dS\,\vec{K}(\vec{r})$. In an axisymmetric object, these contributions are associated with surface annuli located at axial coordinates z and radii $\mathcal{R}_z$, for which $dS = 2\pi\mathcal{R}_z\,d\xi$ with $d\xi \equiv \sqrt{1+\partial_z\mathcal{R}_z^2}\,dz$. We first evaluate the radiated field from such an annulus, considering contributions from the two independently allowed polarizations of axisymmetric current separately, as depicted in Fig. 2.9.

We define the total current as $I_\alpha(z) = 2\pi\mathcal{R}_z\,K_\alpha(z)$ for polarizations $\alpha = z, \rho$. For the z-polarized contribution, integrating Eq. E1 through an annulus about azimuthal angle ϕ obtains

$$\begin{aligned} d\vec{E}_{\mathrm{rad},z} &= -\frac{i\omega}{4\pi c^2}\,\frac{e^{i\omega/c\,\delta r(z)}}{\delta r(z)}\,\sin\theta\,K_z(z)\,d\xi \\ &\quad\times\int_0^{2\pi} d\phi\,\mathcal{R}_z\exp\left(i\omega/c\,\mathcal{R}_z\cos\phi\,\sin\theta\right)\hat{\theta} \\ &= -\frac{i\omega}{4\pi c^2}\,\frac{e^{i\omega/c\,\delta r(z)}}{\delta r(z)}\sin\theta\,I_z(z)\,d\xi \\ &\quad\times J_0(\omega/c\,\mathcal{R}_z\sin\theta)\,\hat{\theta}. \end{aligned}$$

Here $\delta r(z)$ denotes the distance from the center of the z-located annulus to the observation point, and we have applied the approximation $|\vec{r} - \vec{r}\prime|^{-1} \approx \delta r(z)^{-1}$ valid for $\delta r(z) \gg \mathcal{R}_z$. An elementary analysis accounting for rotation of the radiant polarization vector in the integrand of the ρ-polarized contribution similarly results in:

$$d\vec{E}_{\mathrm{rad},\rho} = \frac{\omega}{4\pi c^2} \frac{e^{i\omega/c\,\delta r(z)}}{\delta r(z)} \cos\theta\, I_\rho(z)\, d\xi \times J_1(\omega/c\,\mathcal{R}_z \sin\theta)\, \hat{\theta}.$$

Current $I(z)$ flows on the surface of an axisymmetric conductor along a surface tangent vector

$$\hat{\xi} = \frac{\partial_z \mathcal{R}_z\, \hat{\rho} + \hat{z}}{\sqrt{1 + \partial_z \mathcal{R}_z^2}}.$$

Consequently, the total radiation from the axisymmetric body of length L is given by a commensurate sum of $\hat{z}$- and $\hat{\rho}$-polarized contributions:

$$\vec{E}_{\mathrm{rad}}(\theta) = -\frac{i\omega}{4\pi c^2} \frac{e^{i\omega/c\,\Delta r}}{\Delta r} \int_0^L dz\, \mathcal{E}(z,\theta)\, I(z)\, \hat{\theta} \tag{49}$$

with

$$\mathcal{E} = e^{-i\omega/c\, z\cos\theta} \Big[\sin\theta\, J_0(\omega/c\,\mathcal{R}_z \sin\theta) + i\, \partial_z \mathcal{R}_z \cos\theta\, J_1(\omega/c\,\mathcal{R}_z \sin\theta) \Big]. \tag{50}$$

Note the factor $1/\sqrt{1 + \partial_z \mathcal{R}_z^2}$ has been absorbed by the integration measure dz. Here $\Delta r \equiv \delta r(z) + z\cos\theta$ is the distance from one apex of the object (at $z = 0$) to the observation point, and we have applied the approximation $\delta r(z)^{-1} \approx \Delta r^{-1}$ appropriate for distances $\Delta r \gg L$. After applying the continuity equation for charge $\partial_z I(z) = i\omega\, \lambda_Q(z)$ (with λ_Q the linear charge density) together with the fact that the current vanishes at the extrema of a hypothetically isolated body (at $z = 0,\, L$), integration by parts yields:

$$\vec{E}_{\mathrm{rad}}(\theta) = -\frac{\omega^2}{4\pi c^2}\,\frac{e^{i\omega/c\,\Delta r}}{\Delta r}\int_0^L dz\,\lambda_Q(z)\int_0^z dz'\mathcal{E}(z',\theta)\,\hat{\theta}. \tag{51}$$

Provided an electrodynamically consistent charge distribution $\lambda_Q(z)$ calculated at frequency ω, Eq. (E6) can be evaluated straightforwardly for a given object geometry by quadrature. In the notation of Appendix D, the complex amplitude of the $\hat{\theta}$-polarized radiation field becomes:

$$E_{\mathrm{rad}}(\theta) = -\frac{\omega^2}{4\pi c^2}\,\frac{e^{i\omega/c\,\Delta r}}{\Delta r}\,\vec{\lambda}_Q^{\,T}\,\mathbf{W}\,\overline{\mathbf{W}}\,\vec{\mathcal{E}}_\theta. \tag{52}$$

Here the superscript T denotes vector transpose, and $\vec{\mathcal{E}}_\theta$ indicates evaluation of $\mathcal{E}(z,\theta)$ at the chosen observation angle θ. Together with Eq. (E5), this expression is sufficient to compute the electric field radiated from a conducting axisymmetric system, and constitutes the central result of this section.

Projected onto a detector sensitive to $\hat{\theta}$-polarized light, the radiation contributions $[\vec{e}_{\mathrm{rad}}]_i$ utilized in Sec. II are computed by expressing each single-momentum probe response function (linear charge density) $\Lambda(q_i, z)$ in discretized real space representation $\left[\vec{\lambda}_Q\right]_j \equiv \Lambda(q_i, z_j)$ and applying Eq. (E7), taking $\theta \approx 60°$ relative to the z-axis of the near-field probe as the typical collection angle of experimental detection optics.

2.16 References

1. L. Novotny. The History of Near-field Optics. *Progress in Optics*, 50:137–184, 2007.

2. U. Ch. Fischer and D. W. Pohl. Observation of single-particle plasmons by near-field optical microscopy. *Phys. Rev. Lett.*, 62:458–461, Jan 1989.

3. Yasushi Inouye and Satoshi Kawata. Near-field scanning optical microscope with a metallic probe tip. *Opt. Lett.*, 19(3):159–161, Feb 1994.

4. Bernhard Knoll and Fritz Keilmann. Enhanced dielectric contrast in scattering-type scanning near-field optical microscopy. *Optics Communications*, 182(46):321 – 328, 2000.

5. F. Keilmann and R. Hillenbrand. Near-field microscopy by elastic light scattering from a tip. *Philosophical Transactions of the Royal Society of London. Series A: Mathematical, Physical and Engineering Sciences*, 362(1817):787–805, 2004.

6. A. J. Huber, F. Keilmann, J. Wittborn, J. Aizpurua, and R. Hillenbrand. Terahertz near-field nanoscopy of mobile carriers in single semiconductor nanodevices. *Nano Letters*, 8(11):3766–3770, 2008. PMID: 18837565.

7. S. Amarie and F. Keilmann. Broadband-infrared assessment of phonon resonance in scattering-type near-field microscopy. *Phys. Rev. B*, 83:045404, Jan 2011.

8. Markus Brehm, Albert Schliesser, and Fritz Keilmann. Spectroscopic near-field microscopy using frequency combs in the mid-infrared. *Opt. Express*, 14(23):11222–11233, Nov 2006.

9. Florian Huth, Alexander Govyadinov, Sergiu Amarie, Wiwat Nuansing, Fritz Keilmann, and Rainer Hillenbrand. Nano-ftir absorption spectroscopy of molecular fingerprints at 20 nm spatial resolution. *Nano Letters*, 12(8):3973–3978, 2012.

10. Lewis Gomez, Renaud Bachelot, Alexandre Bouhelier, Gary P. Wiederrecht, Shih hui Chang, Stephen K. Gray, Feng Hua, Seokwoo Jeon, John A. Rogers, Miguel E. Castro, Sylvain Blaize, Ilan Stefanon, Gilles Lerondel, and Pascal Royer. Apertureless scanning near-field optical microscopy: a comparison between homodyne and heterodyne approaches. *J. Opt. Soc. Am. B*, 23(5):823–833, May 2006.

11. Nenad Ocelic, Andreas Huber, and Rainer Hillenbrand. Pseudoheterodyne detection for background-free near-field spectroscopy. *Applied Physics Letters*, 89(10):101124, 2006.

12. R. Hillenbrand and F. Keilmann. Complex optical constants on a subwavelength scale. *Phys. Rev. Lett.*, 85:3029–3032, Oct 2000.

13. Martin Schnell, Aitzol Garcia-Etxarri, Andreas J. Huber, Kenneth B. Crozier, Andrei Borisov, Javier Aizpurua, and Rainer Hillenbrand. Amplitude- and phase-resolved near-field mapping of infrared antenna modes by transmission-mode scattering-type near-field microscopyâ€ . *The Journal of Physical Chemistry C*, 114(16):7341–7345, 2010.

14. P. Scott Carney, Bradley Deutsch, Alexander A. Govyadinov, and Rainer Hillenbrand. Phase in nanooptics. *ACS Nano*, 6(1):8–12, 2012.

15. Xiaoji G. Xu, Mathias Rang, Ian M. Craig, and Markus B. Raschke. Pushing the sample-size limit of infrared vibrational nanospectroscopy: From monolayer toward single molecule sensitivity. *The Journal of Physical Chemistry Letters*, 3(13):1836–1841, 2012.

16. Sergiu Amarie, Paul Zaslansky, Yusuke Kajihara, Erika Griesshaber, Wolfgang W. Schmahl, and Fritz Keilmann. Nano-ftir chemical mapping of minerals in biological materials. *Beilstein Journal of Nanotechnology*, 3:312–323, 2012.

17. Joanna M. Atkin, Samuel Berweger, Andrew C. Jones, and Markus B. Raschke. Nano-optical imaging and spectroscopy of order, phases, and domains in complex solids. *Advances in Physics*, 61(6):745–842, 2012.

18. M. M. Qazilbash, M. Brehm, Byung-Gyu Chae, P.-C. Ho, G. O. Andreev, Bong-Jun Kim, Sun Jin Yun, A. V. Balatsky, M. B. Maple, F. Keilmann, Hyun-Tak Kim, and D. N. Basov. Mott transition in vo2 revealed by infrared spectroscopy and nano-imaging. *Science*, 318(5857):1750–1753, 2007.

19. Andrew C. Jones, Samuel Berweger, Jiang Wei, David Cobden, and Markus B. Raschke. Nano-optical investigations of the metal-insulator phase behavior of individual vo2 microcrystals. *Nano Letters*, 10(5):1574–1581, 2010.

20. Zhe Fei, Gregory O. Andreev, Wenzhong Bao, Lingfeng M. Zhang, Alexander S. McLeod, Chen Wang, Margaret K. Stewart, Zeng Zhao, Gerardo Dominguez, Mark Thiemens, Michael M. Fogler, Michael J. Tauber, Antonio H. Castro-Neto, Chun Ning Lau, Fritz Keilmann, and Dimitri N. Basov. Infrared nanoscopy of dirac plasmons at the graphene–SiO_2 interface. *Nano Letters*, 11(11):4701–4705, 2011.

21. Z. Fei, A. S. Rodin, G. O. Andreev, W. Bao, A. S. McLeod, M. Wagner, L. M. Zhang, Z. Zhao, M. Thiemens, G. Dominguez, M. M. Fogler, A. H. Castro Neto, C. N. Lau, F. Keilmann, and D. N. Basov. Gate-tuning of graphene plasmons revealed by infrared nano-imaging. *Nature*, 487:82–85, 2012.

22. J. Chen, M. Badioli, P. Alonso-Gonzalez, S. Thongrattanasiri, F. Huth, J. Osmond, M. Spasenovic, A. Centeno, A. Pesquera, P. Godignon, A. Zurutuza Elorza, N. Camara, F. J. Garcia de Abajo, R. Hillenbrand, and F. H. L. Koppens. Optical nano-imaging of gate-tunable graphene plasmons. *Nature*, 487:77–81, 2012.

23. A. Charnukha, A. Cvitkovic, T. Prokscha, D. Pröpper, N. Ocelic, A. Suter, Z. Salman, E. Morenzoni, J. Deisenhofer, V. Tsurkan, A. Loidl, B. Keimer, and A. V. Boris. Nanoscale layering of antiferromagnetic and superconducting phases in $\mathrm{rb_2fe_4se_5}$ single crystals. *Phys. Rev. Lett.*, 109:017003, Jul 2012.

24. Martin Wagner, Zhe Fei, Alexander S. McLeod, Aleksandr S. Rodin, Wenzhong Bao, Eric G. Iwinski, Zeng Zhao, Michael Goldflam, Mengkun Liu, Gerardo Dominguez, Mark Thiemens, Michael M. Fogler, Antonio H. Castro-Neto, Chun Ning Lau, Sergiu Amarie, Fritz Keilmann, and Dimitri N. Basov. Ultrafast and nanoscale plasmonic phenomena in graphene revealed by near-field infrared imaging and spectroscopy. *In submission*, 2013.

25. G. W. Ford and W. H. Weber. Electromagnetic interactions of molecules with metal surfaces. *Physics Reports*, 113(4):195–287, November 1984.

26. R. Hillenbrand, B. Knoll, and F. Keilmann. Pure optical contrast in scattering-type scanning near-field microscopy. *Journal of Microscopy*, 202(1):77–83, 2001.

27. Javier Aizpurua, Thomas Taubner, F. Javier García de Abajo, Markus Brehm, and Rainer Hillenbrand. Substrate-enhanced infrared near-field spectroscopy. *Opt. Express*, 16(3):1529–1545, Feb 2008.

28. J. A. Porto, P. Johansson, S. P. Apell, and T. López-Ríos. Resonance shift effects in apertureless scanning near-field optical microscopy. *Phys. Rev. B*, 67:085409, Feb 2003.

29. Kiwon Moon, Euna Jung, Meehyun Lim, Youngwoong Do, and Haewook Han. Quantitative analysis and measurements of near-field interactions in terahertz microscopes. *Opt. Express*, 19(12):11539–11544, Jun 2011.

30. A. Cvitkovic, N. Ocelic, and R. Hillenbrand. Analytical model for quantitative prediction of material contrasts in scattering-type near-field optical microscopy. *Opt. Express*, 15(14):8550–8565, Jul 2007.

31. Benedikt Hauer, Andreas P. Engelhardt, and Thomas Taubner. Quasi-analytical model for scattering infrared near-field microscopy on layered systems. *Opt. Express*, 20(12):13173–13188, Jun 2012.

32. Alexander A Govyadinov, Iban Amenabar, Florian Huth, P. Scott Carney, and Rainer Hillenbrand. Quantitative measurement of local infrared absorption and dielectric function with tip-enhanced near-field microscopy. *The Journal of Physical Chemistry Letters*, 4(9):1526–1531, 2013.

33. R. Carminati and J. J. Sáenz. Scattering theory of bardeen's formalism for tunneling: New approach to near-field microscopy. *Phys. Rev. Lett.*, 84:5156–5159, May 2000.

34. Moritz Esslinger and Ralf Vogelgesang. Reciprocity theory of apertureless scanning near-field optical microscopy with point-dipole probes. *ACS Nano*, 6(9):8173–8182, 2012.

35. Pedro J. Valle, Rémi Carminati, and Jean-Jacques Greffet. Contrast mechanisms in illumination-mode snom. *Ultramicroscopy*, 71(1–4):39 – 48, 1998.

36. Roy Pike and Pierre Sabatier, editors. *Scattering and Inverse Scattering in Pure and Applied Science*, volume 1. Academic Press, 525 B Street, Suite 1900, San Diego, California 92101-4495, 1 edition, 2002.

37. E. Nyström. Über die praktische auflösung von integralgleichungen mit anwendungen auf randwertaufgaben. *Acta Mathematica*, 54:185–204, 1930. 10.1007/BF02547521.

38. L. M. Zhang, G. O. Andreev, Z. Fei, A. S. McLeod, G. Dominguez, M. Thiemens, A. H. Castro-Neto, D. N. Basov, and M. M. Fogler. Near-field spectroscopy of silicon dioxide thin films. *Phys. Rev. B*, 85:075419, Feb 2012.

39. Nicolas Behr and Markus B. Raschke. optical antenna properties of scanning probe tips: Plasmonic light scattering, tip-sample coupling, and near-field enhancement. *J. Phys. Chem. C*, 112:3766–3773, 2008.

40. Achim Hartschuh. Tip-enhanced near-field optical microscopy. *Angewandte Chemie International Edition*, 47(43):8178–8191, 2008.

41. M. Kildemo. Real-time monitoring and growth control of si-gradient-index structures by multiwavelength ellipsometry. *Appl. Opt.*, 37(1):113–124, Jan 1998.

42. A. Kučírková and K. Navrátil. Interpretation of infrared transmittance spectra of SiO_2 thin films. *Appl. Spectrosc.*, 48(1):113–120, Jan 1994.

43. Aitzol García-Etxarri, Isabel Romero, F. Javier García de Abajo, Rainer Hillenbrand, and Javier Aizpurua. Influence of the tip in near-field imaging of nanoparticle plasmonic modes: Weak and strong coupling regimes. *Phys. Rev. B*, 79(125439), 2009.

44. M. Schell, A. García-Etxarri, A. J. Huber, K. Crozier, J. Aizpurua, and R. Hillenbrand. Controlling the near-field oscillations of loaded plasmonic nanoantennas. *Nat. Photonics*, 3:287–291, 2009.

45. Lukas Novotny and Stephan J. Stranick. Near-field optical microscopy and spectroscopy with pointed probes. *Annual Review of Physical Chemistry*, 57(1):303–331, 2006. PMID: 16599813.

46. M. Brehm, A. Schliesser, F. Cajko, I. Tsukerman, and F. Keilmann. Antenna-mediated back-scattering efficiency in infrared near-field microscopy. *Opt. Express*, 16(15):11203–11215, Jul 2008.

47. Florian Huth, Andrey Chuvilin, Martin Schnell, Iban Amenabar, Roman Krutokhvostov, Sergei Lopatin, and Rainer Hillenbrand. Resonant antenna probes for tip-enhanced infrared near-field microscopy. *Nano Letters*, 13(3):1065–1072, 2013.

48. Markus B. Raschke and Christoph Lienau. Apertureless near-field optical microscopy: Tip–sample coupling in elastic light scattering. *Applied Physics Letters*, 83(24):5089–5091, 2003.

49. L. Aigouy, A. Lahrech, S. Gr Asillon, H. Cory, A. C. Boccara, and J. C. Rivoal. Polarization effects in apertureless scanning near-field optical microscopy: an experimental study. *Opt. Lett.*, 24(4):187–189, Feb 1999.

50. Paolo Biagioni, Jer-Shing Huang, and Bert Hecht. Nanoantennas for visible and infrared radiation. *Reports on Progress in Physics*, 75(2):024402, 2012.

51. Wei Bao, Matteo Staffaroni, Jeffrey Bokor, Miquel B. Salmeron, Eli Yablonovitch, Stefano Cabrini, Alexander Weber-Bargioni, and P. James Schuck. Plasmonic near-field probes: a comparison of the campanile geometry with other sharp tips. *Opt. Express*, 21(7):8166–8176, Apr 2013.

52. Yury Alaverdyan, Nick Vamivakas, Joshua Barnes, Claire Lebouteiller, Jack Hare, and Mete Atatüre. Spectral tunability of a plasmonic antenna with a dielectric nanocrystal. *Opt. Express*, 19(19):18175–18181, Sep 2011.

53. Nicolas Large, Martina Abb, Javier Aizpurua, and Otto L. Muskens. Photoconductively loaded plasmonic nanoantenna as building block for ultracompact optical switches. *Nano Letters*, 10(5):1741–1746, 2010.

54. David P. Fromm, Arvind Sundaramurthy, P. James Schuck, Gordon Kino, and W. E. Moerner. Gap-dependent optical coupling of single "bowtie" nanoantennas resonant in the visible. *Nano Letters*, 4(5):957–961, 2004.

55. Pablo Alonso-González, Pablo Albella, Federico Golmar, Libe Arzubiaga, Félix Casanova, Luis E. Hueso, Javier Aizpurua, and Rainer Hillenbrand. Visualizing the near-

field coupling and interference of bonding and anti-bonding modes in infrared dimer nanoantennas. *Opt. Express*, 21(1):1270–1280, Jan 2013.

56. Feliciano Giustino and Alfredo Pasquarello. Infrared spectra at surfaces and interfaces from first principles: Evolution of the spectra across the $\mathrm{Si}(100)$-sio_2 interface. *Phys. Rev. Lett.*, 95:187402, Oct 2005.

57. Alexander A. Balandin, Evghenii P. Pokatilov, and D.L. Nika. Phonon engineering in hetero- and nanostructures. *Journal of Nanoelectronics and Optoelectronics*, 2(2):140–170, 2007.

58. A. Huber, N. Ocelic, T. Taubner, and R. Hillenbrand. Nanoscale resolved infrared probing of crystal structure and of plasmon–phonon coupling. *Nano Letters*, 6(4):774–778, 2006. PMID: 16608282.

59. H. Mutschke, A.C. Andersen, D. Clement, Th. Henning, and G. Peiter. Infrared properties of sic particles. *arXiv:astro-ph/9903031*, 1999.

60. Rainer Hillenbrand. Towards phonon photonics: scattering-type near-field optical microscopy reveals phonon-enhanced near-field interaction. *Ultramicroscopy*, 100(3–4):421 – 427, 2004.

61. S.W. Schmucker, N. Kumar, J.R. Abelson, S.R. Daly, G.S. Girolami, M.R. Bischof, D.L. Jaeger, R.F. Reidy, B.P. Gorman, J.B. Ballard J. Alexander, J.N. Randall, and J.W. Lyding. Field-directed sputter sharpening for tailored probe materials and atomic-scale lithography. *Nature Communications*, 3(935), 2012.

62. Jaan Kiusalaas. *Numerical Methods in Engineering with Python*. Cambridge University Press, New York, NY, USA, 2nd edition, 2010.

63. Donald W. Marquardt. An algorithm for least-squares estimation of nonlinear parameters. *Journal of the Society for Industrial and Applied Mathematics*, 11(2):pp. 431–441, 1963.

64. A. B. Kuzmenko. Kramers–kronig constrained variational analysis of optical spectra. *Review of Scientific Instruments*, 76(8):083108, 2005.

65. Antonino Salvatore Arico, Peter Bruce, Bruno Scrosati, Jean-Marie Tarascon, and Walter van Schalkwijk. Nanostructured materials for advanced energy conversion and storage devices. *Nat. Mater.*, (4):366–377, 2005.

66. H. Y. Hwang, Y. Iwasa, M. Kawasaki, B. Keimer, N. Nagaosa, and Y. Tokura. Emergent phenomena at oxide interfaces. *Nat. Mater.*, (11):103–113, 2012.

67. F. J. García de Abajo and J. Aizpurua. Numerical simulation of electron energy loss near inhomogeneous dielectrics. *Phys. Rev. B*, 56:15873–15884, Dec 1997.

68. R. Zhang, Y. Zhang, Z. C. Dong, S. Jian, C. Zhang, L. G. Chen, L. Zhang, Y. Liao, J. Aizpurua, Y. Luo, J. L. Yang, and J. G. Hou. Chemical mapping of a single molecule by plasmon-enhanced raman scattering. *Nature*, (498):82–86, 2013.

69. X. H. Qiu, G. V. Nazin, and W. Ho. Vibrationally resolved fluorescence excited with submolecular precision. *Science*, 299(5606):542–546, 2003.

70. Ivan V. Pechenezhskiy, Xiaoping Hong, Giang D. Nguyen, Jeremy E. P. Dahl, Robert M. K. Carlson, Feng Wang, and Michael F. Crommie. Infrared spectroscopy of molecular submonolayers on surfaces by infrared scanning tunneling microscopy: Tetramantane on au(111). *Phys. Rev. Lett.*, 111:126101, Sep 2013.

71. J. L. Agudin and A. M. Platzeck. Resolution of the coulomb field into evanescent modes. *J. Opt. Soc. Am.*, 70(11):1329–1337, Nov 1980.

72. S. Twomey. On the numerical solution of fredholm integral equations of the first kind by the inversion of the linear system produced by quadrature. *J. ACM*, 10:97–101, January 1963.

73. David L. Phillips. A technique for the numerical solution of certain integral equations of the first kind. *J. ACM*, 9:84–97, January 1962.

74. L. Novotny and B. Hecht. *Principles of Nano-Optics*. Cambridge University Press, 2006.

75. Lukas Novotny, Erik J. Sanchez, and X. Sunney Xie. Near-field optical imaging using metal tips illuminated by higher-order hermite-gaussian beams. *Ultramicroscopy*, 71(1-4):21 – 29, 1998.

76. Thomas Taubner, F. Keilmann, and R. Hillenbrand. Nanoscale-resolved subsurface imaging by scattering-type near-field optical microscopy. *Opt. Express*, 13(22):8893–8899, Oct 2005.

77. L. M. Zhang, B. Y. Jiang, and M. M. Fogler. *in preparation*, 2013.

78. John D. Jackson. *Classical Electrodynamics Third Edition*. Wiley, third edition, August 1998.

79. H. W. Wyld. *Mathematical Methods for Physics*. Perseus Books Publishing, Reading, Massachussetts, 1999.

CHAPTER 3: Infrared Near-field Spectroscopy and Imaging of Single Li_xFePO_4 Microcrystals

3.1 Abstract

This study demonstrates the unique capability of infrared near-field nanoscopy combined with Fourier transform infrared (FTIR) spectroscopy to map phases distributions in microcrystals of Li_xFePO_4, a positive electrode material for Li-ion batteries. *Ex situ* nano-scale IR imaging provides direct evidence for the coexistence of $LiFePO_4$ and $FePO_4$ phases in partially delithiated single-crystal microparticles. A quantitative 3-dimensional tomographic reconstruction of the phase distribution within a single microcrystal provides new insights into the phase transformation and/or relaxation mechanism, revealing a $FePO_4$ shell surrounding a diamond-shaped $LiFePO_4$ inner core, gradually shrinking in size and vanishing upon delithiation of the crystal. The observed phase propagation pattern supports recent functional models of $LiFePO_4$ operation relating electrochemical performance to material design. This work demonstrates the remarkable potential of near-field optical techniques for the characterization of electrochemical materials and interfaces.

Infrared apertureless near-field scanning optical microscopy (IR ANSOM) was applied to resolve the operational mechanism of $LiFePO_4$ (LFP), a positive electrode material used in commercially viable Li-ion batteries. Although LFP is known to convert to $FePO_4$ (FP) at 3.4 V versus Li^+/Li^0 via a first-order phase transition at least in micron sized particles[1], the specific functional mechanism of $LiFePO_4$ (de)lithiation during battery charge/discharge is still under debate. To enhance extensive studies conducted on composite electrodes, control experiments on model samples must be carefully designed and carried out to reliably probe chemical composition variations within single Li_xFePO_4 particles with different lithium contents at high spatial (nanometer) resolution and with adequate chemical specificity[2]. The present study demonstrates the potential of IR ANSOM[3] imaging and broadband nano-spectroscopy (nano-FTIR) for chemical and structural characterization of Li_xFePO_4 single particles.

Most conventional analytical techniques employed to study fine changes in the local composition of Li_xFePO_4 single particles offer limited descriptions of the reaction mechanism, providing sensitivity only to long-range order (X-ray and electron diffraction, Transmission Electron Microscopy TEM)[4-9], suffering from spectral overlap among elements (Electron Energy Loss Spectroscopy: EELS)[10, 11] or poor contrast in very thin samples (Transmission X-ray Microscopy: TXM)[12, 13], with the concurrent possibility of beam damage from highly energetic particles or photons. Vibrational spectroscopies sensitive to lattice vibrations are of particular interest since the IR/Raman spectral signatures of $LiFePO_4$, $FePO_4$ and their meta-stable intermediates $Li_{0.34}FePO_4$ and $Li_{0.66}FePO_4$ provide excellent chemical contrast[14, 15]. However, the diffraction-limited spatial resolution of conventional far-field optical techniques presents a serious barrier to studying the structure and chemical composition of sub-micrometer specimens, used in commercial batteries.

IR ANSOM is still an emerging near-field imaging and spectroscopic technique, both theory and practice undergoing rapid and promising development[16]. Recent technical improvements including lock-in detection of the optical signal, effective far-field background

suppression schemes[17, 18], and powerful quantum cascade or pulsed broadband IR laser light sources[19-21] have enabled local characterization of well-defined organic and inorganic nano-materials with high sensitivity, specificity[22] and at comparable temporal resolutions[23].

The high spatial resolution afforded by IR ANSOM is determined by the radius of curvature at the AFM tip apex (<30 nm), independent of the free-space wavelength of the illuminating light. The technique operates through extreme polarization sensitivity of a sharp conductive probe to the optical properties of a sampling volume near the probe apex. Upon illumination, the electrically polarized probe tip generates a spatially extended evanescent near-field, which can penetrate a few hundreds of nanometers deep into the IR-transparent samples[24, 25]. The tip-enhanced near-field couples locally to resonant phonon modes of the sample and allows detection of sub-surface objects, provided that they are located within the sub-wavelength sampling volume of the near-field probe. The structural and compositional specificity of IR near-field spectroscopy is analogous to far-field vibrational spectroscopies[22].

$LiFePO_4$ single microcrystals (4×2×0.4 μm along the *c*, *a* and *b* directions, respectively), which exhibit hexagonal platelet shapes were selected for *ex situ* IR ANSOM studies[7]. Figure 3.1 shows SEM micrographs of representative $LiFePO_4$ and chemically delithiated single crystals with average compositions, $Li_{0.5}FePO_4$ and $FePO_4$ single crystals. Near-field nano-FTIR spectra were acquired from single FP and LFP particles and compared with conventional far-field FTIR transmission spectra of the same batch of crystals (see Appendices)[15, 26, 27]

The 2nd harmonic amplitude S_2 (see Methods) nano-FTIR spectra (Figure 3.2a) reveal strong surface phonon modes at 950-1150 cm^{-1} attributable to intramolecular symmetric (n_1) and asymmetric (n_3) stretching vibrations of the PO_4^{3-} anions, which are also clearly resolved in far-field FTIR spectra[15]. However, the signature peaks of these phonon modes appear sharpened and red-shifted in the near-field spectra as compared with their far-field counterparts[28-31]. The observed near-field resonance effect results in a back-scattering response that is highly sensitive to phonon oscillator strengths, inducing strong contrasts in spectral intensity between adjacent

modes. LFP and FP share several surface phonon modes in the 950-1150 cm^{-1} spectral range. However, the nano-FTIR spectrum of LFP exclusively exhibits a strong phonon mode near 1042 cm^{-1} that corresponds to the asymmetric (n_3) stretch of the PO_4^{3-} anion. DFT calculations attribute the increased oscillator strength and frequency red-shift of the n_3 mode in LFP as compared with FP to a redistribution of electron density between the P-O_1 and P-O_2 bonds within the symmetry-distinct oxygen sublattices of the PO_4^{3-} anions (see Appendices)[32, 33].

The IR ANSOM imaging of $LiFePO_4$ and partially and fully delithiated Li_xFePO_4 (x=1, 0.5 and 0.0) microcrystals was realized with the 4th harmonic amplitude S_4 signal at three distinct IR excitation frequencies, 962, 1042 and 1087 cm^{-1} (Figure 3.2b). The observed S_4 image contrasts are associated with different phonon coupling efficiencies in LFP and FP at the given excitation frequencies, and correspond to variations of local crystal structure and/or composition. The sudden drop of signal at the particle boundary originates from the shadowing effect and loss of tip-sample coupling at the steep crystal edges.

The IR ANSOM images collected at 962 cm^{-1} display poor LFP/FP/silicon substrate contrast due to their comparable S_4 signal intensity at this frequency. On the other hand, the images of partially delithiated $Li_{0.5}FePO_4$ crystal at 1042 and 1087 cm^{-1} reveal a diamond-shaped region in the middle of the crystal, which was also observed in the corresponding phase image (see Appendices, Figure 3.8). AFM topography images show no indication that the observed chemical contrast could originate from variations in surface morphology. Interestingly, reverse optical contrast observed in the images of $Li_{0.5}FePO_4$ crystal at 1042 cm^{-1} and 1087 cm^{-1} suggests strong coupling to the n_3 phonon mode in LFP and FP, respectively (Figure 3.2a).

The observed shrinking of the central diamond-shaped region in another delithiated crystal with higher lithium content, $Li_{0.74}FePO_4$ vs. $Li_{0.5}FePO_4$ (Figure 3.2c) indicates a progressive evolution of outer FP-rich region at the expense of the inner LFP-core upon delithiation. The continuous and monotonic variation in observable fill fractions of putative LFP and FP phases as a function of Li content further supports the respective identification of inner

and outer regions in Li_xFePO_4 particles with Li-rich and Li-poor regions. These observations provide direct evidence for the coexistence of LFP and FP phases within individual Li_xFePO_4 microcrystals, as previously inferred from 2-D chemical mapping of thin single crystal particles[13] using Scanning and Full Field Transmission X-Ray Microscopy coupled to Absorption Near Edge Spectroscopy (STXM- and FF TXM-XANES).

A series of nano-FTIR spectra acquired across the a-c surface of pure-phase LFP and FP crystals (Figure 3.3a) appear consistent with the reference spectra displayed in Figure 3.2a. Remarkably, the scan across the partially delithiated $Li_{0.74}FePO_4$ crystal (Figure 3.3b) displays spectral patterns characteristic of an outer Li-depleted zone and a Li-rich region near the crystal center. However, the $Li_{0.74}FePO_4$ spectra do not replicate exactly the reference nano-FTIR spectra for pure-phase LFP or FP (Figure 3.2a) except for the locations close to the edges of the crystal, which exhibit characteristics of pure FP.

The relative IR near-field intensity of the n_3 mode is noticeably smaller throughout $Li_{0.74}FePO_4$ as compared with pure LFP, yet its frequency remains fairly constant at 1042 ± 5 cm^{-1}. This observation appears inconsistent with the presence of a stable homogeneous solid solution[1, 4, 8, 34, 35] at an intermediate state of delithiation. To test this hypothesis, a member of the solid solution Li_xFePO_4 with composition $Li_{0.6}FePO_4$ was investigated (see Appendices, Figure 3.7). A continuous shift of the n_3 mode in the far-field FTIR spectrum of Li_xFePO_4 would be expected for such a solid solution, varying with the mean Fe oxidation state, rather than a superposition of the LFP and FP n_3 modes. Therefore solid solution phases are either completely absent in the Li_xFePO_4 microcrystals or their local concentration is below the detection limit of the IR near-field probe.

On the other hand, the decrease in near-field signal intensity of the n_3 mode at 1042 cm^{-1} in the $Li_{0.74}FePO_4$ crystal center is ascribed to the presence of the $LiFePO_4$ inner core buried under a $FePO_4$ outer layer. Thus the observed n_3 mode intensity variations can be used to determine the local volume ratio and geometric configuration of LFP and FP phases.

The tomographic capabilities of IR ANSOM to image structures buried beneath thick (<100 nm) layers of IR transparent material or to characterize phonon-resonant SiO_2 layers have been demonstrated in previous studies[24, 25]. To reveal the 3-D phase distribution in Li_xFePO_4 microcrystals, nano-FTIR spectra were matched with theoretical predictions obtained from the *lightning rod model* of near-field interactions between the probe and sample (see Methods). The *lightning rod model* accounts for the strong dependence of optical reflections from layered structures on the momentum decomposition of incident light[31].

This algorithm was used to extract the surface reflection coefficients $\beta_{LFP}(\omega)$ and $\beta_{FP}(\omega)$ for the LFP and FP and reproduce their reference nano-FTIR spectra (Figure 3.2a). The calculated pure-phase reflection coefficients were then used to approximate the composite optical response of a model three-layer FP/LFP/FP composite structure[36] . The resultant model spectra (Figure 3.4a) were matched with the experimental nano-FTIR spectra of the $Li_{0.74}FePO_4$ microcrystal to determine local thicknesses of the LFP interlayer t_{LFP} (Figure 3.4b). The corresponding values of t_{LFP} were then used to reconstruct an *idealized* tomographic 3-D phase composition image of the crystal as schematically depicted in Figure 3.5. Such an inverse analysis of nano-FTIR spectra constitutes a successful example of near-field tomographic analysis of functional materials.

The depth sensitivity of IR ANSOM is sufficient in this case to probe more than 100 nm deep into the $Li_{0.74}FePO_4$ microcrystal the IR-transparent character of FP and to the long-range nature of near-field interactions with the LFP n_3 phonon near 1040 cm^{-1}. This phenomenon effectively enables *phonon-enhanced* near-field optical tomography (see Appendices). However, sensitivity to variations in the lithiated core's lower portion is virtually nonexistent, and the presented extrapolation of phase distribution in the bottom part of the crystal (lighter green area in Figure 3.4b) is a simple *ansatz* of symmetric delithiation. Since the depth of the tip's probing electric fields scale inversely with their confinement, the uncertainty of the LFP thickness extraction corresponds with that of the tip's radius of curvature which, in this case was assumed

at 25 nm. Further uncertainties in our tomographic reconstruction due to the instrumental noise level of our measurements are presented in the Appendices.

While t_{LFP} is essentially zero (complete delithiation) at the $Li_{0.74}FePO_4$ particle edges, t_{LFP} reaches ~350 nm at the particle center. Interestingly, the observed diamond-shaped LFP core does not replicate the contours of the crystal i.e., the original orientation of the edges and facets. The central approximately diamond-shaped domain of LFP (Figure 3.2c) shrinks as the average stoichiometry proceeds from $Li_{0.74}FePO_4$ to $Li_{0.5}FePO_4$, and disappears completely at the end of the delithiation process. However, the observed phase transformation mechanism does not follow a simple core-shell model, as phase boundaries appear to form at specific orientations. However, considering the limited spatial resolution of the IR ANSOM and inherent experimental error and uncertainty it is impossible to determine their exact crystallographic directions. This may indicate a complex delithiation-relaxation mechanism in $Li_{0.74}FePO_4$, which can affect local Li^+ transport rate and promote LFP/FP phase boundary propagation along specific directions.

Like many binary systems, Li_xFePO_4 is likely to phase segregate into a mixture of two immiscible phases: heterosite $Fe^{III}PO_4$ and triphylite $LiFe^{II}PO_4$ across a large compositional range $(0.05 < x < 0.89)$[1]. Coexistence of pure LFP and FP or $Li_\alpha FePO_4$ and $Li_{1-\beta}FePO_4$, intermediate phases in Li_xFePO_4 composite electrodes have already been reported[6, 7, 10, 11, 13, 35, 37-39]. However, the exact phase distribution within a single Li_xFePO_4 microcrystal as revealed by the IR ANSOM 3-D tomography has been directly resolved in the present study. Viewed in the context of the previously proposed axial[7] or mosaic[37] phase distribution models, a radial distribution (core-shell structure)[10, 35, 39-41] appears to support best our observations.

Ex situ electron energy-loss spectroscopic (EELS) measurements of chemically delithiated Li_xFePO_4 microparticles showed that Li^+ is removed preferentially from surface regions[11]. On the other hand, Li_xFePO_4 nanoparticles can accommodate the lattice mismatch between LFP and FP frameworks and the resulting elastic strain by locating the phase with

smaller unit-cell volume i.e., $FePO_4$ at the particle core[10, 11, 42, 43]. Elastic relaxation near surfaces leads to the formation of the characteristic stripes along the c-axis morphology[7, 44].

In larger microcrystals, the ratio of surface energy to elastic energy is lower, and internal strain may be relieved through the formation of dislocations, cracks and voids, explaining why such a nucleation and phase propagation mechanism may not be universal. In fact, the partially and fully delithiated microcrystals examined in this study exhibited surface cracks along the c-axis (Figure 3.1). Although these surface imperfections appear disconnected from the LFP and FP phase distribution patterns observed in the IR ANSOM images (Figure 3.2b), the rate and direction of the phase boundary movement upon delithiation may be affected by the formation of these structural defects[13].

The large chemical potential gradient of Li^+ together with the stress developed at the interface between incommensurate LFP and FP lattices may provide the driving force for phase boundary propagation[6, 45]. Anisotropic elastic stiffness and misfit strains lead to formation of low-energy phase boundaries along [101] planes, whereas other phase boundary orientations can originate from by a partial loss of coherency in the [100] direction[44]. Ramana et al.[9] observed $LiFePO_4$ regions in the partially delithiated particles include with phase boundary along the [101] direction but also along the c– and a-directions. These additional interfaces are responsible for maintaining the domain's finite cross-sectional size in the ac-plane. However, their study revealed nothing about the size of domains along the b–direction.

Bazant et al., applied a quantitative phase field theory[42, 44, 46, 47] of nucleation taking account of surface energies, electrochemical potential, and elastic energy to model intercalation waves propagating inward from the side facets while bending from coherency strain upon lithiation of single-crystal $FePO_4$ 150 × 76 nm nanoparticles[42]. This approach produced a central diamond-shaped lithium-depleted zone, which comprises a mirror image of the Li_xFePO_4 microcrystal structure observed experimentally in this work. The striking similarity of these

theoretical and experimental results may suggest similar coherency strain-controlled mechanism of phase propagation in Li_xFePO_4 micron sized particles upon lithiation and delithiation processes.

On the other hand, Malik et al. have suggested that classical nucleation and growth theory is an implausible mechanism for lithiation[38]. Instead, they have proposed a single-phase non-equilibrium overpotential-driven mechanism involving the presence of solid solutions. In their proposed framework, a particle transforms from LFP to FP via a solid solution. However, if the transformation is interrupted and the potential is removed, the Li_xFePO_4 particle will, if sufficiently small, react to form either LFP or FP only, taking up, or giving Li^+ to the solution and nearby particles. For larger particles, where LFP/FP phase boundaries can exist within the *same* particle,[7, 8]rapid relaxation will occur to form an energetically favorable distribution of LFP and FP phases (which minimize strain and chemical potential gradients). The resultant phase boundaries need not lie along main crystallographic orientations. Chemical delithiation may trigger the formation of a solid solution at the LFP/FP interphase providing sufficient overpotential to facilitate this theoretically-predicted pathway[38, 46, 48]. The transition between the nanoparticle and micron size regimes is unclear and LFP and FP interfaces have been observed to exist in particles as small as 200 nm.[13] Liu et al. demonstrated the formation of a nonequilibrium solid solution phase, Li_xFePO_4 ($0 < x < 1$) in nanoparticulate composite electrodes, during high-rate cycling, with compositions that span the entire composition between two thermodynamic phases, $LiFePO_4$ and $FePO_4$ via a continuous change in structure rather than a distinct moving phase boundary between $LiFePO_4$ and $FePO_4$.[49] Similar results were observed by Zhang et al.[50] Bai et al. have proposed that formation of a solid solution phase is driven by high rate cycling. [46]

In conclusion, this study provides evidence that the observed diamond-shaped Li-rich region within Li_xFePO_4 microcrystals at varying degrees of lithiation may correspond to the most energetically favorable distribution of phases at equilibrium, once the chemical driving force for the reaction is removed. Future work will focus on the extension of the method to small particles and to particles with different morphologies.

3.2 Methods: Single-frequency IR ANSOM imaging

Infrared imaging was performed with a NeaSNOM scanning near-field optical microscope (Neaspec GmBH). Platinum/iridium-coated AFM probes (NanoAndMore GmbH; cantilever resonance frequency 250 kHz, tip nominal radius of curvature 20 nanometers) were scanned in tapping mode over the sample while illuminated by a focused infrared laser beam. The resulting back-scattered radiation modulated by the tapping frequency (f_{tap}) interferes at a mercury-cadmium-telluride detector (Kolmar Technologies Inc.) with a reference beam whose phase is modulated continuously by reflection from an oscillating mirror (f_M). The pseudo-heterodyne detection setup (utilizes demodulation of the overall IR signal at frequency side-bands $n\, f_{tap} \pm m\, f_M$ (for integral m) to supply the background-free amplitude (S_n) and phase[51] (ϕ_n) of the IR near-field signal at harmonics n of the probe tapping frequency. The near-exponential dependence of the near-field interaction versus the tip-sample separation distance implies that signal harmonics at $n \geq 2$ are directly attributable to near-field polarization of the tip in the case of harmonic tapping motion. Contrasts in intensity and phase at these near-field signal harmonics therefore correspond with variations in the local chemical composition of the sample.[52] An integration time of 6.5 ms per image pixel allowed fast raster-scan imaging of sample surfaces using tunable fixed-frequency CW lasers (Quantum Cascade Lasers by Daylight Solutions Inc.). AFM topography and the mechanical phase of the probe oscillation were recorded simultaneously with all near-field IR images.

3.3 Methods: Nano-FTIR spectroscopy

Single-point and line-scan near-field spectra were acquired using a NeaSNOM scanning near-field optical microscope at 80 nm probe tapping amplitude under illumination from a tunable broadband mid-infrared (700-2400 cm^{-1}) laser. This coherent mid-infrared light is generated through the nonlinear difference-frequency combination of beams from two near-infrared fiber lasers (TOPTICA Photonics Inc.): a high power 5400 cm^{-1} oscillator and a tunable

supercontinuum near-infrared amplifier, resulting in ~100 fs pulses at a repetition rate of 40 MHz. An asymmetric Michelson interferometer with 1.5 millimeter range translating mirror enables the collection of demodulated near-field amplitude S_n and phase y_n spectra with 3 cm^{-1} resolution.[19,20] All nano-FTIR spectra are normalized to the nominally flat spectrum of the silicon substrate to remove the effect of frequency-dependent instrumental sensitivities and the incident illumination spectrum.

3.4 Methods: Modeling of near-field spectra

Near-field spectra were interpreted through comparison with solutions to the scattering equation describing the optical interaction between an ideally conical conductive probe tip and a planar sample characterized by complex frequency-dependent dielectric function $\varepsilon = \varepsilon_1 + i\,\varepsilon_2$. This so-called *lightning rod model*[31] of probe-sample near-field interaction computes the charge density per unit length $\lambda(z)$ induced along the vertical shaft of the tip, from which both the magnitude and phase of the probe's back-scattered field are computed semi-analytically. This model differs from earlier qualitative models primarily through the absence of *ad hoc* free parameters, explicit consideration of realistic probe tip geometries, and straightforward application to interactions with layered structures. Of key importance in determining the magnitude and phase of the induced charge $\lambda(z)$ and the associated back-scattered radiation is the surface response function of the sample $\beta(\omega)$, equal to the quasi-electrostatic limit of the Fresnel reflection coefficient for *p*-polarized light illuminating a bulk material with frequency-dependent dielectric constant $\varepsilon(\omega)$[3,53]:

$$\beta(\omega) = \frac{\varepsilon - 1}{\varepsilon + 1}$$

Intense back-scattered radiation can result for large values of β near frequencies for which $Re\ \varepsilon(\omega) \approx -1$. For materials whose dielectric behavior is well described by a sum of vibrational oscillators, these frequencies (ω_{SO}) denote *surface optical phonon modes* of the

lattice. The near-field resonance condition is satisfied at frequencies slightly red-shifted from ω_{SO}, providing spectral peaks in the back-scattered ANSOM signal which are the hallmark of these phonons. This forms the basis for an optical spectroscopy sensitive to changes in chemical composition at the nano-scale and well suited to the study of vibrational materials.

3.5 Acknowledgements

This work (LBNL, Stony Brook, University of Cambridge) was supported as part of the Northeastern Center for Chemical Energy Storage, an Energy Frontier Research Center funded by the U.S. Department of Energy, Office of Science, Office of Basic Energy Sciences under Award Number DE-SC0001294. Work at UCSD was supported by U.S. Department of Energy, Office of Science, Office of Basic Energy Sciences. A. S. McLeod acknowledges support from a U.S. Department of Energy Office of Science Graduate Fellowship. We would like to acknowledge the helpful contribution of Simon F. Lux with the near-field IR imaging measurements. We thank the Center for Functional Nanomaterials, Brookhaven National Laboratory, NY, USA, which is supported by the U.S. Department of Energy, Office of Basic Energy Sciences, under contract number DE-AC02-98CH10886 for access to their computer cluster.

This chapter, in full, is a reprint of the material as it appears in the following published article: A. S. McLeod, I. T. Lucas, J. S. Syzdek, D. S. Middlemiss, C. P. Grey, D. N. Basov, R. Kostecki. IR Near-Field Spectroscopy and Imaging of Single Li_xFePO_4 Microcrystals. *Nano Lett.* 15, 1 (2015). The dissertation/thesis author was the co-primary investigator and author of this material.

3.6 Figures

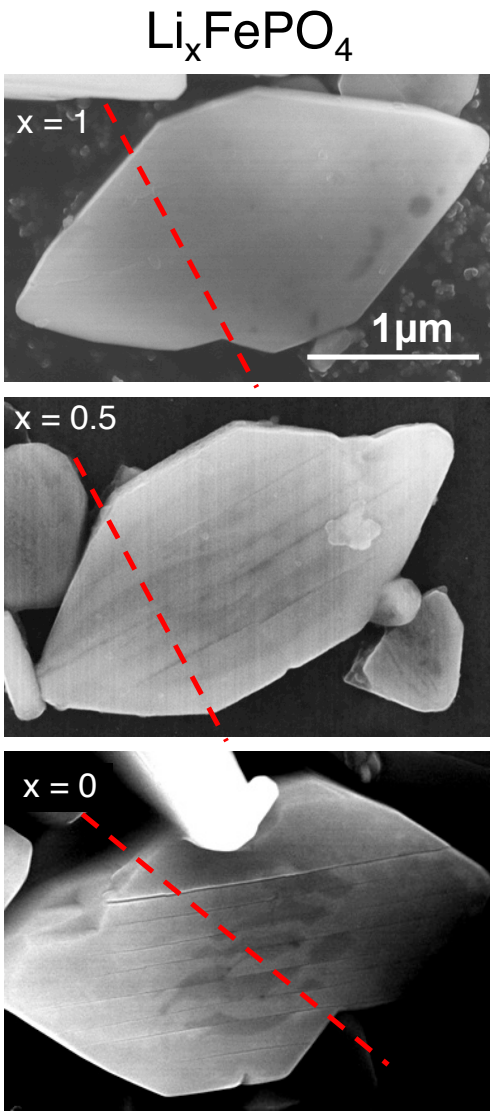

Figure 3.1: Scanning electron micrographs of single $LiFePO_4$, $Li_{0.5}FePO_4$, and $FePO_4$ microcrystals, revealing cracks along the crystal surface after delithiation.

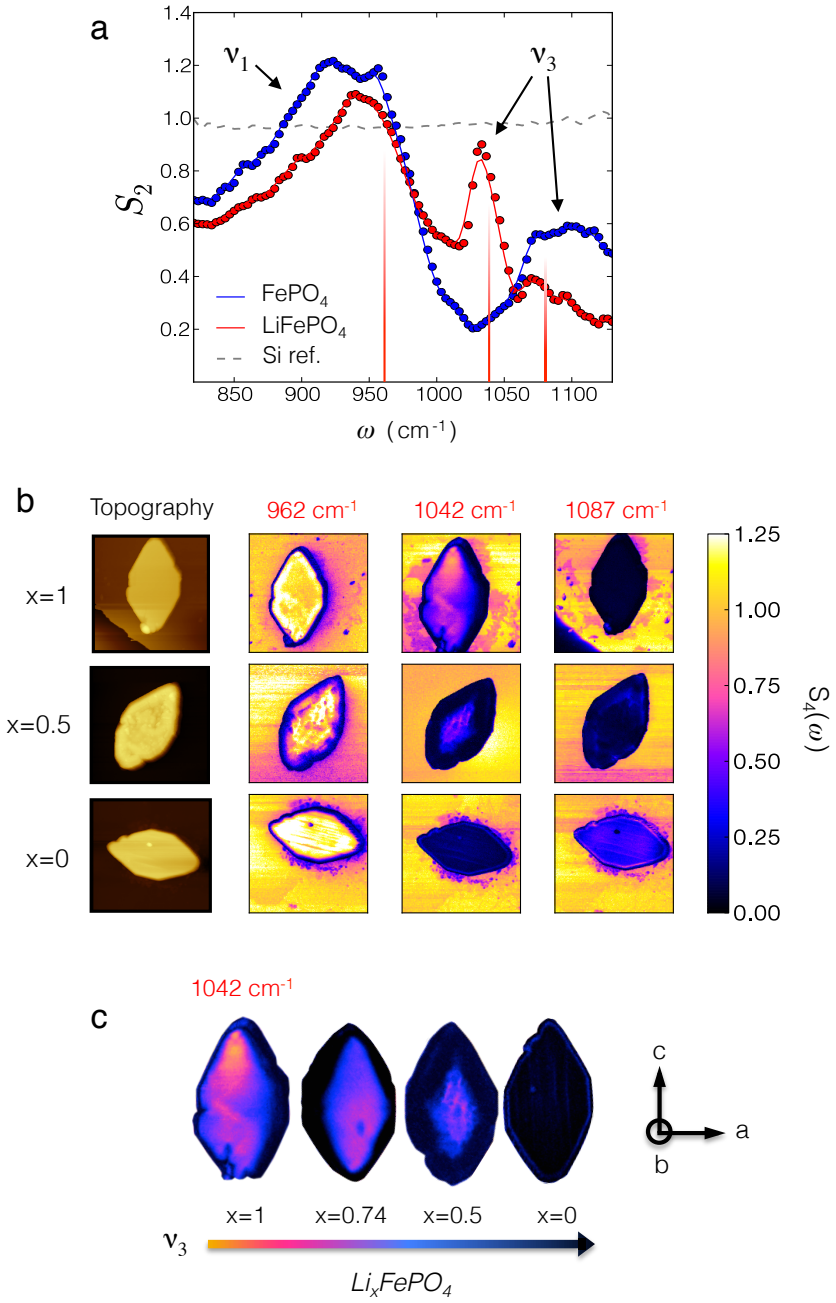

Figure 3.2: Nano-spectroscopy and imaging of LixFePO4 Microcrystals.

a) Nano-FTIR S2 spectra (2nd harmonic amplitude of the back-scattered field) of pure-phase LiFePO4 and FePO4 microcrystals with symmetric (v1) and antisymmetric (v3) vibrational modes indicated (comparison with far-field FTIR transmission spectra is presented in Supplementary Information); b) AFM topography and corresponding infrared near-field amplitude S4 (4th harmonic) images acquired at 1087, 1042 and 962 cm-1 for LiFePO4, Li0.5FePO4 and FePO4 crystals; c) S4 images highlighting the phase distribution and propagation of lithiated/delithiated phases in LiFePO4, Li0.74FePO4 , Li0.5FePO4 and FePO4 crystals.

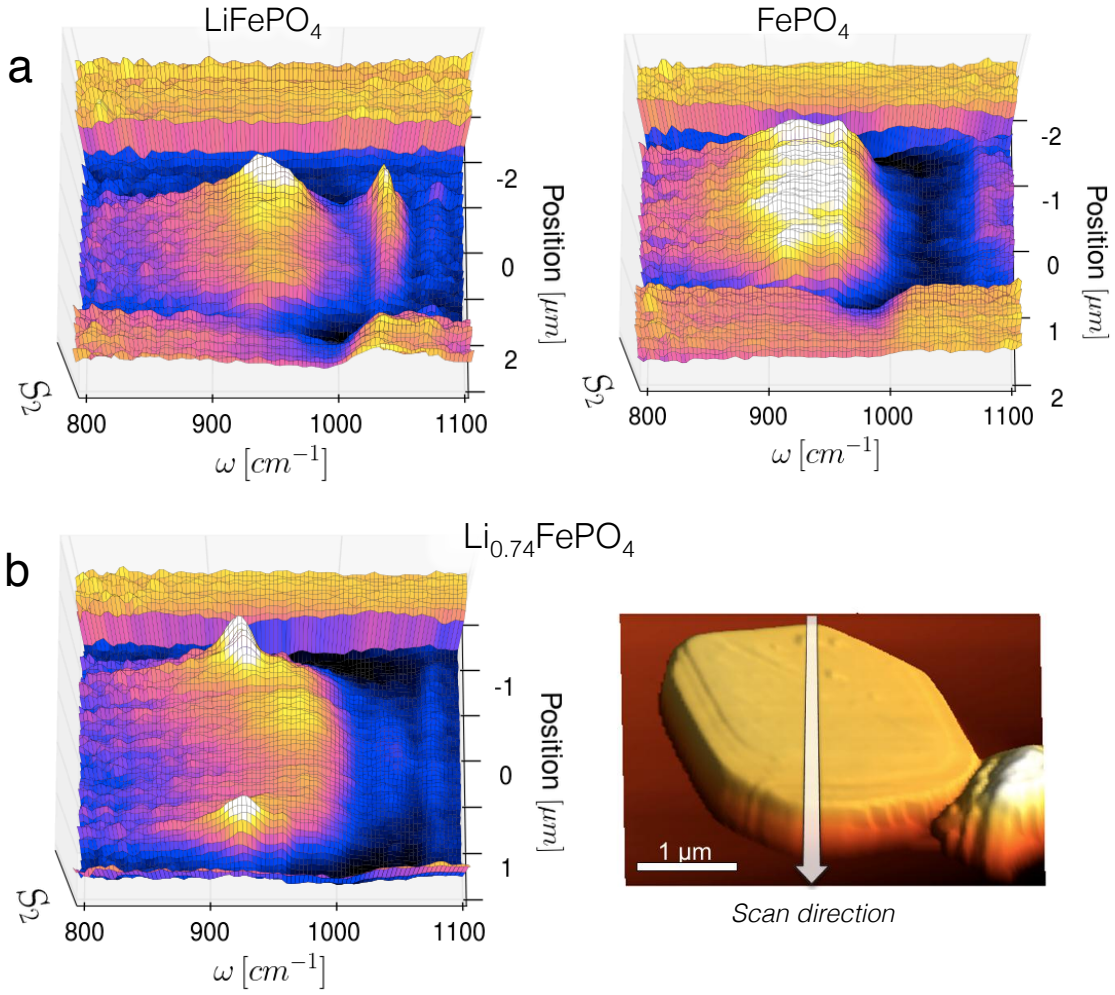

Figure 3.3: Spatially resolved nano-spectroscopy of lithiation in Li_xFePO4 microcrystals.

a) Position-resolved nano-FTIR S_2 spectra acquired along the surface of two pure-phase microcrystals and b) along a partially delithiated $Li_{0.74}FePO_4$ crystal (color scale identical to that in Fig. 3.2b). An AFM topography image (false color height) displays the $Li_{0.74}FePO_4$ crystal and location of the nano-FTIR line-scan.

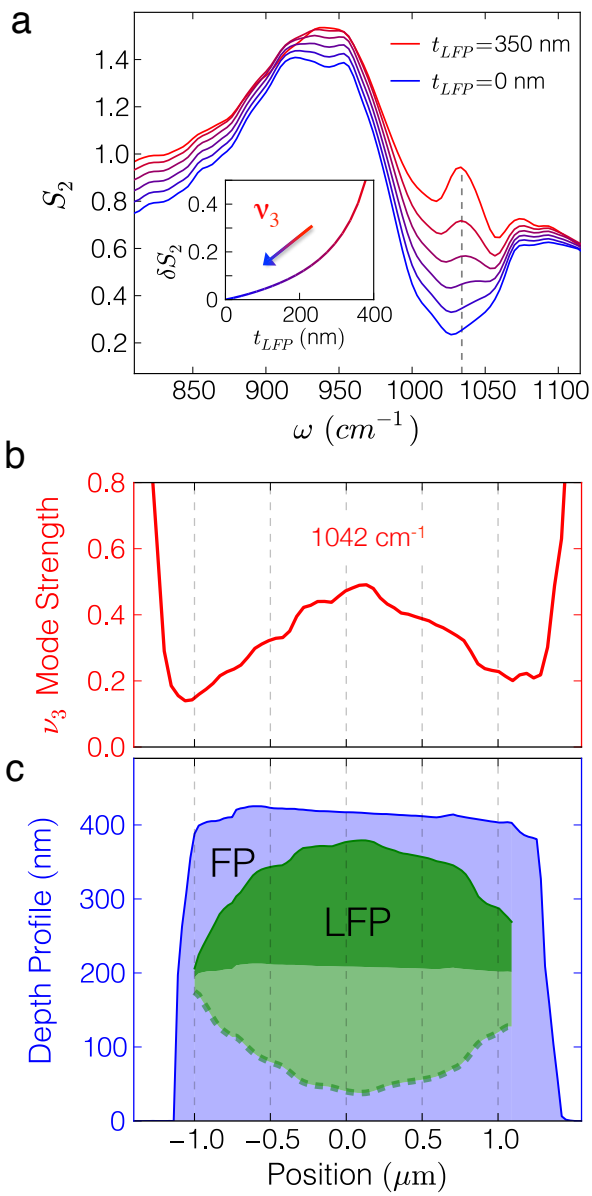

Figure 3.4: Phonon-enhanced near-field tomography of lithiation in a $Li_{0.74}FePO_4$ microcrystal.

a) Theoretical near-field S_2 spectra of a partially delithiated $LiFePO_4$ microcrystal computed using the *lighting rod model* of probe-sample near-field interaction (see text) as a function of the LFP core thickness ranging, from 0 nm (fully FP) to 425 nm (fully LFP); b) the v_3 mode amplitude measured in S_2 at 1040 cm^{-1} across the width of a $Li_{0.74}FePO_4$ crystal, and c) the associated reconstruction of the internal compositional profile (FP in blue, LFP in green).

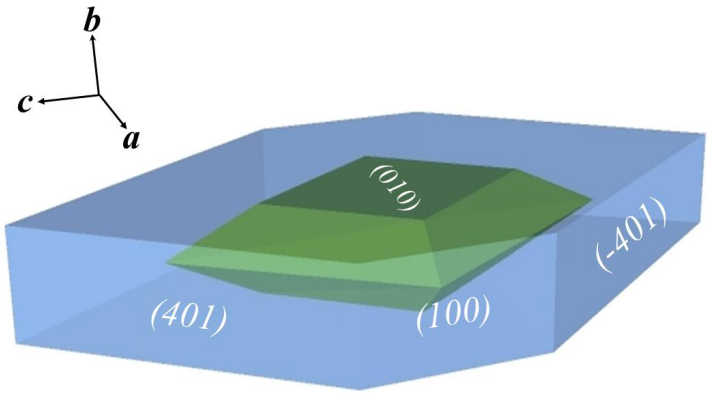

Figure 3.5: Schematic depiction of the FP-LFP-FP core/shell structure inferred from the near-field tomography analysis (see text).

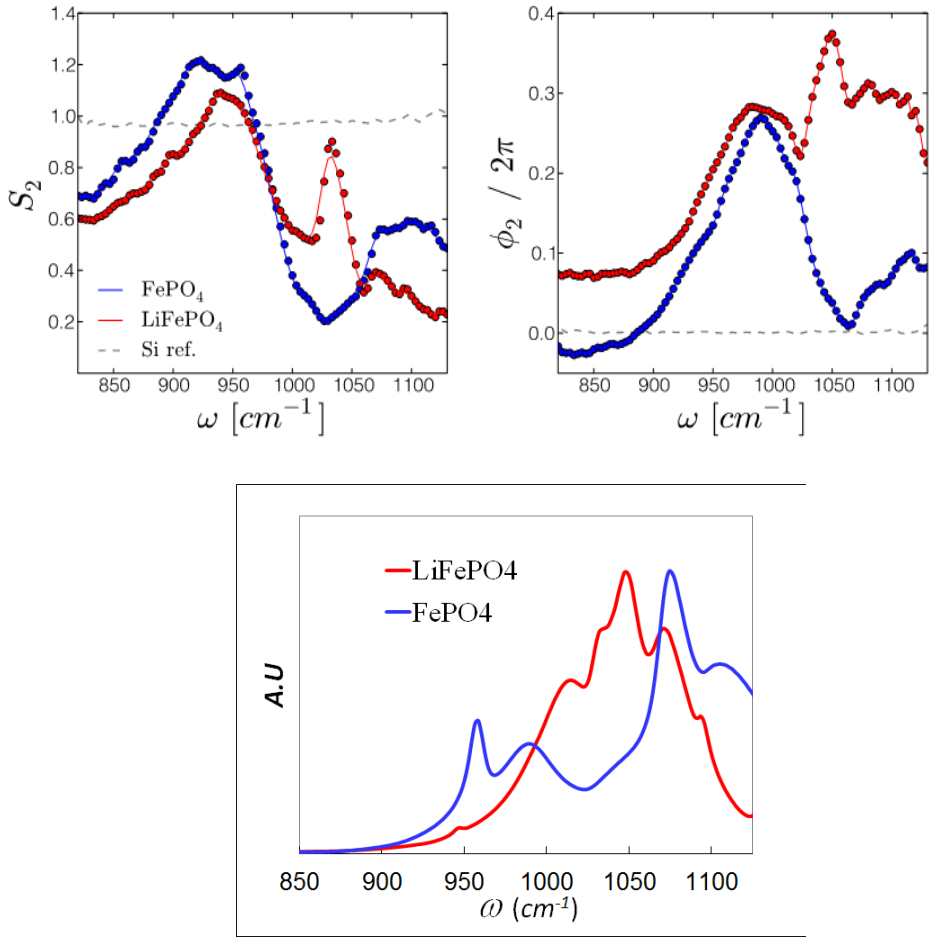

Figure 3.6: Near- and far-field spectroscopies of $LiFePO_4$ and $FePO_4$ end-phases.

Infrared spectra of the end members $LiFePO_4$ (red) and $FePO_4$ (blue) : Near-field spectra amplitude S_2 and phase Φ_2 (top left and right respectively) and their comparison to far-field spectra (absorbance) obtained in the transmission mode (bottom).

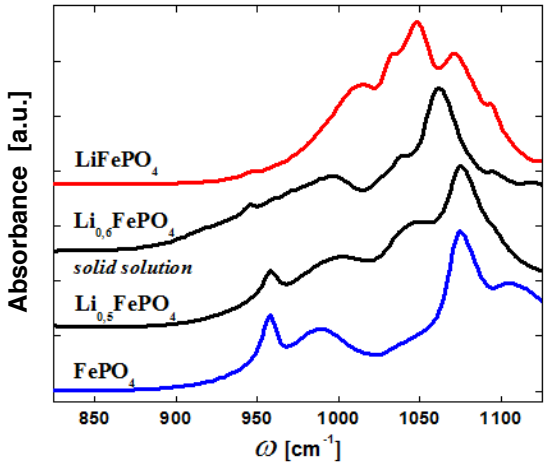

Figure 3.7: Far-field FTIR transmission spectra of crystalline $LiFePO_4$, $FePO_4$, a mixture $Li_{0.5}FePO_4$ thereof, and solid solution $Li_{0.6}FePO_4$.

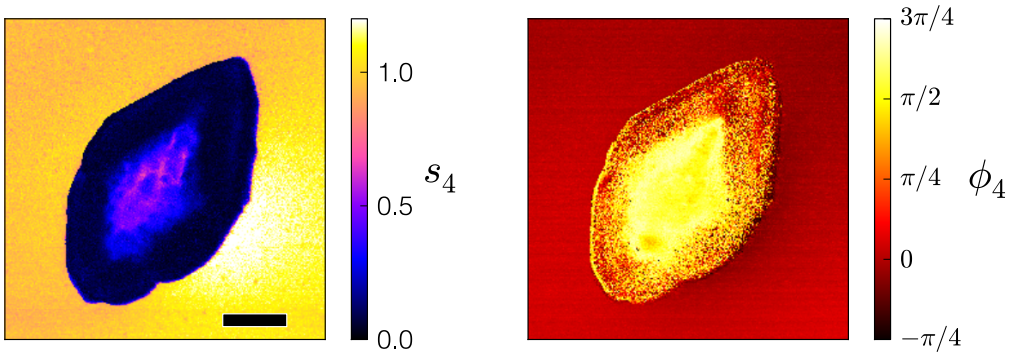

Figure 3.8: Near-field amplitude and phase of a half-lithiated $Li_{0.5}FePO_4$ crystal at 1042 cm^{-1}.

(left) Near-Field amplitude image (4th harmonic) of a half delithiated crystal ($Li_{0.5}FePO_4$) at 1042 cm^{-1} (9.6 μm) and (right) the associated near field phase image indicating a bona-fide contrast in optical absorption present in a diamond-shaped region at the crystal center. Scale bar: 1 micron.

3.7 Appendix A: Li_xFePO_4 samples

Synthesis: Large plate-like $LiFePO_4$ crystals (4 x 2 x 0.2 mm along the a,b, and c-axes) were synthetized by G. Chen (LBNL) using the hydrothermal method. $FeSO_4$ (99%, Aldrich) and H_3PO_4 (85%, J. T. Baker) were mixed in deoxygenated and deionized water, and a LiOH (Spectrum) solution was added slowly to the mixture to give an overall Fe:P:Li ratio of 1:1:3. After stirring under helium gas for about 5 min, the reaction mixture was transferred to a Parr reactor, which was purged with helium and held at 220 °C for 3 h. On cooling to room temperature, the off-white precipitate was filtered, washed with deionized water, and dried at 60 °C under vacuum for 24 h.

Chemical delithiation: Delithiated crystals (Li_xFePO_4) were obtained by stirring in a 0.05 M solution of bromine in acetonitrile (Sigma-Aldrich) for 1 h, by adjusting the molar ratio to achieve the desired stoichiometry. X-ray diffraction (XRD) characterization was implemented in the reflection mode using a Panalytical Xpert pro diffractometer equipped with monochromatized Cu Ka radiation (scan rate was 0.0025°/s from 10 to 70° 2q in 0.01° steps) to determine the final stoichiometry of the chemically delithiated crystals.

Sample preparation for imaging: Li_xFePO_4 crystals were sonicated for 1h in dry hexane. Then ~0.2ml of it was deposited onto a silicon wafer and dried at 70 °C.

3.8 Appendix B: Comparison between Near-field and far-field IR spectra

Fig. 3.6 displays ex situ near-field nano-FTIR spectra (2^{nd} harmonic, amplitude S_2 and phase ϕ_2) obtained from two end-member ($LiFePO_4$ in red and $FePO_4$ in blue) crystals across the frequency range 800-1150 cm^{-1}. Spectra were normalized to the signal from the adjacent silicon substrate, whose spectral response is nominally flat in this frequency range. Fourier Transform Infrared (FTIR) spectra were obtained in the transmission mode on pressed pellets of Li_xFePO_4

crystals (same batch) mixed with KBr powder using a Bomen instrument that covers the range 100 – 6000 cm^{-1} and shown for comparison.

Transmission data reveals strong surface phonon polariton absorption bands at frequencies 950-1150 cm^{-1}. Owing to the near-field resonance condition, the signature peaks of these phonons appear sharpened and red-shifted in the nano-FTIR amplitude spectra. The nature of the near-field interaction also results in a back-scattering response highly nonlinear with phonon oscillator strength, inducing strong contrasts in intensity among adjacent modes. $LiFePO_4$ and $FePO_4$ are observed to share one or more surface phonon modes near $\omega > 950$ cm^{-1}, with regard paid to the anticipated red-shift of peaks measured in near-field, and a weaker surface phonon near 1085 cm^{-1}, whereas $LiFePO_4$ exhibits a uniquely strong surface phonon near 1040 cm^{-1}.

3.9 Appendix C: Observation of a lithiation pattern by near-field phase measurements

In accord with our near-field spectroscopy measurements as presented in Fig. 3.6, a strong optical contrast in the near-field phase is observable within individual crystals of L_xFePO_4 that have been partially delithiated. For example, near-field amplitude and phase images (at the 4th harmonic of the probe tapping frequency) measured at 1042 cm^{-1} for a $Li_{0.5}FePO_4$ crystal are shown in Fig. 3.8. In particular, a strong phase contrast is observed within the same internal region of the crystal in which a positive contrast in near-field amplitude appears. Both observations are consistent with the presence within this localized region of the uniquely strong v_3 surface optical phonon of $LiFePO_4$ at 1040 cm^{-1}. The near-field spectroscopy measurements displayed in Fig. 3.6 imply that this particular fre- quency should present the maximal positive contrast in near-field phase for lithiated over delithiated material, consistent with the interpretation that this diamond-shaped region in- ternal to the crystal strongly retains lithium through the delithiation process.

3.10 Appendix C: Far-field IR signature of solid solution

The surface phonon resonance associated with the lithiated v_3 mode was observed at reduced intensity throughout the partially lithiated particle (relative to the fully lithiated end-member) but its frequency remains constant to within 10 cm^{-1} of 1042 cm^{-1}. This observation seems inconsistent with the notion of so-called solid solutions at partial Li content, given that a continuous shift in the mean v_3 vibrational frequency taken over all phosphate anions in the lattice is expected for such solutions, varying with the average oxidation state of iron.

The IR spectrum of such solid solution for $Li_{0.6}FePO_4$ is given in Figure 3.7. LFP powder was partially delithiated using the same procedure as described above (Br_2/CH_3CN). The amount of Bromine was measured to obtain 40% delithiation. The powder was rinsed in CH3CN and annealed at 400 °C and then cooled down. Powder XRD showed a single phase, a solid solution. FTIR spectra were taken in KBr pellets.

3.11 References

1. Yamada, A.; Koizumi, H.; Nishimura, S.-i.; Sonoyama, N.; Kanno, R.; Yonemura, M.; Nakamura, T.; Kobayashi, Y. *Nature Mater.* 2006, 5, 357-360.

2. Ellis, B. L.; Lee, K. T.; Nazar, L. F. *Chem. Mat.* 2010, 22, 691-714.

3. Keilmann, F.; Hillenbrand, R. *Philosophical Transactions of the Royal Society of London. Series A: Mathematical, Physical and Engineering Sciences* 2004, 362, 787-805.

4. Delacourt, C.; Poizot, P.; Tarascon, J. M.; Masquelier, C. *Nature Mater.* 2005, 4, 254-260.

5. Gibot, P.; Casas-Cabanas, M.; Laffont, L.; Levasseur, S.; Carlach, P.; Hamelet, S.; Tarascon, J.-M.; Masquelier, C. *Nature Mater.* 2008, 7, 741-747.

6. Delmas, C.; Maccario, M.; Croguennec, L.; Le Cras, F.; Weill, F. *Nature Mater.* 2008, 7, 665-671.

7. Chen, G. Y.; Song, X. Y.; Richardson, T. J. *Electrochem. Solid State Lett.* 2006, 9, A295-A298.

8. Chen, G. Y.; Song, X. Y.; Richardson, T. J. *J. Electrochem. Soc.* 2007, 154, A627-A632.

9. Ramana, C. V.; Mauger, A.; Gendron, F.; Julien, C. M.; Zaghib, K. *J. Pow. Sources* 2009, 187, 555-564.

10. Laffont, L.; Delacourt, C.; Gibot, P.; Wu, M. Y.; Kooyman, P.; Masquelier, C.; Tarascon, J. M. *Chem. Mat.* 2006, 18, 5520-5529.

11. Sigle, W.; Amin, R.; Weichert, K.; van Aken, P. A.; Maier, J. *Electrochem. Solid State Lett.* 2009, 12, A151-A154.

12. Meirer, F.; Cabana, J.; Liu, Y. J.; Mehta, A.; Andrews, J. C.; Pianetta, P. *J. Synchrot. Radiat.* 2011, 18, 773-781.

13. Boesenberg, U.; Meirer, F.; Liu, Y.; Shukla, A. K.; Dell'Anna, R.; Tyliszczak, T.; Chen, G.; Andrews, J. C.; Richardson, T. J.; Kostecki, R.; Cabana, J. *Chem. Mat.* 2013.

14. Chueh, W. C.; El Gabaly, F.; Sugar, J. D.; Bartelt, N. C.; McDaniel, A. H.; Fenton, K. R.; Zavadil, K. R.; Tyliszczak, T.; Lai, W.; McCarty, K. F. *Nano Lett.* 2013, 13, 866-872.

15. Burba, C. M.; Frech, R. *J. Electrochem. Soc.* 2004, 151, A1032-A1038.

16. Atkin, J. M.; Berweger, S.; Jones, A. C.; Raschke, M. B. *Advances in Physics* 2012, 61, 745-842.

17. Vaeziravani, M.; Toledocrow, R. *App. Phys. Lett.* 1993, 62, 1044-1046.

18. Ocelic, N.; Huber, A.; Hillenbrand, R. *App. Phys. Lett.* 2006, 89, 101124.

19. Keilmann, F.; Amarie, S. *J. Infrared, Millimeter, and Terahertz Waves* 2012, 33, 479-484.

20. Amarie, S.; Keilmann, F. *Phys. Rev. B* 2011, 83, 045404.

21. Craig, I. M.; Taubman, M. S.; Lea, A. S.; Phillips, M. C.; Josberger, E. E.; Raschke, M. B. *Opt. Express* 2013, 21, 30401-30414.

22. Huth, F.; Govyadinov, A.; Amarie, S.; Nuansing, W.; Keilmann, F.; Hillenbrand, R. *Nano Lett.* 2012, 12, 3973-3978.

23. Wagner, M.; Fei, Z.; McLeod, A. S.; Rodin, A. S.; Bao, W.; Iwinski, E. G.; Zhao, Z.; Goldflam, M.; Liu, M.; Dominguez, G.; Thiemens, M.; Fogler, M. M.; Castro Neto, A. H.; Lau, C. N.; Amarie, S.; Keilmann, F.; Basov, D. N. *Nano Lett.* 2014, 14, 894-900.

24. Zhang, L. M.; Andreev, G. O.; Fei, Z.; McLeod, A. S.; Dominguez, G.; Thiemens, M.; Castro-Neto, A. H.; Basov, D. N.; Fogler, M. M. *Phys. Rev. B* 2012, 85, 075419.

25. Taubner, T.; Keilmann, F.; Hillenbrand, R. *Opt. Express* 2005, 13, 8893-8899.

26. Ait-Salah, A.; Dodd, J.; Mauger, A.; Yazami, R.; Gendron, F.; Julien, C. M. *Zeitschrift für anorganische und allgemeine Chemie* 2006, 632, 1598-1605.

27. Burba, C. M.; Frech, R. *Spectroc. Acta Pt. A-Molec. Biomolec. Spectr.* 2006, 65, 44-50.

28. Hillenbrand, R.; Taubner, T.; Keilmann, F. *Nature* 2002, 418, 159-162.

29. Porto, J. A.; Johansson, P.; Apell, S. P.; Lopez-Rios, T. *Phys. Rev. B* 2003, 67, 085409.

30. Taubner, T.; Keilmann, F.; Hillenbrand, R. *Nano Lett.* 2004, 4, 1669-1672.

31. McLeod, A. S.; Kelly, P.; Goldflam, M. D.; Gainsforth, Z.; Westphal, A. J.; Dominguez, G.; Thiemens, M.; Fogler, M. M.; Basov, D. N. *Phys. Rev. B* 2014, 90, 085136.

32. Dovesi, R.; Orlando, R.; Civalleri, B.; Roetti, C.; Saunders, V. R.; Zicovich-Wilson, C. M. *Z. Kristall.* 2005, 220, 571-573.

33. Dovesi, R.; Saunders, V. R.; Roetti, C.; Orlando, R.; Zicovich-Wilson, C. M.; Pascale, F.; Civalleri, B.; Doll, K.; Harrison, N. M.; Bush, I. J.; D'Arco, P.; Llunell, M., *CRYSTAL09 User's Manual*. University of Torino: Torino, 2009.

34. Delacourt, C.; Rodriguez-Carvajal, J.; Schmitt, B.; Tarascon, J. M.; Masquelier, C. *Solid State Sci.* 2005, 7, 1506-1516.

35. Yamada, A.; Koizumi, H.; Sonoyama, N.; Kanno, R. *Electrochem. Solid State Lett.* 2005, 8, A409-A413.

36. Kildemo, M.; Hunderi, O.; Drévillon, B. *J. Opt. Soc. Am. A* 1997, 14, 931-939.

37. Andersson, A. S.; Thomas, J. O. *J. Pow. Sources* 2001, 97-8, 498-502.

38. Malik, R.; Zhou, F.; Ceder, G. *Nature Mater.* 2011, 10, 587-590.

39. Padhi, A. K.; Nanjundaswamy, K. S.; Goodenough, J. B. *J. Electrochem. Soc.* 1997, 144, 1188-1194.

40. Srinivasan, V.; Newman, J. *J. Electrochem. Soc.* 2004, 151, A1517-A1529.

41. Dargaville, S.; Farrell, T. W. *J. Electrochem. Soc.* 2010, 157, A830-A840.

42. Cogswell, D. A.; Bazant, M. Z. *Nano Lett.* 2013, 13, 3036-3041.

43. Prosini, P. P. *J. Electrochem. Soc.* 2005, 152, A1925-A1929.

44. Cogswell, D. A.; Bazant, M. Z. *ACS Nano* 2012, 6, 2215-2225.

45. Meethong, N.; Huang, H. Y. S.; Speakman, S. A.; Carter, W. C.; Chiang, Y. M. *Adv. Funct. Mat.* 2007, 17, 1115-1123.

46. Bai, P.; Cogswell, D. A.; Bazant, M. Z. *Nano Lett.* 2011, 11, 4890-4896.

47. Singh, G. K.; Ceder, G.; Bazant, M. Z. *Electrochim. Acta* 2008, 53, 7599-7613.

48. Sharma, N.; Guo, X.; Du, G.; Guo, Z.; Wang, J.; Wang, Z.; Peterson, V. K. *J. Am. Chem. Soc.* 2012, 134, 7867-7873.

49. Liu, H.; Strobridge, F. C.; Borkiewicz, O. J.; Wiaderek, K. M.; Chapman, K. W.; Chupas, P. J.; Grey, C. P. *Science* 2014, 344.

50. Zhang, X.; van Hulzen, M.; Singh, D. P.; Brownrigg, A.; Wright, J. P.; van Dijk, N. H.; Wagemaker, M. *Nano Letters* 2014, 14, 2279-2285.

51. Carney, P. S.; Deutsch, B.; Govyadinov, A. A.; Hillenbrand, R. *ACS Nano* 2012, 6, 8-12.

52. Raschke, M. B.; Lienau, C. *App. Phys. Lett.* 2003, 83, 5089-5091.

53. Aizpurua, J.; Taubner, T.; García de Abajo, F. J.; Brehm, M.; Hillenbrand, R. *Opt. Express* 2008, 16, 1529-1545.

CHAPTER 4: Nano-scale Infrared Spectroscopy: a Non-Destructive Probe of Extraterrestrial Materials

4.1 Abstract

Advances in the spatial resolution of modern analytical techniques have tremendously augmented the scientific insight gained from the analysis of natural samples. Yet, while techniques for the elemental and structural characterization of samples have achieved sub-nanometer spatial resolution, infrared spectral mapping of geochemical samples at vibrational "fingerprint" wavelengths has remained restricted to spatial scales larger than 10 microns. Nevertheless, infrared spectroscopy remains an invaluable contactless probe of chemical structure, details of which offer clues to the formation history of minerals. In complement to SEM, EDS, and TEM probes, here we report on the successful implementation of infrared near-field imaging, spectroscopy and analysis techniques capable of sub-micron scale mineral identification within natural samples, including a chondrule from the Murchison meteorite and a cometary dust grain (Iris) from NASA's Stardust mission, evidencing a surprising similarity between chondritic and cometary materials. This work inaugurates a new era of infrared nano-spectroscopy applied to small and invaluable extraterrestrial samples.

4.2 Introduction

Infrared (IR) spectroscopy in the frequency range of 400-4000 cm^{-1} (λ=25-2.5 μm) is widely used for the identification of chemical compositions both in-situ and in remote observations. However, use of this technique for studying sub-micron-scale heterogeneity characteristic of natural samples or individual micron sized samples such as the cometary dust grains retrieved by the NASA's Stardust mission [1, 2, 3, 4, 5, 6] is severely hampered by the spatial resolution afforded by the diffraction limit and the wavelength of IR light [7, 8]. This limitation rules out direct investigations of both sub-micron samples and sub-micron inclusions in larger heterogeneous samples by conventional Fourier transform infrared spectroscopy (FTIR) [9, 10, 11, 12, 13, 14, 15, 16, 17]. Yet, as acknowledged among the first reported findings from the Stardust mission, advances in analytic techniques promise to expose new secrets about the origin and evolution of the solar system contained in recovered microscopic cometary grains [1]. With regard to infrared spectroscopy, this claim cannot be overstated given its reputation as the chemical "fingerprinting" technique of choice. Moreover, the return of invaluable micron-scale samples from spacecraft missions such as Stardust poses an urgent need for new non-destructive, even non-perturbative, nano-scale probes of chemical structure.

In recent years, developments in scattering-type Near-field Scanning Optical Microscopy (s-SNOM) have enabled acquisition of infrared spectral information at sub-micron length scales [18, 19]. Conceptually, this imaging technique relies on an atomic force microscope (AFM) tip acting as an optical antenna (or "near-field probe") to focus incident electromagnetic radiation to areas smaller than the wavelength of incident light. Recent applications of the technique include studies of plasmons in graphene and spatial mapping of electronic transitions in correlated oxides [20, 21, 22, 23, 24, 25, 26, 27]. By incorporating a broadband mid-infrared (MIR) laser and spectroscopic interferometer into an s-SNOM system, investigators have now demonstrated 20 nm-resolved infrared nano-spectroscopy (nanoFTIR)[28,29, 30, 31, 32, 33]. Yet, to the best of our knowledge, heretofore the only attempt at near-field imaging and spectroscopy of natural geochemical

samples has utilized a conventional (thermal) infrared source to produce maps of spectral features limited to ~ 1 micron resolution in a primitive meteorite [34]. However, the absence of background suppression schemes requisite for near-field microscopy places much doubt on their study's efficacy as a *bona fide* sub-diffraction optical probe.

In complement to SEM, EDS, and TEM probes, here we report on the first application of infrared s-SNOM and nanoFTIR with a metallic near-field probe to identify and distinguish silicate minerals in a sample of comet 81P/Wild 2 and a portion of the Murchison meteorite, a CM2 chondrite comprised of organics and stony grains (chondrules), with sub-micron (~20 nm) lateral resolution. We also demonstrate that nano-scale infrared spectroscopy can 1) sense elemental concentration gradients at the level of a few percent caused by rapid cooling, 2) identify sub-micron intergrowths at the confluence of distinct lattice structures, providing evidence for shock within a chondrule, and 3) directly reveal juxtaposed crystalline and amorphous silicates in the Iris cometary grain. NanoFTIR measurements of Iris are consistent with mounting evidence [3, 35, 36, 37] that igneous materials forming at high temperatures deep in the solar nebula were incorporated into cometary bodies, advancing a surprising scenario whereby planetary materials must have been mixed over the grandest scales into the outer solar system[1].

4.3 Material Identification with NanoFTIR

Material identification in spatial volumes smaller than the wavelength of light through s-SNOM requires establishing a physical relationship between an incident electromagnetic field, the dielectric properties of the material directly underneath the probe tip, and the consequently scattered electromagnetic field recorded by the microscope (for our experimental setup see Appendices). In the simplest model of s-SNOM, based on the combination of an atomic force microscope (AFM) with infrared optics, the incident electromagnetic field irradiates the AFM probe, inducing a dipole of electric charge in its tip, as shown schematically in FIg. 4.1. In accordance with the boundary conditions of Maxwell's equations at the surface of the dielectric

material directly underneath, an interacting mirror dipole is induced within the sample. An electric near-field interaction between the tip and charges from its mirror image modifies the amplitude and phase of back-scattered radiation from the probe, which functions therefore as an optical antenna highly sensitive to the dielectric environment near its tip. Using suitable background suppression and techniques, interferometric detection of this back-scattered radiation while scanning the sample beneath the tip provides sensitivity to the sample's local permittivity at a resolution comparable to the radius of curvature at the tip apex (≈20 nm).

A rudimentary connection between the amplitude and phase of this detected radiation ("near-field signal") and the optical properties of the sample can be achieved through a simple dipole approximation [38, 39]. Recently, we have developed more sophisticated models of the optical near-field interaction between the probe and sample and have applied them with excellent results to the study of graphene-substrate optical coupling [22] and oxide thin films [21]. Our latest and most accurate model [40] interrelates the scattered signal with the dielectric function and optical reflection coefficient of the sample (See Figure S1), the same reflectivity accessed by conventional far-field FTIR spectroscopy. Likewise, the infrared extinction coefficient, equal to the imaginary component of the sample's refractive index, describes its infrared absorption efficiency. Maxima in the frequency-dependent infrared extinction coefficient correspond directly to the absorption peaks of "fingerprint" molecular vibrations measured by conventional transmission-mode FTIR or total internal reflectance (ATR) spectroscopies.

However, though related, the frequency-dependent scattered field measured by nanoFTIR is not equivalent to a conventional FTIR absorption spectrum. Surface phonons couple particularly strongly to a near-field probe as their electric dipole vibrates resonantly with the incident probe field, shifting peaks in the scattering spectrum to lower energy by an amount commensurate with their strength [41]. Quantitative comparisons between a sample's near-field spectrum (e.g. Fig. 4.2) and its associated conventional FTIR absorption spectrum requires that the geometry of the near-field interaction be explicitly taken into account by a realistic model of

the tip, such as the one used in this work to “invert” the scattering amplitude and phase spectra to extract nano-resolved dielectric properties of the material underneath the tip apex [30, 40]. Elementary relations connecting the reflection coefficient to the infrared extinction coefficient have been presented elsewhere [31] and, for characterization of the cometary particle Iris, we apply these here for the first time to the direct identification of silicate minerals using nanoFTIR (see Appendices).

4.4 NanoFTIR Characterization of a Chondrule

FIg. 4.2 schematically depicts our s-SNOM and nanoFTIR system (see Appendices) and presents characteristic scattering spectra for a standard crystal of forsterite, one of the most abundant minerals in the solar system and common chondrule constituent. We applied this system first to characterize a sub-millimeter chondrule within the Murchison meteorite, a CM2 chondrite notable for its abundant organics and aqueously altered minerals (preparation in Appendices). The chondrule was first coated with ≈15 nm of conductive carbon and imaged by scanning electron microscopy (SEM); Figs. 3a & b display back-scattered electron (BSE) images. Elemental compositions (displayed in Fig. 4.3d) were measured at < 500 nm resolution using energy dispersive X-ray spectroscopy (EDS). The chondrule was then sputtered with argon to ablate the carbon coat and subsequently imaged with s-SNOM in monochromatic mode (pseudo-heterodyne detection technique [42]) taking illumination from a CO_2 laser at 890 cm^{-1} to quickly reveal an IR contrast map of the region (Fig. 4.3c). Optically reflective or vibrationally resonant materials at this frequency display positive imaging contrast. Infrared scattering contrast is evident among microscopic crystallites, a bright metallic inclusion (iron), and a dark non-resonant background of carbonaceous material (including preparation epoxy).

The chondrule contains Al-, Mg-, and Ca-rich silicate phases, and EDS identifies Mg-rich regions (green in Fig. 4.3d) as forsterite (Mg_2SiO_4). To distinguish extant mineral phases through their vibrational signatures, we collected spectroscopic nanoFTIR linescans 8-10 μm in length

across three distinct microcrystalline sub-regions, acquiring scattered amplitude and phase spectra every 50 nm over the frequency range relevant to the strongly identifying vibrational modes of the silicate minerals (800-1150 cm^{-1}). Scattering amplitude spectra from these linescans are displayed in Fig. 4.4, exhibiting several spectroscopically distinct sub-regions. These linescans verify the ubiquitous presence of forsterite (green in Fig. 4.4) through comparison to reference spectra (Fig. 4.2). Compositional boundaries sharper than 100 nm and distinct silicates as small as 200 nm are resolved spectroscopically. Metallic composition of the large iron inclusion (red spectrum in Fig. 4.4, linescan 2) was confirmed by its exceptionally strong and spectrally uniform induced scattering amplitude, although several superimposed "void bands" provide evidence for a surface oxide layer of probable terrestrial origin, as from "gamma"-FeOOH (lepidocrocite) which exhibits identifying MIR vibrational modes [43]. These resonances are optically "sensed" through near-field coupling with their metallic host, as leveraged previously for the detection of weak molecular vibrations using metal nanoantennas [44].

Stoichiometries for Al- and Ca-rich regions measured by EDS are consistent with several minerals formed from linear chains of silicate tetrahedra (inosilicates) but were insufficient to unambiguously identify the associated mineral species since EDS is insensitive to the presence of -OH. In such cases, concrete identification of mineral phases has conventionally relied on complementary analytic techniques including X-ray diffraction (XRD), transmission electron microscopy (TEM), and various transmission-mode X-ray spectroscopies, which although powerful, demand either sample volumes of many cubic microns or thin slices excised from the bulk sample at the cost of man-hours and destroying the nearby sample. Even the electron backscatter diffraction technique, a powerful high-resolution probe of crystal structure (insensitive to glassy structure), requires careful deposition of carbon over insulating minerals [45]. In stark contrast, nanoFTIR measurements are fundamentally non-destructive, requiring no special sample preparation beyond a surface polish with micron-scale smoothness, which even then might be omitted for smooth or terraced sample regions. Furthermore, since mid-IR energies are

insufficient to break chemical bonds or cause ionization, risk to the sample from beam damage during the nanoFTIR measurement is completely implausible when using illuminating radiation intensities less than 5 milliwatts (0.5 milliwatts were used in this work)[46]. Nevertheless, a lamella along linescan 3 (indicated in Fig. 4.3c and d) was extracted from our Murchison meteorite sample by focused ion beam and examined by transmission electron microscopy (TEM) (see Supplementary Online Material, or SOM, and Fig. 4.S4 [71]). In this case, we undertook this measure to unambiguously establish a correlative TEM and nanoFTIR spectroscopy study of the same region[47]. Whereas the complete focused ion milling and TEM study required three days of instrument time, nanoFTIR measurements were completed within three hours.

Analysis of nanoFTIR data inherits from the rich existing literature of vibrational spectroscopy obtained from bulk terrestrial minerals by conventional FTIR. Pyroxenes constitute a solid solution series of single-chain silicates with chemical formula $M^1M^2T_2O_6$ (M^1, M^2 denoting cation sites, and T the tetrahedral site, typically Si or Al) including Mg-rich (enstatite) and Ca-rich (augite) members common among chondritic meteorites. Established infrared absorption spectra for enstatite [48, 49] match vibrational bands of the first several nanoFTIR spectra (SOM [71]) of linescan 3 (Fig. 4.4 in orange), consistent with Mg-dominated occupancy in M^1 and M^2 sites as confirmed by TEM EDS (Fig. 4.5b). However, EDS also indicates the Murchison Mg-rich pyroxene contains 5.3 wt% aluminum, making this phase aluminous orthopyroxene (OPX). A discrete change in vibrational character is observed by nanoFTIR upon entry to the Ca-rich phase, which compares favorably to attenuated total internal reflectance spectra of augite [50, 51]. Comparatively, such a concrete identification for this compound was otherwise impossible via EDS, since the measured elemental stoichiometry admitted other mineral assignments (SOM Fig. S3 [71]). The abrupt disappearance and replacement of several vibrational modes displayed in Fig. 4.5a (orange to purple) matches an abrupt compositional change observed by EDS with a reduction in Mg by 10 wt% and an increase in Ca by 14 wt%. Accordingly, a phase transition from OPX to CPX (clinopyroxene) was measured by selected area diffraction in TEM (SOM [71]).

While existing infrared studies fail to observe marked differences in vibrational character between ortho- and clinoenstatites [49 52], the monoclinic structure of augite presents yet a distinct space group, C2/c versus the $P2_1/c$ of clinoenstatite. We therefore attribute the resolved boundary in nanoFTIR to differential cation occupations in M^1 and M^2 [53], establishing nanoFTIR as a sensitive indicator of subtle shifts in elemental chemistry at the nano-scale. We infer these cation concentrations resulted from strong temperature gradients as the host pyroxene rapidly crystallized.

Our correlative TEM subsequently resolved the transition zone between OPX and CPX phases Fig. 4.5d, and electron diffraction verified our identification of phases (Fig. 4.5c and SOM Fig. S4 [71]). Moreover, a 300 nm-wide superlattice of CPX and OPX lamella (marked OCPX) is revealed through electron diffraction as a continuum of reflections along the *a**-axis and shows contrast in high-resolution and darkfield TEM imaging. Though only a few hundred unit cells across, this intergrowth region was first resolved by nanoFTIR, manifesting an anomalous infrared vibrational signature at several spectroscopy positions across the OPX / CPX interface in Fig. 4.5a, particularly through the sharp “kink” in several vibrational modes suspiciously characteristic of interlayer-coupled mode repulsion. The lack of such effect for the 1050 cm^{-1} mode likely associates with its short-range vibrational nature – a “breathing” mode among isolated silicate tetrahedra (SOM [71]) – unaffected by broken long-range crystal symmetry. Such interphase ortho/clinopyroxene regions are a common indicator of crystal shock and rapid cooling [54]. Here we interpret the structure as a consequence of collisional events in the history of Murchison’s parent body, in particular the event that may have caused the host chondrule to shatter (Fig. 4.3a and SOM [71]). Sensitivity to these shock phenomena establish nanoFTIR as a promising non-destructive probe of collisional histories among invaluable extraterrestrial samples.

Fig. 4.5a highlights a notable shift in modal frequencies (especially near 1050 cm^{-1}) resolved by nanoFTIR at sub-micron scales in linescan 3, coincident with further lattice displacement of Mg by heavier Ca and Al in CPX at the few-percent level on approach to the

adjacent forsterite (Fig. 4.5b). These vibrational shifts associate with perturbations in the crystal's silicate tetrahedral bond lengths, mediated by commensurate changes in local cation concentration (SOM [71]). Vibrational spectroscopy via nanoFTIR can evidently provide a sensitive sub-micron indicator of cation lattice coordination and concentration variations at the few-percent level. We propose that nanoFTIR might be deployed on extraterrestrial pyroxenes to detect T site occupation by Al and Fe^{3+} which, when compared with other petrographic characteristics, can provide evidence for aqueous alteration or for high fugacity during formation in the solar nebula.

4.5 NanoFTIR Characterization of a Cometary Grain

We next applied nanoFTIR to a cometary particle returned from comet 81P/Wild 2 by the NASA's Stardust recovery mission, a sample for which the non-destructive nature of our probe is of paramount importance. The cometary grain C2052,12,74 ("Iris") was first characterized by synchrotron X-ray, electron, and ion microscopies, as well as secondary ion mass spectroscopy (SIMS) [55]. On a surface of Iris exposed by ultramicrotomy, we first utilized our nanoFTIR system to acquire a broadband integrated image of the particle (Figure 6a & b). This mode of imaging permits rapid acquisition of relatively large infrared maps of the sample in which local contrast indicates the optical response amplitude integrated over the bandwidth of illumination (800-1150 cm^{-1}). For example, chunks of Pb-In alloy introduced during sample preparation for SIMS are brightly resolved at the particle periphery. This same region of Iris was also imaged with EDS as shown in Fig. 4.6c, indicating clear correspondence between the mesostasis region identified previously [35, 36] and the elemental EDS map. We acquired a nanoFTIR linescan 7 microns in length along the dotted line indicated in Figure 6b, measuring local scattering amplitude and phase spectra every 100 nm across the mesostasis between two forsterite crystals, and utilized the aforementioned inversion procedure (detailed in Appendices, SOM Figs. S1 and S2 [71]) to convert our scattering spectra to a more appropriate series of IR extinction spectra (Fig. 4.6d)

suitable for comparison against conventional infrared absorption spectra for candidate silicate minerals [56, 57, 58].

Iris is known to consist of olivines set in a groundmass of plagioclase (a solid-solution series of feldspar minerals) with composition 6-26 mol% in Ca-rich anorthite (An) and Na-rich albitic (Ab) glass that formed from quenched igneous cooling. Since the groundmass grew under non-equilibrium conditions, the crystalline plagioclase presents a continuum of chemical compositions including albite and Ca-rich oligoclase (compositionally intermediate between Ab and An). The remaining liquid was unable to crystalize at all because of rapid cooling. The transition from crystalline to amorphous material is observable in our linescan (Fig. 4.6d), wherein three distinct spectral signatures are resolved. Representative spatially averaged nanoFTIR extinction spectra derived from regions bounded by dashed lines in Fig. 4.6c are shown in Fig. 4.6f for clarity. Fig. 4.6e displays literature-derived IR absorption spectra for mineral standards that present good matches to these regions based on a comparison of prominent infrared absorption band frequencies. Spectra for the purple and red phases (Fig. 4.6f) exhibit vibrational bands at nearly identical frequencies but at varying intensity, consistent with An-rich and Ab-rich regions, respectively. Accordingly, EDS mapping ascribes elemental abundances from these two regions to oligoclase with a slowly varying composition of 20-26 An mol%.

Whereas the anorthite and oligoclase phonon bands resolved by nanoFTIR at 910 and 970 cm^{-1} appear expectedly sharper than those observed in far-field absorption spectra for powders [59, 60, 61] at ~915 and ~990 cm^{-1} (Fig. 4.6e), the measured albite peak is notably broad (70 cm^{-1} full-width at half-maximum; see SOM Fig. 4.S2 [71]), comparing most favorably to spectra for crystals with reduced Al-Si order in the tetrahedral site such as effected by high temperature exposure (>1000K) [58]. On the basis of its coincident presence among far-field infrared spectra of Iris (SOM Fig. 4.S5 [71]), the dip-like feature observed throughout our linescan near 950 cm^{-1} appears to be intrinsic in nature, whether associated with a gap in phonon modes of forsterite or with the absence of absorption between sharp peaks associated with An or oligoclase. Whereas

EDS resolution was limited to about 750 nm, nanoFTIR resolves variations in spectral absorption at the scale of 100 nm. Lacking gradual shifts in absorption frequencies, the most likely explanation for such sharp well-defined variations in nanoFTIR is the detection of two centrally embedded crystallites of anorthite and oligoclase resolved at the sub-micron scale. Comparatively, TEM was also able to detect one such crystallite [36] although its spatial relations were unfortunately scrambled (not atypically) from the requisite extraction of a thin microtomed slice of sample.

Moreover, Fig. 4.6d reveals a third phase (blue in Fig. 4.6f) where peak positions and amplitudes vary gradually as a function of position. EDS excludes the possibility that this region is plagioclase on the basis of stoichiometry, suggesting rather an albitic glass, and TEM diffraction and brightfield measurements verify the presence of glass in contact with oligoclase elsewhere within this particle [36]. NanoFTIR spectra in this region (Figure 6d,f – blue) show the growth of a peak near 1100 cm^{-1} similar to that seen in amorphous SiO_2 standards [57], while retaining some but not all of the peaks expected from plagioclase. This suggests an albitic glass populated by under-resolved nanocrystals of oligoclase, again indicative of rapid cooling from a melt. Demonstrably, nanoFTIR presents a novel means of optical identification and potential compositional characterization [62, 63] for *bona fide* amorphous silicate materials in returned microscale cometary dust grains, as well as in similarly sized interplanetary dust particles or aerosols. The composition of Iris shown here is decidedly inconsistent with the long-held view that comets formed in the outer solar system from agglomerated circum- or interstellar grains [64], comprising e.g. dust, ice, and silicates amorphized by radiation exposure. Instead, the direct infrared spectroscopic evidence presented here for igneous crystalline and amorphous materials coexisting at the micron-scale within a cometary dust grain adds to mounting evidence for a common history of high-temperature formation shared by cometary and chondritic materials deep within the solar nebula [35, 36, 37]. This scenario awaits a suitable explanation for the requisite

mixing of planetary materials into the outer solar system that must have enabled their incorporation among remote cometary bodies such as 81P/Wild 2[1].

4.6 Outlook: NanoFTIR for Geochemical Applications

We have shown that infrared s-SNOM is capable of providing IR spectral identification of natural samples at deeply sub-micron spatial resolutions, probing details of material composition not easily accessed by conventional means. Here we demonstrate this capability within a macroscopic meteorite sample (Murchison) as well as a cometary dust grain (Iris) from NASA's sample return mission, Stardust. Through application of a sophisticated model of the probe-sample near-field interaction, we have shown for the first time that nanoFTIR-extracted infrared extinction spectra can be used to quantitatively probe and identify the underlying geochemistry of natural samples at sub-micron resolutions, enabling identification of resonance frequencies and relative levels of structural disorder in a fashion that removes the influence of complex probe-sample interactions. These samples span the size range encountered in the analysis of natural samples.

Together with corresponding elemental maps from EDS, our nanoFTIR linescans through a chondrule in Murchison clearly capture variations in minerology at sub-micron resolutions and are verified by TEM. Furthermore, our nanoFTIR linescans are capable of resolving subtle shifts in vibrational frequencies associated with small variations in silicate cation concentrations at the sub-micron scale. Future work may explore these shifts in a quantitative manner via first-principles calculations. Our nanoFTIR survey of Iris demonstrates that s-SNOM is also sensitive to contrasts in crystallinity, as indicated by the prominence and width of phonon absorption bands within the plagioclase, and future work may establish quantitative measures of disorder. Whereas the physical mechanism of nanoFTIR spectroscopy is relatively settled, and practical quantitative "inversion" for the interpretation of mineral spectra is now well demonstrated here and elsewhere[40] , fully leveraging its sensitivity will call for a detailed empirical or *ab anitio* approach

connecting nano-scale geochemistry to the local phonon response and associated infrared permittivity.

These results highlight the high potential of nanoFTIR for geochemical studies of crystallization dynamics or other processes producing variations in the chemical environment over sub-micron length scales, inaccessible to conventional diffraction-limited FTIR. Having demonstrated the application of SNOM-based nanoFTIR for characterizing and imaging silicate minerals, it is hoped that this technique can be applied for studying the distribution of more volatile chemical components found within extraterrestrial samples. This sub-micron mapping could in turn, through strong correlations between minerals such as SiC (well-known presolar astromaterial) and organics, for example, provide new insights into the catalytic role that mineral surfaces may play in the production of prebiotic molecules in the early solar system and planetary systems at large. Finally, the ability to non-destructively characterize volatile species before more destructive/altering techniques are applied to precious and unique returned samples is a significant advance. Future applications of infrared s-SNOM and nanoFTIR may also include distribution studies of individual terrestrial aerosol mixing states, examination of synthetic and natural non-equilibrium solids, and sub-micron identification of hydrated and organic chondrite phases. Furthermore, this technique should be suitable for the analysis of additional returned samples from missions including NASA's Stardust spacecraft [1, 2, 6, 65] and Hayabusa [66], as well as interplanetary dust particles (IDPs) and other primitive solar system materials possessing sub-micron heterogeneity [67].

4.7 Acknowledgements

This work was supported by NASA's Laboratory Analysis of Returned Samples program (# NNX11AF24G). The National Center for Microscopy is supported by the Director, Office of Energy Research, Office of Basic Energy Sciences, Materials Sciences Division of the U.S. Department of Energy, under Contract No. DOE-AC03-76SF00098. A. S. McLeod acknowledges support from a U.S. Department of Energy Office of Science graduate research fellowship.

This chapter, in full, is a reprint of the material as it appears in the following published article: A. S. McLeod, G. Dominguez, Z. Gainsforth, P. Kelly, H. A. Bechtel, F. Keilmann, A. Wesphal, M. Thiemens, D. N. Basov. Nanoscale infrared spectroscopy as a non-destructive probe of extraterrestrial samples. *Nat. Commun.* 5, 5445 (2014). The dissertation/thesis author was the co-primary investigator and author of this material.

4.8 Figures

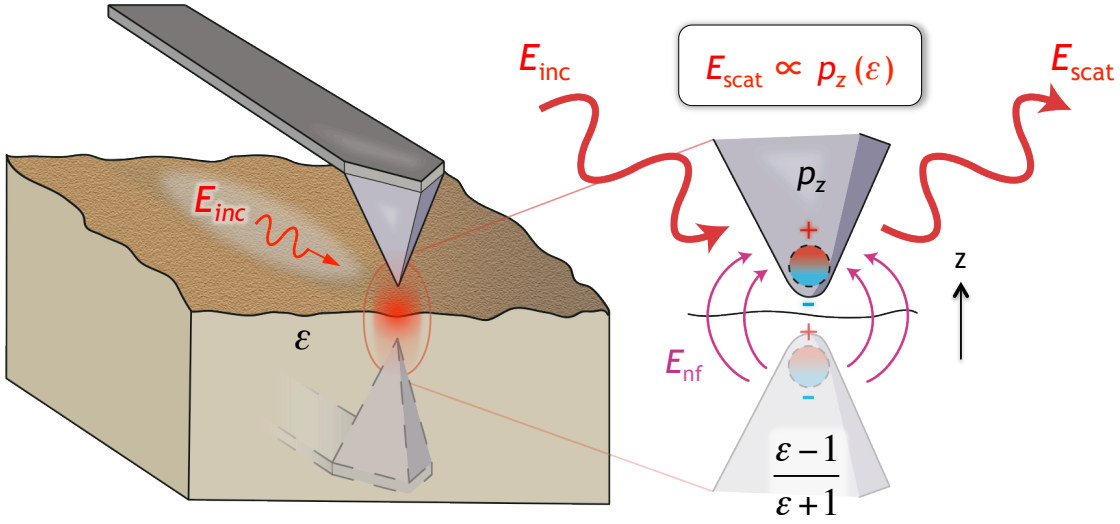

Figure 4.1: Schematic depiction of the probe-sample near-field interaction relevant to s-SNOM.

(left) The probe tip interacts with a thin surface volume characterized by permittivity ε, which is a function of wavelength. (right) The incident electromagnetic field E_{inc} induces a strong dipole moment in the tip, which interacts with a mirror dipole in the sample whose strength is determined by the local permittivity. This interaction sensitively affects the tip polarization p_z, now a function of ε, and therefore locally modulates the amplitude and phase of the tip-scattered field E_{scat}.

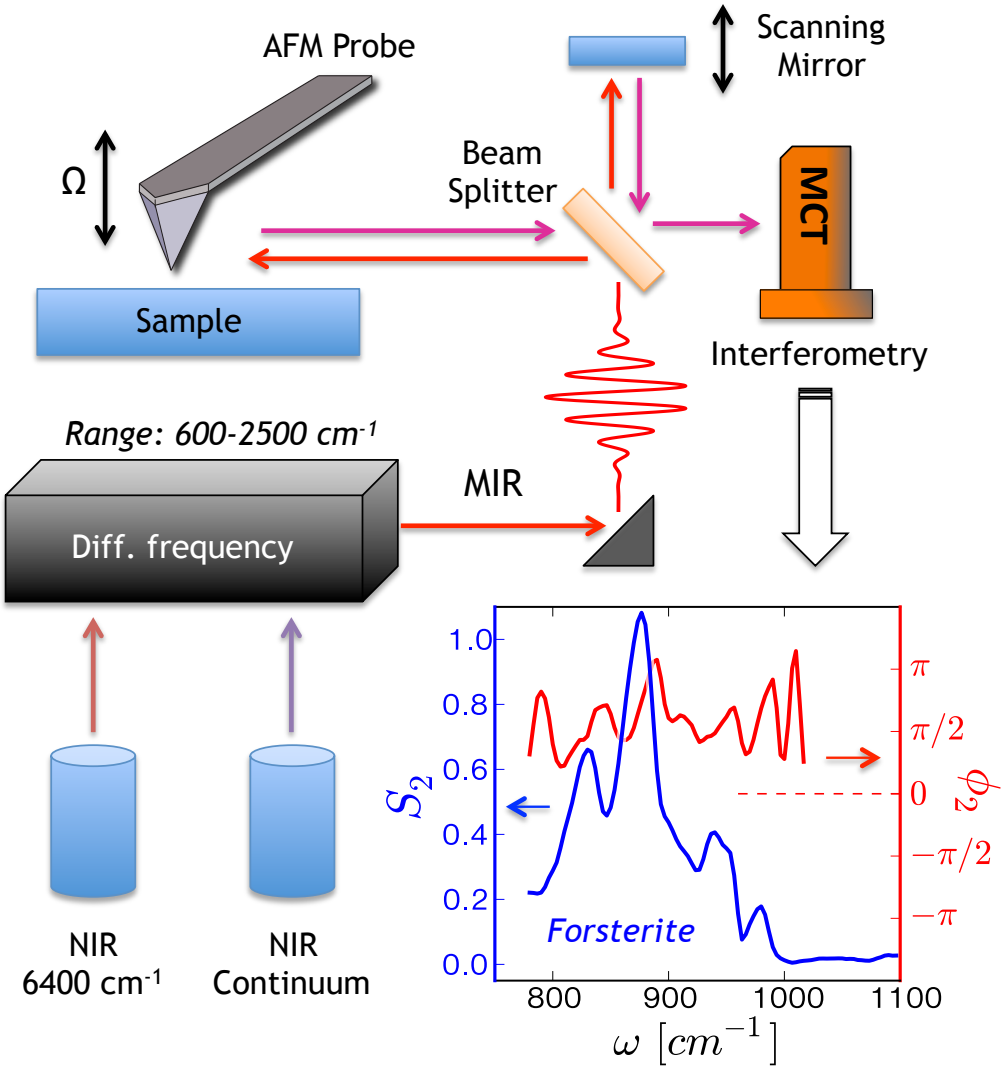

Figure 4.2: Schematic depiction of the nanoFTIR system.

A non-linear optical crystal (GaSe) is used to combine two NIR sources in a difference-frequency generation scheme, producing coherent MIR radiation that is frequency-tunable with a 300 cm^{-1} bandwidth. This beam is focused onto the AFM tip, resulting in strong near-field interactions with the sample and a back-scattered field (characterized by amplitude and phase) modulated at the probe tapping frequency and detected by the HgCdTe (MCT) detector. Interfering this light with a continuously delayed reference beam (scanning mirror) and demodulating at harmonics of the tapping frequency produces an interferogram whose Fourier transform constitutes the desired near-field scattering spectrum. The displayed scattering amplitude and phase spectra are obtained for a forsterite crystal standard (San Carlos olivine).

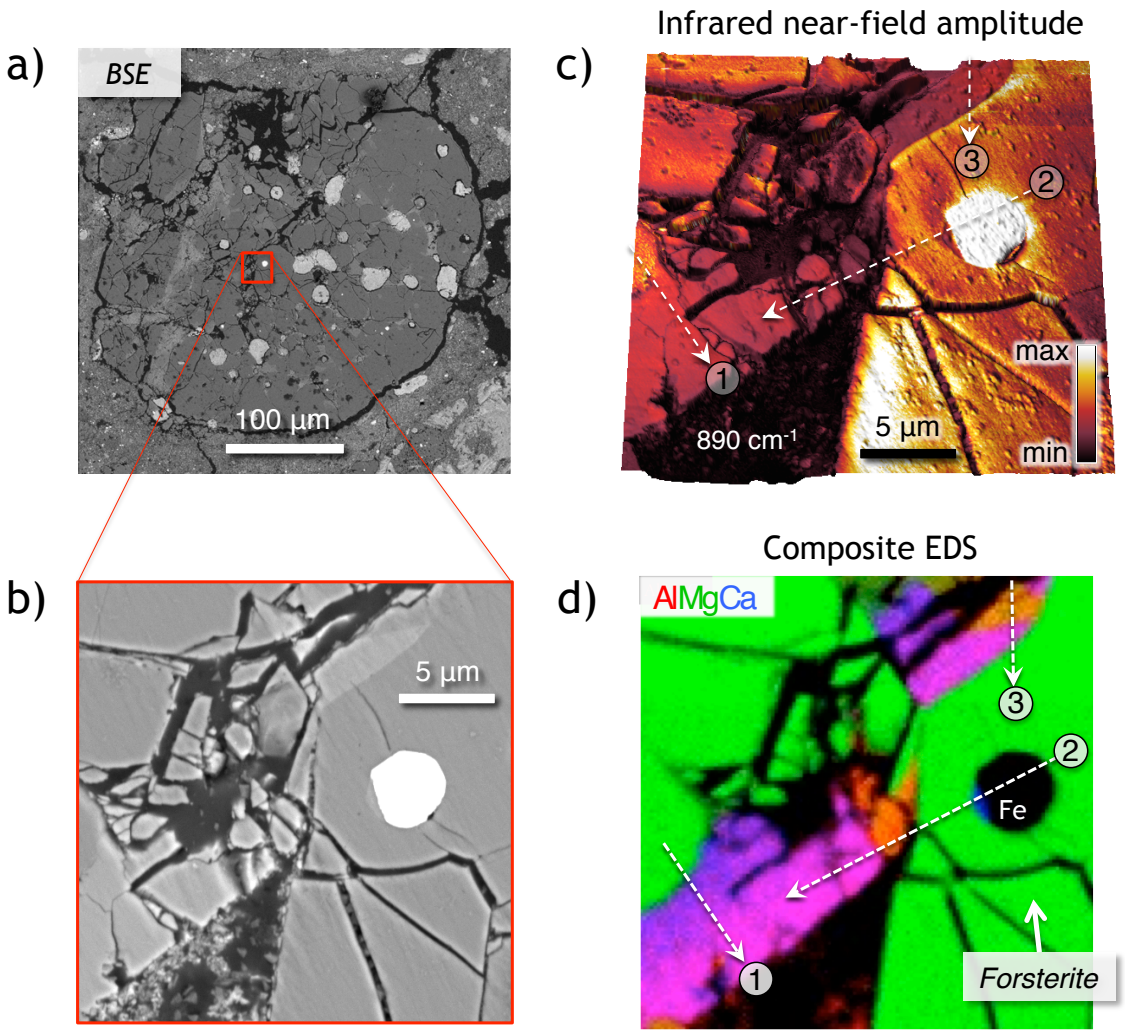

Figure 4.3: Correlative survey of silicate materials in the Murchison meteorite.

(a) Backscattered Secondary Electron (BSE) image of the polished Murchison sample region, with red indicating the field of view for the nanoFTIR images. (b) BSE image of this boxed region in Fig. 4.3a where an iron metal grain can be clearly seen. (c) Infrared near-field amplitude image acquired at ω= 890 cm^{-1} superimposed on simultaneously acquired AFM topography (d) composite EDS map of the same region showing the positions of the three (1-3) nanoFTIR linescans presented in FIg. 4.4. (Green = forsterite, purple = augite, orange = aluminous orthopyroxene)

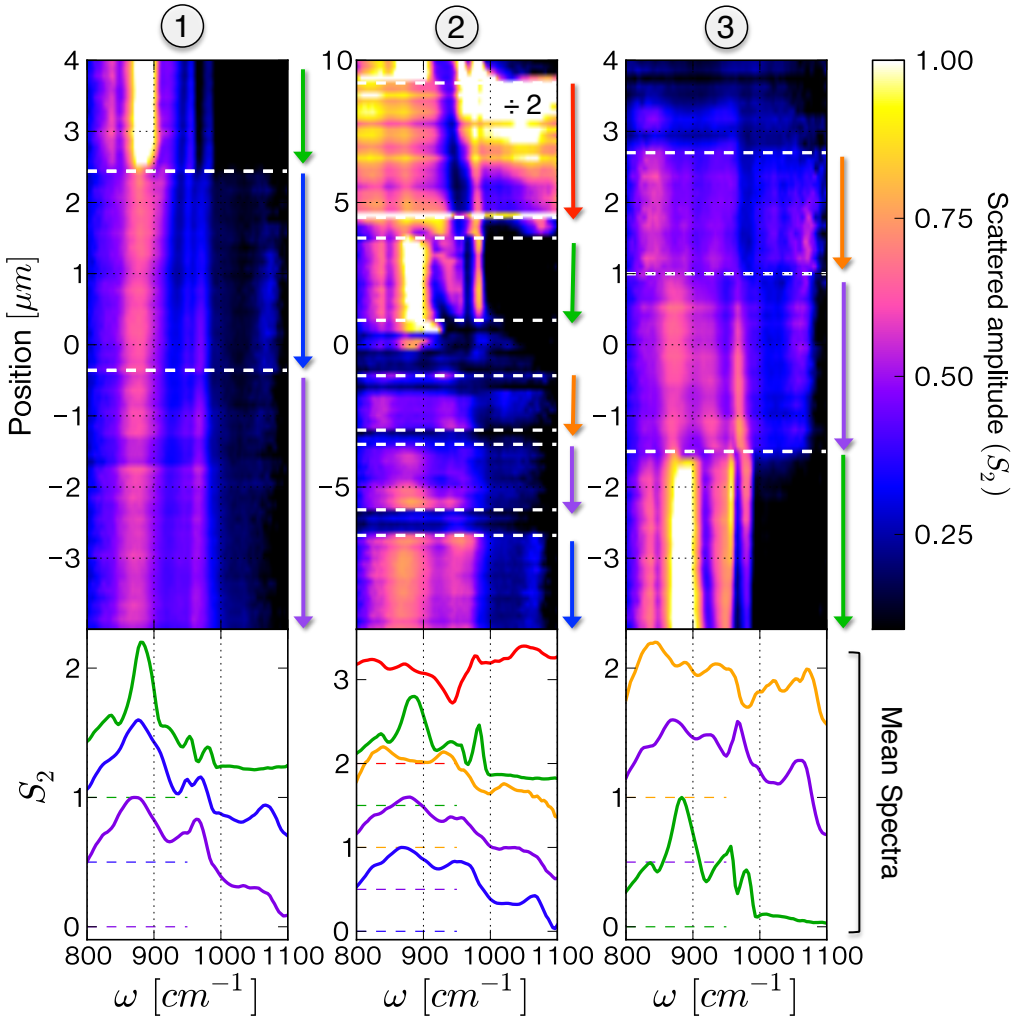

Figure 4.4: Position-resolved nano-spectroscopy of silicates in the Murchison meteorite.

(Top) Three spectral linescans (scattering amplitude versus position) through a chondrule of the Murchison meteorite identify distinct crystalline phases according to their unique near-field spectra. *Region 1*: a sequence of forsterite (green arrow), Al-poor (blue) and Al-rich (purple) augite. *Region 2*: An iron inclusion with suspected phonons -resonant oxide layer (red, amplitude reduced by 2x), followed by forsterite (green), aluminous orthopyroxene (orange), Al-rich and Al-poor augites. Comparatively broad phonon peaks in the final three regions likely indicate structural disorder. Region 3: A progression of aluminous orthopyroxene, augite, and forsterite. (Bottom) Position-averaged spectra of these distinct regions are similarly color-coded (offset for clarity, dashes indicate zero lines).

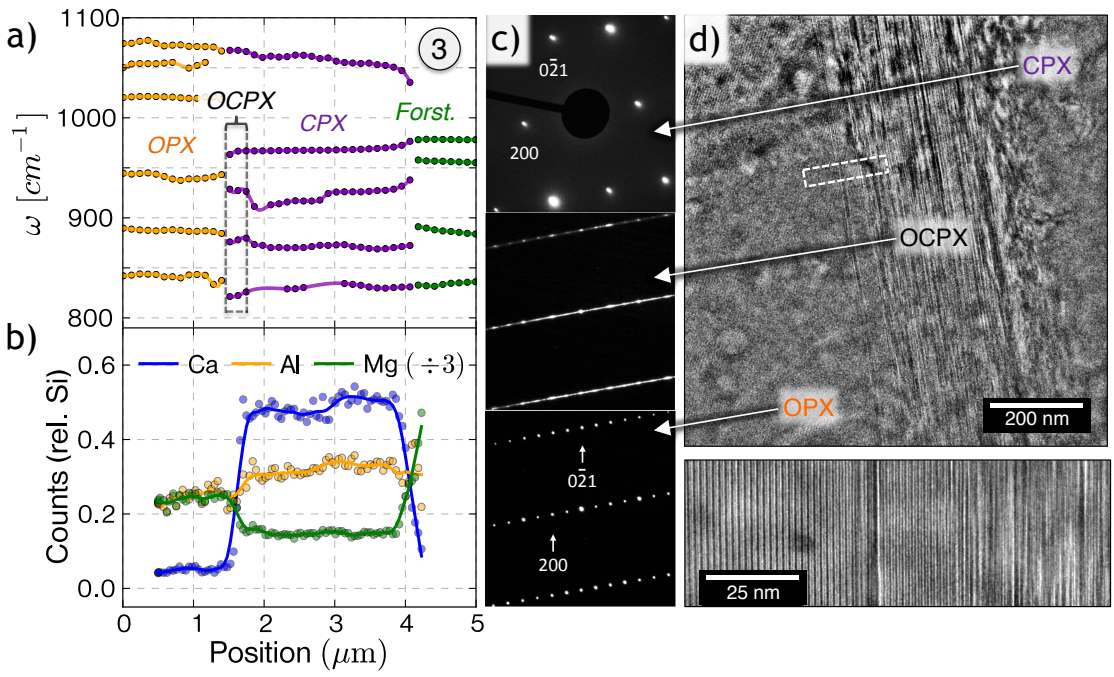

Figure 4.5: Spectroscopic sensitivity to cationic shifts in Murchison pyroxenes.

(a) Modal frequencies versus position resolved by nanoFTIR through linescan 3 of the Murchison meteorite. Forsterite (green) gives way to pyroxene phases: calcium-rich clinopyroxene (CPX, purple) and an aluminous orthopyroxene (OPX, orange). Modulations in modal frequencies correlate with increases in cation concentrations at the few percent level as determined by transmission electron EDS (b). The spectroscopically distinct 300 nm wide transition band between CPX and OPX observed by nanoFTIR is attributed to an OPX / CPX superlattice (OCPX, dashed region) zone verified by TEM (d, top), indicative of crystal shock. (d, bottom) HRTEM zoom in view onto the boxed region resolves the OPX / OCPX interface. (c) Transmission electron diffraction collected from the respective pyroxene phases confirms the aperiodic lattice superstructure of this band.

Figure 4.6: Nano-imaging and spectroscopy of the Iris cometary dust grain.

(a) Broadband IR s-SNOM image of the Iris cometary dust grain (b) with zoom onto the central region; color-scale for spectrally integrated scattering amplitude (800-1150 cm^{-1}) at right; nanoFTIR linescan position indicated by the arrow. (c) Composite EDS map displaying relative atomic concentrations of aluminum (red), sodium (green), and silicon (blue). Silicon-rich forsterite crystals as well as the surrounding SiO_2 aerogel appear blue, whereas the groundmass reveals feldspar (white) and glass (red and pink). (d) Position-resolved IR extinction spectra extracted from the nanoFTIR linescan (see text) across two forsterite crystals (regions labeled 1, 5) and three distinct plagioclase and mesostasis glass phases (2, 3, 4). (e) Literature IR absorption spectra from forsterite, various plagioclase feldspars, and amorphous silica. Oligoclase and anorthite spectra are from powdered samples [56] silica from a thin film [57], and all others from bulk (crystalline) samples [56]. (f) Region-averaged IR extinction spectra extracted from nanoFTIR linescan positions indicated in Fig. 4.6a (numbered by region). Extracted forsterite spectra agree well with reported absorption spectra [56], whereas plagioclase regions exhibit albite (Ab)-rich, anorthite (An)-rich, and glassy signatures according to their phonon absorption frequencies. Sharp anorthite and oligoclase nanoFTIR peaks imply crystalline material, whereas reported spectra for powders (e) display added broadening [59, 61]. The surprisingly broad albite peak resolved by nanoFTIR is consistent with strong Al-Si disorder [58].

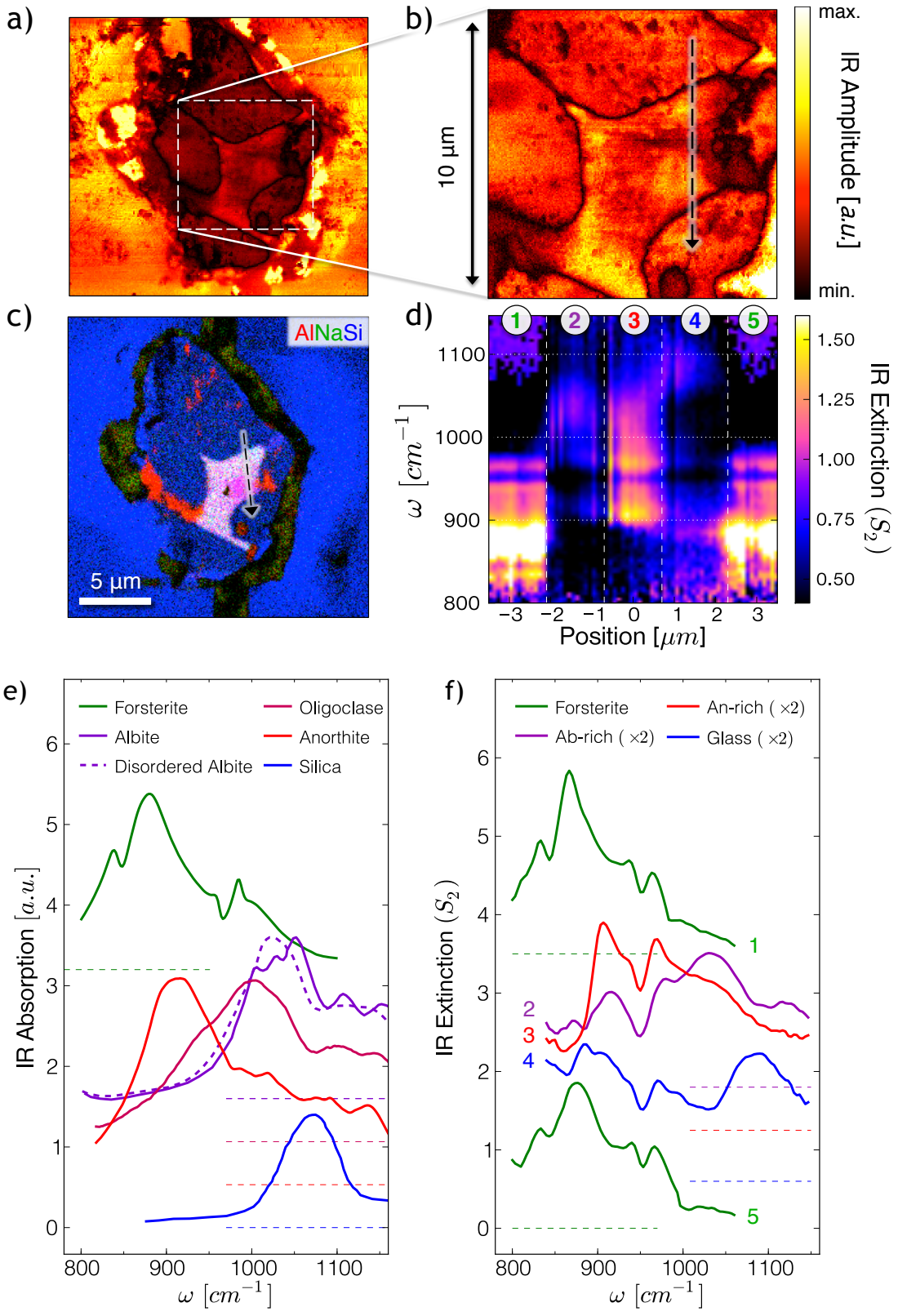
a)
b)
10 µm
max.
IR Amplitude [a.u.]
min.
c)
AlNaSi
5 µm
d)
1
2
3
4
5
1100
1000
900
800
ω [cm⁻¹]
−3 −2 −1 0 1 2 3
Position [µm]
1.50
1.25
1.00
0.75
0.50
IR Extinction (S2)
e)
Forsterite
Albite
Disordered Albite
Oligoclase
Anorthite
Silica
IR Absorption [a.u.]
0 1 2 3 4 5 6
800 900 1000 1100
ω [cm⁻¹]
f)
Forsterite
Ab-rich (×2)
An-rich (×2)
Glass (×2)
IR Extinction (S2)
0 1 2 3 4 5 6
1
2
3
4
5
800 900 1000 1100
ω [cm⁻¹]

4.9 Appendix A: Broadband Infrared Source and NanoFTIR Implementation

We achieved broadband illumination of our samples by using a broadband mid-infrared coherent source (mod. BB from lasnix.com), combining two near-infrared (NIR) laser beams in a GaSe crystal for difference-frequency generation of coherent mid-infrared (MIR) radiation (100 fs pulses, 300 cm^{-1} bandwidth, tunable across 600-2500 cm^{-1}, ~3 mW/cm^{-1}). This beam is coupled to an asymmetric Michelson interferometer, allowing measurement of the amplitude and phase of the back-scattered radiation with 3 cm^{-1} spectral resolution using a broadband mid-infrared coherent source (mod. BB from lasnix.com), [30 68]. This nanoFTIR implementation is depicted schematically in Fig. 4.2.

Because the scattered signal is a strong function of the distance between the near-field probe and the sample surface, we make use of the AFM probe's tapping capability (tapping-mode at a frequency $W \approx 250$ kHz) to modulate the scattered signal and enable distinction from background scattering. The near-exponential dependence of the near-field interaction on the tip-sample distance d implies that scattered field components modulated at harmonics nW, with $n \geq 2$, are directly attributable to near-field polarization of the tip. Sub-diffractional contrasts in the scattered field at these harmonics therefore correspond with variations in the local chemical composition of the sample [41]. NanoFTIR data presented in this work were acquired by lock-in detection of the scattered signal at the second harmonic (2W) of the probe's tapping frequency, resulting in second harmonic amplitude S_2 and phase ϕ_2 signals, whereas imaging data utilize the third harmonic. Finally, quantitative spectral information was obtained by normalizing the frequency-dependent second harmonic signals acquired from sample regions to those spectra acquired from a reference material using the same near-field probe. A silicon wafer with a 100 nm surface layer of evaporated gold (Au) was used for normalization.

4.10 Appendix B: Extraction of Dielectric Properties from NanoFTIR Spectra

The lightning rod model of probe-sample near-field interaction realistically relates the experimental measurables of s-SNOM to the sample's dielectric properties near the probe apex. While this sophisticated model does not yield a closed-form relation, it can still be applied in the inverse sense to extract the self-consistent surface reflection coefficients $\beta(\omega) \approx \frac{\varepsilon-1}{\varepsilon+1}$ from sub-50 nm-resolved nanoFTIR spectra[40], provided that sample material is bulk-like (>100 nm in thickness), the spectra are referenced to a known sample material such as gold, and that the probe geometry approximates a metal cone with rounded tip apex. The inversions performed in this work assume a tip radius of 40 nm (the sharpest feature size resolvable by concurrent AFM), a cone half-angle of $20°$, and probe tapping amplitude of 60 nm, consistent with probe specifications (Arrow™ NCPt from *NanoWorld*) and measurement parameters. The "effective" (indicated by brackets) dielectric constant $\langle\varepsilon(\omega)\rangle$ and extinction coefficient $\langle\kappa(\omega)\rangle$ of the material are then given by [31]

$$\langle\varepsilon\rangle = \frac{1-\beta}{1+\beta} \qquad \text{and} \qquad \langle\kappa\rangle = Im\left[\sqrt{\varepsilon}\right] = \sqrt{\frac{\sqrt{\langle\varepsilon_1\rangle^2+\langle\varepsilon_2\rangle^2}-\langle\varepsilon_1\rangle}{2}}\,.$$

In the case of optically uni- or biaxial crystals, the dielectric properties thus extracted are effective in the sense that they convey optical activity only along crystal axes probed by the incident electric field. However, because near-fields from the probe in the vicinity of the sample are predominantly surface-normal polarized, crystal axes are probed to varying degree, resulting in near-field spectra that reveal all infrared-active vibrational modes possessing a dipole moment perpendicular to the surface [69]. This raises the possibility that "missing" extinction peaks in $\langle\kappa(\omega)\rangle$ could potentially hinder direct comparison to conventional absorption spectra, although this difficulty was not encountered throughout this study.

4.11 Appendix C: Sample Preparation – Murchison: A primitive CM2 meteorite

We prepared a freshly exposed sample of the Murchison meteorite by cleaving an approximately 5 mm-sized chunk from a much larger piece of Murchison. This fresh chunk was placed at the bottom of a cylindrical mold and embedded in resin (Epo-Fix, Electron Microscopy Sciences). After curing for 24 hours, the epoxy cylinder with the Murchison sample was polished using an optical polisher until a region of the sample was exposed. A qualitative determination of optical flatness was achieved by polishing with poly-diamond abrasives, with the final sub-micron polish step performed by hand on a velvet cloth. The sample's flatness was confirmed by briefly imaging in a Tescan Vega 3 scanning electron microscope (SEM) and through atomic force microscopy (AFM) in the s-SNOM apparatus.

4.12 Appendix D: Sample Preparation – Iris: Cometary Dust Grain from Comet Wild 2

Samples of cometary dust grains from Comet 81P/Wild 2 (Wild 2), captured in a nano-porous silica aerogel by the Stardust Mission (1), were extracted and prepared for laboratory analysis using standard techniques [,70]. A notable Stardust particle named Iris, (from track C2052,12,74) has been analyzed with a variety of techniques including Scanning Transmission X-ray Microscopy (STXM) and transmission electron microscopy (TEM) [,35]. Using the nanoFTIR setup that described previously, we present the first sub-micron IR spectral maps of a cometary sample.

4.13 Appendix E: TEM analysis

Murchison linescan 3 (figure 3d, 5) was verified by (scanning) transmission electron microscopy (S/TEM). After nanoFTIR measurements, a lamella was removed from the meteorite using focused ion beam (FIB) milling and examined by TEM at the National Center for Electron Microscopy. The lamella exactly traced the nanoFTIR path so that the IR spectrum at each point might be directly compared to TEM imaging, diffraction and EDS composition. Diffraction and

imaging in brightfield and darkfield were carried out using a Zeiss Libra 200 MC at 200 keV with an in-column Omega energy filter. With the energy filter, ΔE was approximately 10 eV centered around the zero-loss peak. STEM/EDS was carried out using a Phillips CM200 with an Oxford Inca Si(Li) energy dispersive detector.

4.14 References

1. Brownlee, D., Tsou, P., Aléon, J., Alexander, C. M. O., D, Araki, T., Bajt, S., Baratta, G. A., Bastien, R., Bland, P., Bleuet, P., Borg, J., Bradley, J. P., Brearley, A., Brenker, F., Brennan, S., Bridges, J. C., Browning, N. D., Brucato, J. R., Bullock, E., Burchell, M. J., Busemann, H., Butterworth, A., Chaussidon, M., Cheuvront, A., Chi, M., Cintala, M. J., Clark, B. C., Clemett, S. J., Cody, G., Colangeli, L., Cooper, G., Cordier, P., Daghlian, C., Dai, Z., Hendecourt, L., Djouadi, Z., Dominguez, G., Duxbury, T., Dworkin, J. P., Ebel, D. S., Economou, T. E., Fakra, S., Fairey, S. A. J., Fallon, S., Ferrini, G., Ferroir, T., Fleckenstein, H., Floss, C., Flynn, G., Franchi, I. A., Fries, M., Gainsforth, Z., Gallien, J. P., Genge, M., Gilles, M. K., Gillet, P., Gilmour, J., Glavin, D. P., Gounelle, M., Grady, M. M., Graham, G. A., Grant, P. G., Green, S. F., Grossemy, F., Grossman, L., Grossman, J. N., Guan, Y., Hagiya, K., Harvey, R., Heck, P., Herzog, G. F., Hoppe, P., Hörz, F., Huth, J., Hutcheon, I. D., Ignatyev, K., Ishii, H., Ito, M., Jacob, D., Jacobsen, C., Jacobsen, S., Jones, S., Joswiak, D., Jurewicz, A., Kearsley, A. T., Keller, L. P., Khodja, H., Kilcoyne, A. L. D., Kissel, J., Krot, A., Langenhorst, F., Lanzirotti, A., Le, L., Leshin, L. A., Leitner, J., Lemelle, L., Leroux, H., Liu, M.-C., Luening, K., Lyon, I., MacPherson, G., Marcus, M. A., Marhas, K., Marty, B., Matrajt, G., McKeegan, K., Meibom, A., Mennella, V., Messenger, K., Messenger, S., Mikouchi, T., Mostefaoui, S., Nakamura, T., Nakano, T., Newville, M., Nittler, L. R., Ohnishi, I., Ohsumi, K., Okudaira, K., Papanastassiou, D. A., Palma, R., Palumbo, M. E., Pepin, R. O., Perkins, D., Perronnet, M., Pianetta, P., Rao, W., Rietmeijer, F. J. M., Robert, F., Rost, D., Rotundi, A., Ryan, R., Sandford, S. A., Schwandt, C. S., See, T. H., Schlutter, D., Sheffield-Parker, J., Simionovici, A., Simon, S., Sitnitsky, I., Snead, C. J., Spencer, M. K., Stadermann, F. J., Steele, A., Stephan, T., Stroud, R., Susini, J., Sutton, S. R., Suzuki, Y., Taheri, M., Taylor, S., Teslich, N., Tomeoka, K., Tomioka, N., Toppani, A., Trigo-Rodríguez, J. M., Troadec, D., Tsuchiyama, A., Tuzzolino, A. J., Tyliszczak, T., Uesugi, K., Velbel, M., Vellenga, J., Vicenzi, E., Vincze, L., Warren, J., Weber, I., Weisberg, M., Westphal, A. J., Wirick, S., Wooden, D., Wopenka, B., Wozniakiewicz, P., Wright, I., Yabuta, H., Yano, H., Young, E. D., Zare, R. N., Zega, T., Ziegler, K., Zimmerman, L., Zinner, E. & Zolensky, M. Comet 81P/Wild 2 Under a Microscope. *Science* **314**, 1711 (2006).

2. Sandford, S. A., Aléon, J., Alexander, C. M. O., D, Araki, T., Bajt, S. a., Baratta, G. A., Borg, J., Bradley, J. P., Brownlee, D. E., Brucato, J. R., Burchell, M. J., Busemann, H., Butterworth, A., Clemett, S. J., Cody, G., Colangeli, L., Cooper, G., Hendecourt, L., Djouadi, Z., Dworkin, J. P., Ferrini, G., Fleckenstein, H., Flynn, G. J., Franchi, I. A., Fries, M., Gilles, M. K., Glavin, D. P., Gounelle, M., Grossemy, F., Jacobsen, C., Keller, L. P., Kilcoyne, A. L. D., Leitner, J., Matrajt, G., Meibom, A., Mennella, V., Mostefaoui, S., Nittler, L. R., Palumbo, M. E., Papanastassiou, D. A., Robert, F., Rotundi, A., Snead, C. J., Spencer, M. K., Stadermann, F. J., Steele, A., Stephan, T., Tsou, P., Tyliszczak, T., Westphal, A. J., Wirick, S., Wopenka, B., Yabuta, H., Zare, R. N. & Zolensky, M. E. Organics Captured from Comet 81P/Wild 2 by the Stardust Spacecraft. *Science* **314**, 1720 (2006).

3. McKeegan, K. D., Aléon, J., Bradley, J., Brownlee, D., Busemann, H., Butterworth, A., Chaussidon, M., Fallon, S., Floss, C., Gilmour, J., Gounelle, M., Graham, G., Guan, Y., Heck, P. R., Hoppe, P., Hutcheon, I. D., Huth, J., Ishii, H., Ito, M., Jacobsen, S. B., Kearsley, A., Leshin, L. A., Liu, M.-C., Lyon, I., Marhas, K., Marty, B., Matrajt, G., Meibom, A., Messenger, S., Mostefaoui, S., Mukhopadhyay, S., Nakamura-Messenger, K., Nittler, L., Palma, R., Pepin, R. O., Papanastassiou, D. A., Robert, F., Schlutter, D., Snead, C. J., Stadermann, F. J., Stroud, R., Tsou, P., Westphal, A., Young, E. D., Ziegler,

K., Zimmermann, L. & Zinner, E. Isotopic Compositions of Cometary Matter Returned by Stardust. *Science* **314**, 1724 (2006).

4. Keller, L. P., Bajt, S. a., Baratta, G. A., Borg, J., Bradley, J. P., Brownlee, D. E., Busemann, H., Brucato, J. R., Burchell, M., Colangeli, L., Hendecourt, L., Djouadi, Z., Ferrini, G., Flynn, G., Franchi, I. A., Fries, M., Grady, M. M., Graham, G. A., Grossemy, F., Kearsley, A., Matrajt, G., Nakamura-Messenger, K., Mennella, V., Nittler, L., Palumbo, M. E., Stadermann, F. J., Tsou, P., Rotundi, A., Sandford, S. A., Snead, C., Steele, A., Wooden, D. & Zolensky, M. Infrared Spectroscopy of Comet 81P/Wild 2 Samples Returned by Stardust. *Science* **314**, 1728 (2006).

5. Flynn, G. J., Bleuet, P., Borg, J., Bradley, J. P., Brenker, F. E., Brennan, S., Bridges, J., Brownlee, D. E., Bullock, E. S., Burghammer, M., Clark, B. C., Dai, Z. R., Daghlian, C. P., Djouadi, Z., Fakra, S., Ferroir, T., Floss, C., Franchi, I. A., Gainsforth, Z., Gallien, J.-P., Gillet, P., Grant, P. G., Graham, G. A., Green, S. F., Grossemy, F., Heck, P. R., Herzog, G. F., Hoppe, P., Hörz, F., Huth, J., Ignatyev, K., Ishii, H. A., Janssens, K., Joswiak, D., Kearsley, A. T., Khodja, H., Lanzirotti, A., Leitner, J., Lemelle, L., Leroux, H., Luening, K., MacPherson, G. J., Marhas, K. K., Marcus, M. A., Matrajt, G., Nakamura, T., Nakamura-Messenger, K., Nakano, T., Newville, M., Papanastassiou, D. A., Pianetta, P., Rao, W., Riekel, C., Rietmeijer, F. J. M., Rost, D., Schwandt, C. S., See, T. H., Sheffield-Parker, J., Simionovici, A., Sitnitsky, I., Snead, C. J., Stadermann, F. J., Stephan, T., Stroud, R. M., Susini, J., Suzuki, Y., Sutton, S. R., Taylor, S., Teslich, N., Troadec, D., Tsou, P., Tsuchiyama, A., Uesugi, K., Vekemans, B., Vicenzi, E. P., Vincze, L., Westphal, A. J., Wozniakiewicz, P., Zinner, E. & Zolensky, M. E. Elemental Compositions of Comet 81P/Wild 2 Samples Collected by Stardust. *Science* **314**, 1731 (2006).

6. Zolensky, M. E., Zega, T. J., Yano, H., Wirick, S., Westphal, A. J., Weisberg, M. K., Weber, I., Warren, J. L., Velbel, M. A., Tsuchiyama, A., Tsou, P., Toppani, A., Tomioka, N., Tomeoka, K., Teslich, N., Taheri, M., Susini, J., Stroud, R., Stephan, T., Stadermann, F. J., Snead, C. J., Simon, S. B., Simionovici, A., See, T. H., Robert, F., Rietmeijer, F. J. M., Rao, W., Perronnet, M. C., Papanastassiou, D. A., Okudaira, K., Ohsumi, K., Ohnishi, I., Nakamura-Messenger, K., Nakamura, T., Mostefaoui, S., Mikouchi, T., Meibom, A., Matrajt, G., Marcus, M. A., Leroux, H., Lemelle, L., Le, L., Lanzirotti, A., Langenhorst, F., Krot, A. N., Keller, L. P., Kearsley, A. T., Joswiak, D., Jacob, D., Ishii, H., Harvey, R., Hagiya, K., Grossman, L., Grossman, J. N., Graham, G. A., Gounelle, M., Gillet, P., Genge, M. J., Flynn, G., Ferroir, T., Fallon, S., Ebel, D. S., Dai, Z. R., Cordier, P., Clark, B., Chi, M., Butterworth, A. L., Brownlee, D. E., Bridges, J. C., Brennan, S., Brearley, A., Bradley, J. P., Bleuet, P., Bland, P. A. & Bastien, R. Mineralogy and Petrology of Comet 81P/Wild 2 Nucleus Samples. *Science* **314**, 1735 (2006).

7. Maras, A., Macrì, M., Ballirano, P., Calvani, P., Lupi, S., Maselli, P. In Situ Synchrotron Infrared Reflectance Study of Olivine Microcrystals in Meteorite Matrices. *Meteoritics and Planetary Science Supplement* **36**, 121 (2001).

8. Cooney TF, Scott ERD, Krot AN, Sharma SK, Yamaguchi A. Vibrational spectroscopic study of minerals in the Martian meteorite ALH84001. *American Mineralogist* **84**, 1569-1576 (1999).

9. Keller, L. P.; Bradley, J. P.; Bouwman, J.; Molster, F. J.; Waters, L. B. F. M.; Henning, G. J. Flynn T.; Mutschke, H. Sulfides in Interplanetary Dust Particles: A Possible Match to the 23 μm Feature Detected by the Infrared Space Observatory. In: *Lunar and Planetary Institute Science Conference Abstracts* (eds) (2000).

10. Raynal, P. I.; Quirico, E.; Borg, J.; Deboffle, D.; Dumas, P.; d'Hendecourt, L.; Bibring, J.-P.; Langevin, Y. Synchrotron infrared microscopy of micron-sized extraterrestrial grains. *Planetary and Space Science* **48**, 1329-1339 (2000).

11. Keller LP*,* Hony S, Bradley JP, Molster FJ, Waters LBFM, Bouwman J, de Koter A, Brownlee DE, Flynn GJ, Henning T, & Mutschke H*.* Identification of iron sulphide grains in protoplanetary disks. *Nature* **417**, 148-150 (2002).

12. Flynn GJ, Keller LP, Jacobsen C, Wirick S, Stootman F. The Origin of Organic Matter in the Solar System: Evidence from the Interplanetary Dust Particles. In: *Bioastronomy 2002: Life Among the Stars* (ed^(eds Norris R) (2004).

13. Flynn GJ, Keller LP, Jacobsen C, Wirick S. An assessment of the amount and types of organic matter contributed to the Earth by interplanetary dust. *Advances in Space Research* **33**, 57-66 (2004).

14. Keller LP, Messenger S, Flynn GJ, Clemett S, Wirick S, Jacobsen C. The nature of molecular cloud material in interplanetary dust. *Geochimica et Cosmochimica Acta* **68**, 2577-2589 (2004).

15. Morlok A, Jones GC, Grady MM, Stansbery E. FT-IR Micro-spectroscopy of Fine-grained Planetary Materials: Further Results. In: *Lunar and Planetary Institute Science Conference Abstracts* (ed^(eds Mackwell S) (2004).

16. G. Matrajt, J. Borg, P. I. Raynal, Z. Djouadi, L. d'Hendecourt, G. Flynn and D. Deboffle*.* FTIR and Raman analyses of the Tagish Lake meteorite: Relationship with the aliphatic hydrocarbons observed in the Diffuse Interstellar Medium. *Astronomy and Astrophysics* **416**, 983-990 (2004).

17. Matrajt G, Muñoz Caro GM, Dartois E, D'Hendecourt L, Deboffle D, Borg J. FTIR analysis of the organics in IDPs: Comparison with the IR spectra of the diffuse interstellar medium. *Astronomy and Astrophysics* **433**, 979-995 (2005).

18. Knoll B, Keilmann F. Near-field probing of vibrational absorption for chemical microscopy. *Nature* **399**, 134-137 (1999).

19. Yang HU, Hebestreit E, Josberger EE, Raschke MB. A cryogenic scattering-type scanning near-field optical microscope. *Review of Scientific Instruments* **84**, - (2013).

20. Zhe Fei, Gregory O. Andreev, Wenzhong Bao, Lingfeng M. Zhang, Alexander S. McLeod, Chen Wang, Margaret K. Stewart, Zeng Zhao, Gerardo Dominguez, Mark Thiemens, Michael M. Fogler, Michael J. Tauber, Antonio H. Castro-Neto, Chun Ning Lau, Fritz Keilmann, and Dimitri N. Basov. Infrared Nanoscopy of Dirac Plasmons at the Graphene–SiO_2 Interface. *Nano Lett* **11**, 4701-4705 (2011).

21. L. M. Zhang, G. O. Andreev, Z. Fei, A. S. McLeod, G. Dominguez, M. Thiemens, A. H. Castro-Neto, D. N. Basov, and M. M. Fogler*.* Near-field spectroscopy of silicon dioxide thin films. *Phys Rev B*, 075419 (2011).

22. Z. Fei, A. S. Rodin, G. O. Andreev, W. Bao, A. S. McLeod, M. Wagner, L. M. Zhang, Z. Zhao, M. Thiemens, G. Dominguez, M. M. Fogler, A. H. Castro Neto, C. N. Lau, F. Keilmann & D. N. Basov*.* Gate-tuning of graphene plasmons revealed by infrared nano-imaging. *Nature*, 1-13 (2012).

23. M. M. Qazilbash, M. Brehm, Byung-Gyu Chae, P.-C. Ho, G. O. Andreev, Bong-Jun Kim, Sun Jin Yun, A. V. Balatsky, M. B. Maple, F. Keilmann, Hyun-Tak Kim, D. N. Basov. Mott Transition in VO2 Revealed by Infrared Spectroscopy and Nano-Imaging. *Science* **318**, 1750-1753 (2007).

24. Jones AC, Berweger S, Wei J, Cobden D, Raschke MB. Nano-optical Investigations of the Metal-Insulator Phase Behavior of Individual VO2 Microcrystals. *Nano Lett* **10**, 1574-1581 (2010).

25. Atkin JM, Berweger S, Jones AC, Raschke MB. Nano-optical imaging and spectroscopy of order, phases, and domains in complex solids. *Advances in Physics* **61**, 745-842 (2012).

26. Jianing Chen, Michela Badioli, Pablo Alonso-González, Sukosin Thongrattanasiri, Florian Huth, Johann Osmond, Marko Spasenović, Alba Centeno, Amaia Pesquera, Philippe Godignon, Amaia Zurutuza Elorza, Nicolas Camara, F. Javier García de Abajo, Rainer Hillenbrand & Frank H. L. Koppens. Optical nano-imaging of gate-tunable graphene plasmons. *Nature* **487**, 77-81 (2012).

27. Zhang, L. M., Andreev, G. O., Fei, Z., McLeod, A. S., Dominguez, G., Thiemens, M., Castro-Neto, A. H., Basov, D. N. & Fogler, M. M. Near-field spectroscopy of silicon dioxide thin films. *Physical Review B* **85**, 075419 (2012).

28. Amarie S, Ganz T, Keilmann F. Mid-infrared near-field spectroscopy. *Opt Express* **17**, 21794-21801 (2009).

29. Huth F, Govyadinov A, Amarie S, Nuansing W, Keilmann F, Hillenbrand R. Nano-FTIR Absorption Spectroscopy of Molecular Fingerprints at 20 nm Spatial Resolution. *Nano Lett* **12**, 3973-3978 (2012).

30. Amarie S, Keilmann F. Broadband-infrared assessment of phonon resonance in scattering-type near-field microscopy. *Phys Rev B* **83**, 045404 (2011).

31. Govyadinov AA, Amenabar I, Huth F, Carney PS, Hillenbrand R. Quantitative Measurement of Local Infrared Absorption and Dielectric Function with Tip-Enhanced Near-Field Microscopy. *The Journal of Physical Chemistry Letters* **4**, 1526-1531 (2013).

32. Amarie S, Zaslansky P, Kajihara Y, Griesshaber E, Schmahl WW, Keilmann F. Nano-FTIR chemical mapping of minerals in biological materials. *Beilstein J Nanotechnol* **3**, 312-323 (2012).

33. S. Dai, Z. Fei, Q. Ma, A. S. Rodin, M. Wagner, A. S. McLeod, M. K. Liu, W. Gannett, W. Regan, K. Watanabe, T. Taniguchi, M. Thiemens, G. Dominguez, A. H. Castro Neto, A. Zettl, F. Keilmann1, P. Jarillo-Herrero, M. M. Fogler, D. N. Basov. Tunable Phonon Polaritons in Atomically Thin van der Waals Crystals of Boron Nitride. *Science* **343**, 1125-1129 (2014).

34. Kebukawa Y, Nakashima S, Ishikawa M, Aizawa K, Inoue T, Nakamura-Messenger K, & Zolensky ME. Spatial distribution of organic matter in the Bells CM2 chondrite using near-field infrared microspectroscopy. *Meteoritics & Planetary Science* **45**, 394-405 (2010).

35. R. C. Ogliore, G. R. Huss, K. Nagashima, A. L. Butterworth, Z. Gainsforth, J. Stodolna, A. J. Westphal, D. Joswiak, T. Tyliszczak. Incorporation of a late-forming chondrule into Comet Wild 2. *The Astrophysical Journal Letters* **745**, L19 (2012).

36. Gainsforth Z, Butterworth AL, Stodolna J, Westphal AJ, Huss GR, Nagashima K, Ogliore R, Brownlee DE, Joswiak D, & Tyliszczak T. Constraints on the formation environment of two chondrule-like igneous particles from Comet 81P/Wild 2. *Meteoritics & Planetary science (in prep)*, (2013).

37. Tomoki Nakamura, Takaaki Noguchi, Akira Tsuchiyama, Takayuki Ushikubo, Noriko T. Kita, John W. Valley, Michael E. Zolensky, Yuki Kakazu, Kanako Sakamoto, Etsuko Mashio, Kentaro Uesugi, Tsukasa Nakano. Chondrulelike Objects in Short-Period Comet 81P/Wild 2. *Science* **321**, 1664-1667 (2008).

38. Keilmann F, Hillenbrand R. Near-field nanoscopy by elastic light scattering from a tip In: *Nano-Optics and Near-Field Optical Microscopy* (eds Zayats A, Richards D). Artech House (2009).

39. Keilmann F, Hillenbrand R. Near-field microscopy by elastic light scattering from a tip. *Philosophical Transactions of the Royal Society of London Series A: Mathematical, Physical and Engineering Sciences* **362**, 787-805 (2004).

40. Alexander S. McLeod, P. Kelly, M. D. Goldflam, Z. Gainsforth, A. J. Westphal, Gerardo Dominguez, Mark H. Thiemens, Michael M. Fogler, & D. N. Basov. Model for quantitative near-field spectroscopy and the extraction of nanoscale-resolved optical constants. *Phys Rev B*, **90**, 085136 (2014).

41. Hillenbrand R, Taubner T, Keilmann F. Phonon-enhanced light-matter interaction at the nanometre scale. *Nature* **418**, 159-162 (2002).

42. Ocelic N, Huber A, Hillenbrand R. Pseudoheterodyne detection for background-free near-field spectroscopy. *Applied Physics Letters* **89**, - (2006).

43. Glotch TD, Rossman GR. Mid-infrared reflectance spectra and optical constants of six iron oxide/oxyhydroxide phases. *Icarus* **204**, 663-671 (2009).

44. P. Alonso-González, P. Albella, F. Neubrech, C. Huck, J. Chen, F. Golmar, F. Casanova, L. E. Hueso, A. Pucci, J. Aizpurua, & R. Hillenbrand. Experimental Verification of the Spectral Shift between Near- and Far-Field Peak Intensities of Plasmonic Infrared Nanoantennas. *Physical Review Letters* **110**, 203902 (2013).

45. Prior D, Mariani E, Wheeler J. EBSD in the Earth Sciences: Applications, Common Practice, and Challenges. In: *Electron Backscatter Diffraction in Materials Science* (eds Schwartz AJ, Kumar M, Adams BL, Field DP). Springer US (2009).

46. Holman HYN, Martin MC, McKinney WR. Synchrotron-based FTIR spectromicroscopy: Cytotoxicity and heating considerations. *J Biol Phys* **29**, 275-286 (2003).

47. Stiegler JM, Tena-Zaera R, Idigoras O, Chuvilin A, Hillenbrand R. Correlative infrared–electron nanoscopy reveals the local structure–conductivity relationship in zinc oxide nanowires. *Nat Commun* **3**, 1131 (2012).

48. Demichelis R, Suto H, Noel Y, Sogawa H, Naoi T, Koike C, Chihara H, Shimobayashi N, Ferrabone M, & Dovesi R. The infrared spectrum of ortho-enstatite from reflectance experiments and first-principle simulations. *Monthly Notices of the Royal Astronomical Society* **420**, 147-154 (2012).

49. Chihara H, Koike C, Tsuchiyama A, Tachibana S, Sakamoto D. Compositional dependence of infrared absorption spectra of crystalline silicates. I. Mg-Fe pyroxenes. *Astronomy and Astrophysics* **391**, 267-273 (2002).

50. Dowty E, Clark JR. Crystal structure refinement and optical properties of a Ti^{3+} fassaite from the Allende meteorite. *American Mineralogist* **58**, 230-242 (1973).

51. Simon SB, Grossman L. A comparative study of melilite and fassaite in Types B1 and B2 refractory inclusions. *Geochimica et Cosmochimica Acta* **70**, 780-798 (2006).

52. Koike, C., Tsuchiyama, A., Shibai, H., Suto, H., Tanabé, T., Chihara, H. Absorption spectra of Mg-rich Mg-Fe and Ca pyroxenes in the mid- and far-infrared regions. *Astronomy and Astrophysics* **363**, 1115-1122 (2000).

53. Morimoto N, Fabries J, Ferguson AK, Ginzburg IV, Ross M, Seifert FA, Zussman J, Aoki K, & Gottardi G. Nomenclature of pyroxenes. *American Mineralogist* **73**, 1123-1133 (1988).

54. Leroux H. Microstructural shock signatures of major minerals in meteorites. *European Journal of Mineralogy* **13**, 253-272 (2001).

55. R. C. Ogliore, G. R. Huss, K. Nagashima, A. L. Butterworth, Z. Gainsforth, J. Stodolna, A. J. Westphal, D. Joswiak, T. Tyliszczak. Incorporation of a late-forming chondrule into Comet Wild 2. *The Astrophysical Journal Letters* **745**, L19 (2012).

56. Downs RT. The RRUFF Project: an integrated study of the chemistry, crystallography, Raman and infrared spectroscopy of minerals. In: *Program and Astracts of the 19th General Meeting of the International Mineralogical Association* (ed^(eds) (2006).

57. Nakamura M, Kanzawa R, Sakai K. Stress and Density Effects on Infrared Absorption Spectra of Silicate Glass Films. *Journal of The Electrochemical Society* **133**, 1167-1171 (1986).

58. Ming Zhang, E. K. H. Salje, M. A. Carpenter, I. Parsons, H. Kroll, S. J. B. Reed, & Ann Graeme-Barber. Exsolution and Al-Si disorder in alkali feldspars; their analysis by infrared spectroscopy. *American Mineralogist* **82**, 849-857 (1997).

59. Balan E, Delattre S, Roche D, Segalen L, Morin G, Guillaumet, M, Blanchard M, Lazzeri M, Brouder C, & Salje EKH. Line-broadening effects in the powder infrared spectrum of apatite. *Phys Chem Minerals* **38**, 111-122 (2011).

60. Ruppin R, Englman R. Optical phonons of small crystals. *Reports on Progress in Physics* **33**, 149 (1970).

61. Genzel L, Martin TP. Infrared absorption by surface phonons and surface plasmons in small crystals. *Surface Science* **34**, 33-49 (1973).

62. Day DE, Rindone GE. Properties of Soda Aluminosilicate Glasses: I, Refractive Index, Density, Molar Refractivity, and Infrared Absorption Spectra. *Journal of the American Ceramic Society* **45**, 489-496 (1962).

63. Roy BN. Infrared Spectroscopy of Lead and Alkaline-Earth Aluminosilicate Glasses. *Journal of the American Ceramic Society* **73**, 846-855 (1990).

64. Fernandez JA, Jockers K. Nature and origin of comets. *Reports on Progress in Physics* **46**, 665 (1983).

65. Brownlee, D., Tsou, P., Aléon, J., Alexander, C. M. O., D, Araki, T., Bajt, S., Baratta, G. A., Bastien, R., Bland, P., Bleuet, P., Borg, J., Bradley, J. P., Brearley, A., Brenker, F., Brennan, S., Bridges, J. C., Browning, N. D., Brucato, J. R., Bullock, E., Burchell, M. J., Busemann, H., Butterworth, A., Chaussidon, M., Cheuvront, A., Chi, M., Cintala, M. J., Clark, B. C., Clemett, S. J., Cody, G., Colangeli, L., Cooper, G., Cordier, P., Daghlian, C., Dai, Z., Hendecourt, L., Djouadi, Z., Dominguez, G., Duxbury, T., Dworkin, J. P., Ebel, D. S., Economou, T. E., Fakra, S., Fairey, S. A. J., Fallon, S., Ferrini, G., Ferroir, T., Fleckenstein, H., Floss, C., Flynn, G., Franchi, I. A., Fries, M., Gainsforth, Z., Gallien, J. P., Genge, M., Gilles, M. K., Gillet, P., Gilmour, J., Glavin, D. P., Gounelle, M., Grady, M. M., Graham, G. A., Grant, P. G., Green, S. F., Grossemy, F., Grossman, L., Grossman, J. N., Guan, Y., Hagiya, K., Harvey, R., Heck, P., Herzog, G. F., Hoppe, P., Hörz, F., Huth, J., Hutcheon, I. D., Ignatyev, K., Ishii, H., Ito, M., Jacob, D., Jacobsen, C., Jacobsen, S., Jones, S., Joswiak, D., Jurewicz, A., Kearsley, A. T., Keller, L. P., Khodja, H., Kilcoyne, A. L. D., Kissel, J., Krot, A., Langenhorst, F., Lanzirotti, A., Le, L., Leshin, L. A., Leitner, J., Lemelle, L., Leroux, H., Liu, M.-C., Luening, K., Lyon, I., MacPherson, G., Marcus, M. A., Marhas, K., Marty, B., Matrajt, G., McKeegan, K., Meibom, A., Mennella, V., Messenger, K., Messenger, S., Mikouchi, T., Mostefaoui, S., Nakamura, T., Nakano, T., Newville, M., Nittler, L. R., Ohnishi, I., Ohsumi, K., Okudaira, K., Papanastassiou, D. A., Palma, R., Palumbo, M. E., Pepin, R. O., Perkins, D., Perronnet, M., Pianetta, P., Rao, W., Rietmeijer, F. J. M., Robert, F., Rost, D., Rotundi, A., Ryan, R., Sandford, S. A., Schwandt, C. S., See, T. H., Schlutter, D., Sheffield-Parker, J., Simionovici, A., Simon, S., Sitnitsky, I., Snead, C. J., Spencer, M. K., Stadermann, F. J., Steele, A., Stephan, T., Stroud, R., Susini, J., Sutton, S. R., Suzuki, Y., Taheri, M., Taylor, S., Teslich, N., Tomeoka, K., Tomioka, N., Toppani, A., Trigo-Rodríguez, J. M., Troadec, D., Tsuchiyama, A., Tuzzolino, A. J., Tyliszczak, T., Uesugi, K., Velbel, M., Vellenga, J., Vicenzi, E., Vincze, L., Warren, J., Weber, I., Weisberg, M., Westphal, A. J., Wirick, S., Wooden, D., Wopenka, B., Wozniakiewicz, P., Wright, I., Yabuta, H., Yano, H., Young, E. D., Zare, R. N., Zega, T., Ziegler, K., Zimmerman, L., Zinner, E. & Zolensky, M. Comet 81P/Wild 2 Under a Microscope. *Science* **314**, 1711 (2006).

66. Nakamura, T., Noguchi, T., Tanaka, M., Zolensky, M. E., Kimura, M., Tsuchiyama, A., Nakato, A., Ogami, T., Ishida, H., Uesugi, M., Yada, T., Shirai, K., Fujimura, A., Okazaki, R., Sandford, S. A., Ishibashi, Y., Abe, M., Okada, T., Ueno, M., Mukai, T., Yoshikawa, M. & Kawaguchi, J. Itokawa Dust Particles: A Direct Link Between S-Type Asteroids and Ordinary Chondrites. *Science* **333**, 1113 (2011).

67. Rietmeijer FJM. Interplanetary dust particles. *Reviews in Mineralogy and Geochemistry* **36**, 2.1-2.95 (1998).

68. Keilmann F, Amarie S. Mid-infrared Frequency Comb Spanning an Octave Based on an Er Fiber Laser and Difference-Frequency Generation. *Journal of Infrared, Millimeter, and Terahertz Waves* **33**, 479-484 (2012).

69. Amenabar I, Poly S, Nuansing W, Hubrich EH, Govyadinov AA, Huth F, Krutokhvostov R, Zhang L, Knez M, Herberle J, Bittner AM, & Hillenbrand R. Structural analysis and mapping of individual protein complexes by infrared nanospectroscopy. *Nat Commun* **4**, (2013).

70. Andrew J. WESTPHAL, Christopher SNEAD, Anna BUTTERWORTH, Giles A. GRAHAM, John P. BRADLEY, Saöa BAJT, Patrick G. GRANT, Graham BENCH, Sean BRENNAN,

and Piero PIANETTA. Aerogel keystones: Extraction of complete hypervelocity impact events from aerogel collectors. *Meteoritics & Planetary Science* **39**, 1375-1386 (2004).

71. A. S. McLeod, G. Dominguez, Z. Gainsforth, P. Kelly, H. A. Bechtel, F. Keilmann, A. Wesphal, M. Thiemens, D. N. Basov. Supplementary online material to Nanoscale infrared spectroscopy as a non-destructive probe of extraterrestrial samples. *Nat. Commun.* 5, 5445 (2014).

CHAPTER 5: Deployment of infrared near-field optical microscopy at cryogenic temperatures

5.1 Abstract

The preceding chambers of this thesis work make clear the impressive capacity of scanning near-field optical microscopy (SNOM) to resolve the optical properties of materials at nanometer-scales, especially for deeply sub-diffractional chemical characterization. However, opportunities for applying this technique to study nano-scale electronic phenomena in correlated electron ("quantum") materials are equally profound, and admittedly even more intriguing to the condensed mattery physicist. Here in particular, the physics of phase transitions and the exotic ground states (e.g. high-temperature superconductivity) prevalent among correlated oxides remain substantially unresolved.[1,2] Although in this context the high spatial resolution and optical probe of SNOM proves to make a strong experimental contribution,[3] it is necessary to conduct most experiments on quantum materials at low temperatures (down to T = 4K, or -269 C, and even below) where their natural energy scales can remain unperturbed by thermal fluctuations. For the sake of such studies, including that presented in Chapter 6, a high performance cryogenic SNOM ("cryoSNOM") was designed and constructed, incorporating such features as variable sample temperature down to 20K, flexible scanning probe performance, vibration isolation, *in situ* exchange of samples and probes, and an ultra-clean vacuum environment. With its demonstrably high performance and high-throughput operation, this instrument is intended to serve as the model for future extensions of the SNOM technique to novel and "extreme" environments, as well as for ongoing studies of low-temperature physics at the nano-scale.

5.2 Essentials of cryogenic near-field microscopy: cryoSNOM Mark I

The essential features of a cryogenic scanning near-field optical microscope (or more colloquially, “cryoSNOM”) are laid out in Fig. 5.1, which presents the design of a first-generation microscope (so-called “Mark I”) whose development formed a crucial part of the present thesis work. Development of this microscope began under the purview of Dr. G. Andreev, a pioneer of cryogenic near-field microscopy and in whose thesis work more details of the microscope design and operation can be found.[4] Here, we instead defer a more detailed description of the design and operation of a cryoSNOM to the following sections, where we introduce of a next-generation cryoSNOM “Mark II”, whose development has become a centerpiece of the present thesis work.

Fig 5.1 outlines the technical demands of conducting near-field microscopy experiments in a cryogenic sample environment, as met by the cryoSNOM Mark I design. These demands closely parallel those already addressed in other contexts of cryogenic scanning probe microscopy (“cryoSPM”), including scanning tunneling microscopy (STM),[5,6] atomic force microscopy (AFM),[7,8] and magnetic force microscopy,[9] to name but a few. In these contexts, the cooling of a sample surface is routinely accomplished with a cryostat using liquid cryogen such as liquid helium, whose 4K boiling point determines, in principle, the minimum achievable sample temperature by conventional cooling. A continuous “flow” cryostat (*Janis Research ST400*) is used in the Mark I system to provide high cooling power at the expense of cryogen consumption (vaporization). In practice, conduction of heat away from the sample and to the cryostat (“cooling power”) is further limited by the thermally conducting element that brings the sample into thermal contact with the cryostat itself. For this purpose a flexible thermal link of copper foil (*Attocube GmbH*) strikes a suitable balance between high thermal conductance and limited vibrational conductance to the sample; we elaborate on this sensitive matter in Sec. 5.8.

The transition temperatures for attaining quantum phases in many correlated electron materials can this way be readily accessed,[1] and sample temperatures below 150K are routine in cryoSPM. Such temperatures however coincide with the sublimation points of atmospheric gases

(water vapor at 150K, nitrogen gas at 70K, etc.), which provide an inevitable and intolerable source of contamination for the sample surface that inhibit scanning probe measurements. Consequently, cryoSPM must be conducted in the ultra-clean environment of an ultra-high vacuum chamber. Indeed, even a simple model of adsorption will predict the formation of one monolayer of contaminant per hour upon a cold sample surface for every 10^{-9} mbar of ambient pressure. For this reason experiments with cryoSPM (among other surface-sensitive analysis techniques) are conducted in a vacuum environment of 10^{-9} mbar, 10^{-10} mbar (which enters the ultra-high vacuum, or "UHV", regime), or even lower pressure. To achieve and maintain such low pressures around the sample environment, the cryoSNOM Mark I was housed within a stainless steel vacuum chamber equipped with "conflat" (CF) flange fittings, which are sealed by leak-safe compressed copper gaskets. The combination of foreline mechanical pumps and a turbomolecular pump allow bringing the chamber base pressure from 1 bar down to the UHV range within a matter of days, in principle. A non-mechanical ion-getter pump ("ion pump") is included on the chamber to maintain this base pressure during experiments even while the mechanical pumps valved off from the chamber environment and powered down to mitigate vibrations, which can otherwise have a nefarious impact on any SPM experiment.

Besides the cryogenic and vacuum hardware, the heart of any SNOM is a capable integrated AFM. Critically, unlike SPMs in ambient conditions, their cryogenic counterparts must be constructed of vacuum-friendly components and materials free of outgassing. The AFM in cryoSNOM Mark I, as highlighted in Fig. 5.11B, comprises a stack of coarse-positioning piezoelectric actuators ("piezos", *Attocube GmbH*) articulated in X, Y, and Z space to allow macroscopic navigation of the sample surface below the probe, as well as an XYZ-articulated direct-drive piezo scanner for raster scanning and nano-positioning the sample during measurements. Since SNOM involves illuminating the probe with a stationary focus of radiation, it is crucial that such a microscope be sample-scanning rather than tip-scanning. Atop the sample piezos is mounted a thermal isolation stack, to isolate them from the (nominally) cold

sample and to mitigate the conductive heat load on the sample. Unlike in bath-cryostat based SPMs,[10,11] this scheme affords nimple temperature control at the sample location, since the sample stage alone is a minimal heat load on the cryostat. It also affords the scanner piezos their full range of range of motion even down to base sample temperature, since the piezos themselves remain close to room temperature and the high piezoelectric coefficient of PZT (lead zirconate titanate, a piezo ceramic of choice) thus remains uncompromised by low temperature. By cooling only the sample stage, cryogen consumption is minimized, and it is not uncommon with this approach to maintain a sample at low temperature (100K or below) for weeks at a time using, for example, a single 100 liter dewar of liquid helium. This of course requires a highly effective thermal isolator which can establish a thermal gradient of several hundred degrees K, as further discussed in Sec. 5.8.

The probe of the AFM is a commercially manufactured silicon cantilever and tip (batch-etched from a wafer), the latter possessing an apex radius in the range of 10 nanometers, affording near-field microscopy its high spatial resolution. Metal coating, often used to enhance conductivity of the near-field probe especially in the infrared range, contributes a slightly increased effective apex radius. Since the AFM is operating in non-contact (amplitude- or frequency-modulation) modes, the probe cantilever is dithered at its resonance frequency (tens or hundreds of kHz) at an amplitude of several tens of nanometers using an electrically excited dither piezo, to which the probe is mounted. This cantilevered probe is held in the AFM probe head, which also houses a cleaved optical fiber that is brought into close proximity to the cantilever to deliver light from a deflection laser, thus enabling a convenient “interferometric” AFM detection scheme[12] presented in Fig. 5.5b and elaborated in Sec. 5.7. Lastly, the AFM head encloses a pair of lenses that project a top-viewed image of the probe (and sample, if approached to the probe) to outside the vacuum chamber, where this image can me magnified and registered by a simple “navigation optics” visible light microscope, also elaborated in Sec. 5.7.

Four primary technical features bring the near-field optical functionality to such an otherwise commonplace cryoSPM setup. First, an external coherent light source provides radiation for the near-field optical experiment, and a continuous wave (CW) laser is typically employed for its intense monochromaticity; for infrared SNOM a CO_2 gas laser (~10 micron wavelength radiation) is a reliable choice. The laser beam is delivered into the vacuum chamber through an optically transparent window; a CF-mounted antireflection-coated ZnSe viewport (*MPF Products Inc.*) is a convenient choice in the mid-infrared energy range. Second, a focusing optic with high numerical aperture (> 0.3 is desired) is necessary for focusing this light to a precise wavelength-scale focus at the location of the near-field probe tip. This demands mounting the optic atop nano-resolved XYZ-actuated piezos. In cryoSNOM Mark I, a gold-coated off-axis parabolic mirror is employed for its high reflectivity, achromatic focus, and convenient geometry, and mounted atop piezos (*Attocube GmbH*) providing access of the optical focus to a 5x5x5 mm cubed volume. Third, the AFM is designed in a careful fashion to natively maintain the probe close to the center of this accessible focal volume, and to keep the space between the probe and focusing optic as unobstructed as possible, enabling collection of as much probe-scattered radiation as possible. The size of the sample stage and AFM head introduce practical limitations on the focal length of the focusing optic, which impacts its effective aperture and ability to collect this radiation. For this reason, it is clear that optimizations for the sake of SNOM performance are necessary already at the design stage of the underlying AFM. Fourth, detection probe-scattered radiation is accomplished outside the vacuum environment using interferometric techniques as outlined in Chapter 1.

While this accounting of necessary cryoSNOM features is reasonably complete, user experience with cryoSNOM Mark I from 2012-2013 served to make clear the practical need for a further enhanced feature set of the microscope to 1) enhance overall performance, 2) enhance the user experience, and 3) dramatically boost the throughput of measurements with the apparatus. These enhanced demands are discussed in the next section.

5.3 High-throughput cryogenic near-field microscopy: impediments and implementations

Here we briefly enumerate the shortcomings and conceptual solutions to the "bare" design of cryoSNOM Mark I. Subsequent sections of this chapter highlight specific improvements implemented in the high-performance cryoSNOM Mark II design.

- ***Isolation from vibrational noise:*** User experience quickly proves that the signal-to-noise performance of a SNOM is limited first and foremost by the AFM performance. To wit, the primary obstacle to maintaining stability of the probe-sample gap is the transmission of environmental and mechanical vibrations (including accoustic noise) into the microscope. Rigidity of the microscope housing and other hardwares ("mechanical loop") that physically connect the AFM probe to the sample holder forms the first line of defense in vibrational noise rejection, and supporting the microscope atop pneumatic isolators (or "optical table legs") confers a second. However these features alone may provide insufficient noise rejection for high-performance cryoSPM, owing to a subtlety of non-contact AFM operation in a vacuum environment. Non-contact AFM utilizes feedback loops that lock certain attributes of the probe cantilever's oscillation at fixed set-points by sensitively adjusting the probe-sample separation, thus achieving a constant probe-sample contact. The probe oscillation amplitude is a therefore a crucial parameter. However, absent the viscous damping of a surrounding atmosphere, the probe oscillation can attain a quality factor of many thousand in a vacuum environment[13], and consequently the transient response of a probe to sample vibration is equally enhanced. Therefore, a commensurate demand for increased vibration isolation attends any increases in probe sensitivity afforded by AFM under vacuum. In turn, AFM instability unsurprisingly translates into instability (noise) in the SNOM performance,

owing to the exponential dependence of the SNOM signal on the probe-sample separation (Chapters 1 and 2). Therefore, cryoSNOM performance is ultimately only as good as that of the underlying cryoSPM. Sec. 5.5 presents a scheme for dramatically improved vibration isolation in cryoSNOM Mark II.

- ***Replacement of probes and samples:*** Essential for a high throughput of experiments, it is imperative that samples can be straightforwardly exchanged in and out of the microscope. For the Mark I design, this required re-pressurizing the vacuum environment, opening the chamber, physically removing the (delicate) AFM head, and replacing samples by hand on the sample stage. Moroever, it is commonly necessary to replace the near-field probe when it becomes inadvertantly fouled by surface contaminants or damaged by contact with the sample surface, and this replacement was similarly cumbersome with Mark I. Most problematically, after such replacement and before re-starting subsequent experiments, pumping the chamber pressure back down to high- or ultra-high vacuum pressures was a time consuming necessity (as long as 1 week, depending on the cleanliness of operation). Heating the vacuum envelope to temperatures of ~100C ("baking") during pump-down is a common method to accelerate the desorption of water vapor within the chamber and improve the pressure attainable with finite pumping time. However, this procedure can risk thermal damage to newly introduced samples, especially oxides, which can lose oxygen in the low pressure environment. As discussed in Sec. 5.6, the solution to this shortcoming is a standardized *in situ* exchange system for quickly exchanging probes and samples all while maintaining low pressures in the microscope chamber.
- ***AFM detection, and design of the AFM head:*** In the Mark I design, the placement of a cleaved optical fiber end within tens of microns of the top surface of the AFM probe cantilever is a simple way to introduce a deflection laser beam into the vacuum chamber and to implement interferometric detection of cantilever motion for

AFM.[12] However, the unsubtle design compromises convenience. The delicate optical fiber catch be damaged when attempting to manually align new AFM probes to fiber end face. The presence of the optical fiber end also partially obscures top-down visible microscopy views of the probe and sample surface, as with the navigation optics implemented in cryoSNOM Mark I. Moreover, the necessary support structures in the AFM head partially block access of incoming radiation illumination to the probe for the purpose of SNOM. "Opening up" the AFM head design therefore allows protecting the AFM optics from damage, improves optical access to the probe for SNOM illumination and navigation optics, and further enables convenient *in situ* access to the probe with a manipulator for the purpose of probe replacement. Sec. 5.7 discusses improvements to the AFM head implemented in the Mark II design.

5.4 High performance cryogenic near-field microscopy: cryoSNOM Mark II

The design and construction of a high performance cryoSNOM to improve upon the Mark I design was undertaken over a period of several years, chiefly from 2013 to 2015. The microscope was designed completely with detailed computer-aided design (CAD) modeling, and constructed from a combination of custom home-built components (e.g. microscope componenets, vibration isolation stage, etc., all machined in-house) and commercially available hardware (e.g. AFM piezos and control electronics from *Attocube GmbH*, and vacuum flange components from *Kimball Physics*, *Kurt J. Lesker*, etc.). Performance of the vibration isolation stage and AFM unit were evaluated in atmospheric conditions before placing within the vacuum chamber, with similar evaluations (together with SNOM imaging) performed under vacuum conditions. The latter evaluations are presented in Sec. 5.9.

The cryoSNOM Mark II system is, at the time of this writing, actively engaged in dozens of distinct experimental projects including near-field optical studies of quantum phase transitions in correlated electron oxides and low-temperature charge dynamics in low-dimensional electronic

systems. It has consumed many thousands of liters of liquid cryogen over cumulative months of time spent with samples maintained at low temperature, often for weeks at a stretch. It has demanded unexpectedly “breaking vacuum” and exposure of the microscope to atmospheric conditions on merely four occasions since its commissioning, and on all occasions for the sake of replacing a faulty component (e.g. piezo actuator). The microscope has experienced hundreds of occasions of probe and sample replacement by way of its *in situ* exchange capabilities. These factors attest to its high-throughput experimental capacity. Primary features of the cryoSNOM Mark II are detailed in the forthcoming sections.

5.5 Vibration isolation system

Sec. 5.3 highlighted the demand for effective vibration isolation in a cryoSNOM operating under vacuum, even when the microscope is mounted atop the pneumatically isolating legs of a conventional optical table. This challenge has long been contemplated and carefully addressed in the designs of countless cryoSPMs, chiefly among them the low temperature scanning tunneling microscopes, where the demand for a vibrationally “quiet” probe-sample gap is inarguably severe. Evaluation of anticipated performance for any vibration isolation scheme in SPM should take account of the net *spectral transmission amplitude* for vibrations intruding into the probe-sample gab. Fig. 5.2C schematically depicts the role of mechanical *transmission functions* among staged (“stacked”) components, whose cummulative product in the simplest case determines the transmission amplitude for vibrations that reach the innermost stage. Shown are representative optimal transmission functions for the outer isolation stage (blue) and the inner stage (red) whose product provides a tremendous net reduction of vibration transmission across the bandwidth of relevant measurement frequencies (in the case SNOM, this is usually several kHz). The conceptual goal of two-stage vibration isolation can be thereby understood as combining a low-pass filtering outer stage (low frequency resonator) with a high-pass filtering inner stage (high frequency resonator). Mechanical excitations (vibrations) of intermediate

frequency are thereby rejected from the system. The latter stage is conventionally comprised by a small and rigid microscope design, whose housing admits only high frequency resonances (eigenmodes) to impart relative displacements into the probe-sample gab. We now discuss implementation of an outer low-pass isolation stage.

Among the proposed schemes for vibration isolation in the context of low-noise SPM,[14,15] one method has proven an excellent balance of cost, compactness, performance, and elegance. This scheme comprises the combination of spring suspension isolation with an magnetic eddy current damping stage, and its principle of operation is depicted in Fig. 5.2A. The microscope itself (intentionally compact) is suspended from three or four stainless steel springs possessing of constant *k*, affording a low internal (vertical) resonance frequency of $f \sim \sqrt{k/M}$ or, equivalently, $\sqrt{L/g}$, with *M* the microscope mass, *L* the spring extension, and *g* the gravitational constant. With a small and compact microscope, *M* is limited, and transmission frequencies as low as a few Hz are achievable only with very low spring constants. This condition in turn establishes the extended length of the spring suspension stage, with lengths at least ~20 cm necessary for the lowest frequencies. Fig. 5.2B presents the spectrally resolved transmission function of such an isolation stage with and without a *damper*, whose role is to mitigate the sharp resonant tranmission of the springs on-resonance. Fig. 5.3 presents an overview of the microscope design, including vibration isolation stage, within cryoSNOM Mark II. The “floating” microscope platform (counterbalanced by brass weights, in yellow) is vertically suspended by three 7-inch stainless steel springs (*Century Spring Corp.*) housed within hollowed posts and equipped with adjustable top suspension for height adjustment, accomplishing a low-pass resonance frequency of ~2 Hz.

Springs of low spring constant lack internal damping, so an external damping source is necessary to dissipate kinetic energy of the transiently excited spring resonance. A most elegant and contactless implementation under vacuum conditions relies on eddy currents that develop within a conductive block when subject to a temporally varying magnetic field, a consequence of

Faraday's law of induction. Practically speaking, mounting a conductive element (e.g. copper block) onto the isolated microscope platform in close (but contactless) proximity to a stationary permanent magnet will stimulate eddy currents when the springs are set to oscillate (Fig. 5.2A), thus sapping resonant kinetic energy into heat – an effective source of damping. Chief design factors for enhancing the damping rate include the overall number of conductor / magnet pairs, the strength of the permanent magnet field, the electrical conductivity of the conductors, and their proximity to the magnets. To this end, multiple magnets are routinely arranged in a ring-like spatial arrangement to establish field lines circulating unidirectionally around the ring circumference. When conductors are placed into the gaps between pairs of such magnets, the penetrating magnetic flux is optimal.

As shown in Fig. 5.3, this magnetic eddy current damping design was implemented in cryoSNOM Mark II with three sets of five (stationary) magnets and six (mobile) interdigitating copper fins positioned below and around the periphery of the microscope platform, affording an excellent damping effect. More detail can be seen in Fig. 5.9. Samarium cobaltate magnets are used for their combination of high remanance field and high Curie temperature, suitable for withstanding the routine bake-out temperatures (as high as 150C) applied to the enclosing ultra high vacuum chamber. An adjustable trio of soft lateral springs below the microscope platform (not shown) are employed for lateral adjustment of the microscope platform position to ensure no physical contact between 1) the microscope platform (and connected copper fins) and 2) the stationary magnets, or any other stationary (vibration-prone) part of the microscope. Adjustability is the paramount rule for a design of this kind, since the microscope center of mass, along with minute torques at the spring connection points, can play subtle roles in determinating the equilibrium position of the suspended platform, and must be compensated. A piezo actuator (*picomotor* from *New Focus*, not shown) is incorporated at the microscope base to remotely "de-float" the isolation platform (and "re-float" it again on command), and thus immobilize the

microscope during e.g. probe or sample exchange manipulations (Sec. 5.6). This *in situ* functionality enables unambiguous characterization of the vibration isolation performance.

As presented in Sec. 5.9, the rate of vibration rejection afforded by the “floating” stage is found to exceed one order of magnitude among mechanical vibrations observable during routine microscope operation. As a more heuristic measure of performance, the operation of turbomolecular pumps on the vacuum chamber has no noticable vibrational impact on SPM operation with the microscope, provided that the vibration isolation stage is enabled. This feature enables routine SPM measurements even during simultaneous operation of a turbomolecular pump adjoining the chamber. The latter can thereby be used on a near-constant basis to depressurizing a quick-entry load-lock chamber and to introduce new probes / samples from ambient into the vacuum environment, without any undue interruption to the workflow of measurements. As a second heuristic measure of performance, the deployment of vibration isolation for the microscope combined with a *stationary* SNOM focusing optic (parbolic mirror) allows mechanical decoupling between these components. Consequently, piezoelectric adjustments to the SNOM optical focus make no noticable impact on the AFM stability whenever the probe maintains contact with a sample. Therefore, focal adjustments can be performed to optimize delivery of light to the SNOM probe while the probe and sample are afforded uninterrupted near-field interaction, all without any mechanical degradation or damage to the probe that might otherwise result as a consequence of mechanical coupling.

Meanwhile, from an optical point of view, “floating” the entire SNOM AFM (effectively one arm of the SNOM interferometer) can have an undesirable impact on the phase stability of the detected SNOM signal whenever ambient disturbances allow excitation of the isolation stage’s low frequency resonances. However, as discussed in Sec. 5.9, this impact is quite tolerable at the long light wavelengths (~10 microns) relevant to operating SNOM in the mid-infrared.

5.6 Scheme for in situ exchange of probes and samples

Sec. 5.3 highlighted the demand for *in situ* exchange of probes and samples for a cryoSNOM to maintain high experimental throughput. Implementation schemes for such exchange are too numerous to name in conventional cryoSPM, but cryoSNOM Mark II presents the first such scheme deployed to suit the demands of a near-field microscope. Enabled by a large ion-getter pump, titantium sublimation pump, and vacuum-friendly materials within the vacuum envelope base pressure of the cryoSNOM Mark II is in the range of several 10^{-10} mbar. As confirmed by residual gas analysis, the dominant partial pressure under these vacuum conditions associates with hydrogen contamination (from e.g. diffusion through stainless steel vacuum fittings). In order to maintain this level of pressure without any demand for time consuming pump-down to resume base pressure, the vacuum envelope is never directly broken during the introduction of new probes or samples. Instead, the following delivery scheme is used (elements thereof depicted in Fig. 5.9).

A differentially pumped quick-entry load-lock chamber is the only vacuum space periodically exposed to ambient conditions. New probes and samples are inserted into the load-lock delivery apparatus, the minute load-lock space is pumped down to ~10^{-7} mbar in a few hours' time by turbomolecular pump, and the introduced probes / samples are linearly translated through a vacuum valve into the main chamber, where a manipulator arm on a dual-axis "wobble-stick" can place them either into a 1) long-term in-vacuum storage space within the main chamber, or 2) the microscope itself. Samples and expended probes may be removed from the chamber by the reverse process, and the valved-off load-lock chamber can be then re-pressurized to ambient conditions with a noble gas purge valve. Probes and samples are thereby removed from the microscope system. In this section, we detail novel aspects of this process.

First, a unified scheme for mounting and receiving samples and probes within the microscope was conceived based on the exchangeable *Omicron* flag-style sample plates. As shown in the inset of Fig. 5.8B, this style of sample plate possesses a "key hole" that enables

manipulation by a keyed manipulator (Fig. 5.7). Co-developed with *Ferrovac GmbH*, these sample plates are equipped with as many as 13 on-board electrical pin contacts, and mount kinematically (spring-loaded “snap-in”) into a specially designed compact vacuum-compatible receiver that provides immediate electrical access to all contacts by way of micro-coax cable. The variant of exchangeable sample plate (“sample carriage”) used in the cryoSNOM Mark II incorporates a built-in temperature sensing silicon diode (DT-670 from *Lakeshore Cryotronics*) for accurate thermometry of cooled samples, and features a removable electrically insulating (but thermally conductive) ceramic top-plate to which samples can be conveniently glued. Since this plate is a disposable part, samples may be permanently mounted, and are then tranferrable to and from a sample carriage by way of a pair of screws. Even small electrical device samples can be mounted in this fashion and electrically contacted to the on-board electrical contacts by way of thin wires, enabling electrical access to the sample device from outside the vacuum chamber.

AFM probes are mounted in a similar fashion to “probe carriages” (Fig. 5.8B) that utilize on-board electrical contacts for excitation of an on-board dither piezo to excite the probe cantilever, as well as for electrical access to the probe itself, as utilized for various electrical scanning force modalities (e.g. electrostatic force microscopy, piezoresponse force microscopy, and Kelvin probe force microscopy). Many of these probe carriages were fabricated for the cryoSNOM mark II suitable for introducing new probes into the chamber, offering a steady availability of fresh cantilevered probes of any type offered by commercial vendors (e.g. magnetically coated, ultra-sharp silicon, etc. from *Nanosensors*).

The protocol for removing a probe or sample from the microscope at the conclusion of an experiment requires direct access to the microscope by the manipulator. However, during SNOM measurements the parabolic mirror focusing optic is in position directly in front of the probe and sample (Fig. 5.4) in order to illuminate the probe and collect back-scattered radiation. In the cryoSNOM mark II design, one piezo-positioning axis of the focusing optic is long-range (50 mm), enabling the parabolic mirror to shuttle completely across the vacuum chamber and out of the

way of the microscope, thereby enabling direct access to the microscope by the manipulator (Fig. 5.7), which can readily insert or remove sample carriages from the sample receiver. Meanwhile, in order to bring the probe carriage forward into suitable position for addressing with the manipulator, the probe head itself is XYZ-articulated by piezo positioners (PPS-20 from *Micronix USA*). During replacement of new probes, these positioners remotely move the probe back into suitable position rearwards for alignment to the deflection laser of the AFM as detailed in Sec. 5.7, thereby enabling new experiments as immediately as possible.

This integrated scheme for exchange and replacement of probes and samples is an integral feature to the high-throughput experimental capacity of the cryoSNOM Mark II design.

5.7 AFM detection and optical navigation within a confined vacuum environment

Fig. 5.5 presents two common implementations of cantilever deflection detection in an AFM, of which the latter, interferometric detection (Fig. 5.5B), is often the method of choice for the confined vacuum environment of a cryoSPM. However, Sec. 5.3 highlighted shortcomings of this scheme when implemented in the most straightforward and subtle fashion using a cleaved, bare optical fiber to deliver deflection laser radiation. In cryoSNOM Mark II, this AFM detection scheme was developed deployed fashion that is more modular, robust, accurate, and convenient. Namely, while an optical fiber (single-mode at the deflection laser wavelength, 1.3 microns) is still used to introduce the deflection laser beam into the UHV chamber, light is first delivered from the commercially polished fiber end face (FC/PC terminated) into an optical fiber collimator. From there, the light is directed to a focusing lens inside the AFM head with ~1.5 cm focal length, which tightly focuses the deflection laser to the AFM probe cantilever to surface, all from a comfortable distance away from the probe itself. These optical componenets are indicated in Fig. 5.4.

With assistance from a pilot laser directed down the optical fiber, remote XYZ-actuated positioning of the probe head enables bringing the probe precisely into the deflection laser focus. Such careful positioning is made possible by two redundant direct views of the AFM cantilever

and projected pilot laser, the first from a high magnification CCD camera outside a side viewport in the microscope chamber, and the second from enhanced top-down navigation optics housed in the AFM head, to be discussed momentarily. The process of 1) introducing a new probe into the probe head by way of the manipulator and 2) aligning the new probe to achieve AFM deflection signal this way typically requires only a few minutes.

Deflection laser radiation reflected from the probe is still coupled back into the deflection laser optics in the usual fashion for interferometric detection, however the Fabry-Perot cavity (indicated in Fig. 5.4) now established between the cantilever and fiber end face is effectively several cm in dimension. Nominally, a dramatic increase in cavity size (from 10s of microns to several cm) would be expected to decrease its finesse and enhance sensitivity to noise in laser wavelength and to mechanical drifts in cavity dimension. However, minimal drifts in the latter were found to be neglibile during normal microscope operation, and noise from the former, while in principle limiting, contributes in practice only a few parts per thousand to noise in the effective AFM cantilever oscillation signal. This remarkable and fortunate finding is perhaps tied to the fact wavelength fluctuations contribute only “at second order” to the oscillation signal, whereas their influence is more direct upon the absolute deflection signal.

By bringing deflection laser optics further from the tip, there is consequently more allocated space in the AFM head to allow larger aperture optical elements for the navigation optics, presented in Fig. 5.6. An improved achromatic doublet of lenses within the AFM head thereby can project an image of the probe and sample outside the top vacuum chamber viewport with much reduced distortion and enhanced resolution as compared with that so limited in cryoSNOM Mark I. In cryoSNOM Mark II, machine vision optics (*InfiniTube*^{TM}), long working distance objective lens (*Mitutoyo*), and CCD camera thus produce an excellent navigation view of the near-field probe above the sample, facilitating remote navigation to micron-scale sample features.

Lastly, the newly designed AFM head affords bringing the SNOM parabolic focusing mirror twice closer to the near-field probe, thus enabling use of 1-inch effective focal length optics and a signifcant improvement in numerical aperture for illumination and collection of back-scattered radiation from the probe across wider solid angles. Such improvements to optical aperture relevant to SNOM are a critical factor for enhancing the signal-to-noise ratio of high-sensitivity SNOM measurements, and the cryoSNOM Mark II design attests that such improvements are achievable with a concerted design of the AFM head hardware.

5.8 Agile control of variable sample temperatures

In the cryoSNOM Mark II, the sample receiver (*Ferrovac GmbH*; see Fig. 5.8A) is made of conductive beryllium copper and thermally contacted rearwards to the microscope cryostat (ST-400 from *Janis Research*) via a thin flexible copper link (*Attocube GmbH,* see Fig. 5.9). At the sample side, the thermal link houses an integrated temperature sensing silicon diode (DT-670 from *Lakeshore Cryotronics*) and resistive 50 Ohm heater that together permit rapid PID feedback-controlled adjustments to the sample temperature with a digital temperature controller (*Model 336* from *Lakeshore Cryotronics*). Registered accuracy and stability of temperatures at the sample temperature sensor reaching 1 mK are routinely achieved. Controlled temperature ramp-rates at the sample can exceed 4K / min. to within a few 10s of K of base temperature, attesting to the nimble temperature control enabled by stand-alone cooling of the sample and sample holder.

Electrical contacts to the sample are directed to an electrical feedthrough on the microscope cryostat to avoid thermal gradients along the electrical connections and to avoid undue heat load on the sample. In order to mitigate transmission of vibrations from the cryostat to the sample stage, both the thermal link and the cold electrical sample contacts are rigidly anchored to the microscope housing (titanium) using thermally insulating clamps machined from the vacuum-compatible thermoplastic polyether ether ketone (PEEK). This ensures that the

transmission of vibrations to the sample stage remain dictated chiefly by rigidity of the microscope housing combined with the spring-suspension vibration isolation stage.

As in cryoSNOM Mark I, an effective thermal isolation stage (Figs. 5.7, 5.8A) isolates the cold sample and its receiver from the room-temperature microscope. Together with radiation load on the sample (there is no radiation shield surrounding the sample, and the AFM probe head is uncooled), the practically achievable thermal isolation from this stage establishes a base temperature of ~20K with a cryostat base temperature of ~6K at highest cryogen flow rates. These base temperatures are inferior to those routinely achievable within helium bath cryostat SPMs; however, the nimble, widely variable control and accuracy of sample temperatures afforded by cryoSNOM Mark II makes ours a desirable approach for the careful temperature study of quantum phase transitions in correlated electron oxides.[1,2]

5.9 Performance of the microscope

Fig. 5.10 presents characteristic measures of performance for the cryoSNOM Mark II after assembly, mounting into the vacuum chamber, and pumping the system down to a high vacuum environment. As measured by the AFM itself engaged with a sample in non-contact mode, Fig. 5.10A presents the noise spectral density in the probe-sample gap as a function of frequency with the spring suspension vibration isolation system enabled (red) and disabled (blue). For the latter, noise peaks in a bandwidth of 500 Hz associate with transmission of mechanical noise from the environment into the microscope, and these features are attenuated by more than an order of magnitude by engaging the vibration isolation system. Remaining noise sources in the AFM measurement include sensitivity of the deflection photodiode, and stability of the deflection laser wavelength and amplitude.

Fig. 5B and 5C reveal the back-scattered near-field signal amplitude (S2) and phase (P2) demodulated at the second harmonic of the probe dither frequency, with the metal-coated AFM probe engaged with a gold substrate. Interestingly, it can be seen that broadband noise intrudes

across the measurement bandwidth of the optical signal unless the vibration isolation system is diligently enabled. The overall improvement in SNOM signal-to-noise has been found to easily exceed a factor of 5 under typical measurement conditions after enabling the vibration isolation. Both SNOM and AFM performance of the cryoSNOM Mark II are found to greatly exceed those of the Mark I system, as evidenced already in the inaugural near-field scan conducted with the former on a test grating of etched silicon oxde (Fig. 5.11). However, sensitivity of the near-field phase measurement is found limited to a few degrees at the imaging wavelength of 11 microns, and this limitation can be traced to the vibration isolation stage by inspection of Fig. 5.10D. Chief contributions to the noise spectral density of the P2 signal coincide in frequency with resonant modes of the vibration isolation system. Although such low frequency motions are completely suppressed at the probe-sample gab by way of the microscope's rigidity, any relative motion of the vibration isolation stage itself can still be identified as an optical phase instability within the interferometer arm comprised of the SNOM AFM and focusing optic. Here, this effective phase instability is precisely the limiting factor for unambiguous identification of the sample's near-field phase response at levels below a few degrees. The effect is exacerbated by presence of low frequency noise sources in the laboratory environment, and remains arguably the sole technical challenge to be circumvented for the routine application of high-performance cryogenic scanning near-field optical microscopy. Improvements in this regard should be a focus of ongoing instrumental efforts. At the time of this writing, this limitation plays no crucial role in the ongoing nano-infrared studies of quantum phases in correlated oxides at low temperatures.

Lastly, Fig. 5.12 highlights the possibility to simultaneously combine near-field imaging capabilities with other scanning force microscopy modalities, without sacrificing performance of either. This possibility has been recently demonstrated with cryoSNOM Mark II in the context of 1) magnetic force microscopy, in which probes coated in magnetic metal can resolve small magnetic forces over the sample surface, and 2) Kelvin probe force microscopy, where the surface work function (or more generally, the surface electrostatic potential) can be resolved with

careful application of differential bias between tip and sample and registry of electrostatic forces. Neither modality has been found to interefere with the routine application of SNOM imaging, and both are functionally important for resolving novel magnetic and electronic phases emerging at low temperatures in correlated electron oxides. The combination of these complementary scanning probe techniques will form an experimental centerpiece of future studies using low-temperature SNOM.

5.10 Acknowledgments

This chapter comprises a discussion of hardware design and development undertaken in close collaboration with M. D. Goldflam and D. N. Basov, who contributed enormously to its realization.

5.11 Figures

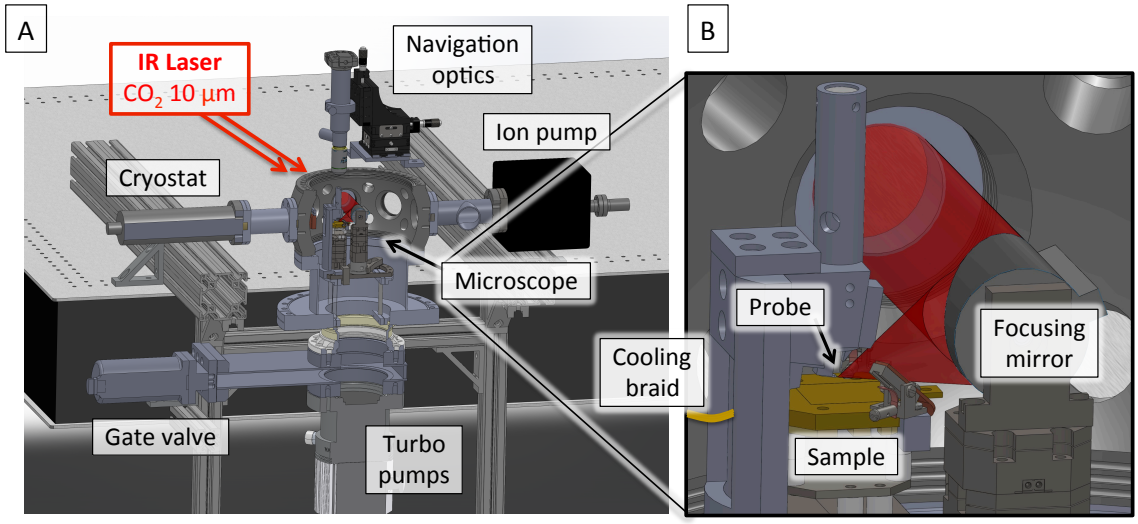

Figure 5.1: Features overview of cryogenic scanning near-field optical microscope (cryoSNOM) Mark I.

This first-generation system includes all essential components for conducting near-field optical experiments in a cryogenic environment. A) The chief elements include an ultra-high vacuum chamber (center) along with associated vacuum valves, mechanical (turbomolecular) and quiet (Ion getter) vacuum pumps, and most importantly an interior compact atomic force microscope equipped with free-space focusing optics. External navigation optics outside the vacuum environment facilitate observing the probe over the sample surface. B) The microscope proper consists of 1) a cantilevered AFM probe and associated deflection-sensing optics housed in the AFM head, 2) a sample atop coarse positioners and a nano-resolved scanner, and 3) a large numerical-aperture articulated focusing optic for accurately focusing light to the AFM probe and for collecting back-scattered radiation. All positioning apparati within the vacuum space operate with vacuum-compatible piezoelectric mechanisms (“piezos”) and are XYZ-articulated.

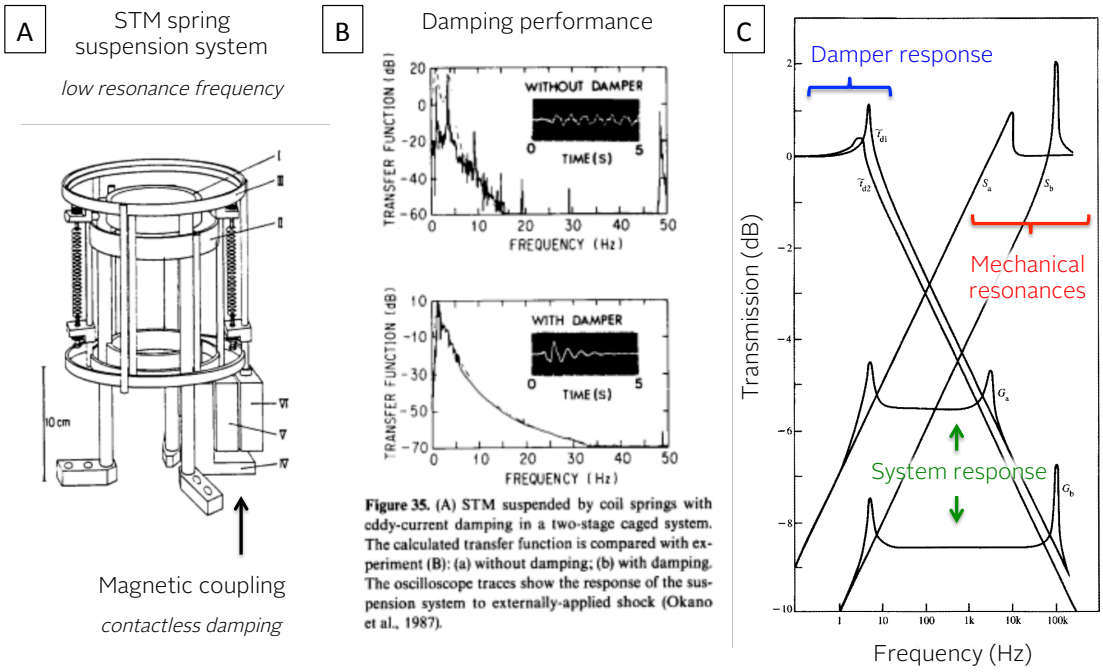

Figure 5.2: Principles of vibration isolation for scanning probe microscopy.

A) & B) Adapted from Okano et al. 1987.[15] A) Example vibration isolation scheme comprised of low spring constants springs suspending and isolating a microscope platform. Contactless damping of spring motion is afforded through magnetic coupling of an immobile permanent magnet with a conductive block (e.g. copper) on the suspended stage. The coupling converts relative motion into eddy currents. B) Example transfer functions of vibrations coupled to the microscope stage, with (below) and without (above) eddy current damping; resonant modes are attenuated by 10 dB. C) Adapted from Pohl et al. 1986.[14] The concept of vibration isolation for scanning probe microscopy consists in combining structural features of the microscope with high mechanical resonance frequency (high-pass transfer function, in red) with a low resonant frequency vibration isolation stage (e.g. spring suspension; low-pass transfer function, in blue). In a noisy environment, microscope performance is dictated by the product of transfer functions (in green), resulting in even several orders of magnitude noise of rejection across all frequencies relevant for measurements.

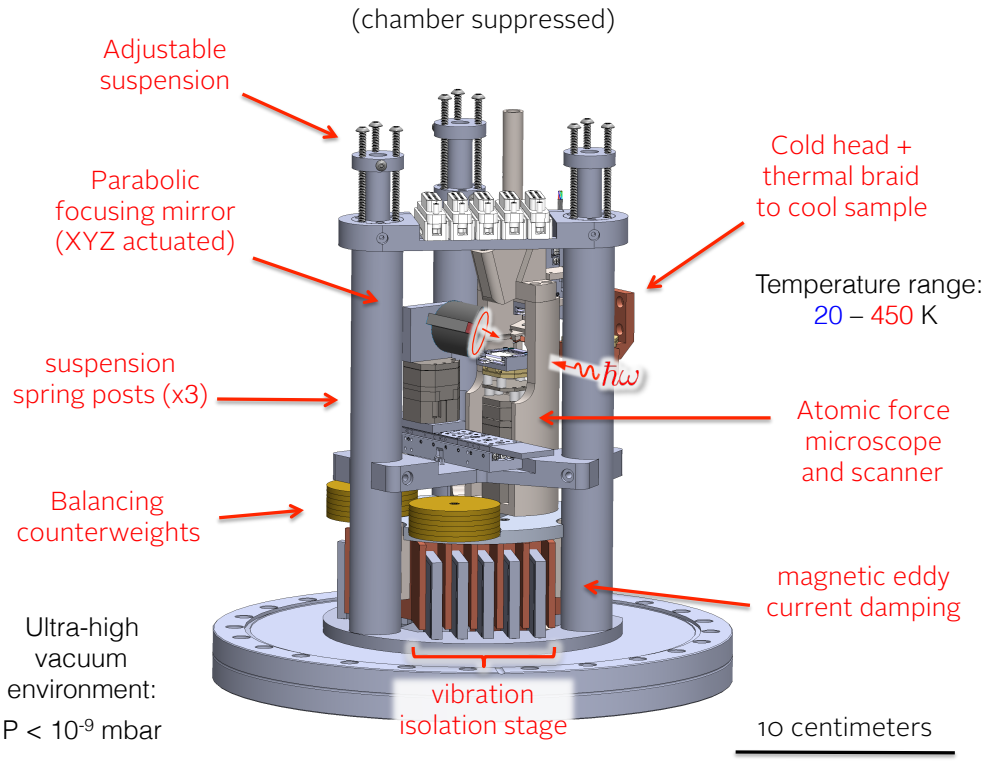

Figure 5.3: Features overview of cryoSNOM mark II.

The outer vacuum chamber is suppressed for this interior view. Forming a stand-alone modular unit, the interior microscope design of cryoSNOM mark II consists of four main elements: 1) an atomic force microscope, 2) a vibration isolation stage comprised of soft 7-inch springs and magnetic eddy current damping stage, 3) a parabolic focusing mirror atop nanopositioning stages for illumination of the SNOM probe and collection of probe-scattered light, and 4) a cold-head cooled by the cryostat that provides thermal contact to the sample stage through a soft and thin copper braid.

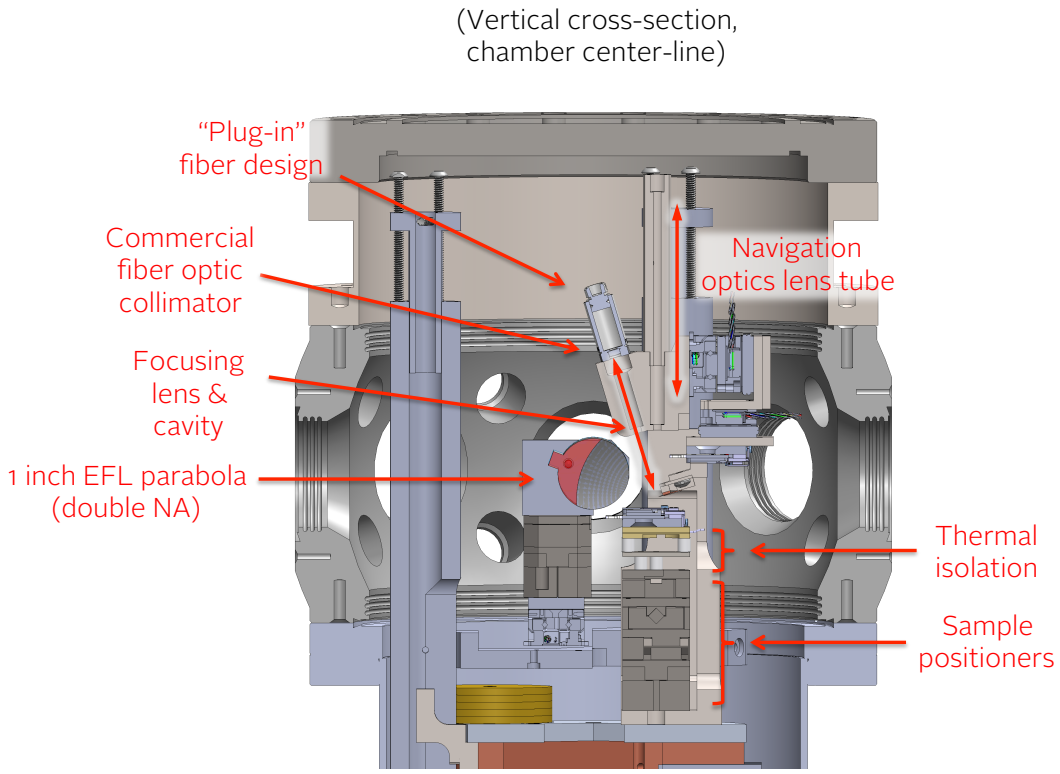

Figure 5.4: Cross-sectional overview (part 1 of 3) of cryoSNOM Mark II chamber.

Novel features of the microscope include a 1 inch effective focal length parabolic focusing mirror, effectively doubling the numerical aperture of illumination and light collection optics as compared with cryoSNOM Mark I. The combination of "plug-in" fiber optic deflection signal and effective navigation optics makes a very effective use of constrained space in the atomic force microscope head. Thermal isolation between the sample stage and piezo scanner is afforded by two layers of steatite spacers bolted with teflon screws, keeping the operating temperature of the scanner close to room temperature while admitting low sample temperatures (~20 K).

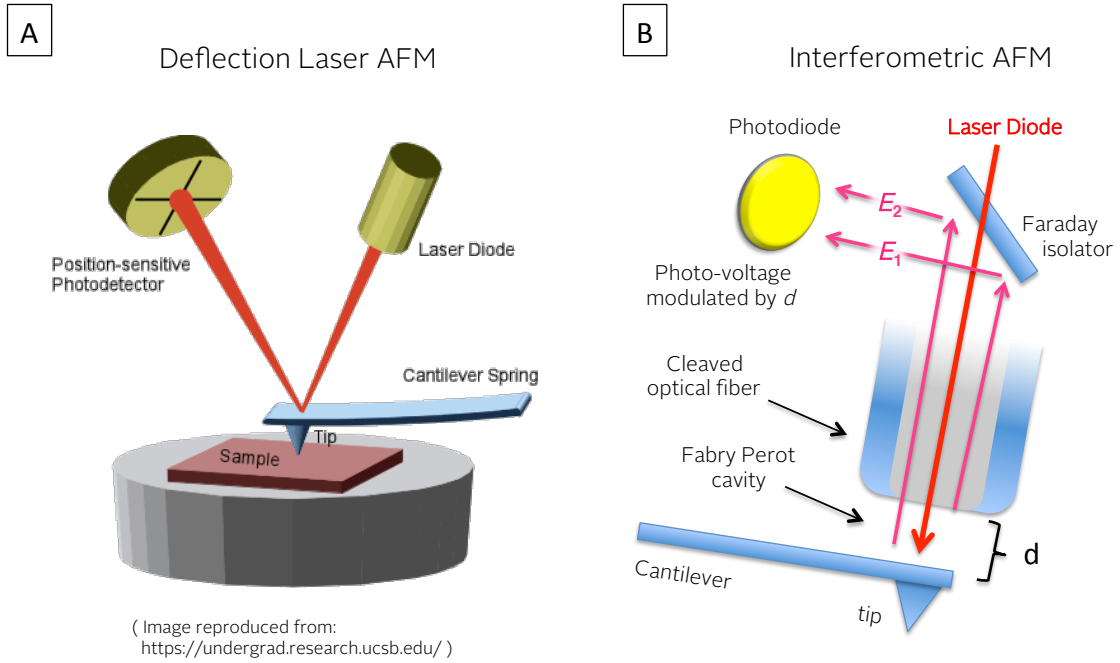

Figure 5.5: Principles of AFM detection in an ultra-high vacuum (UHV) environment.

Two approaches are commonly used for detection of probe cantilever deflection to enable atomic force microscopy operation in an ultra-high vacuum environment. A) Angled specular reflection of a focused deflection laser off the cantilever surface onto a position-sensitive photodiode enables detection of vertical and torsional flexures of the cantilever, but is difficult to implement in the confinement and ultra-clean environment of a vacuum chamber. B) Interferometric (Fabry-Perot) detection of cantilever displacements relies on detected interference between laser fields reflected from the cantilever and from the end of an optical fiber, the latter being used for compactly delivering the deflection laser to the cantilever. This method requires merely an optical fiber within the ultra-clean vacuum space.[12]

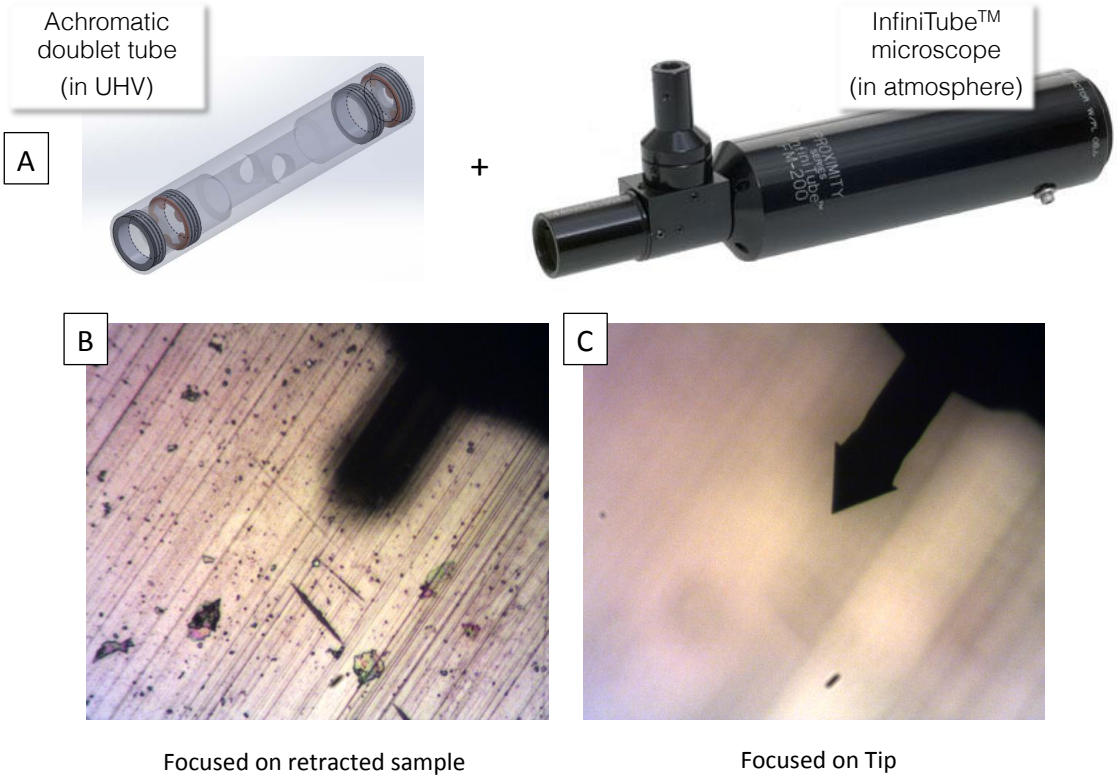

Figure 5.6: Implementation of navigation optics for cryoSNOM Mark II.

Navigation optics are implemented by way of an achromatic doublet inside the vacuum space, which project an image of the probe & sample to just above the top viewport of the microscope chamber, combined with a machine-vision microscope (InfiniTube™) outside the vacuum environment. A long-working distance objective lens (Mitutoyo Corp.) allows the microscope to project this image onto a CCD camera at 50X magnification. The navigation optics system also allows careful vertical approach of the sample, together with straightforward positioning of the sample for the interrogation of micron-scale structures using the AFM probe. The navigation optics are also used to ensure *in situ* positioning of the AFM probe cantilever into the deflection laser focus when probes are replaced.

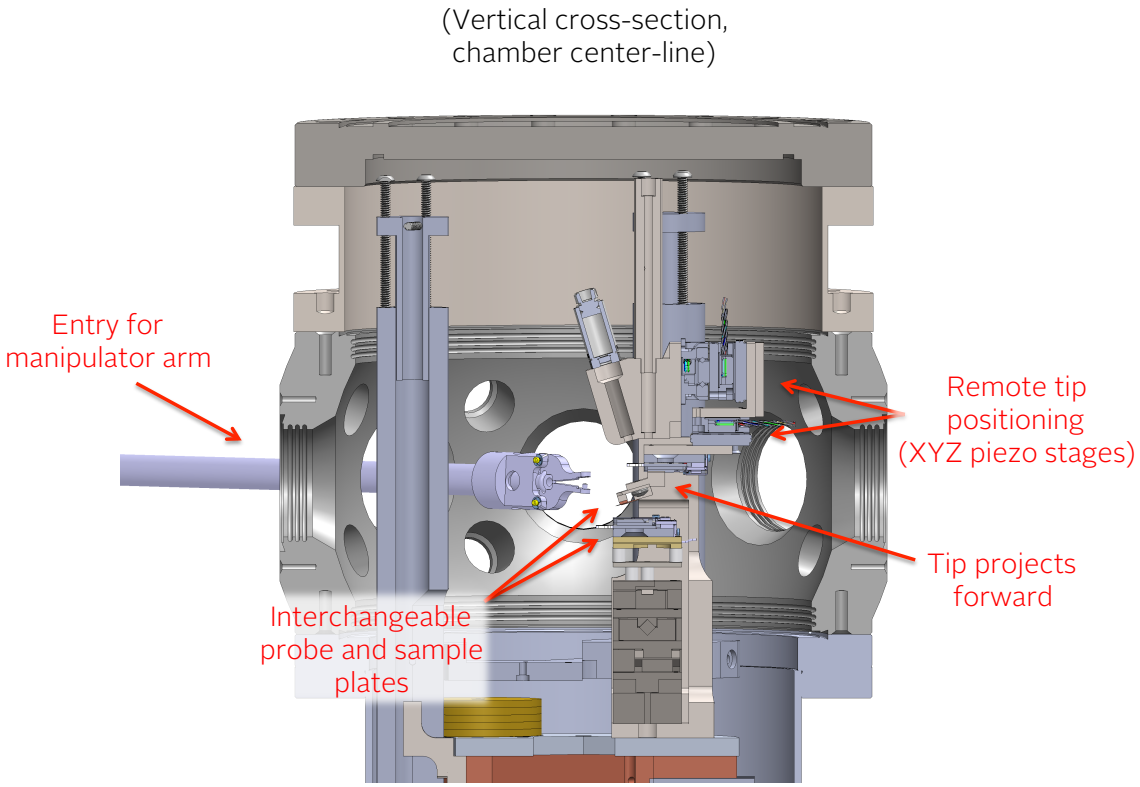

Figure 5.7: Cross-sectional overview (part 2 of 3) of cryoSNOM Mark II chamber.

The multi-flanged vacuum chamber (Kimball Physics) enables entry of a manipulator arm to interchange probe and sample carriages within the vacuum environment whenever needed. To facilitate replacement of probes, an XYZ trio of nano-positioning stages (Micronix USA) allows remotely projecting the probe carriage forward for replacement, with subsequent *in situ* positioning into the focus of AFM deflection optics and the microscope navigation optics.

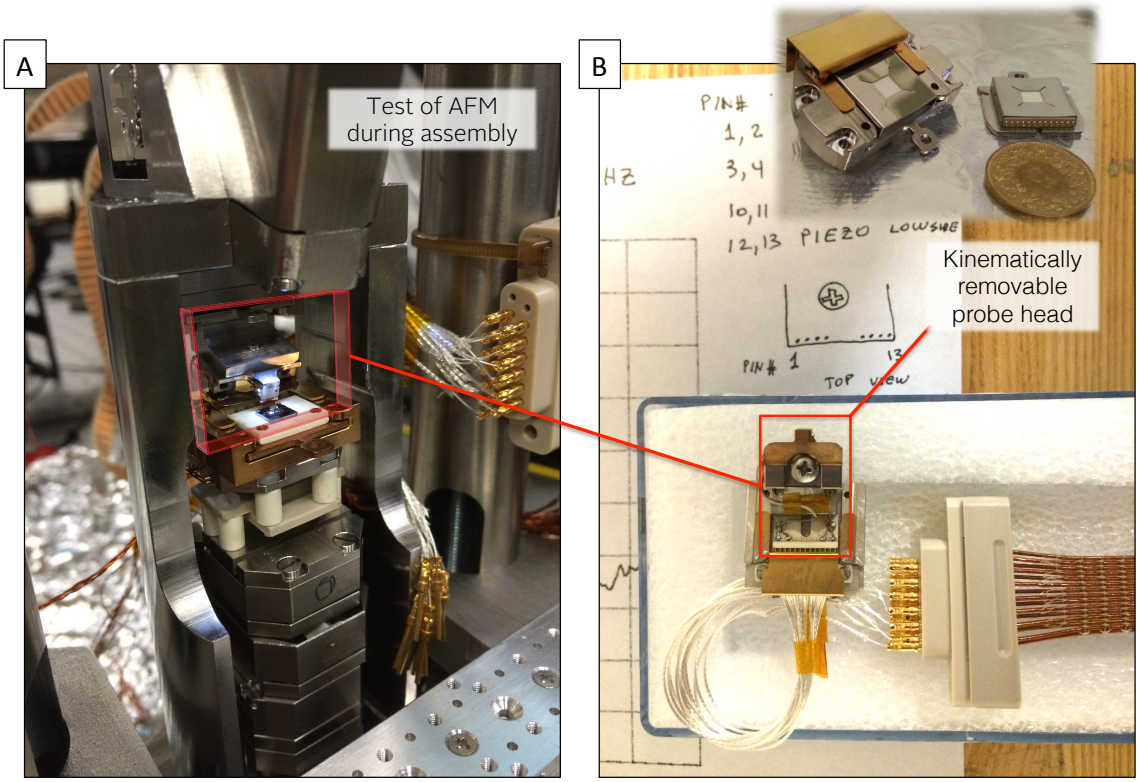

Figure 5.8: Scheme for exchangeable probe-heads in cryoSNOM Mark II.

A) The AFM unit of the microscope is shown during initial AFM testing under ambient conditions. The AFM probe is illuminated over a silicon oxide calibration sample (faint blue color). The probe head is highlighted red, and in B) shown removed from the microscope for clarity. The probe carriage (probe head) is kinematically removable from a spring-loaded receiver (Ferrovac GmbH). As many as 13 micro-pins on the probe carriage and associated electrical contacts inside the receiver together enable automatic electrical contact to the carriage for delivering excitation voltages to an on-board excitation (dither) piezo. Other electrical contacts enable delivery and measurement of electrical signals to and from the probe.

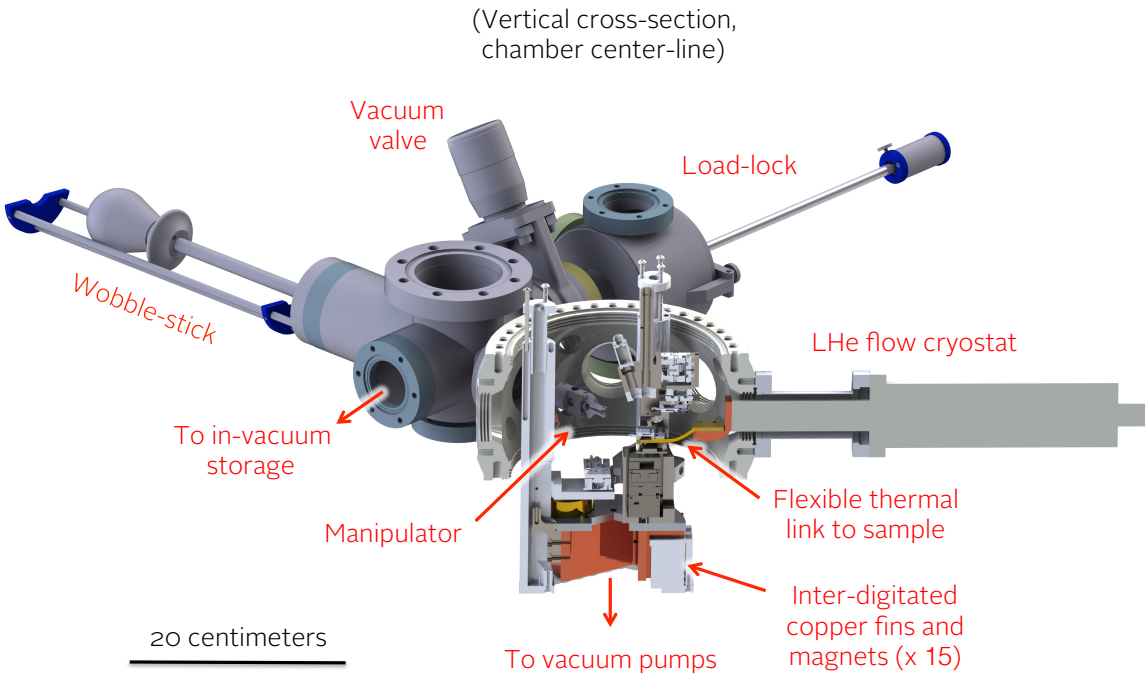

Figure 5.9: Cross-sectional overview (part 3 of 3) of cryoSNOM Mark II.

Vacuum hardware for probe and sample exchange are shown adjoined to the main vacuum chamber. A load-lock quick-entry chamber (differentially pumped) allows bringing probes or samples from atmospheric conditions into the 10^{-9} mbar vacuum space within a matter of hours. A dual-shaft wobble-stick allows positioning the manipulator to remove or replace probes and samples from / into both 1) the load-lock delivery apparatus and 2) an in-vacuum storage space. Linear translation of the wobble stick enables similar manipulations within the microscope chamber, for inserting or removing probes and samples. Below the microscope, the cut-away displays elements of the magnetic eddy current damping system. The microscope cryostat resides on a flange behind the AFM, and delivers cooling power from flowing liquid cryogen (helium) to the sample stage by way of a thin thermal link of copper foil (Attocube GmbH).

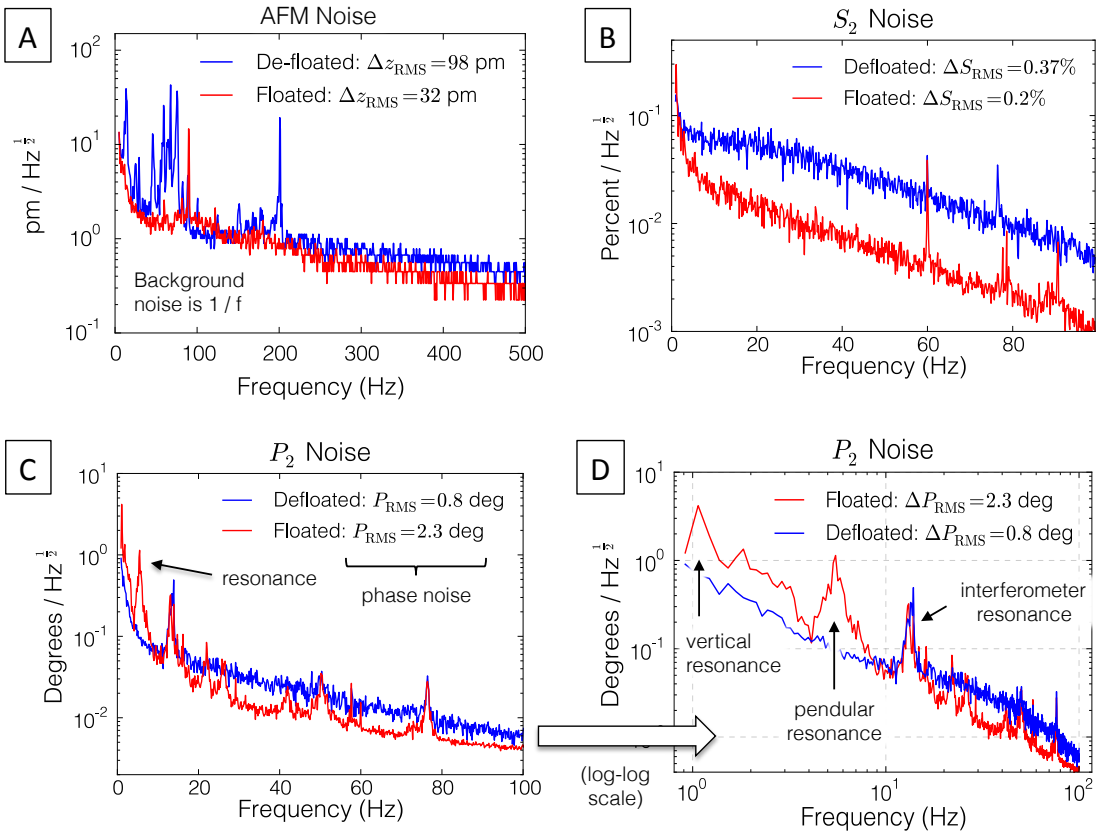

Figure 5.10: Performance metrics for cryoSNOM Mark II.

A) The spectral density of noise in the probe-sample gap is a defining characteristic of scanning probe microscope performance. *In situ* suspension of the microscope ("Floated") on its vibration isolation stage displays more than one order of magnitude attenuation of mechanical vibrational noise, and overall a more than three-fold reduction in RMS vibrational noise in the operational 500 Hz bandwidth. Remaining 1 / f ("pink") noise is largely attributable to deflection laser jitter and sensitivity of the AFM photodiode. B) Signal-to-noise of the second-harmonic near-field signal amplitude is dramatically improved by employing the vibration isolation, by way of stabilizing the AFM performance. C) Signal-to-noise of the second-harmonic near-field signal phase is reduced somewhat, since relative motion of the vibration-isolated stage contributes instability to interferometric detection of near-field signals. D) Focusing on the low-frequency regime, vertical and pendular resonance frequencies of the vibration isolation system are discernible.

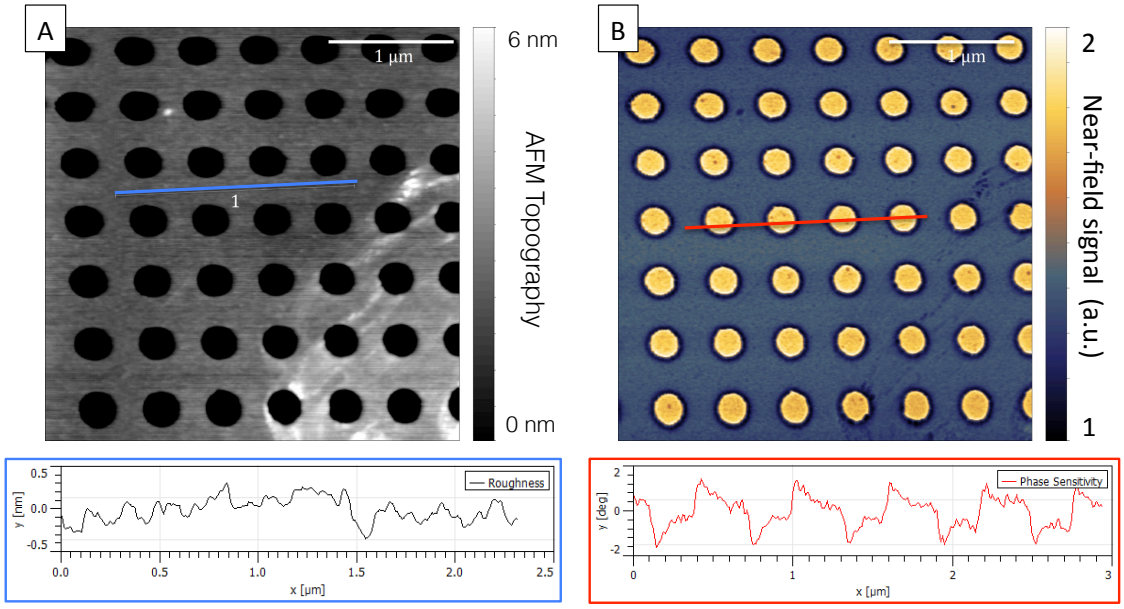

Figure 5.11: Inaugural infrared near-field image from the cryoSNOM Mark II.

A) Topographic sensitivity from the associated AFM scan is approximately 1 angstrom. B) At an imaging wavelength of 11 microns, etched holes in the thin silicon oxide layer reveal the near-field response of silicon. Sensitivity of the near-field phase is as good as 2 degrees at this imaging wavelength. Scan time: 6 ms per pixel; scan resolution: 20 nm per pixel.

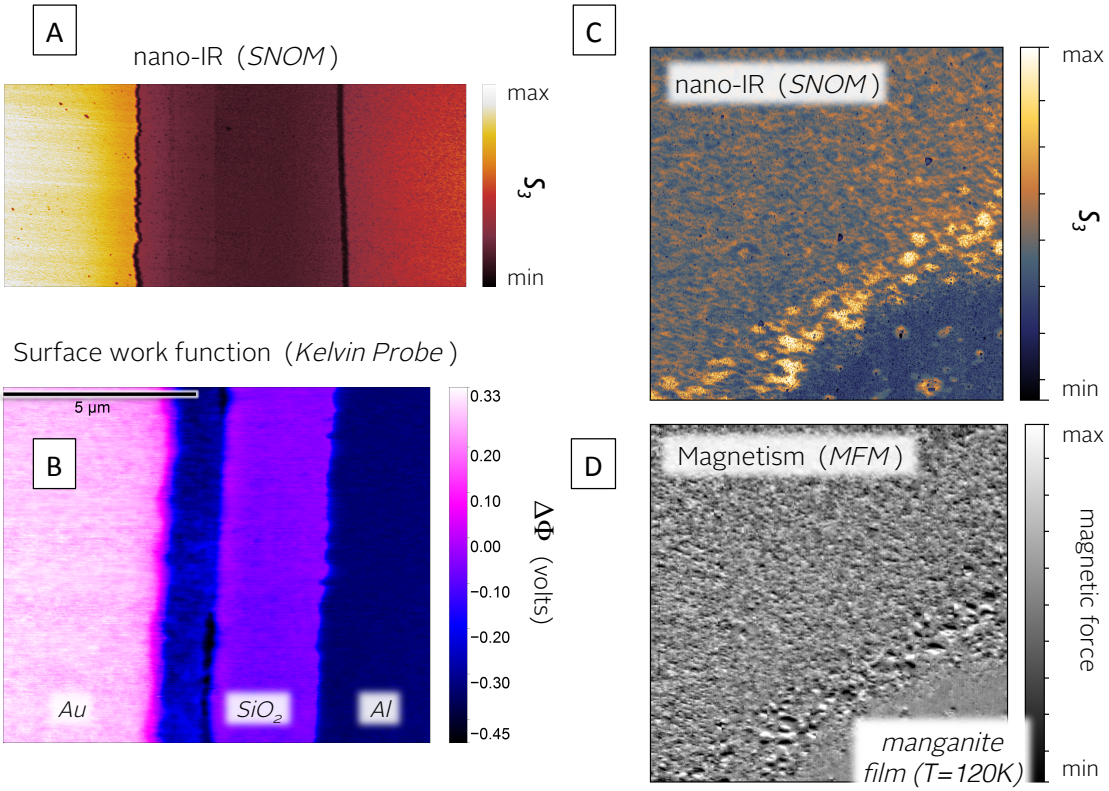

Figure 5.12: Correlative modes of scanning probe microscopy enabled in cryoSNOM Mark II.

Signals from these “extra” modalities can be acquired unobtrusively and simultaneously with the performance of a near-field scan.

5.12 References

1 Dagotto, E. Complexity in Strongly Correlated Electronic Systems. *Science* **309** (2005).

2 Tokura, Y. Correlated-Electron Physics in Transition-Metal Oxides. *Physics Today* **56** (2016).

3 Qazilbash, M. M., Brehm, M., Chae, B.-G., Ho, P.-C., Andreev, G. O., Kim, B.-J., Yun, S. J., Balatsky, A. V., Maple, M. B., Keilmann, F., Kim, H.-T. & Basov, D. N. Mott Transition in VO2 Revealed by Infrared Spectroscopy and Nano-Imaging. *Science* **318**, 1750-1753, doi:10.1126/science.1150124 (2007).

4 Andreev, G. Application of Infrared Nanooptics to Ultrathin Materials. *Thesis* (2011).

5 Eigler, D. M. & Schweizer, E. K. Positioning single atoms with a scanning tunnelling microscope. *Nature* **344**, 524-526 (1990).

6 Binnig, G. & Rohrer, H. Scanning tunneling microscopy - from birth to adolescence. *Reviews of Modern Physics* **59**, 615-625 (1987).

7 Binnig, G., Quate, C. F. & Gerber, C. Atomic Force Microscope. *Physical Review Letters* **56**, 930-933 (1986).

8 Giessibl, F. J. Advances in atomic force microscopy. *Reviews of Modern Physics* **75**, 949-983 (2003).

9 Hartmann, U. Magnetic Force Microscopy. *Annu. Rev. Mat. Sci.* **29**, 53-87 (1999).

10 Hug, H. J., Stiefel, B., Schendel, P. J. A. v., Moser, A., Martin, S. & Güntherodt, H.-J. A low temperature ultrahigh vaccum scanning force microscope. *Review of Scientific Instruments* **70**, 3625-3640, doi:10.1063/1.1149970 (1999).

11 Gaisch, R., Gimzewski, J. K., Reihl, B., Schlittler, R. R., Tschudy, M. & Schneider, W. D. Low-temperature ultra-high-vacuum scanning tunneling microscope. *Ultramicroscopy* **42–44, Part 2**, 1621-1626, doi:http://dx.doi.org/10.1016/0304-3991(92)90495-6 (1992).

12 Rugar, D., Mamin, H. J. & Guethner, P. Improved fiber‐optic interferometer for atomic force microscopy. *Applied Physics Letters* **55**, 2588-2590, doi:10.1063/1.101987 (1989).

13 Lübbe, J., Tröger, L., Torbrügge, S., Bechstein, R., Richter, C., Kühnle, A. & Reichling, M. Achieving high effective Q-factors in ultra-high vacuum dynamic force microscopy. *Measurement Science and Technology* **21**, 125501 (2010).

14 Pohl, D. W. Some design criteria in scanning tunneling microscopy. *IBM J. Res. Dev.* **30**, 417-427, doi:10.1147/rd.304.0417 (1986).

15 Okano, M., Kajimura, K., Wakiyama, S., Sakai, F., Mizutani, W. & Ono, M. Vibration isolation for scanning tunneling microscopy. *Journal of Vacuum Science & Technology A: Vacuum, Surfaces, and Films* **5**, 3313-3320, doi:10.1116/1.574189 (1987).

CHAPTER 6: Exploring nanotextured phase coexistence in the correlated insulator V_2O_3

6.1 Abstract

The insulator-metal transition remains among the most studied phenomena in correlated electron physics. However, the spontaneous formation of spatial patterns amidst insulator-metal phase coexistence remains poorly explored at the meso- and nano-scales. Here we present real-space evolution of the insulator-metal transition in a V_2O_3 thin film imaged at high spatial resolution by cryogenic near-field infrared microscopy. We resolve spontaneously nanotextured coexistence of metal and correlated (Mott) insulator phases near the insulator-to-metal transition (~160-180K) associated with percolation and an underlying structural phase transition. Augmented with macroscopic temperature-resolved x-ray diffraction measurements of the same film, a quantitative analysis of nano-infrared images acquired across the transition suggests decoupling of electronic and structural transformations. Persistent low-temperature metallicity is accompanied by unconventional critical behavior, implying that long-range Coulomb interactions may govern the nanotexture of phase coexistence through the film's first-order insulator-metal transition.

6.2 Introduction

The subtle interplay of charge, spin, and orbital degrees of freedom in complex correlated oxides is known to result in strongly inhomogeneous phases, even in equilibrium.[1] In several families of correlated oxides including cuprates.[2,3] and manganites,[4,5,6] competing short- and long-range interactions give rise to emergent real-space patterns[7] that can provide fundamental clues to the principles underlying exotic behavior of these systems. Spontaneous self-organization of coexistent phases remains largely unexplored in real-space among many classes of materials exhibiting a first-order insulator-metal transition (IMT), attributable mostly to the absence of real-space probes capable of imaging the highly insulating side of the transition with nano-scale resolution. Enabled by nano-resolved infrared (nano-IR) imaging,[8] we demonstrate how a self-organized real-space electronic nanotexture underlies a five orders-of-magnitude change in resistivity through the IMT of V_2O_3. Furthermore, we resolve hitherto unreported characteristics of this correlated electron system, which challenge the conventional conventional picture of an abrupt first-order insulator-metal transition.

The IMT in V_2O_3 from paramagnetic metal (PM) to low temperature (T~160K) antiferromagnetic insulator (AFI)[9] arises from a thermally perturbed balance of entropy, kinetic energy, and Coulomb repulsion among conduction electrons,[10,11] leading to abrupt electron localization and a 0.7 eV energy gap.[12] These features appear intimately associated with a structural phase transition (SPT) from a corundum lattice to a lower symmetry monoclinic structure.[10] Increasingly refined studies have revealed unforeseen aspects of this transition,[13,14,9] hypothesizing a more subtle phase diagram where real-space phase inhomogeneities play an essential role. The IMT and SPT have been found to decouple in the related compound VO_2, whereby a strongly correlated monoclinic metal emerges between low temperature monoclinic insulating and high temperature rutile metallic phases.[15,16] However, the exact role of Mott physics in VO_2 remains hotly debated, calling for a critical examination of real-space features

entering the IMT of V_2O_3 at low T, where the role of electron localization by Coulomb repulsion is more conclusive. [11,17,18,19]

We developed cryogenic infrared near-field (nano-IR) imaging (see Appendices) to assess nano-scale phase inhomogeneity[20,21] emerging through the classic IMT in V_2O_3. Here, we imaged a 300 nm thick highly oriented V_2O_3 thin film (Appendices) at 25 nm resolution, revealing a spontaneous real-space nanotexture reflective of interactions governing the IMT. Upon first cooling into the transition, our local nano-optical probe resolves bi-directional stripes of the correlated insulator phase percolating through the parent paramagnetic metal, whereas macroscopic x-ray diffraction (XRD) of the same film reveals a concurrent corundum-to-monoclinic structural phase transition. Lower temperatures of the IMT render a complete structural transition, whereas metallic patches persist in an insulating background, implying that a novel monoclinic metal phase endures amidst the correlated insulator phase. Evolving real-space correlations and critical scaling among electronic domains suggest a crossover in the character of long-range interactions governing the electronic nanotexture: stripes stabilized by structural coexistence give way to a "droplet" texture as predicted by frustrated mean-field theories that account for long-range Coulomb interactions.[22,23,24,25]

6.3 Sub-diffractional imaging across the insulator-metal transition

Throughout this work we examine images of nano-IR signal *S* (Fig. 6.1a) normalized to an absolute reference through inclusion of a lithographically defined gold electrode within the imaging field of view (FOV) (not shown). We report details of nano-IR image processing in the online Supplementary Information (SI.II)[51]. Contrasts in the nano-IR signal form a reliable probe of local metallicity and therefore of the nano-scale IMT in correlated oxides (Appendices).[20,15,21] Here, we apply a color scheme in which *red* represents high nano-IR signal, indicating metallic regions. In contrast, insulating domains where the dielectric function is positive present reduced nano-IR signal[20,21] and are represented in *blue.* Fig. 6.1c displays a subset of images extracted

from a fixed 20 × 20 μm^2 FOV at select temperatures through a cooling and warming cycle measured with 920 cm^{-1} (~11 μm wavelength), probing predominantly the free-carrier optical (Drude) response of V_2O_3 according to far-field spectroscopy.[12,11] The most prominent features of these images are bi-directional stripes emerging spontaneously through the transition. Upon cooling from the metallic state (204 K), stripes of insulating material appear (175 K), grow (172 K), and fragment the metallic state (169 K), producing a striped pattern of metallicity. As the film resistance rapidly grows (160-170 K), metallic stripes disconnect (164 K), disorder into patches, and subsequently vanish into an insulating background (162 K). The transition follows a reverse trajectory upon heating, albeit with a 6 K hysteresis. Images acquired at higher spatial resolution (25 nm pixels) are presented in Fig. 6.1b, clearly showing the growth of metallic domains in an insulating background upon warming.

Images in Fig.1 show that the IMT progresses upon decreasing temperature through four successive stages: i) a homogeneous metallic state, ii) a striped nanotexture of percolating electronic phase coexistence, iii) an inhomogeneous insulating state populated with metallic patches, and iv) a homogeneous correlated insulator state. The bipartite character of phase coexistence suggests a first-order phase transition with two characteristic values of the "order parameter" (carrier density), in accord with conventional expectations for the Mott transition into an AFI state.[11,10,26] The majority of "domain walls" between metallic and insulating regions are sharp within our spatial resolution (Fig. 6.1b). Most surprisingly, we note that nano-IR signal levels characteristic of the distinct phases themselves evolve gradually across the transition, uncovering *bona fide* thermal evolution of the electronic response, in contrast to a "monolithic" phase transition between end-phases. Fig. 6.2b quantifies the *binary* yet *thermally evolving* character of the transition via a histogram representation of nano-IR signals recorded at distinct temperatures upon warming. Each bimodal nano-IR signal distribution consists of two distinct populations amidst the IMT. We identify these with "insulating" (dashed blue curve) and "metallic"

(dashed red) sub-populations, each well fit by an asymmetric (skew) normal distribution. Such binary behavior has been previously observed in VO_2.[20]

6.4 Thermal evolution of insulator and metallic phases

Significant thermal evolution of the observed "metallic phase" is attributable to continuous changes in optical conductivity of these domains. This evolution is consistent with a suppression of quasiparticle weight or pseudogap across the Mott IMT as predicted theoretically[27] and suggested by area-averaged spectroscopies of V_2O_3.[26,13,12] Meanwhile, systematic temperature dependence of the nano-IR signal from "insulating" regions is also noteworthy. An increase in their nano-optical signal while warming suggests a scenario whereby the insulating band-gap of the AFI state narrows through the IMT until becoming comparable to our probing energy (110 meV). Accordingly, calculations by cellular dynamical mean-field theory have proposed a narrow- to large-gap progression of the Mott insulating state in the phase-coexistent regime of the Hubbard model,[29] and area-averaged optical probes also report an emergent pseudogap close to the IMT.[12,26] Moreover, mean-field treatments of photoexcitation in the related compound VO_2 find that changes in d-orbital occupancy can induce smooth collapse of the insulating gap preceding the abrupt IMT.[30] Our imaging results lend support to such scenarios among nano-scale regions in V_2O_3.

To bolster our attribution of insulating and metallic regions, we applied a binarization procedure (Appendices) to analyze evolving cluster sizes and areal fractions of insulating and metallic phases. The dash-dotted curves of Fig. 6.2a obtained by this analysis display the area A_{max} (percentage of the FOV) of the largest cluster observed at each temperature. Fig. 6.2a shows that A_{max} peaks at a temperature identifiable as the percolation threshold T_{perc}. At this temperature the percolating phase switches in identity from "metallic" to "insulating" upon cooling, or *vice versa* upon warming. T_{perc} thus marks the percolation event, *i.e.* the formation of an "infinite" conducting pathway across the entire FOV and, by inference, the whole V_2O_3 film.

Meanwhile, T_{perc} is also identifiable from the film's temperature dependent electrical resistance R or conductance $G = R^{-1}$. Viewed as an effective circuit comprising parallel conductive pathways, the greatest change in film conductance is expected when the largest conductive pathway is formed or removed. Accordingly, the thermal derivative of the film conductance $\partial G \equiv \frac{d}{dT} R^{-1}$ (solid curves in Fig. 6.2a, obtained from *ex situ* resistance measurements) reaches a maximum value when the largest conducting pathway (spanning the film electrodes) is broken up. Our comparison between A_{max} and ∂G shows that percolation thresholds identified both *in* and *ex situ* agree to within 1 K and percolation occurs at 168 K (174 K) upon cooling (warming).

Having established a nano-scale classification of metal and insulator, our binary images can reliably estimate the relative fill fractions of the two phases. Moreover, *ex-situ* XRD measurements of the same V_2O_3 film reveal relative intensities of corundum and monoclinic diffraction peaks (Appendices), allowing assessment of constituent structural phase fractions (Fig. 6.2d). Fig. 6.2c compares the thermometry-calibrated (SI.III [51]) metallic fraction (symbols) obtained by nano-IR to the corundum fraction (solid curves) obtained by XRD, revealing a 6 K thermal offset between electronic and structural transitions. Consistent with the percolation temperature identified *in* and *ex situ*, we find the metallic constituent is about 60% at 168 K while cooling, whereas the occupation of the corundum phase at this temperature remains ~25%, with an uncertainty of about 10%. This implies that some metallic regions must exhibit the monoclinic structure. Combined nano-IR and XRD measurements thus provide the first clear evidence that electronic and structural transitions can decouple in a V_2O_3 film.

Enabled by co-localized images at numerous temperatures, the binarizing threshold signal $S_{thresh}(T)$ pinpoints the temperature at which an individual image pixel switches from one electronic sub-population to the other. This protocol defines a local insulator-metal transition temperature T_{IMT} resolved at each pixel with 25 nm precision (see also Fig. S11 [51]). Fig. 6.3a presents the thermal distribution of T_{IMT} from all image pixels, with consolidated data from cooling and warming (after removing the relative 6K hysteresis). We identify the peak of the distribution

with a characteristic temperature T_E for the electronic transition, equal to 164K (169K) for cooling (warming). The distribution shows that the IMT is most likely to occur at this temperature, a full 10K below the structural phase transition temperature T_{SPT} where XRD indicates the SPT is most rapid (and where structural phases are detected at 50% fraction). Fig. 6.3b presents a phase diagram comprised of phase fractions (PF) obtained from our data, with electronic and structural transitions shown on orthogonal axes. Moreover, the temperature range for the implied monoclinic metal (MM) is denoted in proximity to T_E.

6.5 Striped nanotexture and the structural phase transition

The most striking feature in our images is the spontaneous formation of bi-directional stripes (Fig. 6.3d), suggesting an underlying organizational principle that could further elucidate the interplay between structural and electronic transitions. To characterize growth of these stripes, we quantify the extent of orientational anisotropy presented by domain walls as a function of temperature (S.IV). Fig. 6.3c reveals this anisotropy is maximized 10K above T_E, matching well the structural phase transition temperature T_{SPT}. Likewise, we detect a pattern of <1 nm topographic corrugations (Fig. 6.3e) emerging at temperatures of the underlying SPT (Fg. S9 [51]). Nanometer-scale surface buckling likely accompanies the differential unit cell volumes of coexisting structural domains.[15,31] These topographic features broadly coincide in real-space with the electronic nanotexture revealed by nano-IR (Fig. 6.3d&3e), and their spatial cross-correlation is maximal at temperatures where the IMT and SPT overlap (Fig. S9 [51]). Moreover, the striped electronic nanotexture exhibits periodicity that is best revealed through the temperature dependent *static structure factor*, obtained as the spatial Fourier transform of the 2-dimensional correlation function for phase coexistence (see Appendices).[6,32] Panels in Fig. 6.3f present the structure factor amplitude while cooling through three characteristic temperatures: close to T_{SPT} (T_E+10K), above T_E (T_E+4K), and below T_E (T_E-5K). Peaks in the structure factor that appear sharpest near T_{SPT} reflect preferential wave-vectors for the spontaneous formation of anisotropic

stripes. Spaced at 60° or 120° angular separations, these wave-vectors explicitly reveal that 3-fold rotational symmetry of the high-temperature corundum structure is broken bi-directionally by at least two monoclinic twin configurations.[33] A third crystallographic twin is expected but unobserved in our images, perhaps due to excess elastic mismatch of this domain orientation with the substrate. The mean length scale corresponding to wave-vectors in Fig. 6.3f encodes the emergent periodicity resulting from phase coexistence in our film.[34,35] We associate this periodicity with a structural correlation length ξ_{struct}, as visualized in Fig. 6.4a, which shows a section of the correlation function perpendicular to stripes observed near T_{SPT} (see Appendices, Fig. S10 [51]). As shown in Fig. 6.4b, ξ_{struct} rises abruptly to a value of about 1.2 μm with a broad plateau centered also in the temperature range identified by XRD with the SPT.

The association of long-range spatial correlations and striped nanotexture with T_{SPT} is unmistakable. Indeed, a well-known real-space pattern of equilibrium structural phase coexistence (SPC) can emerge spontaneously during a SPT, taking the form of a “tweed” texture to minimize elastic strain energies among structural domains and the substrate.[7,34,35] Detailed studies of the sister compound VO_2 have revealed similar real-space patterns of SPC tunable by temperature and by intrinsic or extrinsic stress.[36,31] Therefore, the observed temperature dependent anisotropy and ξ_{struct} both suggest that the striped electronic nanotexture revealed by our images within this ~20K temperature window is largely a consequence of the IMT “guided” by the underlying SPT. For temperatures near T_{SPT}, the lattice mismatch between monoclinic and corundum structural domains produces long-range elastic interactions (accommodation strain) governing the coexistence of electronic phases.[34,35] Additional nano-IR imaging of a thinner (100 nm) V_2O_3 film (SI.V and Figs. S12 & 13 [51]) reveals that ξ_{struct} is tunable with thickness in a fashion consistent with nanotexture mediated by accommodation strain.

6.6 Hallmarks of the electronic Mott transition

As temperature decreases further towards T_E, we encounter clues concerning the character of monoclinic metallicity in this V_2O_3 film. First, we confirm that the low-temperature IMT proceeds by a clear first-order electronic phase transition even among persistent metallic domains. Fig. 6.4g presents characteristic transition curves (S vs. T) for *loci* of pixels that exhibit the same transition temperature T_{IMT} upon cooling. Taking the transition curve corresponding to T_{IMT}=176K (red) for reference, Fig. 6.4h reveals a sharp first-order discontinuity in S for all T_{IMT}, and by implication, abrupt decrease in the Drude response. Sir Neville F. Mott's idealization of this IMT predicted such discontinuity on the basis of the long-range Coulomb interaction.[10] Dynamical mean field theory studies of the Hubbard model have rigorously predicted a first-order Mott transition.[37,11,24] Such a first order transition is now first evidenced among remnant metallic domains in the monoclinic phase. However, owing to further thermal evolution of the insulating phase observed throughout the IMT (Fig. 6.2b), we note that this first-order transition does not immediately yield the ultimate low-temperature AFI state appearing at T<160K.

The size and shape of persistent metallic domains is pertinent to the interactions governing their transition. The Landau theory for phase transitions holds that a thermally fluctuating balance between volumetric and surface free energies (associated in the Mott transition with electronic degrees of freedom[27]) among patches of the emerging phase will determine their spatial extent by way of short-range correlations.[38] We denote this spatial scale the electronic correlation length ξ_{elec}, and extract it at each temperature from the central full-width at half maximum of the correlation function (Fig. 6.4a; see Appendices). Fig. 6.4e and 4f show ξ_{elec}, which quantifies the characteristic isotropic length scale of electronic domains, reaching a maximum (~400 nm) at T_E. The growth and peak in ξ_{elec} near T_E reveals the tendency for metallic domains to form "droplets" at these temperatures rather than stripes (Figs. 4f and 4i). This behavior resembles the strong temperature dependence of spatial correlations that exhibit universal scaling near a critical point.[38,17,39] Similarly, we observe robust critical scaling through

the transition in the temperature dependence of the largest electronic domain size $d_{\max} \equiv \sqrt{A_{\max}}$ ($A_{\max}$ as presented in Fig. 6.2a) observed to scale as $\left|T - T_{\mathrm{perc}}\right|^{-\upsilon}$ with $\nu = 0.96 \pm 0.07 \approx 1$ (Fig. 6.4d). Our directly resolved scaling shows quantitative agreement with the scale invariant nucleation site density inferred from area-averaged optical studies of similar V_2O_3 films.[40]

While considering the thermal evolution of these metallic domains, it is worth noting that our V_2O_3 film presents a metal-insulator transition among the cleanest (most abrupt) yet reported. Indeed, as evidenced by dissimilar maps of T_{IMT} for cooling and warming (Fig. S11 [51]), positions of low-temperature metallic patches are largely spontaneous, implying a decoupling from pinning sites. Although critical scaling behaviors are unexpected amidst the first-order transition of a clean system, here they might be reconciled with predictions for frustrated phase separation in the Hubbard model. Below the Mott transition temperature, uniform band filling in the homogeneous state is proposed to become unstable at a fixed chemical potential, and the system phase-separates into regions with distinct charge density *n* associated with the insulating state at half band-filling and a slightly doped metallic state.[25] This charge disproportionation Δn is theorized to reach a few percent amidst the transition.[24] Consequently, long-ranged Coulomb interactions between domains are expected to penalize macroscopic charge separation, whereas interfacial domain wall energy σ favors few coexistent domains. This competition can produce a frustrated texture of droplet-shaped domains with characteristic size $d \sim \left(\frac{\sigma}{\Delta n^2}\right)^{1/3}$ whose correlation length $\xi_{\mathrm{elec}} \propto \Delta n^{-1}$ is determined by screening.[23,25,22,41] The weak divergence of ξ_{elec} we observe in this temperature regime may arise from vanishing Δn as *T* approaches the probable IMT temperature T_E.[24] Moreover, mean-field treatments of Coulomb frustrated phase transitions have predicted power-law scaling of the characteristic droplet domain size with temperature, consistent with our observations for $d_{\max}(T)$.[22] Most importantly, the intermediate appearance of a spontaneously nanotextured state across a first-order transition points to the

relevance of long-range interactions that fundamentally prohibit a conventionally abrupt transition between end-phases.[41]

6.7 Epitaxy and the low-temperature metallic phase

Coulomb interactions can account for the crossover near T_E to a spontaneous droplet nanotexture that forms independently of the structural transition. Nevertheless, the origin for a novel monoclinic metal (MM) phase still invites explanation. Such a low temperature metallic phase is reminiscent of reports for the related correlated oxide VO_2.[16,20,15,32,42] Whereas a transient or pressure-induced MM has been observed even in VO_2 single-crystals,[43,44] its more robust appearance in thinner extrinsically or epitaxially strained samples suggests a general mechanism decoupling the IMT from the SPT. For example, studies of the semi-infinite Hubbard model have predicted that interfacial metallicity stabilizes amidst a bulk Mott insulating state.[45] Meanwhile, X-ray absorption studies of V_2O_3 have identified inequivalent metallic states accessed through thermal and pressure-driven transitions[46] and have revealed a novel pressure-induced MM phase,[14] related perhaps to that detected here.

We propose that epitaxial strain and the consequent striped SPT nanotexture play a crucial role among films. Indeed, a stabilized intermediate electronic state with attributes of the high-temperature phase has previously been observed below the magnetoresistive transition temperature of manganite films.[47] This intermediate state was linked to accommodation strain from coexistent structural phases. Consequently, we speculate that an intermediate MM phase in epitaxial V_2O_3 may be stabilized by epitaxial strain. Alternating regions of tensile and compressive accommodation strain in the striped nanotexture[15] may produce local deviations in the c/a lattice constant ratio. These deviations are expected to modulate orbital occupancy of both IMT end-phases,[46,48] perhaps giving rise to their temperature dependent optical response as observed here. Indeed, phase coexistence in a thinner V_2O_3 film, where effects of epitaxial strain are yet more prominent (see SI [51]) reveals even further “coarsening” of the optical distinction between metal and insulator phases. Although tuning of orbital occupancy has been studied[30]

and demonstrated in epitaxial VO_2,[49] such effects have not yet been investigated at the nanoscale. Moreover, the crossover observed here in V_2O_3 from striped (strain-mediated) to droplet nanotexture awaits observation in VO_2.

6.8 Conclusion

Associating the persistent low-temperature metallic phase of V_2O_3 with a strain-induced or Coulomb-frustrated phase implies novel real-space features of the insulator-metal transition, hitherto unexplored. Our study reveals that a rich interplay of short- and long-range interactions can lead to spontaneously nanotextured phase coexistence across the low temperature insulator-metal transition in V_2O_3. Nano-optical imaging affirms that unexpectedly rich behaviors can underlie even this classic insulator-metal transition, while demanding modifications to the conventional phase diagram for strained epitaxial structures.[17,10] Low-temperature nano-spectroscopic probes and X-ray magnetic imaging will be essential to further elucidate the electronic character of intermediate phases emerging amidst the insulator-metal transition in V_2O_3 and other correlated oxides.

6.9 Acknowledgements

Personnel involved in this work were supported by grants DOE-DE-SC0012375, DOE-DE-SC0012592, and AFOSR FA9550-12-1-0381, and by the EPiQS Initiative through Grant GBMF4533. A. S. McLeod acknowledges support from a U.S. Department of Energy Office of Science Graduate Fellowship (SCGF). Development of methods for cryogenic nano-infrared imaging is supported by ARO-w911NF-13-1-0210, ONR-N00014-15-1-2671.

This chapter, in full, is a reprint of the material as it appears in the following published article: A. S. McLeod, E. van Heumen, J. G. Ramirez, S. Wang, T. Saerbeck, S. Guenon, M. Goldflam, L. Anderegg, P. Kelly, A. Mueller, M. K. Liu, I. K. Schuller, D. N. Basov. Nanotextured phase coexistence in the correlated insulator V_2O_3. *Nat. Phys.* DOI: 10.1038/NPHYS3882. The dissertation/thesis author was the co-primary investigator and author of this material.

6.10 Figures

Figure 6.1: nano-IR imaging of the insulator-metal transition in V_2O_3.

a) Schematic depiction of near-field microscopy of phase coexistence in a V_2O_3 thin film; nano-IR signal superimposed on film topography at 171K (cooling). b) High-resolution co-localized near-field images of coexisting phases evolving upon warming the film from the antiferromagnetic insulator (AFI) to paramagnetic metal (PM) phase; 1 micron scale bar; color scale as in c). c) Large-area co-localized nano-IR images of the electronic phase transition upon cooling (blue arrows) and warming (orange arrows); 5 microns scale bar. The color scale (bottom) distinguishes metallic from insulating regions by their nano-IR signal *S*. d) Resistance of the film versus temperature upon cooling (blue arrow) and warming (orange arrow); dashed lines demarcate the temperature range of phase-coexistence in the insulator-to-metal transition (IMT). Inset: schematic arrangement of gold pads on the film surface used as in-situ transport electrodes and for quantitative normalization of near-field images.

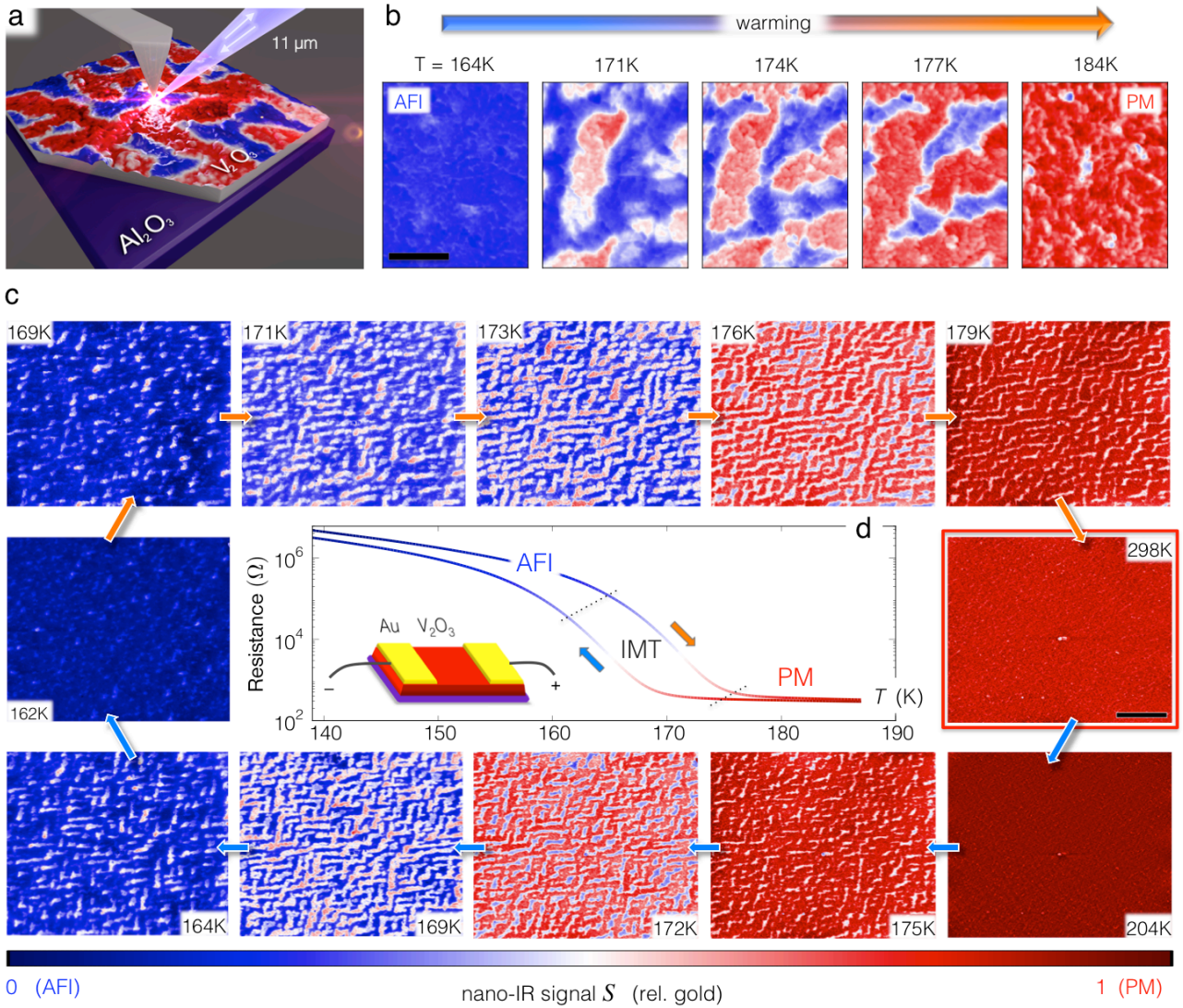
a
11 μm
V_2O_3
Al_2O_3
b
warming
T = 164K
171K
174K
177K
184K
AFI
PM
c
169K
171K
173K
176K
179K
298K
162K
164K
169K
172K
175K
204K
d
Resistance (Ω)
10^6
10^4
10^2
AFI
IMT
PM
Au
V_2O_3
–
+
140
150
160
170
180
190
T (K)
0 (AFI)
nano-IR signal S (rel. gold)
1 (PM)

Figure 6.2: Bimodal analysis of phase distributions in V_2O_3.

a) Comparison of the size of the largest insulating or metallic cluster observed by near-field microscopy (A_{max}) against changes in film transport conductance per unit temperature ∂G for both cooling and warming; both metrics identify a coincident percolation threshold. b) Histogram representation of near-field signal amplitudes (*viz.* optical near-field reflectance) collected from the film at a subset of temperatures upon warming from 164K to 184K, relative to an ideal metal (gold); an example fit to the distribution at 173K by two asymmetric normal distributions reveals insulating (dashed blue) and metallic (dashed red) populations evolving with temperature, demarcated by a temperature-dependent threshold value of the near-field signal S_{thresh}, indicated from above by arrows; note vertical log scale. c) Thermometry-calibrated comparison of areal fill fractions for the metallic phase identified by nano-IR imaging against volumetric fractions for the high-temperature structural phase (corundum) identified by XRD; an anomalous thermal offset suggests persistent metallicity in the monoclinic structural phase. d) Bimodal decomposition of diffraction peaks measured by X-ray diffraction (XRD) admits measurement of structural fill fractions (Methods).

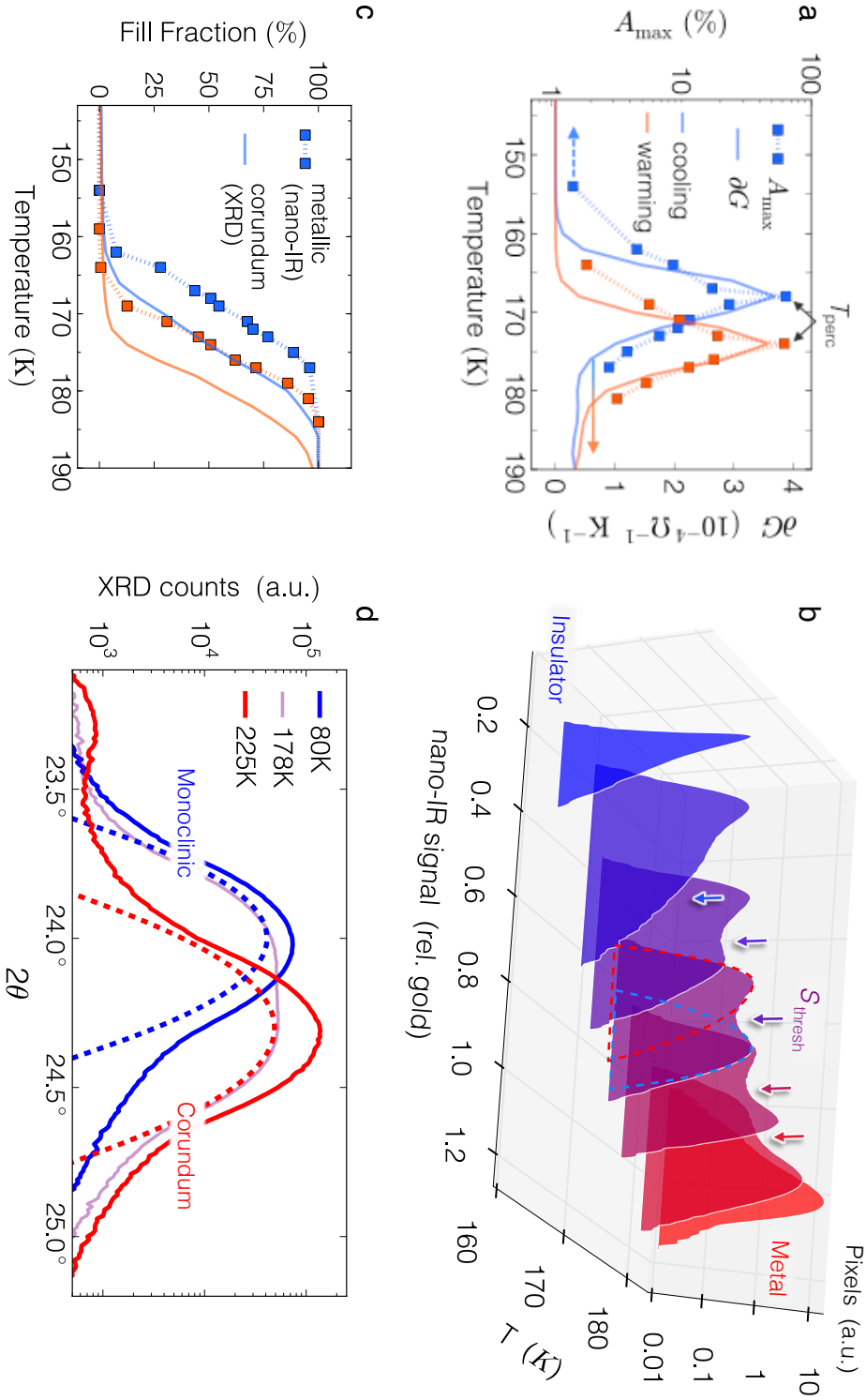
a
A_{max} (%)
A_{max}
∂G
cooling
warming
T_{perc}
∂G ($10^{-4}\Omega^{-1}$ K^{-1})
Temperature (K)
b
Insulator
Metal
S_{thresh}
Pixels (a.u.)
nano-IR signal (rel. gold)
T (K)
c
Fill Fraction (%)
metallic (nano-IR)
corundum (XRD)
Temperature (K)
d
XRD counts (a.u.)
80K
178K
225K
Monoclinic
Corundum
2θ

Figure 6.3: Phase diagram for electronic and structural phases in thin-film V_2O_3.

a) Distribution of insulator-metal transition temperatures T_{IMT} obtained as the fraction of observed pixels to transition per degree K; data from cooling and warming together. The peak in the transition indicates the characteristic transition temperature, T_E. b) Phase diagram presenting *T*-dependent fill phase fractions (PF) for electronic and structural phases (orthogonal axes) measured by nano-IR imaging and X-ray diffraction (XRD). *EPC* = electronic phase coexistence; *SPT* = structural phase coexistence; *MM* = monoclinic metal. c) Directional anisotropy of electronic domain walls versus temperature as obtained from a binary insulator-metal classification of nano-IR image pixels; anisotropy maximizes abruptly at the structural phase transition temperature T_{SPT}, associating electronic anisotropy with “guiding” by the SPT. d) Subset of nano-IR image at T_E+4K (warming) compared with e) topographic corrugations (relative to 298K) detected simultaneously by AFM; scale bar: 5 microns. f) Static structure factor (see text) of EPC measured near T_{SPT}, above T_E, and below T_E, revealing preferred structural wave-vectors emerging at 60^o lateral separations; colored dots indicate temperatures on the phase diagram panel b).

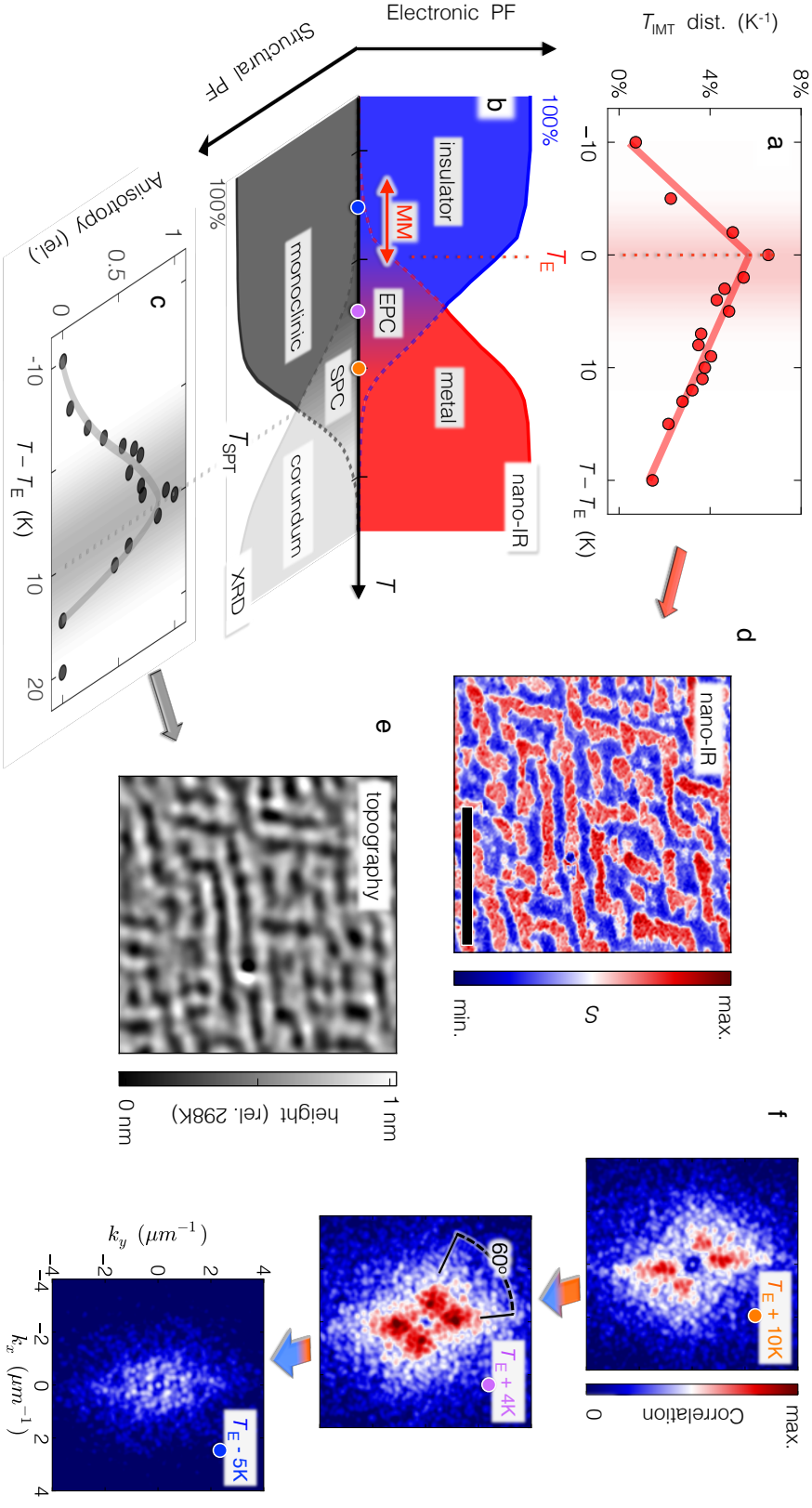
a
T_{IMT} dist. (K^{-1})
8%
4%
0%
−10
0
10
$T - T_E$ (K)
b
Electronic PF
Structural PF
100%
100%
insulator
MM
monoclinic
EPC
SPC
metal
nano-IR
corundum
XRD
T_E
T_{SPT}
T
c
Anisotropy (rel.)
1
0.5
0
-10
10
20
$T - T_E$ (K)
d
nano-IR
min.
S
max.
e
topography
height (rel. 298K)
0 nm
1 nm
f
T_E + 10K
Correlation
0
max.
60°
T_E + 4K
T_E - 5K
k_y (μm^{-1})
k_x (μm^{-1})

Figure 6.4: Composite phenomena amidst the insulator-metal transition in V_2O_3.

a) Trace from the image correlation function obtained 9K above T_E, perpendicular to the direction of stripes; relevant correlation lengths are indicated. b) The structural correlation length associated with periodic correlations; ξ_{struct} plateaus at T_{SPT} and originates from structural phase coexistence. c,f,i) Acquisition temperatures for nano-IR images indicated by colored dots in panel e). c) Indication of ξ_{struct} associated with real-space stripe periodicity; scale bar: 2 microns. d) Scale invariance of the largest electronic domain size d_{max}, fitting a power law with critical exponent $\nu \approx 1$ close to the percolation threshold temperature T_{perc}. e) The electronic correlation length associated with short-range correlations; ξ_{elec} peaks abruptly at T_E. f) Indication of ξ_{elec} associated with the characteristic size of metallic droplets; field of view is a subset of panel c); scale bar: 1 micron. g) Average transition curves (nano-IR signal S vs. T) acquired from pixels exhibiting insulator-metal transition temperatures T_{IMT}=176K (red) to 160K (blue) upon cooling. h) Curves from g) after referencing to T_{IMT}=176K, revealing a first-order discontinuity in S down to T_{IMT}=160K. i) Monoclinic metallic matches are observed to persist even 10K below T_E (~19K below T_{SPT}); scale bar: 1 micron.

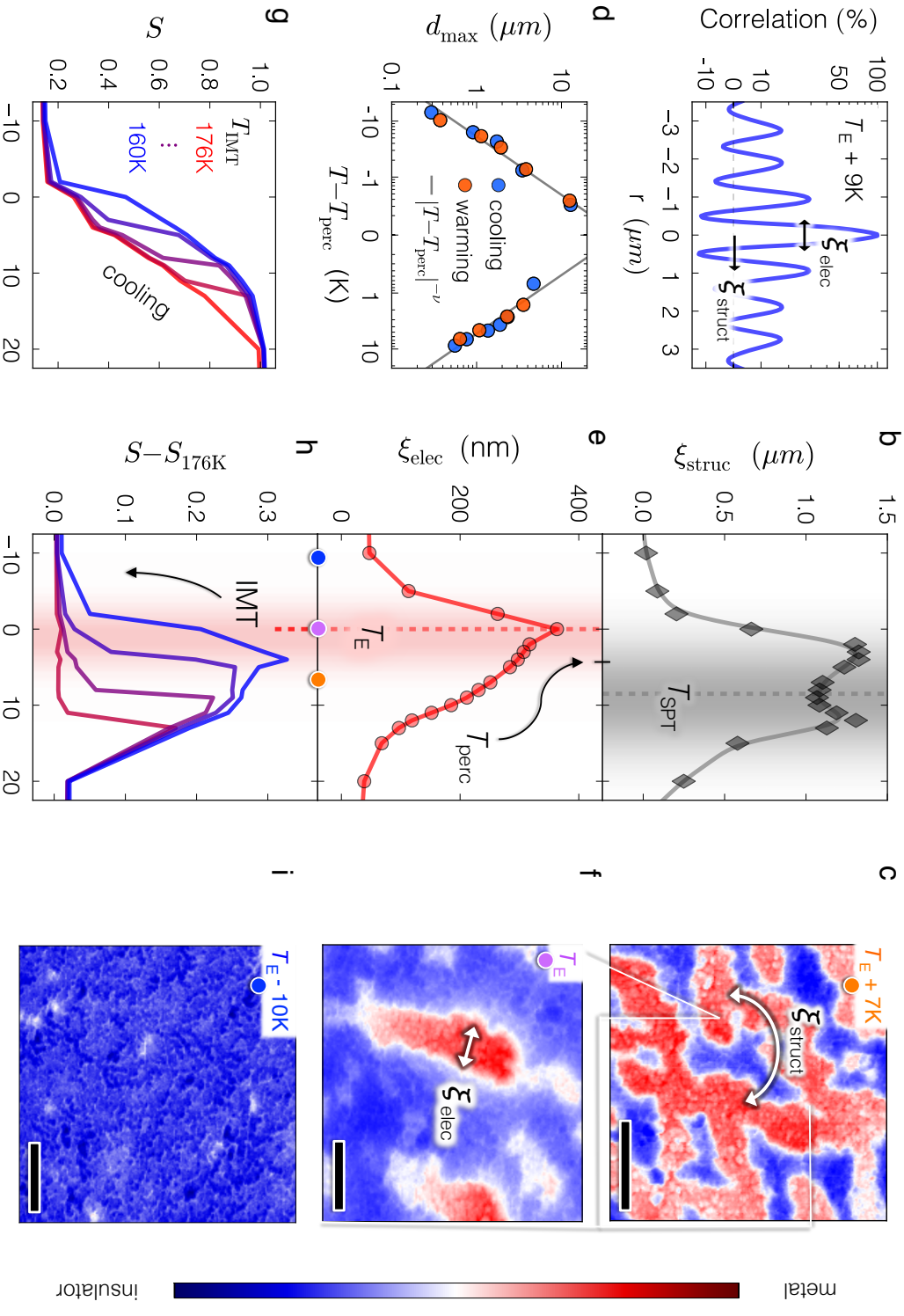
a
Correlation (%)
T_E + 9K
ξ_{elec}
ξ_{struct}
r (μm)
b
ξ_{struc} (μm)
T_{SPT}
c
T_E + 7K
ξ_{struct}
d
d_{max} (μm)
cooling
warming
$|T-T_{perc}|^{-\nu}$
$T-T_{perc}$ (K)
e
ξ_{elec} (nm)
T_E
T_{perc}
f
T_E
ξ_{elec}
g
S
T_{IMT}
176K
160K
cooling
$T-T_E$ (K)
h
$S-S_{176K}$
IMT
$T-T_E$ (K)
i
T_E - 10K
metal
insulator

6.11 Appendix A: Cryogenic near-field optical nanoscopy

Scattering-type scanning near-field optical microscopy (s-SNOM) enables imaging of surface optical properties at variable temperatures[50] below the diffraction limit, with a resolution limited only by the geometric probe sharpness. [21,28] Here, we present images of the locally back-scattered near-field signal amplitude (abbreviated to *nano-IR signal*, or *S*) collected at low temperatures using a newly developed cryogenic near-field optical microscope (SI.I and Figs. S1 & S2 [51]). Metallic regions where the *DC*-conductivity is high and the real part of the dielectric function is negative (at the probing IR frequency) yield high nano-IR signals comparable to that of good metals (*viz.* gold). We recorded nano-IR images upon cooling from room temperature across the IMT down to *T*=24 K with a temperature interval of 2-4K between 160K - 180K, followed by a similar number of measurements upon warming to room temperature. Consistent results were also obtained on a 100 nm V_2O_3 film (SI.V and Figs. S12 & 13 [51]). All measurements were conducted in an ultra-high vacuum ($<10^{-8}$ mbar) environment to prevent surface contamination.

6.12 Appendix B: Growth of V_2O_3 Films

This work focuses on a 300 nm thick highly oriented V_2O_3 film (3 nm RMS surface roughness, see SI [51]; surface topography presented in Fig. 8) which displays a five-orders of magnitude increase in electrical resistance across the IMT from 180K to 150K (Fig. 6.1d) with a cooling/warming hysteresis of 6K, characteristic of a first-order phase transition. Lithographically patterned gold pad electrodes on the film enabled *in situ* resistance measurements for accurate thermometry calibrations between nano-IR imaging and *ex situ* measurements of the same film (see SI [51]). This film together with a similar 100 nm film were both epitaxially grown on (012)-plane sapphire substrate by RF magnetron sputtering from a V_2O_3 target (1.5" diameter, > 99.7%, ACI Alloys, Inc.). The samples are prepared in a high vacuum system with a base pressure of 1×10^{-7} Torr. The substrate temperature was kept at 750°C during the deposition. 4 mTorr

ultrahigh purity (99.999%) Ar and 100 W RF power were used for the deposition of V_2O_3. These conditions yield a deposition rate of 0.67 Å/s. Based on X-ray diffraction characterization of the film, compressive strain from lattice mismatch between hexagonal lattice constants for room temperature sapphire and V_2O_3, combined with stress relief by film buckling and granularity, induces lattice expansion along the film c-axis and a concomitant increase in the c/a ratio relative to bulk crystals. Previous studies of sapphire-grown V_2O_3 films have equated this expansion with tensile hydrostatic chemical pressure attainable through chromium doping, affecting a putative decrease in bandwidth and increase in the Mott transition critical temperature.[48] Indeed, the transition temperature for our film is as much as 16K higher than for bulk crystalline V_2O_3. Notably, previously grown films displayed characteristics similar to the best available single crystal samples.[12]

6.13 Appendix C: Determination of structural phase fractions by X-ray diffraction

We have determined the SPT temperature and the crystallographic phase fraction in our film by performing temperature-dependent X-ray diffraction (XRD) measurements. We measured the out-of-plane XRD of the rhombohedral (012) peak shifts from $2\theta = 24.30°$ above the SPT (300 K) to the monoclinic (011) $2\theta = 24.05°$ below it (100 K). The peaks were then fitted with two Gaussian curves; keeping fixed the 2θ values of the low and high temperature phases. The area under each Gaussian was normalized to the total area and the percentage volume fraction of each phase was thus obtained. The temperature T_{SPT} is identified as that where the structural transition is most likely, and incidentally where both phases are equally populated.

6.14 Appendix D: Binarization procedure

As presented in Fig. 6.2b, the histogram distributions of near-field signal values S measured at temperatures amidst the IMT are strongly bi-modal. Each of these distributions is

well fit by a pair of skew normal (asymmetric Gaussian) distributions, which we associate with insulator and metal sub-populations. The point of intersection for these two normally distributed sub-populations (Fig. 6.2b) yields a threshold nano-IR signal that most probably distinguishes metal from insulator. We apply this temperature-dependent threshold $S_{thresh}(T)$ to assign individual pixels to the sub-populations of higher or lower conductivity (*viz.* metal or insulator). Having thus binarized our images, we then rigorously identified both the individual electronic clusters (contiguous domains of the minority phase) and overall electronic phase fractions from our images, enabling the results of Figs. 2a&c and Fig. 6.4d.

6.15 Appendix E: Correlation Analysis

Informally, the correlation function $g(\delta\vec{r})$ of an image $I(\vec{r})$ (evaluated at lateral positions $\vec{r}$) expresses the level of statistical similarity between image features separated by a displacement $\delta\vec{r}$. Formally, the correlation function is given by [38]:

$$g(\delta\vec{r}) = \langle \delta I(\vec{r}), \delta I(\vec{r}+\delta\vec{r}) \rangle = \int d^2\vec{r}\, [I(\vec{r}) - \langle I(\vec{r}) \rangle]\, [I(\vec{r}+\delta\vec{r}) - \langle I(\vec{r}+\delta\vec{r}) \rangle] \quad (1)$$

Here $\langle \cdots \rangle$ indicates an areal average of the enclosed value. Appearance of the mean value $\langle I(\vec{r}) \rangle$ in Eq. (1) reflects that only image inhomogeneities ("features") are relevant for the characterization of spatial correlations. Eq. (1) was used to compute the correlation function for each nano-IR image across the insulator-metal transition of our V_2O_3 film. Each correlation function was normalized to unity at $\delta\vec{r} = \vec{0}$, taken by construction to indicate 100% correlation.

The correlation function is known to reveal intrinsic periodicities more clearly within noisy data than would be possible to identify through direct inspection alone. We use this feature to identify periodicity in our nano-IR images, whose mean length scale we identify as ξ_{struct}. The characteristic wave-vector for this periodicity $k = 2\pi/\xi_{\mathrm{struct}}$ is most easily identified from the static structure factor $\tilde{g}(\vec{k})$, computed as the 2-dimensional Fourier transform of the correlation function:

$$\tilde{g}(\vec{k}) = \frac{1}{L^2}\int_{-L/2}^{L/2} d^2\vec{r}\, e^{-i\,\vec{k}\cdot\vec{r}}\; g(\vec{r}) \tag{2}$$

Here, *L* denotes the size of the image over which the correlation function is computed. Meanwhile, the rotational average of the correlation function (yielding $g(r)$, evaluated at displacement magnitude r alone) was used to identify ξ_{elec} according to its central full-width at half-maximum. This correlation length reflects the typical scale for statistical correlations to locally decay by e^{-1} and corresponds intuitively with the average characteristic dimension of image inhomogeneities. In our case these comprise puddles of the minority electronic phase – whether insulating in character above the percolation temperature, or metallic below. The weakly "divergent" character of ξ_{elec} revealed by our correlation analysis and the thermal scaling of metallic "droplet" sizes both resemble the phenomenology of Landau theory for scale-invariant spatial fluctuations proximate to the critical point of a *continuous* phase transition[38]. In the case of a first-order phase transition, long-range interactions can provide an alternative route to critical behavior.[22]

6.16 References

1. Dagotto, E., Complexity in strongly correlated electronic systems. *Science* **309**, 257 (2005).

2. Tranquada, J. M., Sternlieb, B. J., Axe, J. D., Nakamura, Y. & Uchida, S., Evidence for stripe correlations of spins and holes in copper oxide superconductors. *Nature* **375**, 561-563 (1995).

3. M. J. Lawler, K. Fujita, Jhinhwan Lee, A. R. Schmidt, Y. Kohsaka, Chung Koo Kim, H. Eisaki, S. Uchida, J. C. Davis, J. P. Sethna & Eun-Ah Kim. Intra-unit-cell electronic nematicity of the high-Tc copper-oxide pseudogap. *Nature* **466**, 347-351 (2010).

4. Uehara, M., Mori, S., Chen, C. H. & Cheong, S. W., Percolative phase separation underlies colossal magnetoresistance in mixed-valent manganites. *Nature* **399**, 560-563 (1999).

5. Ahn, K. H., Lookman, T. & Bishop, A. R., Strain-induced metal-insulator phase coexistence in perovskite manganites. *Nature* **428**, 401-404 (2004).

6. Keji Lai, Masao Nakamura, Worasom Kundhikanjana, Masashi Kawasaki, Yoshinori Tokura, Michael A. Kelly, & Zhi-Xun Shen. Mesoscopic Percolating Resistance Network in a Strained Manganite Thin Film. *Science* **329**, 190-193 (2010).

7. Seul, M. & Andelman, D., Domain Shapes and Patterns: The Phenomenology of Modulated Phases. *Science* **267**, 476-483 (1995).

8. Knoll, B. & Keilmann, F., Near-Field probing of vibrational absorption for chemical microscopy. *Nature* **399**, 134-137 (1999).

9. Frandsen, B. A.; Liu, L.; Cheung, S. C.; Guguchia, Z.; Khasanov, R.; Morenzoni, E.; Munsie, T. J. S.; Hallas, A. M.; Wilson, M. N.; Cai, Y.; Luke, G. M.; Chen, B.; Li, W.; Jin, C.; Ding, C.; Guo, S.; Ning, F.; Ito, T. U.; Higemoto, W.; Billenge, S. J. L.; Sakamoto, S.; Fujimori, A.; Murakami, T.; Kageyama, H.; Alonso, J. A.; Kotliar, G.; Imada, M.; & Uemura, Y. J. Volume-wise destruction of the antiferromagnetic Mott insulating state through quantum tuning. *Nature Communications* **accepted** (2016).

10. Imada, M., Fujimori, A. & Tokura, Y., Metal-insulator transitions. *Rev. Mod. Phys.* **70**, 1039 (1998).

11. Rozenberg, M. J.; Kotliar, G.; Kajueter, H.; Thomas, G. A.; Rapkine, D. H.; Honig, J. M.; & Metcalf, P. Optical Conductivity in Mott-Hubbard Systems. *Physical Review Letters* **75**, 1 (1995).

12. M. K. Stewart, D. Brownstead, S. Wang, K. G. West, J. G. Ramirez, M. M. Qazilbash, N. B. Perkins, I. K. Schuller, & D. N. Basov. Insulator-to-metal transition and correlated metallic state of V2O3 investigated by optical spectroscopy. *Phys. Rev. B* **85**, 205113 (2012).

13. S. Lupi, L. Baldassarre, B. Mansart, A. Perucchi, A. Barinov, P. Dudin, E. Papalazarou, F. Rodolakis, J. -P. Rueff, J. -P. Itié, S. Ravy, D. Nicoletti, P. Postorino, P. Hansmann, N. Parragh, A. Toschi, T. Saha-Dasgupta, O. K. Andersen, G. Sangiovanni, K. Held & M.

Marsi. A microscopic view on the Mott transition in Chromium-doped V2O3. *Nature Comm.* **1**, 105 (2010).

14. Yang Ding, Cheng-Chien Chen, Qiaoshi Zeng, Heung-Sik Kim, Myung Joon Han, Mahalingam Balasubramanian, Robert Gordon, Fangfei Li, Ligang Bai, Dimitry Popov, Steve M. Heald, Thomas Gog, Ho-kwang Mao, and Michel van Veenendaal. Novel High-Pressure Monoclinic Metallic Phase of V_2O_3. *Phys. Rev. Lett.* **112**, 056401 (2014).

15. M. K. Liu, M. Wagner, E. Abreu, S. Kittiwatanakul, A. McLeod, Z. Fei, M. Goldflam, S. Dai, M. M. Fogler, J. Lu, S. A. Wolf, R. D. Averitt, and D. N. Basov. Anisotropic Electronic State via Spontaneous Phase Separation in Strained Vanadium Dioxide Films. *Phys. Rev. Lett.* **111**, 096602 (2013).

16. Bong-Jun Kim, Yong Wook Lee, Sungyeoul Choi, Jung-Wook Lim, Sun Jin Yun, Hyun-Tak Kim, Tae-Ju Shin, and Hwa-Sick Yun. Micrometer x-ray diffraction study of VO2 films: Separation between metal-insulator transition and structural phase transition. *Phys. Rev. B* **77**, 235401 (2008).

17. P. Limelette, A. Georges, D. Jérome, P. Wzietek, P. Metcalf, J. M. Honig. Universality and Critical Behavior at the Mott Transition. *Science* **302**, 89-92 (2003).

18. S. Guénon, S. Scharinger, Siming Wang, J. G. Ramírez, D. Koelle, R. Kleiner & Ivan K. Schuller., Electrical breakdown in a V2O3 device at the insulator-to-metal transition. *Europhysics Letters* **101**, 57003 (2013).

19. Gebhard, F., *The Mott Metal-Insulator Transition: Models and Methods* (Springer Tracts in Modern Physics, Berlin, 1997).

20. M. M. Qazilbash1, M. Brehm, Byung-Gyu Chae, P.-C. Ho, G. O. Andreev, Bong-Jun Kim, Sun Jin Yun, A. V. Balatsky, M. B. Maple, F. Keilmann, Hyun-Tak Kim, & D. N. Basov. Mott Transition in VO2 Revealed by Infrared Spectroscopy and Nano-Imaging. *Science* **318**, 1750-1753 (2007).

21. Atkin, J. M., Berweger, S., Jones, A. C. & Raschke, M. B., Nano-optical imaging and spectroscopy of order, phases, and domains in complex solids. *Advances in Physics* **61** (6), 745-842 (2012).

22. Muratov, C. B., Theory of domain patterns in systems with long-range interactions of Coulomb type. *Phys. Rev. E* **66**, 066108 (2002).

23. Ortix, C., Lorenzana, J. & Di Castro, C., Universality classes for Couomb frustrated phase separation. *Physica B* **404**, 499-502 (2009).

24. Macridin, A., Jarell, M. & Maier, T., Phase separation in the Hubbard model using the dynamical cluster approximation. *Phys. Rev. B* **74**, 085104 (2006).

25. Yee, C.-H. & Balents, L., Phase Separation in Doped Mott Insulators. *Phys. Rev. X* **5**, 021007 (2015).

26. L. Baldassarre, A. Perucchi, D. Nicoletti, A. Toschi, G. Sangiovanni, K. Held, M. Capone, M. Ortolani, L. Malavasi, M. Marsi, P. Metcalf, P. Postorino, and S. Lupi. Quasiparticle

evolution and pseudogap formation in V2O3: An infrared spectroscopy study. *Phys. Rev. B* **77**, 113107 (2008).

27. Georges, A., Krauth, W. & Rozenberg, M. J., Dynamical mean-field theory of strongly correlated fermion systems and the limit of infinite dimensions. *Rev. Mode. Phys.* **68**, 3 (1996).

28. Hillenbrand, R. & Keilmann, F., Complex optical constants on a subwavelength scale. *Phys. Rev. Lett.* **85** (14), 3029-3032 (2000).

29. Park, H., Haule, K. & Kotliar, G., Cluster dynamical mean field theory of the Mott transition. *Phys. Rev. Lett.* **101**, 186403 (2008).

30. He, Z. & Millis, A. J., Photoinduced phase transitions in narrow-gap Mott insulators: The case of VO_2. *Phys. Rev. B* **93**, 115126 (2016).

31. Alexander Tselev, Evgheni Strelcov, Igor A. Luk'yanchuk, John D. Budai, Jonathan Z. Tischler, Ilia N. Ivanov, Keith Jones, Roger Proksch, Sergei V. Kalinin, & Andrei Kolmakov. Interplay between Ferroelastic and Metal-Insulator Phase Transitions in Strained Quasi-Two-Dimensional VO_2 Nanoplatelets. *Nano Letters* **10**, 2003-2011 (2010).

32. J. Laverock S. Kittiwatanakul, A. A. Zakharov, Y. R. Niu, B. Chen, S. A. Wolf, J. W. Lu, and K. E. Smith. Direct observation of decoupled structural and electronic transitions and an ambient pressure monocliniclike metallic phase of VO_2. *Phys. Rev. Lett.* **113**, 216402 (2014).

33. Roytburd, A. L., Thermodynamics of polydomain heterostructures I. Effect of macrostresses. *Appl. Phys. Lett.* **83**, 228 (1998).

34. Gao, Y. F., Lu, W. & Suo, Z., A mesophase transition in a binary monolayer on a solid surface. *Aca Materialia* **50**, 2297-2308 (2002).

35. Bratkovsky, A. M., Marais, S. C., Heine, V. & Salje, E. K. H., The theory of fluctuations and texture embryos in structural phase transitions mediated by strain. *J. of Phys.: Condensed Matter* **6**, 3679-3696 (1994).

36. J. Cao, E. Ertekin, V. Srinivasan, W. Fan, S. Huang, H. Zheng, J. W. L. Yim, D. R. Khanal, D. F. Ogletree, J. C. Grossman & J. Wu. Strain engineering and one-dimensional organization of metal–insulator domains in single-crystal vanadium dioxide beams. *Nat. Nanotechnology* **4**, 732-737 (2009).

37. Chitra, R. & Kotliar, G., Effect of Long Range Coulomb Interactions on the Mott Transition. *Phys. Rev. Lett.* **84** (16), 3678-3681 (2000).

38. Kadanoff, L. P.; Götze, W.; Hamblen, D.; Hecht, R.; Lewis, E. A. S.; Palciauskas, V. V.; Rayl, M.; & Swift, J. Static Phenomena Near Critical Points: Theory and Experiment. *Rev. Mod. Phys.* **39** (2), 395-431 (1967).

39. Shuo Liu, B. Phillabaum, E. W. Carlson, K. A. Dahmen, N. S. Vidhyadhiraja, M. M. Qazilbash, & D. N. Basov. Random Field Driven Spatial Complexity at the Mott Transition in VO_2. *Phys. Rev. Lett.* **116**, 036401 (2016).

40. Elsa Abreu, Siming Wang, Juan Gabriel Ramírez, Mengkun Liu, Jingdi Zhang, Kun Geng, Ivan K. Schuller, & Richard D. Averitt. Dynamic conductivity scaling in photoexcited V_2O_3 thin films. *Phys. Rev. B* **92**, 085130 (2015).

41. Spivak, B. & Kivelson, S. A., Transport in two dimensional electronic micro-emulsions. *Annals of Phys.* **321**, 2071-2115 (2006).

42. Ramirez, J.-G., Sharoni, A., Dubi, Y., Gomez, M. E. & Schuller, I. K., First-rder reversal curve measurements of the metal-insulator transition in VO_2: Signatures of persistent metallic domains. *Phys. Rev. B* **79**, 235110 (2009).

43. Baum, P., Yang, D.-S. & Zewail, A. H., 4D Visualization of Transitional Structures in Phase Transformations by Electron Diffraction. *Science* **318**, 788 (2007).

44. E. Arcangeletti, L. Baldassarre, D. Di Castro, S. Lupi, L. Malavasi, C. Marini, A. Perucchi, and P. Postorino. Evidence of a Pressure-Induced Metallization process in Monoclinic VO_2. *Phys. Rev. Lett.* **98**, 196406 (2007).

45. Potthoff, M. & Nolting, W., Metallic surface of a Mott insulator–Mott insulating surface of a metal. *Phys. Rev. B* **60** (11), 7834 (1999).

46. F. Rodolakis, P. Hansmann, J.-P. Rueff, A. Toschi, M. W. Haverkort, G. Sangiovanni, A. Tanaka, T. Saha-Dasgupta, O. K. Andersen, K. Held, M. Sikora, I. Alliot, J.-P. Itié, F. Baudelet, P. Wzietek, P. Metcalf, & M. Marsi. Inequivalent Routes across the Mott Transition in V_2O_3 Explored by X-Ray Absorption. *Phys. Rev. Lett.* **104**, 047401 (2010).

47. Podzorov, V., Kim, B. G., Kiryukhin, V., Gershenson, M. E. & Cheong, S.-W., Martensitic acommodation strain and the metal-insulator transition in manganites. *Phys. Rev. B* **64**, 140406(R) (2001).

48. Sakai, R., Limelette, P. & Funakubo, H., Transport properties and c/a ratio of V2O3 thin films grown on C- and R-plane sapphire substrates by pulsed laser deposition. *Applied Phyics Letters* **107**, 241901 (2015).

49. Nagaphani B. Aetukuri, Alexander X. Gray, Marc Drouard, Matteo Cossale, Li Gao, Alexander H. Reid, Roopali Kukreja, Hendrik Ohldag, Catherine A. Jenkins, Elke Arenholz, Kevin P. Roche, Hermann A. Dürr, Mahesh G. Samant, & Stuart S. P. Parkin. Control of the metal-insulator transition in vanadium dioxide by modifying orbital occupancy. *Nature Physics* **9**, 661-666 (2013).

50. Yang, H. U., Hevestreit, E., Josberger, E. E. & Raschke, M. B., A cryogenic scattering-type scanning near-field optical microscope. *Rev. Sci. Instrum.* **84**, 023701 (2013).

51. A. S. McLeod, E. van Heumen, J. G. Ramirez, S. Wang, T. Saerbeck, S. Guenon, M. Goldflam, L. Anderegg, P. Kelly, A. Mueller, M. K. Liu, I. K. Schuller, D. N. Basov. Supplementary Information to Nanotextured phase coexistence in the correlated insulator V_2O_3. *Nat. Phys.* DOI: 10.1038/NPHYS3882.